Fabrication and Optimisation of High-Performance Nanoplasmonic Sensors for Biosensing Applications

Iain Christie

MEng

Submitted in fulfilment of the requirements for the Degree of Doctor of Philosophy (Ph.D.)

School of Engineering

College of Science & Engineering

University of Glasgow

April 2024

Abstract

Plasmonic sensors are established as an effective, label-free technique for many applications. This thesis focuses on localised surface plasmon resonance (LSPR) sensors and how to optimise them for sensing applications. Although there are examples of lithographically-defined nanostructures being deployed in biosensing applications, few of these studies make attempts to use nanostructures optimised for sensing performance. For this reason, in this thesis we examine different ways of optimising plasmonic nanostructures with the aim of improving their performance in biosensing applications.

We first focus on the properties and sensing abilities of different nanostructure geometries including experimentally assessing both the bulk and localised refractive index sensitivity of different nanostructure arrays. This includes a discussion of the merits of different nanostructure geometries for different applications and the important role which resonance wavelength plays in a sensors refractive index sensing capability.

Next, we focus on the optimisation of nanostructure arrays using annealing techniques. There are few studies on the effect of annealing on the sensing performance of nanostructure arrays and this chapter serves as a discussion as to the benefits and drawbacks of thermal annealing for plasmonic nanostructure sensing arrays. As well as discussing the positive effects of annealing, remedies to the main drawback of annealing, structure deformation, are investigated. Structure deformation results in a reduced electromagnetic field concentration, resulting in diminished sensing performance. To mitigate these issues, we explore the use of a protective layer during annealing to prevent deformation as well as the use of a femtosecond laser as an alternative method for annealing.

Finally, we present work towards a cross-reactive method of sensing proteins. This begins by presenting different methods of making the plasmonic sensors reusable after proteins have adhered to the surface including optimising a cleaning protocol and investigating different surface chemistries that may allow for temporary protein interactions. This culminates in initial testing of a cross-reactive system which shows some success in discriminating between different proteins in solution without the need for specific receptors.

Table of Contents

List of Tables

List of Figures

Acknowledgements

I would first like the thank my supervisors, Prof. Alasdair Clark and Dr. William Peveler for all their support throughout the course of my research.

I must also thank Prof. Andrés Guerrero-Martínez, from Complutense University of Madrid, and Prof. Ovidio Peña-Nieto, from Polytechnic University of Madrid who collaborated with myself and Dr. Santana-Vega to conduct the studies using their femtosecond laser to anneal gold nanostructures.

I could not have completed this PhD without all of the brilliant PhD students and post-doctoral researchers I have worked with throughout the years – Olivia, Greig, Ashley, Justin, Jiajia, Hammed, Jamie, Siri and Badri – thank you all for your support and friendship.

I must reserve a special thank you for Marina (Dr. Santana Vega) without whom I would have been lost. From the day you arrived in this lab you have changed everything around you for the better. Without your constant support, guidance, friendship and (most of the time) patience, I would have never got through this thesis. Thank you.

I would also like to thank my friends, Hannah for always being there for me, Lydia for putting up with my constant jibes about her height and Greig for being awful at chess. Thank you guys.

Finally, I would like to thank my family, who have put up with listening to me moan without complain for years now. Without the constant support of my parents and siblings, I would never have made it this far in life, let alone this Ph.D. A final shoutout to all my dog's past and present, Hudson, Katie, Rosie and Walter who never failed to brighten my day.

Author's declaration

The work presented in this thesis was conducted by the author and has not previously been submitted for a degree or diploma at this university or any other institution.

Chapter 1 – Introduction

Plasmonics is the study of electron resonances at a metal/dielectric interface. This field encompasses both surface plasmon resonance and localised surface plasmon resonance. This chapter will discuss the theory behind both of these resonances and will explain the differences between the two. Following on from this, the different types of plasmonic sensors will be examined including different surface plasmon resonance setups as well as the different kind of localised surface plasmon resonance sensors, namely colloidal sensors, pinned nanoparticle sensors and lithographically-defined sensors. In addition to this, ways in which the design of localised surface plasmon resonance sensors can be adapted to optimise sensing performance is discussed including post-fabrication techniques such as annealing and the implementation of metal-insulator-metal sensors. Finally, the current state of plasmonic biosensing is reviewed including the applications seen with all different types of plasmonic sensors and how sensing performance has been improved with signal amplifiers or microfluidic systems.

1.1. Surface Plasmon Resonance

1.1.1. Conditions for Surface Plasmon Resonance

A plasmon is the oscillation of free electrons around a positively charged metal core. Surface plasmon resonance (SPR) occurs when the momentum of this plasmon in a thin sheet of metal is matched to that of incoming light at a metal/dielectric interface. This creates a surface plasmon polariton (SPP) whose momentum can be described with Equation 1.1.

$$k_{spp} = k_0 \sqrt{\frac{\varepsilon_m \varepsilon_d}{\varepsilon_m + \varepsilon_d}} \tag{1.1}$$

where: k_{spp} is the wavevector of a surface plasmon, k_o is the wavevector in free-space, ε_d is the dielectric constant of the dielectric material at the resonance interface, and ε_m is the dielectric constant of the metal.

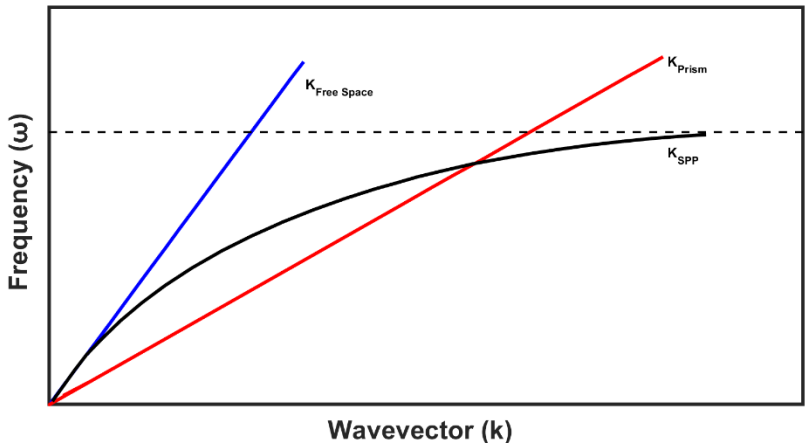

Figure 1.1 - The dispersion relation of light compared to that of surface plasmon polaritons depending on refractive index of the media (Dashed line represents the surface plasma frequency of the metal. Above this frequency the metal is unable to form a surface plasmon (1))

Figure 1.1 demonstrates that regardless of frequency, the wavevector of light in free space is never matches that of a surface plasmon resonance mode. This is because the momentum of light in a medium is a function of the refractive index of its environment (Eqn 1.2, Eqn 1.3) (2).

$$k_0 = \frac{2\pi}{\lambda} \tag{1.2}$$

$$k_x = k_0 n \sin(\theta) \tag{1.3}$$

where: k_0 is the wavevector of light in a vacuum, k_x is the wavevector of light parallel to the dielectric interface, n is the refractive index of the environment, θ is the angle of the incident light and λ is the wavelength of light.

As air has a lower refractive index than a thin film plane, the momentum indicated by this equation will never match that of the SPP at any given wavelength (Eqn 1.1). However, as this momentum is reliant on refractive index, by increasing the refractive index (or permittivity as $\varepsilon=n^2$) of the surrounding medium, we can increase the momentum of the light and cause coupling. Different setups used to accomplish this are displayed in Figure 1.2 (3).

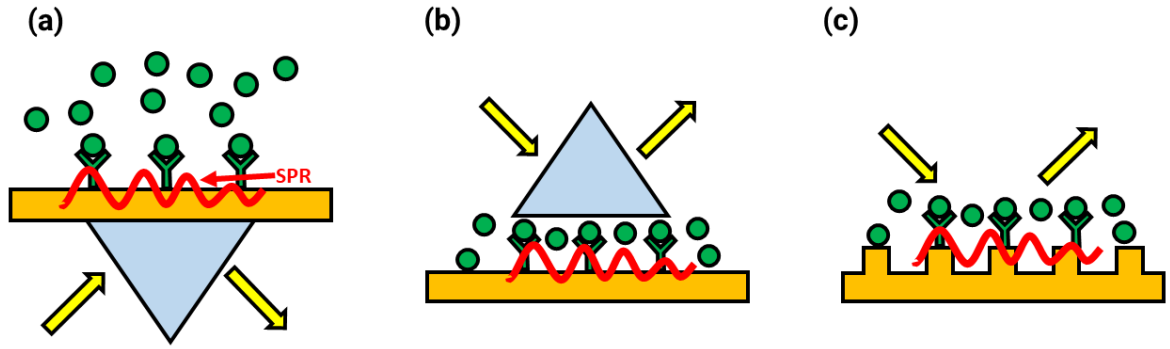

Figure 1.2 - Different setups used to measure SPR. (a) Kretshmann Setup, (b) Otto configuration and (c) using a grating coupler.

Prisms are fabricated out of high refractive index material, which increases the magnitude of the wavevector (Eqn. 1.2) causing coupling to occur indicated by the wavevectors of an SPP and light in a prism and intersecting in Figure 1.1.

$$k_{inc} = \frac{\omega_{inc}}{c} . n \tag{1.2}$$

where: ω_{inc} is the frequency of incident light, n is the refractive index of the media, c is the speed of light and k_{inc} is the wavevector of the incident light.

The most common setups used to excite SPR using a prism are the Kretshmann configuration and the Otto Configuration. In the Kretshmann configuration, a metal layer is directly applied to the surface of a coupling prism to create the conditions for SPR (Fig. 1.2(a)). In the Otto configuration, (Fig 1.2(b)) the SPP is contained within a gap between the metal and the glass prism.

Another method for coupling light to a surface plasmon is to use a grating. The grating splits the light into its constituent modes, and when the condition in Eqn. 1.3 is met, resonance will occur (Fig. 1.2(c)) (2).

$$k_{spp} = n_a \sin(\theta) + m\frac{\lambda}{\Lambda} \tag{1.3}$$

where: n_a is the refractive index of the analyte layer, θ is the angle of incident light, m is an integer, λ is the incident light wavelength and Λ is the pitch of the grating.

While a grating allows SPR resonance without the need for a bulky prism, it does come with the drawback of requiring the grating to be on the same side of the metal interface as the analyte. This means that for opaque mixtures, a grating technique is not suitable (2,4). Gratings also require precise fabrication techniques unlike prism-coupled setups.

1.1.2. Methods of Sensing using SPR

SPR is sensitive to changes in the refractive index of the surrounding medium and can be detected by monitoring four different variables: wavelength, angle, intensity, or phase (5,6). Wavelength-based and angle-based SPR detection are the most popular choice for SPR-based sensors (Fig. 1.3). Wavelength-based detection requires the sensor to be interrogated with polychromatic light which allows a full absorbance spectrum to be obtained. The peak absorbance can then be monitored to detect any refractive index change. Angle-based detection only requires monochromatic light whose incident angle on the sensor must be adjusted to find the angle of maximum absorbance as the refractive index changes. Intensity interrogation also uses a monochromatic light source, but instead of searching for the point of maximum adsorption, it monitors the change of reflected light intensity at a set wavelength. Finally, phase-based SPR sensors monitor the change in phase of reflected light at an SPR interface (7). Phase-based SPR offers higher sensitivity but requires significantly more complex optical setups and hence is much less common than the methods previously described.

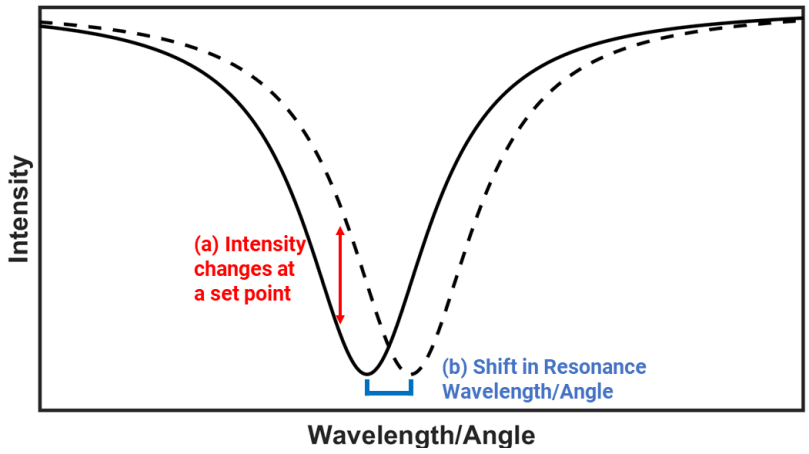

Figure 1.3 - The different methods of measuring shifts in SPR resonance. The dashed line represents an arbitrary increase in refractive index and the shift as measured by (a) wavelength/angle interrogation or (b) angle interrogation.

By applying these principles, SPR can be used as a sensing mechanism for biological molecules as will be discussed in Section 1.4.

1.2. Localised Surface Plasmon Resonance

1.2.1. Fundamentals of Localised Surface Plasmon Resonance

Localised surface plasmon resonance (LSPR) occurs when light encounters noble metal nanoparticles which are smaller than the wavelength of light. Due to the small size of the resonating structures compared to the wavelength of light, all the free electrons in the

structure resonate in response to incident light as shown in Figure 1.4. This resonance mode does not require a coupling mechanism as is needed for SPR.

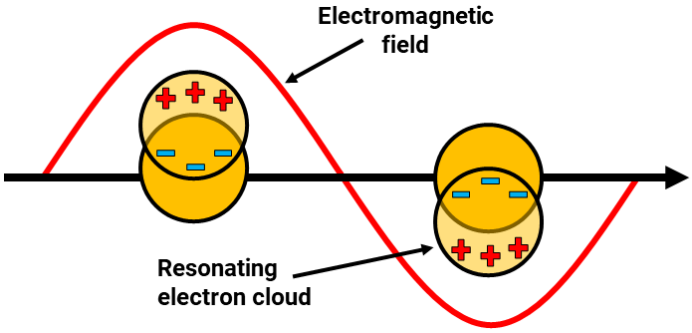

Figure 1.4 - LSPR occurs when all the free electrons of the particle resonate around the positive core.

The resonance wavelength of the metal nanoparticles is dependent on many factors such as the nanoparticle shape, size, material and, crucially, the refractive index surrounding the nanoparticle. As a representative, idealised example, the quasi-static approximation for the resonance of a spherical particle is shown in Equation 1.4 (8).

$$\alpha = 4\pi a^3 \frac{\mathrm{Re}[\varepsilon(\omega)_m] - \varepsilon_d}{\mathrm{Re}[\varepsilon(\omega)_m] + 2\varepsilon_d} \tag{1.4}$$

where: α is polarizability, a is the radius of the sphere, ε_d is the dielectric constant of the surroundings and $\varepsilon(\omega)$ is the dielectric function of the material with both real and imaginary parts as shown in Equation 1.5.

$$\varepsilon(\omega) = \varepsilon_1(\omega) + i\varepsilon_2(\omega) \tag{1.5}$$

From Eqn. 1.4 and 1.5, we can draw two conclusions. First, the resonance wavelength of an idealised particle is dictated by its dielectric function and geometry. This means that material choice and any process affecting the material properties or geometry will affect the resonance. Second, the polarizability of the particle will dramatically increase as the denominator approaches zero. This will occur when the Frohlich condition occurs (Eqn. 1.6).

$$\mathrm{Re}[\varepsilon(\omega)_m] = -2\varepsilon_d \tag{1.6}$$

This also leads us to the conclusion that as the dielectric constant (ε_d) surrounding the nanosphere increases, the resonance wavelength will increase. This concept is the basis of the biosensing applications that will be discussed in Section 1.4. By attracting analytes to the surface of a resonating structure, the resonance wavelength increases allowing the detection of different biomarkers (Fig. 1.5).

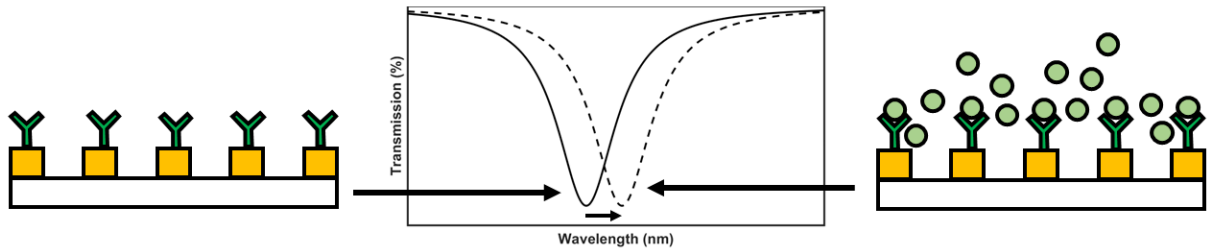

Figure 1.5 - Biosensing using LSPR sensors.

The detection mode for LSPR sensors is the same as the wavelength-based interrogation used in SPR sensors. By monitoring the transmission spectra of nanostructures as the refractive index of their surroundings changes, we can monitor events such as analyte binding.

1.2.2. LSPR Resonances

For LSPR, there are a range of different resonance types that can be created including: surface lattice resonance, fano resonance, and extraordinary optical transmission. The type of resonance created is controlled by the exact type and placement of nanostructures. This section will briefly describe these different resonances.

1.2.2.1. Surface Lattice Resonance

Surface lattice resonance (SLR) comes from the periodic arrangement of nanoparticles which under the right circumstances can result in far field coupling of the nanoparticles. This can occur when the spacing of the nanoparticles is approximately the same as their resonance wavelength, as this can create a constructive interference between the resonance of the single nanoparticle and the nanoparticles surrounding it (9,10). This results in a very narrow absorbance peak with a full-width half max (FWHM) as low as 1-2 nm.

1.2.2.2. Fano Resonance

Fano resonance is a resonance characterised by an asymmetrical spectral profile and occurs when a narrow, discrete mode and a broad, continuous mode interact with each other (11,12). In this context, a discrete mode is normally the result of the resonance of a single nanostructure whereas the continuous mode is often the resonance mode that is produced by a collection of nanostructures in an array or cluster. In plasmonic nanostructures this most often requires two different resonating structures. Examples of these resonating structures can be two nanoparticles held a defined distance apart or an array of nanoparticles lifted off a continuous metal sheet by a dielectric spacer (12,13). Regardless of how the two modes are created, for a fano resonance to occur, they interfere with each other in such a way that results in a very narrow resonance spectra which in turn will increase sensing performance.

1.2.2.3. Extraordinary Optical Transmission

According to conventional optical theory, the transmission of light through nanoholes diminishes proportionally to the fourth power of both the wavelength of the light and the radius of the hole (Fig. 1.6) (14).

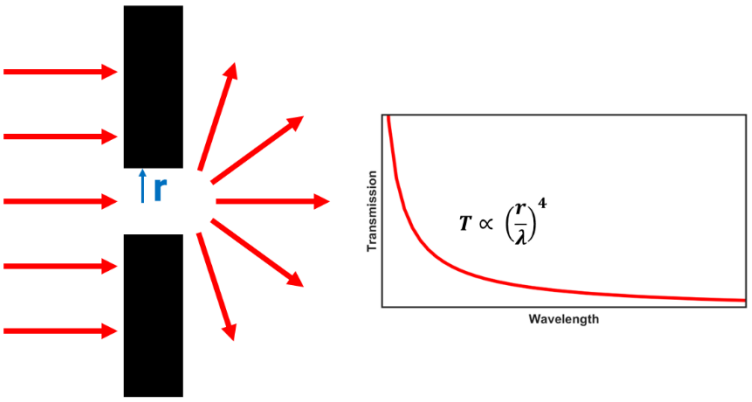

Figure 1.6 - The relation between light wavelength and transmission through a nanoaperture as defined by Bethe (14)**.**

However, when the light is incident to an array of nanoholes in a plasmonic substrate, this no longer applies. When light is incident on a nanohole or an array of nanoholes on a metal sheet, there is a significant increase in the intensity of light transmitted at a particular wavelength which cannot be explained by traditional wave theory. This is known as Extraordinary optical transmission (EOT) (15). This enhanced transmission is a result of the plasmonic properties of a nanohole array which has elements of both a SPR and a LSPR (16–18). The way the light couples to the electrons in the metal material is by coupling as a grating would for an SPR setup and these propagating surface waves in turn create a localised resonance within the nanohole itself. This light within the nanohole is then transmitted at a wavelength defined by the geometrical parameters of the nanohole array (16–18).

1.2.3. Fabricating LSPR Sensors

1.2.3.1. Choice of Plasmonic Material

LSPR can be supported by nanostructures made from many metals including copper, aluminium, silver, and gold (19–21). In addition to being an economical choice, aluminium is thought to be stable due to its oxide layer and its dielectric function allows for a degree of tunability across the UV-Vis spectra (21,22). However, aluminium has significantly higher losses when compared to silver or gold meaning its resonances are often of a lower quality and it is not biocompatible making it unsuited for any *in-vivo* application. Silver has the best resonance properties of the metals listed with minimal ohmic losses but it is unstable as a result of being prone to degradation due to oxidation (23). Gold is stable, biocompatible, has

low ohmic losses and is tuneable across a wide range of wavelengths. As a result, gold is by far the most commonly used material for LSPR sensors (24,25). Each metal has its own dielectric function which describes how its optical properties change with wavelength (26).

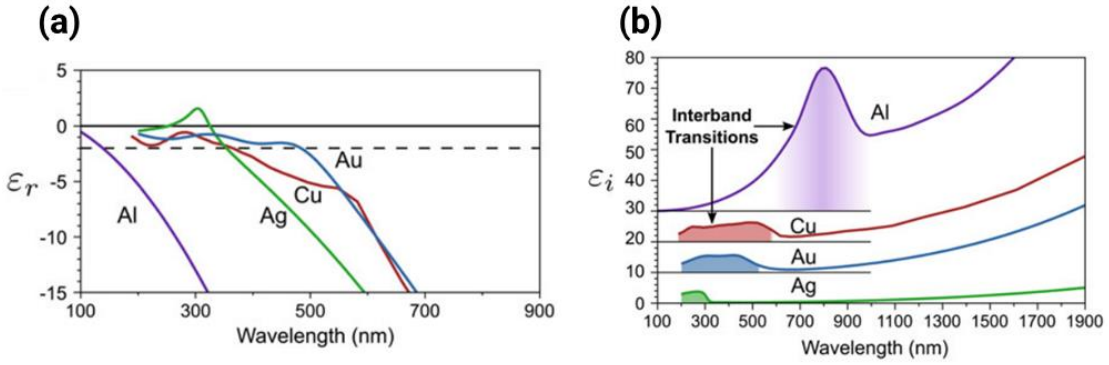

Figure 1.7 – The dielectric functions of gold, copper, aluminium and silver as adapted from (26) (a) The real component (b) The imaginary component.

The real part of the dielectric function dictates the ability of the metal to form a plasmon resonance. If the real part of the dielectric function is below zero, a plasmonic resonance can be formed whereas if it becomes positive the surface plasma frequency (Fig 1.X) has been crossed and the metal starts to act more as a dielectric (26). The imaginary part of the dielectric function dictates the losses and damping of the metal at this wavelength with a smaller imaginary value indicating lower losses (26). We can see that losses are influenced by interband transitions at different wavelengths. Fortunately, interband transitions are not a factor for gold within the wavelengths used in this thesis. From this we can see that different metals will form resonances with less losses at different wavelengths.

1.2.3.2. Colloidal Nanoparticle Sensors

Nanoparticles can be fabricated with different wet chemistry techniques. The most common technique is the Turkevich method which gives a good degree of control of spherical nanoparticles (27). In brief, gold hydrochlorate and sodium citrate are added to hot water, the citrate acts as a reducing agent and a stabiliser, causing gold nanoparticles to form and subsequently be protected by a citrate layer (27,28). By altering the temperature, concentration of reactants and reaction time, different sizes of relatively monodisperse nanoparticles can be fabricated (27,28). Other techniques are used to fabricate more complex structures including nanocages and nanostars which give colloidal nanoparticle sensors access to more complex plasmonic nanostructures (29,30).

One of the main advantages that colloidal sensors have is how inexpensive they are to create. The methods mentioned above can be carried out in most chemistry laboratories without the expense of cleanroom and lithography facilities. Drawbacks include the limited control of

geometry and the difficulty in reproducibly fabricating nanoparticles from batch to batch. Additionally, nanoparticle-based sensors are often not reusable due to the inability to unbind analytes and remove them from solution. As will be further discussed in Section 1.4.2.1, colloidal sensors are also not able to be easily integrated with microfluidics which limits their use in industrial or portable settings.

1.2.3.3. Pinned Nanoparticle Sensors

To remedy some of the drawbacks seen with colloidal sensors, nanoparticles can be pinned to a surface. Most often this occurs on a glass surface with molecules like (3-Aminopropyl)triethoxysilane (APTES) and 3-aminopropyl trimethoxysilane (AMPTES). Silane groups create a covalent bond with the glass substrate while the positively charged amine groups anchor the metallic nanoparticles to the surface via electrostatic interactions (Figure 1.7) (31–36).

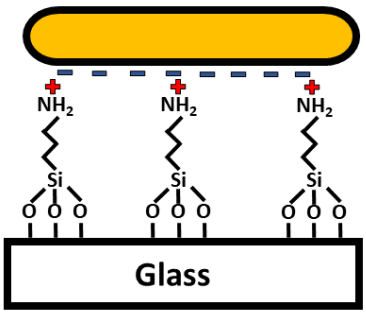

Figure 1.8 - APTES molecules pinning gold nanorods to a glass surface.

This method retains the cost-effective nature of the colloidal sensors while allowing these sensors to be integrated into microfluidic channels and opening the possibility of reusability. These advantages mean that nanoparticles pinned to a substrate are commonly used as an LSPR sensor in literature (33–39).

However, the stochastic nature of the pinning process results in nanoparticles coupling in undefined groups leading to significant broadening of the resonance of the sensor, negatively effecting sensing performance. These drawbacks can be negated if nanostructures are defined lithographically.

1.2.3.4. Lithographically Defined Structures

Lithographic techniques used to fabricate plasmonic sensors include nanosphere lithography (NSL), electron beam lithography (EBL), photolithography, focused ion-beam (FIB) lithography among others. In almost all cases, these fabrication techniques present a trade-off whereby increased resolution comes with increased fabrication time and cost.

The most cost-effective of these techniques is NSL because the process only requires a metal evaporator with the rest of the fabrication able to be done on a benchtop (40–48). In brief, the first step for NSL involves adhering polystyrene beads onto a substrate and then evaporating on a metal layer before removing the remaining polystyrene beads. By altering the conditions under which the spheres are immobilised, there is a limited degree of control over the structure's shape. The most commonly reported shapes made with NSL are triangles, nanoholes, and rings (48–50).

EBL and FIB, on the other hand, provide more control over the shape of the structure. Both EBL and FIB are direct write techniques meaning they expose each nanostructure individually. FIB accomplishes this by projecting a high energy stream of ions onto a material to etch it with a defined pattern. Long write times are a particularly pertinent issue with FIB as in addition to deflecting a beam to write each individual structure, FIB must allow time for the ions to etch through the material at each point (51–53). EBL utilises magnetic lenses to precisely control beams of electrons to expose resists in a defined pattern. By doing so, structures with features sizes below 10 nm can be repeatedly and reliably achieved. The unprecedented control EBL provides allows almost any geometry of nanoparticle to be investigated. In addition to this, by changing the tone of the resist used, EBL can be used to fabricate either positive or negative structures making it flexible as well as precise. These advantages do come at a price however, EBL is extremely expensive as it requires specialised equipment and dedicated fabrication facilities. In addition to this, EBL is difficult to scale to an industrial level of production as due to the direct-write nature of the fabrication process, each sample requires a significant period to write.

1.3. Methods of Improving LSPR Sensor Performance

1.3.1. Quantifying Sensor Performance

When defining the quality of a LSPR-based sensor there are two main variables that need to be considered: sensitivity and full width at half maximum (FWHM). Sensitivity in relation to a LSPR sensor is a measure of how much the resonance wavelength shifts with refractive index and as a result is measured in nanometres per refractive index unit (nm/RIU) (Eq. 1.6). FWHM is another important variable in determining sensor performance, generally, narrower peaks can be tracked with a greater degree of accuracy leading to better sensing performance. Often these two variables are combined into a number called Figure of Merit (FoM) (Eq. 1.8) (54–62).

$$\text{Sensitivity } \left(\frac{\text{nm}}{\text{RIU}}\right) = \frac{\Delta\lambda}{\Delta n} \tag{1.7}$$

$$\text{Figure of Merit} = \frac{\text{Sensitivity}}{\text{FWHM}} \tag{1.8}$$

where $\Delta\lambda$ is change in resonance wavelength and Δn is change in refractive index.

Sensitivity and FoM are useful metrics but for many biosensing applications they are often not fully indicative of how a sensor will perform.

When the electromagnetic (EM) field extends beyond the biomolecule interacting with the sensor's surface and into the surrounding medium, a significant portion of the field remains unaffected by the presence of the biomolecule. Consequently, this unaffected portion does not contribute to the sensor's performance. In such scenarios, a sensor that generates a stronger localized field may perform better compared to one with an extended field despite the sensor with the extended field featuring a higher FoM. This concept is illustrated in Figure 1.8.

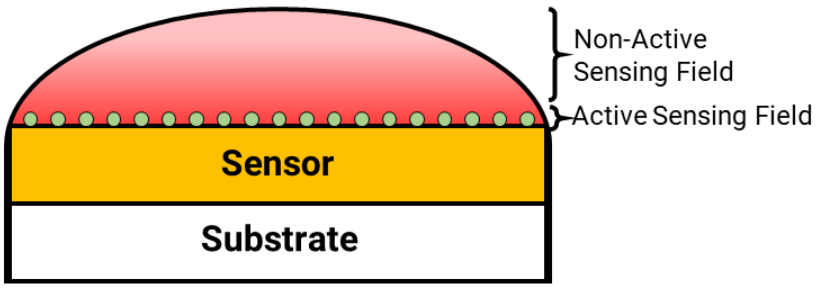

Figure 1.9 - The effect of field confinement on sensing. The more confined the field is to the surface of the sensor, the greater the sensitivity to surface bound analytes.

The reason the distinction between localised and bulk sensitivity is often dismissed lies in the difficulty to differentiate between the two. Some successful attempts to quantify localised sensitivity include EM field mapping using scattering scanning nearfield optical microscopy on gold nanostructures and functionalising gold nanostructures with monolayers of different thicknesses and assessing the relationship between chain length and resonance shift (63,64). Although these techniques are available, due to the time consuming and complex nature of these techniques, they are rarely used when discussing the design of new plasmonic structures.

1.3.2. Designing Sensors to Increase Sensitivity

1.3.2.1. Single Plane Sensor Geometry

The geometry of the plasmonic sensing elements is by far the most common and extensively explored method of increasing the sensitivity of LSPR sensors. The geometry is usually altered to create 'hotspots' which are areas of highly concentrated EM fields.

The most common ways of creating these hotspots are either through the coupling of tightly packed nanoparticles or by creating sharp vertices. Sharp vertices have been shown to increase hotspot intensity in both nanoparticles in solution and lithographically defined structures (65–76). For example, Jeon *et al*. compared the sensitivity of gold nanocubes and gold nanospheres in solution and concluded that the sharp corners of the nanocubes resulted in an increase in sensitivity (74). When looking at lithographically defined structures, bowtie dimers are a commonly utilised structure that takes advantage of sharp corners to concentrate an electromagnetic field (Fig 1.9(a)) (77–80). In addition to having sharp points, these bowtie dimers also take advantage of the coupling that occurs between resonating structures.

Coupling between nanostructures is also an established way to increase electromagnetic field intensity and hence increase localised sensitivity. Nanorods are a common model for discussing the effects of coupling with different variables being investigated such as the dimensions of the rods, the distance between the rods and the shape of the gap between the rods (66,68,81,82). The most crucial point emphasised by all these studies is that the closer the resonating structures are, the higher the magnitude of the EM field. Plasmonic elements with different geometries have been fabricated to take advantage of the high intensity electromagnetic fields created by coupling nanostructures. Split rings consist of rings with a varying number of breaks in the ring structure as displayed in Figure 1.9(b). This creates multiple sub-sections of the rings which can couple with each other during resonance.

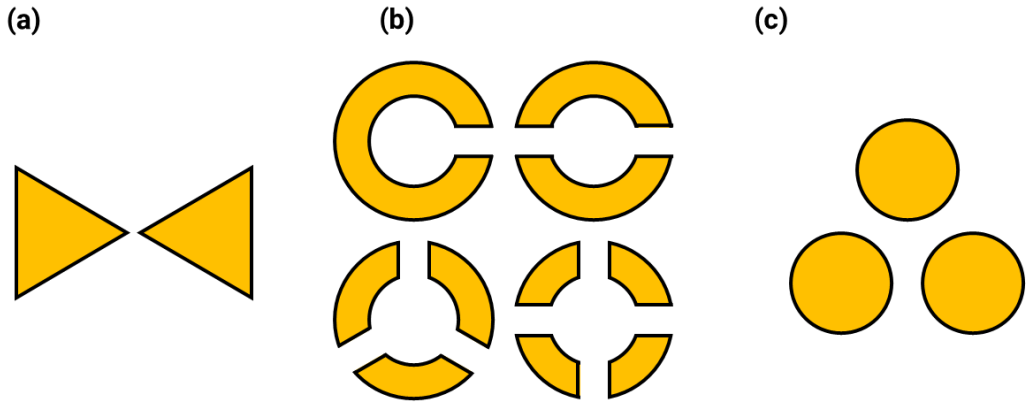

Figure 1.9 - Different plasmonic geometries explored in literature. (a) Bowtie Dimers. (b) Split rings with a varying number of splits. (c) A circle trimer.

When the rings have either one or two splits, they are found to be polarisation dependant with the polarisation dependence being almost entirely negated when the rings were tested with three, four or five splits (83). Split rings constructed of both gold and silver have been shown to be effective for concentrating the electromagnetic field (84–86). Multiple papers show the effectiveness of these rings for detecting deoxyribonucleic acid (DNA) hybridisation using surface enhanced resonance raman spectroscopy however there is little literature on the refractive index sensing capabilities of these rings (85,87). Other trimers structures seen in literature include circle trimers (Fig. 1.9(c)). The plasmonic properties of circle trimers have been experimentally examined when they have been fabricated out of both gold and silver (88,89). One paper by Lin *et al*. examines the refractive index sensing capabilities of gold circle trimers and saw that the infrared peak (~1200 nm resonance wavelength in air) had a refractive index sensitivity of 373.9 nm/RIU (101) (88).

Hollow shapes are another way in which the geometry of plasmonic elements can be manipulated to enhance EM field localisation. Hollow shapes couple with themselves within the confines of their walls creating strong electromagnetic fields. The most common of these hollow shapes are nanorings, which have been investigated as both standalone structures and as a part of dimers or trimers of nanorings (49,64,90–92). Larsson *et al.* showed both the bulk sensitivity and local sensitivity of nanorings was much higher than of solid nanodiscs confirming the potential of hollow plasmonic structures for enhancing sensing abilities (64).

When considering the geometrical parameters that can be optimised for negative structures, the literature is less extensive. Almost every study on nanohole arrays uses circular holes as they are the least complex to fabricate using techniques such as FIB or NSL (93–108). The one parameter that is often changed is the arrangement of circular holes into either a hexagonal or square lattice pattern although there is no accepted conclusion as to if one layout is superior to the other. An exception to the use of circular holes comes from Liu *et al*. who created a nanohole structure consisting of three separated rectangular holes placed to form a U-shape (109). This resulted in a refractive index sensitivity of 588 nm/RIU at a resonance wavelength of approximately 1.6 μm showing the potential of altering nanohole geometry for increasing sensing performance.

1.3.2.2. Three-Dimensional Geometry - Metal-Insulator-Metal Structures

Metal-insulator-metal (MiM) nanostructures have been employed by several groups to increase sensitivity. By holding two resonating metal structures apart with an insulator, their resonances couple which creates a hotspot between the two metal structures which increases sensitivity (13,56,65,110–121).

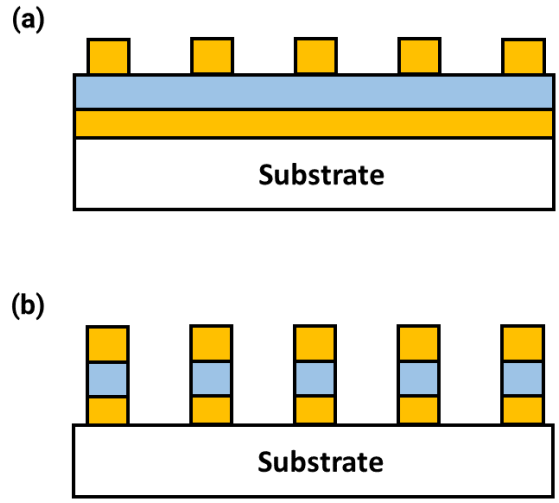

Figure 1.10 - The basic structure of MiMs. (a) A plasmonic sensor coupled to a sheet of gold through a dielectric spacer, (b) A plasmonic sensor coupled to an additional nanostructure through a dielectric spacer.

These structures have been investigated in detail and come in different forms with sensing element geometry, insulator geometry, and insulator material all varying between sensors. A particularly relevant example of the potential of MiM sensors comes from Chang *et al*. who created MiM plasmonic sensors on a flexible polydimethylsiloxane substrate (56). In doing so, they examined the sensitivity of three different types of MiM sensors defined by the number of etched layers. A single layer sensor had only one material layer with a defined geometry (Fig. 1.10(a)) whereas a tri-layer MiM sensor had all three constituent layers etched (Fig. 1.10(b)). They show experimentally that the tri-layer MiM sensor had a significantly larger sensitivity when compared to the single layer or bi-layer MiM sensors (Single layer: 210 nm/RIU, Bi-layer:1330 nm/RIU, Tri-layer:1500 nm/RIU respectively) (56). Other examples of MiM sensors combine the EM field focusing potential of previously mentioned custom plasmonic geometries with MiM setups to further increase the intensity of the EM field. Geometries that have been used in a MiM setup include bowtie dimers, nanocrosses and gold nanorings (116,118,121).

1.3.2.3. Directed Binding of Analytes

As previously described, the distribution of the electric field around a plasmonic nanostructure is not uniform with ‘hotspots’ forming at sharp points or between coupled structures. To take advantage of this, different techniques have been developed to specifically bind analytes of interest to these areas in order to allow for a larger shift per molecule bound to the sensors surface (122–127).

One method to direct analytes to hotspots utilises the way in which the stabilising molecule hexadecylcetyltrimethylammonium bromide (CTAB) is distributed around colloidal gold nanorods. Due to the curvature at the ends of gold nanorods, CTAB is less densely packed

at the ends of the rods where the plasmonic resonance is at its most intense. This means that when surface modifications such as antibodies or molecularly imprinted polymers (MIPs) are attached to these nanorods, they have a larger affinity for the areas at which the greatest EM field occurs, increasing molecular sensitivity (123,126). There are also examples of substrate bound LSPR sensors taking advantage of hotspots. Jo *et al*. passivized the top of truncated gold cones using an SiO_2 to force the analyte of interest to bind nearer to the plasmonic hotspots (124). By doing this, they were able to detect alpha fetoprotein (AFP) with a 6-fold higher limit of detection (LoD) than for uncapped structures (124). Another method of directing analyte binding to specific hotspots takes advantage of the different attachment chemistries that can be used on gold, glass, and titanium. By passivizing the gold and glass surfaces using polyethylene glycol (PEG), biomolecules can be directed to bind onto a titanium surface (122,127). This active surface can then be placed between two coupling structures which leads to a much higher shift per molecule bound as opposed to allowing biomolecules to bind over the entire structures (122,127).

A critique of these kind of techniques would be that the absolute magnitude of the plasmonic shift at the same concentration of analyte is much larger when the biomolecules are simply allowed to bind to the entire gold structures without the use of a specified active binding site. This means that unless there is a very low concentration of analyte or a very small sample volume, the benefit of these techniques may be limited.

1.3.3. Annealing

Annealing plasmonic nanostructures is an established method to increase their FoM. When metals are heated past their recrystallisation temperature, their constituent grains recrystalise resulting in bigger grains with fewer grain boundaries and a smoother surface (128). It has been shown that by reducing the number of grain boundaries and creating a smoother surface, the imaginary portion of the dielectric function (Eqn. 1.5) is reduced as there are less collision sites for resonating electrons. This causes the resonance peak to blue-shift and decreases the FWHM which increases the FoM of the sensors (129–133). This effect can be modelled with the Drude-Lorentz equation (Eqn 1.9) (134).

$$\varepsilon(\omega) = 1 - \frac{{\omega_p}^2}{\omega^2 + i\Gamma_p\omega} + \sum_m \frac{f_m {\omega_m}^2}{{\omega_m}^2 - \omega^2 - i\Gamma_m\omega} \tag{1.9}$$

where $\varepsilon(\omega)$ is the dielectric function of the gold, ω_p is the plasmon frequency, ω is the wavelength of incident light, Γ is the damping constant, f_m is the weighting of each resonance mode and ω_m is the resonance wavelength of each mode. The Drude component (1st term) of

the equation accounts for freely resonating electrons while the Lorentz component (2nd term) accounts for interband effects. By combining these two terms, we can make accurate predictions about both the resonance wavelength and resonance peak width of a metallic nanostructure. By annealing structures, the damping constant (Γ) that appears in both terms of the equation can be reduced, resulting in a narrower peak. Although many studies have observed this narrowing effect, very few discuss the effect annealing has on sensor performance in terms of localised or bulk sensing ability.

One of the main drawbacks to annealing plasmonic structures is deformation of the structures after annealing (128–131,133,135–137). As discussed in Section 1.3.2.1, geometry is an important factor in determining the sensitivity of plasmonic nanostructures. To try to maintain geometry, encapsulation layers, such as HSQ or aluminium oxide, can be used to encase the nanostructure and prevent deformation upon the partial melting of the metal (133,135,137). For example, Bosman *et al*. demonstrated a 40% increase in quality factor (Q-factor) upon annealing of single gold nanorods while using a HSQ layer to decrease the deformation experienced by the nanorods (135). Here, the Q-factor is a measure related to the bandwidth of the peak and hence an increased Q-factor indicates a narrower peak and hence better sensing performance. In a similar manner, Higashino *et al*. also used an encapsulation method on a silver nanoparticle array (137). Using atomic layer deposition, they deposited a layer of Al_2O_3 on an array of silver nanoparticles and observed a notable increase in Q-factor when the annealing temperature exceeded the melting point of silver while simultaneously maintaining the geometry of the nanostructures. Neither of these studies examine the effects this encapsulated annealing had on either localised or bulk sensitivity and so it is experimentally examined in Chapter 4.

In addition to geometry deformation, annealing changes the surface roughness of nanostructures, which can have knock-on effects to the desired ligand-binding and anchoring via self-assembled monolayer (SAM) formation on that structure (138–143). For example, gold nanostructures used in biosensing applications (Section 1.4) rely on the formation of SAMs through thiolation. The reduction in surface roughness brought about by annealing is regularly discussed in literature as a factor effecting the conformity of thiol monolayers (138–143). However, there is disagreement as to whether smooth surfaces improve or degrade the quality of SAMs. The most up to date study on the matter by Green *et al*. offers some indications as to why this disagreement may exist. Green *et al.* found that when examining the formation of decanethiol monolayers on gold, the defects on smooth and rough gold surfaces formed in different ways (139). The smooth gold surfaces in general had

a denser thiol layer but the voids in the layer were much larger on average than the ones on the rough surface which had a greater number of small voids. The larger voids on the smooth surface may have more potential to be a problem in biosensing applications when SAMs are often used as anti-fouling layers. This issue will be explored experimentally in Chapter 4.

1.4. Biosensing Applications of Plasmonic Sensors

An accurate, early diagnosis of a disease is crucial to improved health outcomes in almost all cases. Plasmonic sensors are a quick, label-free way of sensing important analytes and quantifying their concentration. This section will explore the current state of plasmonic sensors in the field of biosensing.

1.4.1. Applications of SPR Biosensors

In the early 1990's, it was demonstrated that the concentrations and binding characteristics of biological analytes in solution could be quantified using SPR (144–147). Since then, SPR sensors have been used to detect and monitor the behaviour of many different biomarkers at increasingly low concentrations. This is normally facilitated by a receptor with specificity for the analyte of interest such as an antibody or DNA aptamer. Direct detection is the simplest form of SPR sensing whereby the binding of an analyte to the surface of the SPR sensor causes a shift in resonance wavelength that can then be detected (148–150). Direct detection is particularly effective for large analytes or analytes at a high concentration. For example, Calvo-Lozano *et al*. created a SPR sensor for detecting repeatedly severe acute respiratory syndrome coronavirus 2 (SARS-COV-2) antibodies in clinical samples which reached a LoD as low as 21.1 ng/mL using specific SARS-COV-2 antigens (150).

For some analytes, getting a specific biological receptor can be a hurdle to detection. Molecularly imprinted polymers (MIPs) offer a solution to this problem. MIPs are synthetic polymers with imprinted cavities that are specific to a molecule of interest. By attaching these polymers to plasmonic sensors, they can obtain a high level of selectivity without the need for a biological receptor (151–153). Choudhary and Altintas recently published work showing how the cardiovascular disease biomarker cardiac troponin I (cTnI) could be detected down to a level of 0.52 ng/mL with a high level of specificity using a custom-made MIP (151). Despite their promise to allow for the detection of almost any molecule, MIPs still have room to improve in terms of sensitivity and robustness, for example many MIPs are affected by changes in pH which can negate their use for detecting biomarkers in certain conditions (154–156). In addition, MIPs are currently made in academic laboratories for

specific applications and hence with current production methods would not be scalable for real-world use (156).

Plasmonic sensors are not as effective when the analyte has a small mass or is at a very low concentration as the change in refractive index created by the binding of the analyte alone may be too small to be detected. A signal multiplier is a way of increasing the refractive index change created by a small analyte by attaching a larger particle to it. This aids in increasing the LoD for molecules that may otherwise be hard to detect (Fig. 1.11).

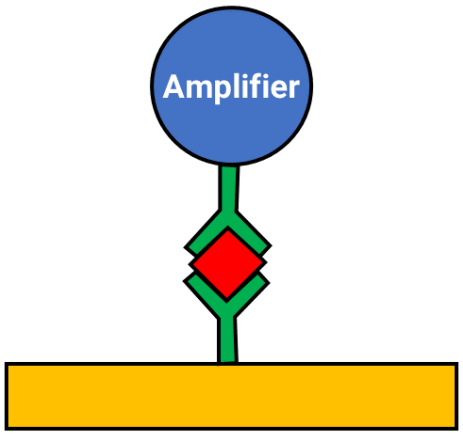

Figure 1.10 - The use of a signal multiplier to increase LoD.

These signal multipliers come in many forms including quantum dots, secondary metallic nanoparticles, or larger biological molecules which further increase the refractive index surrounding the sensor (157–162). The amplifiers can be applied to the analyte either before or after capture on the sensor surface. Amplification after the analyte is captured on the sensors surface is generally preferred as it ensures there is no alteration to the structure or behaviour of the analyte prior to capture. For example, Law *et al*. used gold nanorods coated in specific antibodies as a signal multiplier when detecting tumour necrosis factor alpha resulting in a 40-fold increase in sensor response after the signal amplifier binds (159). Although signal amplifiers increase the time and resources required for a biosensor, they can allow for the detection of either very small analytes or analytes at low concentrations meaning they can be worth the extra resources in some situations.

Traditional SPR is fundamentally limited by low throughput as only one analyte can be detected at a time. Surface Plasmon Resonance Imaging (SPRi) offers a solution to this limitation. SPRi uses a camera to monitor large areas so many different spots on the sensor can be tracked at once vastly increasing throughput. This allows for the simultaneous observation of multiple analytes by simultaneously monitoring many points on the same sensor. This kind of system can significantly reduce the time it takes to obtain binding kinetic

information when compared to running many separate experiments with traditional SPR or allow different analytes to be monitored simultaneously on the same chip (163–167). For example, Zeidan *et al*. used SPRi to monitor two biomarkers indicating renal and liver failure simultaneously down to a clinically relevant LoD of 5 pg/mL with the aid of a sandwich style signal enhancer (165). Despite the clear advantages of SPRi as a technique, it is limited by its lower sensitivity when compared to traditional SPR sensing. This loss in sensitivity is due to a few factors, one of the main ones being that SPRi sensing is normally carried out using the intensity mode of SPR sensing due to limitations of the camera monitoring the sensing array. In this mode, the noise in the excitation light source limits the ability of the sensor to detect small shifts in resonance frequency. Despite this loss of sensitivity, SPRi has the potential to be used as a quick, high-throughput diagnostic system.

1.4.2. Applications of LSPR Biosensors

LSPR is different from SPR in several crucial aspects which have the potential to improve its biosensing performance. Firstly, LSPR sensors do not require the bulky equipment needed for SPR sensing as no coupling mechanisms are required to induce plasmon resonance. Additionally, LSPR creates an EM field with a higher degree of confinement to the surface of the metallic nanoparticles. While this causes a significant reduction in bulk refractive index sensitivity, it also results in an increased sensitivity to molecular interactions close to the surface of the sensor, making it adept at detecting binding events at the surface of the nanostructure.

1.4.2.1. Colloidal LSPR Sensors

Many LSPR-based sensors utilise metal nanoparticles in a colloidal solution. As with SPR sensors, the simplest variety of these sensors take advantage of the refractive index dependence of LSPR by attracting target analytes to the surface of the nanoparticle, resulting in a shift of the plasmon resonance. In relation to biosensing, this is generally accomplished by bonding an antigen that will specifically bind to of a target analyte such as with an antibody or a DNA aptamer (168–174). Tang and Casas used this specific recognition to quantify the concentrations of different cardiac biomarkers using gold nanorods with immobilised antibodies. This approach was able to determine the concentration of myoglobin and cTnI in solution with a very high specificity and the ability to detect ng/mL concentrations of analyte (172). Alternatively, direct sensing can be accomplished with less specific recognition systems as displayed by hydrogel coated nanoparticles which are able to distinguish between protein lysozyme and lactoferrin via electrostatic interactions with the hydrogel (173). Although this non-specific sensing comes with the benefits of removing

the need for a specific receptor and the ability to detect more than one biomarker, it is limited by a significant reduction in sensitivity and LoD as well as increased interference from complex solutions.

An alternative sensing mechanism for colloidal-based LSPR sensors is nanoparticle aggregation. Aggregation sensors capitalise on the fact that the LSPR spectral profile and resonance wavelength are both dependent on nanoparticle geometry. Larger nanoparticles, or nanoparticle aggregates will resonate at longer wavelengths. Taking advantage of this, researchers have utilised a variety of methods to increase the effective size of nanoparticles upon interaction with analytes. In aggregation assays, the analyte can cause aggregation by either displacing the capping agent responsible for nanoparticle stability or by changing the environment in a way that encourages nanoparticle aggregation. This aggregation then results in larger red-shifts or the collapse of the plasmonic spectra allowing for analyte detection (175–180). Sun *et al*. utilised this approach to identify 12 different proteins with various modified nanoparticles showing different levels of aggregation depending on the specific protein that was introduced (181). In addition to sensors where the nanoparticles aggregate, systems can also work on the principle of anti-aggregation whereby analytes cause the dispersion of nanoparticle aggregates resulting in a blue-shift although these sensors are much less common (182,183).

RI-based sensors and aggregation assays are the most numerous among colloidal sensing methods, but other approaches exist. Monitoring nanoparticle growth in the presence of analytes is an alternative method for biomarker sensing which takes advantage of the fact that the mass of metal reduced onto the nanoparticle surface can be affected by environmental conditions (179,184–186). The reduction of metal ions can be caused directly by analytes as in the work published by Jafarinejad *et al*. wherein neurotransmitters acted as reduction agents to grow a silver nanoshell onto a gold seed (185). As the silver shell grows, the adsorption peak on the LSPR spectra shifts, indicating the presence of neurotransmitters. The effect of the analyte on the reduction reaction can also be indirect as shown by Guo *et al*. when detecting alkaline phosphatase (ALP) (186). As ALP is an enzyme, its concentration in solution determines the amount of ascorbic acid 2-phosphate which will be converted to ascorbic acid. The ascorbic acid in turn then causes reduction of silver ions onto a gold nanoparticle template in a concentration dependant manner giving an indirect quantification of the ALP concentration in solution (186).

Although useful in a laboratory setting, solution-based sensors can be limited. Generally, colloidal plasmonic sensors are not reusable with a non-reversible colour change used for

detection. It is also challenging to integrate solution-based sensors into fluidic setups whether in an industrial setting or in a medical laboratory as they are not attached to a surface. To overcome these limitations, many plasmonic sensors are based on nanoparticles tethered to a substrate.

1.4.2.2. Substrate-based Biosensing

Nanoparticle arrays can be fabricated on a substrate using a variety of different techniques as discussed in Section 1.2.3. Using a substrate-based system gives sensors the ability to be integrated with microfluidic systems which gives them more potential to become modular, user-friendly, portable sensors for many different applications.

1.4.2.2.1. Pinned Nanoparticles

One way to create a LSPR-based sensor on a substrate is to simply pin nanoparticles to the surface as described in Sections 1.2.3.3 and 1.2.3.4 this allows sensors to be created without the expense of lithographically defined nanofabrication. Nanoparticles can be pinned in a few different ways, the most common is via electrostatic interactions on chemically modified glass but they may also be imbedded in a polymer.

Sensors fabricated in this manner have been used to detect many different biomarkers including proteins and DNA (33–39). For example, a multiplexed DNA sensor was created using islands of gold nanoparticles pinned to a substrate using APTES (Fig. 1.7). Each island was modified with a unique DNA capture strand resulting in the sensor being able to detect five different gold nanoparticle labelled DNA strands down to a concentration of 60 nM (34). This enabled the sensors to detect five different gold nanoparticle labelled DNA strands down to an LoD of approximately 60 nM. Other studies utilising pinned nanoparticles have increased sensor performance in interesting ways. This includes pinning the nanoparticles to a surface using an alternative method such as imbedding the nanoparticles into a polymer matrix for better nanoparticle distribution and the utilisation of different sandwich style amplifiers including silver nanoparticles and secondary antibodies (35,36,187).

However, sensors based on pinned nanoparticles have their limitations. The stochastic nature of the pinning limits the reproducibility of the sensors in addition to reducing sensing performance due to spectral broadening originating from both particle inhomogeneity and random coupling of particles.

1.4.2.2.2. Lithographically Defined Structures

Lithographically-defined plasmonic structures negate the limitations of sensors constructed of pinned nanoparticles. With the ability to write arbitrary patterns both the geometry of each individual nanostructure and the packing of these nanostructures can be precisely controlled. This gives lithographically designed LSPR sensors the potential of enhanced sensing performance when compared to nanoparticles (Section 1.3.2.1).

Due to its relative affordability, NSL is widely utilised for biosensing in the literature. NSL structures are fabricated of gold or silver and often create triangular nanostructures in a distinctive pattern due to the nanosphere packing (40–48). Structures fabricated using NSL have been used to sense DNA hybridisation as well as the presence of entire cells. Hu *et al*. used a sandwich setup to anchor a biotinylated DNA sequence to a sensing surface (46). As this DNA aptamer was specific to a surface marker on Pseudomonas Aeruginosa bacteria, there was a large degree of specificity to the recognition of these cells which could be detected even in small numbers (46). Although NSL fabricated sensors have been seen to have a good ability to sense a variety of biomarkers, they are limited in terms of structure flexibility. The pattern set out on the substrate by the nanospheres can only be manipulated so much meaning it is only able to create a few different plasmonic geometries, often with limited control of the exact outcome.

As discussed in Section 1.2.3.4, EBL provides a very high resolution and is versatile in the patterns it can create but is very expensive. Despite the costs, there are plenty of example of direct-write methods being used to create plasmonic sensors for biosensing applications (96,98,100,102,188–196). The limits of detection for these applications vary significantly depending on the analyte but can be as low as the pM range. Bringing together the complimentary fields of microfluidics and plasmonic sensing, Li *et al*. recently showed a novel application of a nanohole plasmonic sensor (99). By culturing cells inside a microfluidic chamber, they could monitor their output of a specific growth factor in real time as the effluent from the cell culture flowed over the sensing region (99). In another show of the potential of microfluidics and EBL, Yavas *et al*. created a microfluidic system featuring micromechanical valves to allow for 3 different solutions to be introduced to the system in a systematic manner (196). This system allowed first for four different antibodies to be captured on separate rows of sensors, then a mix of analytes to be introduced to each different sensing region and then an amplifying step to take place in the form of more antibodies being introduced to bind to any bound analyte in a sandwich format (196). By doing this, four different breast cancer markers could be detected down to the ng/mL level, but this system

could easily be altered to utilise antibodies for any disease due to the use of microfluidics to modify the sensors (196).

Despite the successes of lithographically defined plasmonic sensors in biosensing applications, the potential of the fine resolution and high degree of control provided by direct write methods is yet to be fully explored. By utilising plasmonic geometries, the sensing performance of LSPR sensors could be further optimised.

1.5. Research Work Describe Herein

The work in this thesis is split into three main chapters. The first results chapter (Chapter 3) will discuss the properties of different plasmonic structures and how these properties may affect their sensing performance. This includes geometries that have been previously fabricated such as split rings and trimers but gives a more in-depth look at the role size plays in their properties as well as quantifying both their bulk and local sensing properties. In addition to these previously fabricated geometries, entirely novel geometries such as triangular trimers are investigated which combine the benefits of sharp points as well as coupling for enhancing the electromagnetic field. Nanohole arrays with unique plasmonic geometries are also experimentally investigated including square and triangular nanoholes on both square and hexagonal grids. This provides new insights into the geometric effects present when designing negative structures and the effects these parameters have on sensing performance. As all the structures investigated in Chapter 3 are annealed, it also serves as one of the only investigations into the properties of different plasmonic nanostructures after annealing.

Chapter 4 further compares annealed geometries to non-annealed ones, including many of the geometries discussed in Chapter 3. The benefits and drawbacks of annealing are also discussed including the effect of annealing on nanoparticle geometry and the effect of changing surface properties on the formation of SAMs. Utilising a technique similar to that presented in literature, an attempt is made to minimise the deformation associated with annealing to investigate if this can positively benefit the sensing abilities of different plasmonic geometries. Following this, an alternative method of annealing, laser excitation is compared to the more standard process of annealing using a rapid thermal annealer.

The final results chapter (Chapter 5) investigates the use of these plasmonic sensors for biosensing applications. In this case, the aim is to create a novel cross-reactive sensor for the discrimination of proteins. Towards this goal, the ability of SAMs to promote the reversable interaction of proteins with plasmonic sensors is investigated. After validating a microfluidic

system utilising a more traditional specific protein interaction, the ability of an array of modified LSPR sensors to discriminate between different protein solutions is then investigated.

References

1. Zhang Y, Min C, Dou X, Wang X, Urbach HP, Somekh MG, et al. Plasmonic tweezers: for nanoscale optical trapping and beyond. Light Sci Appl [Internet]. 2021 Mar 17;10(1):59. Available from: https://www.nature.com/articles/s41377-021-00474-0

2. Koudela I, Yee SS. Surface plasmon resonance sensors based on diffraction gratings and prism couplers: sensitivity comparison. Vol. 54, Sensors and Actuators B. 1999.

3. Kretschmann E, Raether H. Radiative Decay of Non Radiative Surface Plasmons Excited by Light. Vol. 19, Phys. Rev. Letters. 1968.

4. Long S, Cao J, Wang Y, Gao S, Xu N, Gao J, et al. Grating coupled SPR sensors using off the shelf compact discs and sensitivity dependence on grating period. Sensors and Actuators Reports. 2020 Nov 1;2(1).

5. Nguyen H, Park J, Kang S, Kim M. Surface Plasmon Resonance: A Versatile Technique for Biosensor Applications. Sensors [Internet]. 2015 May 5;15(5):10481–510. Available from: http://www.mdpi.com/1424-8220/15/5/10481

6. Zhou J, Qi Q, Wang C, Qian Y, Liu G, Wang Y, et al. Surface plasmon resonance (SPR) biosensors for food allergen detection in food matrices. Biosens Bioelectron [Internet]. 2019 Oct 1;142:111449. Available from: https://linkinghub.elsevier.com/retrieve/pii/S0956566319305287

7. Deng S, Wang P, Yu X. Phase-sensitive surface plasmon resonance sensors: Recent progress and future prospects. Vol. 17, Sensors (Switzerland). MDPI AG; 2017.

8. Maier SA. Localized Surface Plasmons. In: Plasmonics: Fundamentals and Applications [Internet]. New York, NY: Springer US; 2007. p. 65–88. Available from: http://link.springer.com/10.1007/0-387-37825-1_5

9. Cherqui C, Bourgeois MR, Wang D, Schatz GC. Plasmonic Surface Lattice Resonances: Theory and Computation. Acc Chem Res. 2019 Sep 17;52(9):2548–58.

10. Kravets VG, Kabashin A V., Barnes WL, Grigorenko AN. Plasmonic Surface Lattice Resonances: A Review of Properties and Applications. Chem Rev [Internet]. 2018 Jun 27;118(12):5912–51. Available from: https://pubs.acs.org/doi/10.1021/acs.chemrev.8b00243

11. Luk'Yanchuk B, Zheludev NI, Maier SA, Halas NJ, Nordlander P, Giessen H, et al. The Fano resonance in plasmonic nanostructures and metamaterials. Nat Mater. 2010;9(9):707–15.

12. Christ A, Ekinci Y, Solak HH, Gippius NA, Tikhodeev SG, Martin OJF. Controlling the Fano interference in a plasmonic lattice. Phys Rev B Condens Matter Mater Phys. 2007 Nov 16;76(20).

13. Nicolas R, Lévêque G, Marae-Djouda J, Montay G, Madi Y, Plain J, et al. Plasmonic mode interferences and Fano resonances in Metal-Insulator- Metal nanostructured interface. Sci Rep. 2015 Sep 24;5.

14. Bethe HA. Theory of Diffraction by Small Holes. Physical Review. 1944 Oct 1;66(7–8):163–82.

15. Ebbesen TW, Lezec HJ, Ghaemi HF, Thio T, Wolff PA. Extraordinary optical transmission through sub-wavelength hole arrays. Nature [Internet]. 1998 Feb 12;391(6668):667–9. Available from: https://www.nature.com/articles/35570

16. Genet C, Ebbesen TW. Light in tiny holes. Nature [Internet]. 2007 Jan 4;445(7123):39–46. Available from: https://www.nature.com/articles/nature05350

17. Rodrigo SG, De León-Pérez F, Martín-Moreno L. Extraordinary Optical Transmission: Fundamentals and Applications. Proceedings of the IEEE. 2016 Dec 1;104(12):2288–306.

18. Cetin AE, Dršata M, Ekşioğlu Y, Petráček J. Extraordinary Transmission Characteristics of Subwavelength Nanoholes with Rectangular Lattice. Plasmonics. 2017 Jun 1;12(3):655–61.

19. Indhu AR, Dharanya C, Dharmalingam G. Plasmonic Copper: Ways and Means of Achieving, Directing, and Utilizing Surface Plasmons. Plasmonics [Internet]. 2023 Oct 5; Available from: https://link.springer.com/10.1007/s11468-023-02034-1

20. Li W, Ren K, Zhou J. Aluminum-based localized surface plasmon resonance for biosensing. TrAC Trends in Analytical Chemistry [Internet]. 2016 Jun 1;80:486–94. Available from: https://linkinghub.elsevier.com/retrieve/pii/S0165993615300455

21. Gerard D, Gray SK. Aluminium plasmonics. J Phys D Appl Phys. 2015 May 13;48(18).

22. Martin J, Plain J. Fabrication of aluminium nanostructures for plasmonics. J Phys D Appl Phys. 2015 May 13;48(18).

23. Baburin AS, Merzlikin AM, Baryshev A V., Ryzhikov IA, Panfilov Y V., Rodionov IA. Silver-based plasmonics: golden material platform and application challenges [Invited]. Opt Mater Express [Internet]. 2019 Feb 1;9(2):611. Available from: https://opg.optica.org/abstract.cfm?URI=ome-9-2-611

24. West PR, Ishii S, Naik G V., Emani NK, Shalaev VM, Boltasseva A. Searching for better plasmonic materials. Vol. 4, Laser and Photonics Reviews. 2010. p. 795–808.

25. Naik G V., Shalaev VM, Boltasseva A. Alternative plasmonic materials: Beyond gold and silver. Vol. 25, Advanced Materials. 2013. p. 3264–94.

26. Shahbazyan T V., Stockman MI, editors. Plasmonics: Theory and Applications [Internet]. Dordrecht: Springer Netherlands; 2013. (Challenges and Advances in Computational Chemistry and Physics; vol. 15). Available from: https://link.springer.com/10.1007/978-94-007-7805-4

27. Turkevich J, Stevenson PC, Hillier J. A study of the nucleation and growth processes in the synthesis of colloidal gold. Discuss Faraday Soc [Internet]. 1951;11(2):55. Available from: http://xlink.rsc.org/?DOI=df9511100055

28. FRENS G. Controlled Nucleation for the Regulation of the Particle Size in Monodisperse Gold Suspensions. Nature Physical Science [Internet]. 1973 Jan;241(105):20–2. Available from: https://www.nature.com/articles/physci241020a0

29. Sau TK, Murphy CJ. Room temperature, high-yield synthesis of multiple shapes of gold nanoparticles in aqueous solution. J Am Chem Soc. 2004 Jul 21;126(28):8648–9.

30. An K, Hyeon T. Synthesis and biomedical applications of hollow nanostructures. Vol. 4, Nano Today. 2009. p. 359–73.

31. Chen B, Liu C, Watanabe M, Hayashi K. Layer-by-Layer Structured AuNP Sensors for Terpene Vapor Detection. IEEE Sens J [Internet]. 2013 Nov;13(11):4212–9. Available from: http://ieeexplore.ieee.org/document/6519263/

32. Hong Y, Lee E, Ku M, Suh JS, Yoon DS, Yang J. Femto-molar detection of cancer marker-protein based on immuno-nanoplasmonics at single-nanoparticle scale. Nanotechnology. 2016 Mar 24;27(18).

33. Lo KM, Lai CY, Chan HM, Ma DL, Li HW. Monitoring of DNA-protein interaction with single gold nanoparticles by localized scattering plasmon resonance spectroscopy. Methods. 2013 Dec 15;64(3):331–7.

34. Zopf D, Pittner A, Dathe A, Grosse N, Csáki A, Arstila K, et al. Plasmonic Nanosensor Array for Multiplexed DNA-based Pathogen Detection. ACS Sens [Internet]. 2019 Feb 22;4(2):335–43. Available from: https://pubs.acs.org/doi/10.1021/acssensors.8b01073

35. Ye W, Zhang W, Wang C, Li W, Yu H, Liu G. Double-layer silver nanoparticle arrays-based localised surface plasmon resonance optical sensor for sensitive detection of concanavalin A. Micro Nano Lett [Internet]. 2014 Apr;9(4):294–6. Available from: https://onlinelibrary.wiley.com/doi/10.1049/mnl.2013.0720

36. Lu M, Peng W, Lin M, Wang F, Zhang Y. Gold Nanoparticle-Enhanced Detection of DNA Hybridization by a Block Copolymer-Templating Fiber-Optic Localized Surface Plasmon Resonance Biosensor. Nanomaterials [Internet]. 2021 Mar 1;11(3):616. Available from: https://www.mdpi.com/2079-4991/11/3/616

37. Nan M, Darmawan BA, Go G, Zheng S, Lee J, Kim S, et al. Wearable Localized Surface Plasmon Resonance-Based Biosensor with Highly Sensitive and Direct Detection of Cortisol in Human Sweat. Biosensors (Basel). 2023 Feb 1;13(2).

38. Hwang Y, Koo DJ, Ferhan AR, Sut TN, Yoon BK, Cho NJ, et al. Optimizing Plasmonic Gold Nanorod Deposition on Glass Surfaces for High-Sensitivity Refractometric Biosensing. Nanomaterials. 2022 Oct 1;12(19).

39. Huang C, Bonroy K, Reekmans G, Laureyn W, Verhaegen K, De Vlaminck I, et al. Localized surface plasmon resonance biosensor integrated with microfluidic chip. Biomed Microdevices. 2009;11(4):893–901.

40. Haes AJ, Chang L, Klein WL, Van Duyne RP. Detection of a biomarker for Alzheimer's disease from synthetic and clinical samples using a nanoscale optical biosensor. J Am Chem Soc. 2005 Feb 23;127(7):2264–71.

41. Lai T, Hou Q, Yang H, Luo X, Xi M. Clinical application of a novel sliver nanoparticles biosensor based on localized surface plasmon resonance for detecting the microalbuminuria. Acta Biochim Biophys Sin (Shanghai). 2010 Nov;42(11):787–92.

42. Haes AJ, Van Duyne RP. A nanoscale optical biosensor: Sensitivity and selectivity of an approach based on the localized surface plasmon resonance spectroscopy of triangular silver nanoparticles. J Am Chem Soc. 2002 Sep 4;124(35):10596–604.

43. Yonzon CR, Jeoung E, Zou S, Schatz GC, Mrksich M, Van Duyne RP. A comparative analysis of localized and propagating surface plasmon resonance sensors: The binding of Concanavalin A to a monosaccharide functionalized self-assembled monolayer. J Am Chem Soc. 2004 Oct 6;126(39):12669–76.

44. Riboh JC, Haes AJ, McFarland AD, Yonzon CR, Van Duyne RP. A nanoscale optical biosensor: Real-time immunoassay in physiological buffer enabled by improved nanoparticle adhesion. Journal of Physical Chemistry B. 2003 Feb 27;107(8):1772–80.

45. Haes AJ, Hall WP, Chang L, Klein WL, Van Duyne RP. A localized surface plasmon resonance biosensor: First steps toward an assay for Alzheimer's disease. Nano Lett. 2004 Jun;4(6):1029–34.

46. Hu J, Fu K, Bohn PW. Whole-Cell Pseudomonas aeruginosa Localized Surface Plasmon Resonance Aptasensor. Anal Chem. 2018 Feb 6;90(3):2326–32.

47. Huang C, Ye J, Wang S, Stakenborg T, Lagae L. Gold nanoring as a sensitive plasmonic biosensor for on-chip DNA detection. Appl Phys Lett. 2012 Apr 23;100(17).

48. Xiang G, Zhang N, Zhou X. Localized surface plasmon resonance biosensing with large area of gold nanoholes fabricated by nanosphere lithography. Nanoscale Res Lett. 2010 May;5(5):818–22.

49. Pravitasari A, Negrito M, Light K, Chang WS, Link S, Sheldon M, et al. Using Particle Lithography to Tailor the Architecture of Au Nanoparticle Plasmonic Nanoring Arrays. Journal of Physical Chemistry B. 2018 Jan 18;122(2):730–6.

50. Haes AJ, Zou S, Schatz GC, Van Duyne RP. Nanoscale optical biosensor: Short range distance dependence of the localized surface plasmon resonance of noble metal nanoparticles. Journal of Physical Chemistry B. 2004 Jun 3;108(22):6961–8.

51. Wang Q, Wang L. Lab-on-fiber: plasmonic nano-arrays for sensing. Nanoscale [Internet]. 2020 Apr 14;12(14):7485–99. Available from: http://xlink.rsc.org/?DOI=D0NR00040J

52. Kasani S, Curtin K, Wu N. A review of 2D and 3D plasmonic nanostructure array patterns: fabrication, light management and sensing applications. Nanophotonics [Internet]. 2019 Dec 18;8(12):2065–89. Available from: https://www.degruyter.com/document/doi/10.1515/nanoph-2019-0158/html

53. Kim HM, Uh M, Jeong DH, Lee HY, Park JH, Lee SK. Localized surface plasmon resonance biosensor using nanopatterned gold particles on the surface of an optical fiber. Sens Actuators B Chem [Internet]. 2019 Feb 1;280:183–91. Available from: https://linkinghub.elsevier.com/retrieve/pii/S0925400518318227

54. Offermans P, Schaafsma MC, Rodriguez SRK, Zhang Y, Crego-Calama M, Brongersma SH, et al. Universal scaling of the figure of merit of plasmonic sensors. ACS Nano. 2011 Jun 28;5(6):5151–7.

55. Chang P, Liu K, Jiang J, Zhang Z, Ma J, Zhang J, et al. Performance Enhancement of the Surface Plasmon Resonance Sensor through the Annealing Process. IEEE Access. 2020;8:33990–7.

56. Chang CY, Lin HT, Lai MS, Shieh TY, Peng CC, Shih MH, et al. Flexible Localized Surface Plasmon Resonance Sensor with Metal–Insulator–Metal Nanodisks on PDMS Substrate. Sci Rep. 2018 Dec 1;8(1).

57. Otte MA, Sepúlveda B, Ni W, Juste JP, Liz-Marzán LM, Lechuga LM. Identification of the optimal spectral region for plasmonic and nanoplasmonic sensing. ACS Nano. 2010 Jan 26;4(1):349–57.

58. Ye J, van Dorpe P. Improvement of Figure of Merit for Gold Nanobar Array Plasmonic Sensors. Plasmonics. 2011 Dec;6(4):665–71.

59. Verellen N, Van Dorpe P, Huang C, Lodewijks K, Vandenbosch GAE, Lagae L, et al. Plasmon line shaping using nanocrosses for high sensitivity localized surface plasmon resonance sensing. Nano Lett. 2011 Feb 9;11(2):391–7.

60. Shen Y, Liu T, Zhu Q, Wang J, Jin C. Dislocated Double-Layered Metal Gratings: Refractive Index Sensors with High Figure of Merit. Plasmonics. 2015 Dec 1;10(6):1489–97.

61. Zhu J, Meng L na, Weng G jun, Li J jun, Zhao J wu. Improve the plasmonic optical tunability of Au nanorod by Pt coating: the application in refractive index sensing. European Physical Journal D. 2021 Jul 1;75(7).

62. Wang S, Sun X, Ding M, Peng G, Qi Y, Wang Y, et al. The investigation of an LSPR refractive index sensor based on periodic gold nanorings array. J Phys D Appl Phys. 2018 Jan 4;51(4).

63. Krug MK, Schaffernak G, Belitsch M, Gašparić M, Leitgeb V, Trügler A, et al. Mapping the local particle plasmon sensitivity with a scanning probe. Nanoscale. 2016 Sep 28;8(36):16449–54.

64. Larsson EM, Alegret J, Käll M, Sutherland DS. Sensing characteristics of NIR localized surface plasmon resonances in gold nanorings for application as ultrasensitive biosensors. Nano Lett. 2007 May;7(5):1256–63.

65. Wang B, Singh SC, Lu H, Guo C. Design of Aluminum Bowtie Nanoantenna Array with Geometrical Control to Tune LSPR from UV to Near-IR for Optical Sensing. Plasmonics. 2020 Jun 1;15(3):609–21.

66. Kessentini S, Barchiesi D, D'Andrea C, Toma A, Guillot N, Di Fabrizio E, et al. Gold Dimer Nanoantenna with Slanted Gap for Tunable LSPR and Improved SERS. The Journal of Physical Chemistry C [Internet]. 2014 Feb 13;118(6):3209–19. Available from: https://pubs.acs.org/doi/10.1021/jp409844y

67. Lu TW, Chen PY, Lee PT. Gold Bowtie-Shaped Dimer Arrays in a Stretchable Substrate with Tunable LSPR. Plasmonics. 2018 Dec 1;13(6):2183–8.

68. Stetsenko MO, Rudenko SP, Maksimenko LS, Serdega BK, Pluchery O, Snegir S V. Optical Properties of Gold Nanoparticle Assemblies on a Glass Surface. Nanoscale Res Lett. 2017;12.

69. Omrani MK, Mohammadi H, Fallah H. Ultrahigh sensitive refractive index nanosensors based on nanoshells, nanocages and nanoframes: effects of plasmon hybridization and restoring force. Sci Rep. 2021 Dec 1;11(1).

70. Chen H, Kou X, Yang Z, Ni W, Wang J. Shape- and size-dependent refractive index sensitivity of gold nanoparticles. Langmuir. 2008 May 20;24(10):5233–7.

71. Kaniber M, Schraml K, Regler A, Bartl J, Glashagen G, Flassig F, et al. Surface plasmon resonance spectroscopy of single bowtie nano-antennas using a differential reflectivity method. Sci Rep. 2016 Mar 23;6.

72. Katyal J, Soni RK. Size- and shape-dependent plasmonic properties of aluminum nanoparticles for nanosensing applications. J Mod Opt. 2013 Nov 1;60(20):1717–28.

73. Nehl CL, Hafner JH. Shape-dependent plasmon resonances of gold nanoparticles. J Mater Chem [Internet]. 2008;18(21):2415. Available from: http://xlink.rsc.org/?DOI=b714950f

74. Jeon H Bin, Tsalu PV, Ha JW. Shape Effect on the Refractive Index Sensitivity at Localized Surface Plasmon Resonance Inflection Points of Single Gold Nanocubes with Vertices. Sci Rep. 2019 Dec 1;9(1).

75. Dodson S, Haggui M, Bachelot R, Plain J, Li S, Xiong Q. Optimizing electromagnetic hotspots in plasmonic bowtie nanoantennae. Journal of Physical Chemistry Letters. 2013 Feb 7;4(3):496–501.

76. Ma WY, Yang H, Hilton JP, Lin Q, Liu JY, Huang LX, et al. A numerical investigation of the effect of vertex geometry on localized surface plasmon resonance of nanostructures. Opt Express [Internet]. 2010 Jan 18;18(2):843. Available from: https://opg.optica.org/oe/abstract.cfm?uri=oe-18-2-843

77. Mayer KM, Hafner JH. Localized Surface Plasmon Resonance Sensors. Chem Rev [Internet]. 2011 Jun 8;111(6):3828–57. Available from: https://pubs.acs.org/doi/10.1021/cr100313v

78. Hatab NA, Hsueh CH, Gaddis AL, Retterer ST, Li JH, Eres G, et al. Free-standing optical gold bowtie nanoantenna with variable gap size for enhanced Raman spectroscopy. Nano Lett. 2010 Dec 8;10(12):4952–5.

79. Wang Q, Liu L, Wang Y, Liu P, Jiang H, Xu Z, et al. Tunable Optical Nanoantennas Incorporating Bowtie Nanoantenna Arrays with Stimuli-Responsive Polymer. Sci Rep. 2015 Dec 18;5.

80. Khalil UK, Farooq W, Iqbal J, Ul Abideen Kazmi SZ, Khan AD, Ur Rehman A, et al. Design and optimization of bowtie nanoantenna for electromagnetic field enhancement. Eur Phys J Plus. 2021 Jul 1;136(7).

81. Farooq S, Rativa D, De Araujo RE. High Performance Gold Dimeric Nanorods for Plasmonic Molecular Sensing. IEEE Sens J. 2021 Jun 15;21(12):13184–91.

82. Kawawaki T, Zhang H, Nishi H, Mulvaney P, Tatsuma T. Potential-Scanning Localized Plasmon Sensing with Single and Coupled Gold Nanorods. Journal of Physical Chemistry Letters. 2017 Aug 3;8(15):3637–41.

83. Clark AW, Cooper JM. Optical properties of multiple-split nanophotonic ring antennae. Advanced Materials. 2010 Sep 22;22(36):4025–9.

84. Cleary A, Clark A, Glidle A, Cooper JM, Cumming D. Fabrication of double split metallic nanorings for Raman sensing. Microelectron Eng. 2009 Apr;86(4–6):1146–9.

85. Clark AW, Glidle A, Cumming DRS, Cooper JM. Plasmonic split-ring resonators as dichroic nanophotonic DNA biosensors. J Am Chem Soc. 2009 Dec 9;131(48):17615–9.

86. Sheridan AK, Clark AW, Glidle A, Cooper JM, Cumming DRS. Multiple plasmon resonances from gold nanostructures. Appl Phys Lett. 2007;90(14).

87. Clark AW, Cooper JM. Nanogap ring antennae as plasmonically coupled serrs substrates. Small. 2011 Jan 3;7(1):119–25.

88. Lin VK, Teo SL, Marty R, Arbouet A, Girard C, Alarcon-Llado E, et al. Dual wavelength sensing based on interacting gold nanodisk trimers. Nanotechnology. 2010;21(30).

89. Alegret J, Rindzevicius T, Pakizeh T, Alaverdyan Y, Gunnarsson L, Käll M. Plasmonic properties of silver trimers with trigonal symmetry fabricated by electron-beam lithography. Journal of Physical Chemistry C. 2008 Sep 18;112(37):14313–7.

90. Panaretos AH, Yuwen YA, Werner DH, Mayer TS. Tuning the optical response of a dimer nanoantenna using plasmonic nanoring loads. Sci Rep. 2015 May 11;5.

91. Near R, Tabor C, Duan J, Pachter R, El-Sayed M. Pronounced effects of anisotropy on plasmonic properties of nanorings fabricated by electron beam lithography. Nano Lett. 2012 Apr 11;12(4):2158–64.

92. Teo SL, Lin VK, Marty R, Large N, Llado EA, Arbouet A, et al. Gold nanoring trimers: a versatile structure for infrared sensing. Opt Express [Internet]. 2010 Oct 11;18(21):22271. Available from: https://opg.optica.org/oe/abstract.cfm?uri=oe-18-21-22271

93. Thio T, Ghaemi HF, Lezec HJ, Wolff PA, Ebbesen TW. Surface-plasmon-enhanced transmission through hole arrays in Cr films. Journal of the Optical Society of America B [Internet]. 1999 Oct 1;16(10):1743. Available from: https://opg.optica.org/abstract.cfm?URI=josab-16-10-1743

94. Wu T, Lin YW. Surface-enhanced Raman scattering active gold nanoparticle/nanohole arrays fabricated through electron beam lithography. Appl Surf Sci. 2018 Mar 30;435:1143–9.

95. Van Beijnum F, Rétif C, Smiet CB, Liu H, Lalanne P, Van Exter MP. Quasi-cylindrical wave contribution in experiments on extraordinary optical transmission. Nature. 2012 Dec 20;492(7429):411–4.

96. Ding T, Hong M, Richards AM, Wong TI, Zhou X, Drum C. Quantification of a cardiac biomarker in human serum using extraordinary optical transmission (EOT). PLoS One. 2015 Mar 16;10(3).

97. Vala M, Ertsgaard CT, Wittenberg NJ, Oh SH. Plasmonic Sensing on Symmetric Nanohole Arrays Supporting High-Q Hybrid Modes and Reflection Geometry. ACS Sens. 2019 Dec 27;4(12):3265–74.

98. Cetin AE, Etezadi D, Galarreta BC, Busson MP, Eksioglu Y, Altug H. Plasmonic Nanohole Arrays on a Robust Hybrid Substrate for Highly Sensitive Label-Free Biosensing. ACS Photonics. 2015 Aug 19;2(8):1167–74.

99. Kee JS, Lim SY, Perera AP, Zhang Y, Park MK. Plasmonic nanohole arrays for monitoring growth of bacteria and antibiotic susceptibility test. Sens Actuators B Chem. 2013;182:576–83.

100. Li X, Soler M, Özdemir CI, Belushkin A, Yesilköy F, Altug H. Plasmonic nanohole array biosensor for label-free and real-time analysis of live cell secretion. Lab Chip. 2017 Jul 7;17(13):2208–17.

101. Li N, Lu Y, Li S, Zhang Q, Wu J, Jiang J, et al. Monitoring the electrochemical responses of neurotransmitters through localized surface plasmon resonance using nanohole array. Biosens Bioelectron. 2017 Jul 15;93:241–9.

102. Monteiro JP, de Oliveira JH, Radovanovic E, Brolo AG, Girotto EM. Microfluidic Plasmonic Biosensor for Breast Cancer Antigen Detection. Plasmonics. 2016 Feb 1;11(1):45–51.

103. Zhao E, Jia P, Ebendorff-Heidepriem H, Li H, Huang P, Liu D, et al. Localized surface plasmon resonance sensing structure based on gold nanohole array on beveled fiber edge. Nanotechnology. 2017 Oct 2;28(43).

104. Im H, Shao H, Park Y Il, Peterson VM, Castro CM, Weissleder R, et al. Label-free detection and molecular profiling of exosomes with a nano-plasmonic sensor. Nat Biotechnol. 2014;32(5):490–5.

105. Yu Q, Guan P, Qin D, Golden G, Wallace PM. Inverted size-dependence of surface-enhanced Raman scattering on gold nanohole and nanodisk arrays. Nano Lett. 2008 Jul;8(7):1923–8.

106. Malani S B, Viswanath P. Impact of ordering of gold nanohole arrays on refractive index sensing. Journal of the Optical Society of America B. 2018 Oct 1;35(10):2501.

107. Ohno T, Wadell C, Inagaki S, Shi J, Nakamura Y, Matsushita S, et al. Hole-size tuning and sensing performance of hexagonal plasmonic nanohole arrays. Opt Mater Express. 2016 May 1;6(5):1594.

108. Xiong K, Emilsson G, Dahlin AB. Biosensing using plasmonic nanohole arrays with small, homogenous and tunable aperture diameters. Analyst. 2016 Jun 21;141(12):3803–10.

109. Liu N, Weiss T, Mesch M, Langguth L, Eigenthaler U, Hirscher M, et al. Planar metamaterial analogue of electromagnetically induced transparency for plasmonic sensing. Nano Lett. 2010 Apr 14;10(4):1103–7.

110. Negahdari R, Rafiee E, Kordrostami Z, Rafiei E. Sensitive MIM plasmonic biosensors for detection of hemoglobin, creatinine and cholesterol concentrations. Diam Relat Mater. 2023 Jun 1;136.

111. Miyazaki HT, Kurokawa Y. Controlled plasmon resonance in closed metal/insulator/metal nanocavities. Appl Phys Lett. 2006;89(21).

112. Chen Y, Dai J, Yan M, Qiu M. Metal-insulator-metal plasmonic absorbers: influence of lattice. Opt Express. 2014 Dec 15;22(25):30807.

113. Aoyama Y, Toyotama A, Okuzono T, Hirashima N, Imai H, Uchida F, et al. Surface Plasmon Resonance of Two-Dimensional Gold Colloidal Crystals Formed on Gold Plates. Vol. 70, Chem. Pharm. Bull. 2022.

114. Liu F, Jia H, Chen Y, Luo X, Huang M, Wang M, et al. Dual-Function Meta-Grating Based on Tunable Fano Resonance for Reflective Filter and Sensor Applications. Sensors. 2023 Jul 1;23(14).

115. Taghipour A, Heidarzadeh H. Design and Analysis of Highly Sensitive LSPR-Based Metal–Insulator–Metal Nano-Discs as a Biosensor for Fast Detection of SARS-CoV-2. Photonics. 2022 Aug 1;9(8).

116. Najem M, Carcenac F, Taliercio T, Gonzalez-Posada F. Aluminum Bowties for Plasmonic-Enhanced Infrared Sensing. Adv Opt Mater. 2022 Oct 1;10(20).

117. Malinovskis U, Popļausks R, Jurkevičiū Tė A, Dutovs A, Berzins K, Perkanuks V, et al. Optimization of Colloidal Gold Nanoparticles on Porous Anodic Aluminum Oxide Substrates for Refractometric Sensing. ACS Omega. 2022 Nov 8;7(44):40324–32.

118. Yue W, Wang Z, Yang Y, Han J, Li J, Guo Z, et al. High Performance Infrared Plasmonic Metamaterial Absorbers and Their Applications to Thin-film Sensing. Plasmonics. 2016 Dec 1;11(6):1557–63.

119. Butt MA, Khonina SN, Kazanskiy NL. Hybrid plasmonic waveguide-assisted Metal–Insulator–Metal ring resonator for refractive index sensing. J Mod Opt [Internet]. 2018 May 21;65(9):1135–40. Available from: https://www.tandfonline.com/doi/full/10.1080/09500340.2018.1427290

120. Sharma Y, Zafar R, Tharani L, Salim M. Ag-SiO2-Ag based plasmonic waveguide for refractive index sensing. In: Materials Today: Proceedings. Elsevier Ltd; 2020. p. 214–6.

121. Liu Z, Ye J. Highly controllable double Fano resonances in plasmonic metasurfaces. Nanoscale. 2016 Oct 28;8(40):17665–74.

122. Zhou X, Deeb C, Kostcheev S, Wiederrecht GP, Adam PM, Béal J, et al. Selective functionalization of the nanogap of a plasmonic dimer. ACS Photonics. 2015 Jan 21;2(1):121–9.

123. Paulo PMR, Zijlstra P, Orrit M, Garcia-Fernandez E, Pace TCS, Viana AS, et al. Tip-Specific Functionalization of Gold Nanorods for Plasmonic Biosensing: Effect of Linker Chain Length. Langmuir. 2017 Jul 5;33(26):6503–10.

124. Jo N rae, Shin YB. Enhancing biosensing sensitivity of metal nanostructures through site-selective binding. Sci Rep. 2020 Dec 1;10(1).

125. Goerlitzer ESA, Speichermann LE, Mirza TA, Mohammadi R, Vogel N. Addressing the plasmonic hotspot region by site-specific functionalization of nanostructures. Nanoscale Adv. 2020;2(1):394–400.

126. Abbas A, Tian L, Morrissey JJ, Kharasch ED, Singamaneni S. Hot spot-localized artificial antibodies for label-free plasmonic biosensing. Adv Funct Mater. 2013 Apr 12;23(14):1789–97.

127. Zhang N, Liu YJ, Yang J, Su X, Deng J, Chum CC, et al. High sensitivity molecule detection by plasmonic nanoantennas with selective binding at electromagnetic hotspots. Nanoscale. 2014 Feb 7;6(3):1416–22.

128. Chen KP, Drachev VP, Borneman JD, Kildishev A V., Shalaev VM. Drude relaxation rate in grained gold nanoantennas. Nano Lett. 2010 Mar 10;10(3):916–22.

129. Deng S, Li R, Park JE, Guan J, Choo P, Hu J, et al. Ultranarrow plasmon resonances from annealed nanoparticle lattices. 2020;117(38):23380–4.

130. Tinguely JC, Sow I, Leiner C, Grand J, Hohenau A, Felidj N, et al. Gold Nanoparticles for Plasmonic Biosensing: The Role of Metal Crystallinity and Nanoscale Roughness. Bionanoscience. 2011 Dec;1(4):128–35.

131. Oikawa S, Minamimoto H, Murakoshi K. Low-Temperature Annealing of Plasmonic Metal Arrays for Improved Light Confinement. The Journal of Physical Chemistry C [Internet]. 2022 Jan 20;126(2):1188–95. Available from: https://pubs.acs.org/doi/10.1021/acs.jpcc.1c08931

132. Zheng YB, Juluri BK, Mao X, Walker TR, Huang TJ. Systematic investigation of localized surface plasmon resonance of long-range ordered Au nanodisk arrays. J Appl Phys. 2008;103(1).

133. Zhang F, Proust J, Gérard D, Plain J, Martin J. Reduction of Plasmon Damping in Aluminum Nanoparticles with Rapid Thermal Annealing. The Journal of Physical Chemistry C [Internet]. 2017 Apr 6;121(13):7429–34. Available from: https://pubs.acs.org/doi/10.1021/acs.jpcc.7b00909

134. Li Y. Optical Properties of Plasmonic Materials. In: Plasmonic Optics Theory and Applications [Internet]. SPIE PRESS; Available from: http://ebooks.spiedigitallibrary.org/content.aspx?bookid=2051&sectionid=153917732

135. Bosman M, Zhang L, Duan H, Tan SF, Nijhuis CA, Qiu CW, et al. Encapsulated annealing: Enhancing the plasmon quality factor in lithographically-defined nanostructures. Sci Rep. 2014 Jul 2;4.

136. Holm VRA, Greve MM, Holst B. Temperature induced color change in gold nanoparticle arrays: Investigating the annealing effect on the localized surface plasmon resonance. Journal of Vacuum Science & Technology B, Nanotechnology and Microelectronics: Materials, Processing, Measurement, and Phenomena. 2016 Nov;34(6):06K501.

137. Higashino M, Murai S, Tanaka K. Improving the plasmonic response of silver nanoparticle arrays via atomic layer deposition coating and annealing above the melting point. Journal of Physical Chemistry C. 2020 Dec 17;124(50):27687–93.

138. Creager SE, Hockett LA, Rowe GK. Consequences of microscopic surface roughness for molecular self-assembly. Langmuir [Internet]. 1992 Mar 1;8(3):854–61. Available from: https://pubs.acs.org/doi/abs/10.1021/la00039a020

139. Green JBD, Clarke E, Porter MD, McDermott CA, McDermott MT, Zhong CJ, et al. On the Counter-intuitive Heterogeneous Electron Transfer Barrier Properties of Alkanethiolate Monolayers on Gold: Smooth versus Rough Surfaces. Electroanalysis. 2022 Dec 1;34(12):1936–52.

140. Li Z, Zhang L, Zeng S, Zhang M, Du E, Li B. Effect of surface pretreatment on self-assembly of thiol-modified DNA monolayers on gold electrode. Journal of Electroanalytical Chemistry. 2014 May 1;722–723:131–40.

141. Guo LH, Facci JS, McLendon G, Mosher R. Effect of Gold Topography and Surface Pretreatment on the Self-Assembly of Alkanethiol Monolayers. Langmuir [Internet]. 1994 Dec 1;10(12):4588–93. Available from: https://pubs.acs.org/doi/abs/10.1021/la00024a033

142. Losic D, Shapter JG, Gooding JJ. Atomically Flat Gold for Biomolecule Immobilization and Imaging. Aust J Chem [Internet]. 2001;54(10):643. Available from: http://www.publish.csiro.au/?paper=CH01122

143. Losic D, Shapter JG, Gooding JJ. Influence of surface topography on alkanethiol SAMs assembled from solution and by microcontact printing. Langmuir. 2001 May 29;17(11):3307–16.

144. Malmqvist M. Surface plasmon resonance for detection and measurement of antibody-antigen affinity and kinetics. Curr Opin Immunol [Internet]. 1993 Jan;5(2):282–6. Available from: https://linkinghub.elsevier.com/retrieve/pii/095279159390019O

145. Liedberg B, Nylander C, Lundström I. Biosensing with surface plasmon resonance — how it all started. Biosens Bioelectron [Internet]. 1995 Jan;10(8):i–ix. Available from: https://linkinghub.elsevier.com/retrieve/pii/0956566395969652

146. Jönsson U, Fägerstam L, Ivarsson B, Johnsson B, Karlsson R, Lundh K, et al. Real-time biospecific interaction analysis using surface plasmon resonance and a sensor chip technology. Biotechniques [Internet]. 1991 Nov;11(5):620–7. Available from: http://www.ncbi.nlm.nih.gov/pubmed/1804254

147. Fägerstam LG, Frostell-Karlsson Å, Karlsson R, Persson B, Rönnberg I. Biospecific interaction analysis using surface plasmon resonance detection applied to kinetic, binding site and concentration analysis. J Chromatogr A [Internet]. 1992 Apr;597(1–2):397–410. Available from: https://linkinghub.elsevier.com/retrieve/pii/002196739280137J

148. Su JL, Youn BS, Ji WP, Niazi JH, Yeon SK, Man BG. ssDNA aptamer-based surface plasmon resonance biosensor for the detection of retinol binding protein 4 for the early diagnosis of type 2 diabetes. Anal Chem. 2008 Apr 15;80(8):2867–73.

149. He L, Pagneux Q, Larroulet I, Serrano AY, Pesquera A, Zurutuza A, et al. Label-free femtomolar cancer biomarker detection in human serum using graphene-coated surface plasmon resonance chips. Biosens Bioelectron. 2017 Mar 15;89:606–11.

150. Calvo-Lozano O, Sierra M, Soler M, Estévez MC, Chiscano-Camón L, Ruiz-Sanmartin A, et al. Label-Free Plasmonic Biosensor for Rapid, Quantitative, and Highly Sensitive COVID-19 Serology: Implementation and Clinical Validation. Anal Chem. 2022 Jan 18;94(2):975–84.

151. Choudhary S, Altintas Z. Development of a Point-of-Care SPR Sensor for the Diagnosis of Acute Myocardial Infarction. Biosensors (Basel). 2023 Feb 1;13(2).

152. Arcadio F, Noël L, Del Prete D, Maniglio D, Seggio M, Soppera O, et al. Soft molecularly imprinted nanoparticles with simultaneous lossy mode and surface plasmon multi-resonances for femtomolar sensing of serum transferrin protein. Sci Rep. 2023 Dec 1;13(1).

153. Ertürk G, Özen H, Tümer MA, Mattiasson B, Denizli A. Microcontact imprinting based surface plasmon resonance (SPR) biosensor for real-time and ultrasensitive detection of prostate specific antigen (PSA) from clinical samples. Sens Actuators B Chem. 2016 Mar 1;224:823–32.

154. Lazarević-Pašti T, Tasić T, Milanković V, Potkonjak N. Molecularly Imprinted Plasmonic-Based Sensors for Environmental Contaminants—Current State and Future Perspectives. Chemosensors [Internet]. 2023 Jan 2;11(1):35. Available from: https://www.mdpi.com/2227-9040/11/1/35

155. Alberti G, Zanoni C, Spina S, Magnaghi L, Biesuz R. Trends in Molecularly Imprinted Polymers (MIPs)-Based Plasmonic Sensors. Chemosensors [Internet]. 2023 Feb 15;11(2):144. Available from: https://www.mdpi.com/2227-9040/11/2/144

156. Kadhem AJ, Gentile GJ, Fidalgo de Cortalezzi MM. Molecularly Imprinted Polymers (MIPs) in Sensors for Environmental and Biomedical Applications: A Review. Molecules [Internet]. 2021 Oct 15;26(20):6233. Available from: https://www.mdpi.com/1420-3049/26/20/6233

157. Kausaite-Minkstimiene A, Popov A, Kalvaityte U, Bernotiene E, Mobasheri A, Ramanaviciene A. An ultra-sensitive SPR immunosensor for quantitative determination of human cartilage oligomeric matrix protein biomarker. Biosens Bioelectron. 2023 Aug 15;234.

158. Krishnan S, Mani V, Wasalathanthri D, Kumar C V., Rusling JF. Attomolar Detection of a Cancer Biomarker Protein in Serum by Surface Plasmon Resonance Using Superparamagnetic Particle Labels. Angewandte Chemie International Edition [Internet]. 2011 Feb 22;50(5):1175–8. Available from: https://onlinelibrary.wiley.com/doi/10.1002/anie.201005607

159. Law WC, Yong KT, Baev A, Prasad PN. Sensitivity improved surface plasmon resonance biosensor for cancer biomarker detection based on plasmonic enhancement. ACS Nano. 2011 Jun 28;5(6):4858–64.

160. Altintas Z, Uludag Y, Gurbuz Y, Tothill IE. Surface plasmon resonance based immunosensor for the detection of the cancer biomarker carcinoembryonic antigen. Talanta. 2011 Oct 30;86(1):377–83.

161. Kausaite-Minkstimiene A, Popov A, Ramanaviciene A. Surface Plasmon Resonance Immunosensor with Antibody-Functionalized Magnetoplasmonic Nanoparticles for Ultrasensitive Quantification of the CD5 Biomarker. ACS Appl Mater Interfaces. 2022;

162. Moon J, Byun J, Kim H, Lim EK, Jeong J, Jung J, et al. On-site detection of aflatoxin B1 in grains by a palm-sized surface plasmon resonance sensor. Sensors (Switzerland). 2018 Feb 15;18(2).

163. Zeng Y, Zhou J, Sang W, Kong W, Qu J, Ho HP, et al. High-Sensitive Surface Plasmon Resonance Imaging Biosensor Based on Dual-Wavelength Differential Method. Front Chem [Internet]. 2021 Dec 8;9. Available from: https://www.frontiersin.org/articles/10.3389/fchem.2021.801355/full

164. Shao Y, Li Y, Gu D, Zhang K, Qu J, He J, et al. Wavelength-multiplexing phase-sensitive surface plasmon imaging sensor. Opt Lett [Internet]. 2013 May 1;38(9):1370. Available from: https://opg.optica.org/abstract.cfm?URI=ol-38-9-1370

165. Zeidan E, Li S, Zhou Z, Miller J, Sandros MG. Single-Multiplex Detection of Organ Injury Biomarkers using SPRi based Nano-Immunosensor. Sci Rep [Internet]. 2016 Oct 31;6(1):36348. Available from: https://www.nature.com/articles/srep36348

166. Malinick AS, Stuart DD, Lambert AS, Cheng Q. Surface plasmon resonance imaging (SPRi) in combination with machine learning for microarray analysis of multiple sclerosis biomarkers in whole serum. Biosens Bioelectron X [Internet]. 2022 May 1;10:100127. Available from: https://linkinghub.elsevier.com/retrieve/pii/S259013702200022X

167. Ladd J, Taylor AD, Piliarik M, Homola J, Jiang S. Label-free detection of cancer biomarker candidates using surface plasmon resonance imaging. Anal Bioanal Chem. 2009 Feb;393(4):1157–63.

168. CAO Y, JIN R, THAXTON C, MIRKIN C. A two-color-change, nanoparticle-based method for DNA detection. Talanta. 2005 Sep 15;67(3):449–55.

169. Sun W, Yuan S, Huang H, Liu N, Tan Y. A label-free biosensor based on localized surface plasmon resonance for diagnosis of tuberculosis. J Microbiol Methods. 2017 Nov 1;142:41–5.

170. Campu A, Lerouge F, Chateau D, Chaput F, Baldeck P, Parola S, et al. Gold NanoBipyramids Performing as Highly Sensitive Dual-Modal Optical Immunosensors. Anal Chem. 2018 Jul 17;90(14):8567–75.

171. Tang L, Casas J, Venkataramasubramani M. Magnetic Nanoparticle Mediated Enhancement of Localized Surface Plasmon Resonance for Ultrasensitive Bioanalytical Assay in Human Blood Plasma. Anal Chem [Internet]. 2013 Feb 5;85(3):1431–9. Available from: https://pubs.acs.org/doi/10.1021/ac302422k

172. Tang L, Casas J. Quantification of cardiac biomarkers using label-free and multiplexed gold nanorod bioprobes for myocardial infarction diagnosis. Biosens Bioelectron [Internet]. 2014 Nov 15;61:70–5. Available from: https://linkinghub.elsevier.com/retrieve/pii/S0956566314003108

173. Culver HR, Wechsler ME, Peppas NA. Label-Free Detection of Tear Biomarkers Using Hydrogel-Coated Gold Nanoshells in a Localized Surface Plasmon Resonance-Based Biosensor. ACS Nano. 2018 Sep 25;12(9):9342–54.

174. Schneider T, Jahr N, Jatschka J, Csaki A, Stranik O, Fritzsche W. Localized surface plasmon resonance (LSPR) study of DNA hybridization at single nanoparticle transducers. Journal of Nanoparticle Research. 2013 Apr 1;15(4).

175. Xia F, Zuo X, Yang R, Xiao Y, Kang D, Vallée-Bélisle A, et al. Colorimetric detection of DNA, small molecules, proteins, and ions using unmodified gold nanoparticles and conjugated polyelectrolytes. Proceedings of the National Academy of Sciences [Internet]. 2010 Jun 15;107(24):10837–41. Available from: https://pnas.org/doi/full/10.1073/pnas.1005632107

176. Mirkin CA, Letsinger RL, Mucic RC, Storhoff JJ. A DNA-based method for rationally assembling nanoparticles into macroscopic materials. Nature [Internet]. 1996 Aug;382(6592):607–9. Available from: https://www.nature.com/articles/382607a0

177. Medley CD, Smith JE, Tang Z, Wu Y, Bamrungsap S, Tan W. Gold nanoparticle-based colorimetric assay for the direct detection of cancerous cells. Anal Chem. 2008 Feb 15;80(4):1067–72.

178. Polavarapu L, Pérez-Juste J, Xu QH, Liz-Marzán LM. Optical sensing of biological, chemical and ionic species through aggregation of plasmonic nanoparticles. J Mater Chem C Mater. 2014 Sep 28;2(36):7460–76.

179. Mao J, Lu Y, Chang N, Yang J, Yang J, Zhang S, et al. A nanoplasmonic probe as a triple channel colorimetric sensor array for protein discrimination. Analyst. 2016 Jul 7;141(13):4014–7.

180. Pitou M, Papi RM, Tzavellas AN, Choli-Papadopoulou T. ssDNA-Modified Gold Nanoparticles as a Tool to Detect miRNA Biomarkers in Osteoarthritis. ACS Omega. 2023 Feb 28;8(8):7529–35.

181. Sun J, Lu Y, He L, Pang J, Yang F, Liu Y. A colorimetric sensor array for protein discrimination based on carbon nanodots-induced reversible aggregation of AuNP with GSH as a regulator. Sens Actuators B Chem. 2019 Oct 1;296.

182. Shellaiah M, Sun KW. Review on Anti-Aggregation-Enabled Colorimetric Sensing Applications of Gold and Silver Nanoparticles. Chemosensors [Internet]. 2022 Dec 16;10(12):536. Available from: https://www.mdpi.com/2227-9040/10/12/536

183. Xu H, Wang Y, Huang X, Li Y, Zhang H, Zhong X. Hg2+-mediated aggregation of gold nanoparticles for colorimetric screening of biothiols. Analyst. 2012 Feb 21;137(4):924–31.

184. He MQ, Chen S, Meng J, Shi W, Wang K, Yu YL, et al. Capping Ligand Size-Dependent LSPR Property Based on DNA Nanostructure-Mediated Morphological Evolution of Gold Nanorods for Ultrasensitive Visualization of Target DNA. Anal Chem. 2020 May 19;92(10):7054–61.

185. Jafarinejad S, Ghazi-Khansari M, Ghasemi F, Sasanpour P, Hormozi-Nezhad MR. Colorimetric Fingerprints of Gold Nanorods for Discriminating Catecholamine Neurotransmitters in Urine Samples. Sci Rep. 2017 Dec 1;7(1).

186. Guo Y, Wu J, Li J, Ju H. A plasmonic colorimetric strategy for biosensing through enzyme guided growth of silver nanoparticles on gold nanostars. Biosens Bioelectron. 2016 Apr 15;78:267–73.

187. Guo L, Kim DH. LSPR biomolecular assay with high sensitivity induced by aptamer-antigen-antibody sandwich complex. Biosens Bioelectron. 2012 Jan 15;31(1):567–70.

188. Lesuffleur A, Im H, Lindquist NC, Oh SH. Periodic nanohole arrays with shape-enhanced plasmon resonance as real-time biosensors. Appl Phys Lett. 2007;90(24).

189. Kaye S, Zeng Z, Sanders M, Chittur K, Koelle PM, Lindquist R, et al. Label-free detection of DNA hybridization with a compact LSPR-based fiber-optic sensor. Analyst. 2017 Jun 7;142(11):1974–81.

190. Aćimović SS, Ortega MA, Sanz V, Berthelot J, Garcia-Cordero JL, Renger J, et al. LSPR chip for parallel, rapid, and sensitive detection of cancer markers in serum. Nano Lett. 2014 May 14;14(5):2636–41.

191. Cinel NA, Bütün S, Özbay E. Electron beam lithography designed silver nano-disks used as label free nano-biosensors based on localized surface plasmon resonance. Opt Express [Internet]. 2012 Jan 30;20(3):2587. Available from: https://opg.optica.org/oe/abstract.cfm?uri=oe-20-3-2587

192. Lin Y, Zou Y, Mo Y, Guo J, Lindquist RG. E-Beam Patterned Gold Nanodot Arrays on Optical Fiber Tips for Localized Surface Plasmon Resonance Biochemical Sensing. Sensors [Internet]. 2010 Oct 20;10(10):9397–406. Available from: http://www.mdpi.com/1424-8220/10/10/9397

193. Sanders M, Lin Y, Wei J, Bono T, Lindquist RG. An enhanced LSPR fiber-optic nanoprobe for ultrasensitive detection of protein biomarkers. Biosens Bioelectron. 2014 Nov 15;61:95–101.

194. Sperling JR, Macias G, Neale SL, Clark AW. Multilayered Nanoplasmonic Arrays for Self-Referenced Biosensing. ACS Appl Mater Interfaces. 2018 Oct 10;10(40):34774–80.

195. Horrer A, Krieg K, Freudenberger K, Rau S, Leidner L, Gauglitz G, et al. Plasmonic vertical dimer arrays as elements for biosensing. Anal Bioanal Chem. 2015 Sep 7;407(27).

196. Yavas O, Aćimović SS, Garcia-Guirado J, Berthelot J, Dobosz P, Sanz V, et al. Self-Calibrating On-Chip Localized Surface Plasmon Resonance Sensing for Quantitative and Multiplexed Detection of Cancer Markers in Human Serum. ACS Sens. 2018 Jul 27;3(7):1376–84.

Chapter 2 – Materials and Methods

2.1. Introduction

This chapter will detail the different fabrication and characterisation methods employed in this thesis. This will include a brief explanation of the working principles of the different tools used and descriptions of the fabrication processes utilised to create the plasmonic sensors that were the basis for this thesis. In addition, descriptions and discussions of different experimental setups will be presented. The manner in which the data was analysed will also be explained and simulation parameters will be disclosed.

2.2. Simulations

Finite-Difference Time-Domain (FDTD) simulations deconstruct a simulation space into a three-dimensional grid constructed of cells with a defined size. The electric and magnetic fields within each cell of the simulation are calculated using Maxwell's equations using the neighbouring cells as inputs (1). By carrying out these calculations, the response of plasmonic structures to a pulse of light can be calculated and the behaviour of these structures can be approximated.

All simulations in this work were carried out using Ansys Lumerical. The structures were all simulated as 50 nm pillars of gold with a 2 nm titanium adhesion layer as this is a necessary component for attaching nanostructures to a glass substrate which unfortunately causes dampening of the plasmonic resonance (2–4). As an aqueous solution is the most common use case for these plasmonic nanostructures, all simulations were carried out with a background refractive index of 1.333 to match water. Gold and titanium dielectric data were obtained from the CRC library and the glass data came from the Palik library (5,6).

The grid size was set at 3 nm and the light source was polarised in the y-direction from below the glass substrate to replicate the direction of incident light in the experimental setup (Section 2.6.2). The boundaries in the XZ and YZ planes surrounding each simulation space were set to be periodic in order to replicate a metamaterial of repeating elements. Boundaries parallel to the XZ plane were perfectly matched layers to prevent reflection of transmitted light. Electromagnetic fields were recorded at the surface of each structure in the XY plane at z = 52 nm as well as being recorded through the centre of the structure along the XZ plane. All figures displayed in this thesis are from the XY plane at z = 52 nm. The magnitude of the electromagnetic fields was recorded as the absolute value without normalisation. Figure 2.1 shows a picture of the simulation setup.

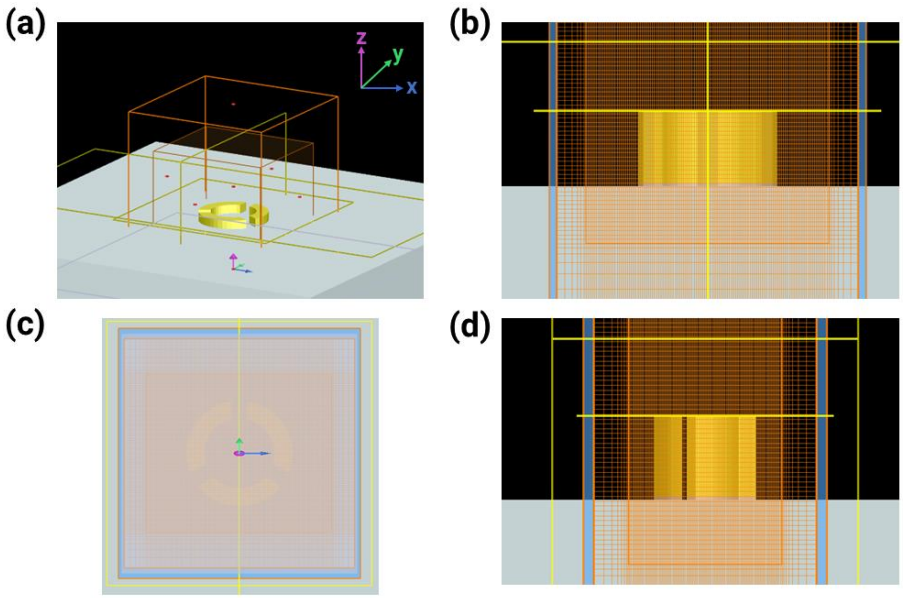

Figure 2.1 - The simulation setup. (a) An isometric view including coordinate system (b) XZ plane (c) XY plane (d) YZ plane. Light in polarised in the x-direction.

For some more complex geometries, GDSII files were imported directly from L-Edit (Siemens) to ensure an accurate replication of the structure's geometry.

2.3. Fabrication Tools and Theory

2.3.1. Electron Beam Lithography

Electron beam lithography (EBL) tools use magnetic or electrostatic lenses to focus electrons onto a substrate. These lenses allow the electron beam to be very precisely controlled to write patterns with sub-10 nm resolution onto electron beam resists. Electron beam resists come in two types, positive and negative resists. Positive resists are weakened when exposed to an electron beam as their polymer chains are broken up into shorter pieces (7). The weakened section can then be selectively removed leaving behind a hole in the resist layer creating a mask for the fabrication of nanostructures. In this thesis, polymethylmethacrylate (PMMA) is used as a positive electron beam resist. Negative resists on the other hand, cross-link when exposed to electrons meaning that exposed areas are not removed during development. Examples include Hydrogen Silsesquioxane (HSQ) and Ma-N series resists. This is useful when creating arrays of nanoholes (Section 2.4.3). Different parameters effect the patterns written using EBL. These factors include the dose, beam current and beam step size. The electron beam dose defines the amount of energy that is to be delivered to each area (measured in $\mu C/cm^2$) and hence, the exposure of the resist. The beam current defines how quickly this dose can be delivered to the sample with larger beam currents writing patterns significantly faster. This faster writing time can compromise pattern resolution as

beams with a larger current also have a larger spot size. This intrinsic trade-off of resolution versus write time is also controlled by beam step size with a smaller step between adjacent beam exposures allowing for a finer resolution while increasing write time. To determine the correct dose for writing with a given set of parameters, a dose test is carried out. This involves exposing multiple regions with incrementally increasing doses and measuring the average size of each shape against the designed shape.

Another important feature of EBL is that it requires a conductive substrate. Without the substrate grounding incoming electrons, charge will build up on the surface of the substrate causing deflection of incoming electrons which will result in a distorted pattern (Fig. 2.2).

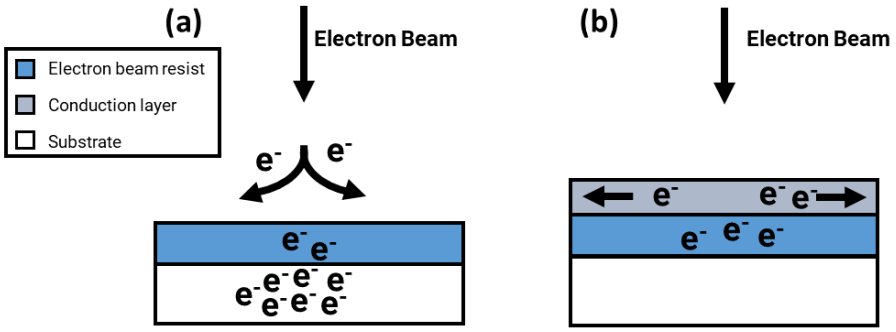

Figure 2.2 - The effect of substrate conductivity on electron beam lithography. (a) Deflection occurring without a conduction layer. (b) Electrons being conducted away through a conduction layer.

For non-conductive substrates such as glass, this issue can be overcome by applying a conductive layer such as a layer of aluminium (Fig. 2.2(b)). Another phenomenon that must be considered when using EBL is electron backscattering. Backscattered electrons elastically scatter within the substrate resulting in a larger area of the resist being exposed than initially designed. The effect of backscattered electrons can be corrected using proximity effect correction (PEC). PEC varies the dose across the extent of a pattern resulting in the centre of the pattern receiving a lower dose due to its increased exposure to backscattered electrons and the edges of the pattern receiving a larger dose. The result of the proximity effect can vary depending on the resist stack with some not requiring PEC to write consistent arrays and other resist stacks becoming almost unusable without it.

2.3.2. Metal Evaporation

In many nanofabrication processes, it is important to be able to deposit thin layers of metal onto the sample. This was accomplished using metal evaporation tools (Plassys MEB 550S, Plassys MEB 400S). The working principle of these evaporators is that by applying high currents to metal within a crucible, the metal will become molten and then a vapour. Metals are deposited under very high vacuum conditions ($1x10^{-6}$ mbar) as some more reactive

metals, such as aluminium or silver, will react with any remaining gas molecules to create oxides which reduce the purity of the deposited metal. Even for relatively unreactive metals such as gold, remaining gas molecules can interact with the substate and freshly deposited metal to pin grain boundaries which decreases sensor performance (8). The rate of metal deposition is monitored by a quartz crystal microbalance which allows precise control of both deposition rate and the layer thickness by closing a shutter between the sample and the metal source as soon as the desired thickness has been deposited.

2.3.3. Rapid Thermal Annealing

Rapid Thermal Annealing (RTA) was used to increase the quality of plasmonic sensors after fabrication by changing the grain structure of the gold (Jipelec JetFirst RTA). Using infrared halogen lamps, the RTA precisely controls both the heating rate of the devices as well as giving very accurate temperature control. In addition to this, it allows for annealing under a nitrogen atmosphere as opposed to annealing in air.

2.3.4. Oxygen Plasma Treatment

Oxygen plasma can be used to clean samples or create functional groups on the surface of a substrate (Asher PlasmaFab RF 505). Due to the high reactivity of the oxygen radicles created in the plasma, they react with and destroy any organic matter within the chamber. This can be used to clean substrates before fabrication or to clean fabricated nanostructures. In addition to this, as shown and discussed in Section 2.4.3.1, oxygen plasma can change the surface properties of a substrate which can be useful for fabrication purposes.

2.3.5. Scanning Electron Microscopy

Scanning electron microscopy (SEM) was used to characterise the fabricated nanostructures (Hitachi SU8240, Hitachi SU8230). Within an SEM, electrons are created using a cold field emission source and these electrons are focused onto the sample using electrostatic or magnetic lenses. The electrons then either scatter elastically (back-scattered electrons) or inelastically (secondary electrons) within the sample. Either type of scattered electron can be detected and used to form an image although secondary electrons are generally used for high resolution images as they are generated close to the surface of the material. Due to the use of electrons in this imaging technique, samples must be conductive for the same reasons explained in Figure 2.2. In this thesis, samples were either coated in aluminium (Plassys MEB 550S, Plassys MEB 400S) or gold/palladium to prevent charge accumulation (Agar Auto Sputter Coater). The voltage for each SEM is listed in all provided figures however the amperage was always set at 10 μA.

2.4. Fabrication of Plasmonic Sensors

2.4.1. Fabrication Design

The first step of nanostructure design is to define the pattern using L-Edit IC (Siemens). Within L-Edit the dimensions and geometries of nanostructures can be defined including the periodicity of the nanostructure arrays. These patterns are exported as a GDS file for the next step of the design process.

The next software used was Genisys Beamer where patterns are fractured to be readable by the EBL tool. Fracturing consists of breaking up patterns into simpler shapes with a fracture algorithm. In this thesis, the Large Rectangles Fine Trapezoids (LRFT) fracturing algorithm was used which fills the shape first with as many large rectangles as possible and then fills the gaps with trapezoids. In addition to fracturing the shapes, writing parameters are defined in Beamer including the beam step size, mainfield resolution and subfield resolution. Following this, a GFP file is then exported containing fractured shapes and beam placement information.

Finally, Raith Cjob is used to arrange structures onto the wafer as well as defining beam dose and beam current. This software is also where alignment parameters can be set if the job needs to be aligned to a previously fabricated layer.

2.4.2. Fabricating Positive Structures

2.4.2.1. Fabricating Positive Shapes with a PMMA Mask

Borosilicate glass wafers were cleaned by sonication in methanol, acetone and isopropyl alcohol (IPA) for 5 minutes each. A bilayer of resist was then spun onto the wafer (Layer 1: 200K molecular weight, 1% PMMA dissolved in anisole, Layer 2: 950K molecular weight, 2% PMMA dissolved in ethyl lactate. Both resists sourced from AllResist). Both layers were spun on at 4000 rpm for 60 seconds before being baked at 180 ˚C for 3 minutes to give a PMMA layer approximately 150 nm thick. Following resist deposition, a 20 nm layer of aluminium was evaporated onto the sample using a metal evaporation tool (Plassys MEB 550S, Plassys MEB 400S) to act as a conduction layer for EBL.

Table 2.1 - Parameters used for fracturing and exposure of EBL patterns.

Parameter	Setting
Resolution (writing position grid)	1 nm
Beam step size (writing grid position)	2 nm
Resolution (mainfield settings)	1 nm
Resolution (subfield settings)	0.5 nm
Fracturing (Beamer)	LRFT – high resolution
Beam size (CJob)	2 nA
Theoretical Beam Spot Size	6 nm
Dose (CJob)	800 $\mu C/cm^2$

EBL used the parameters summarised in Table 2.1. Following electron beam exposure, the aluminium conduction layer was removed using 2.5% tetramethylammonium hydroxide (TMAH) (Microposit MF CD-26 developer, Shipley). The resist, which was weakened by the electron beam exposure, was then removed from the wafer using a solution of methyl isobutyl ketone (MIBK, Merck Chemicals) and IPA (2.5:1) for 1 minute before rinsing with IPA. Following resist development, a 2 nm titanium / 50 nm gold layer was evaporated onto the wafer. Finally, the wafer was immersed in acetone and placed in a 50 ˚C water bath for an hour. With gentle circulation of acetone, the excess PMMA was then removed leaving behind the fabricated sensor. This process is summarised in Figure 2.3.

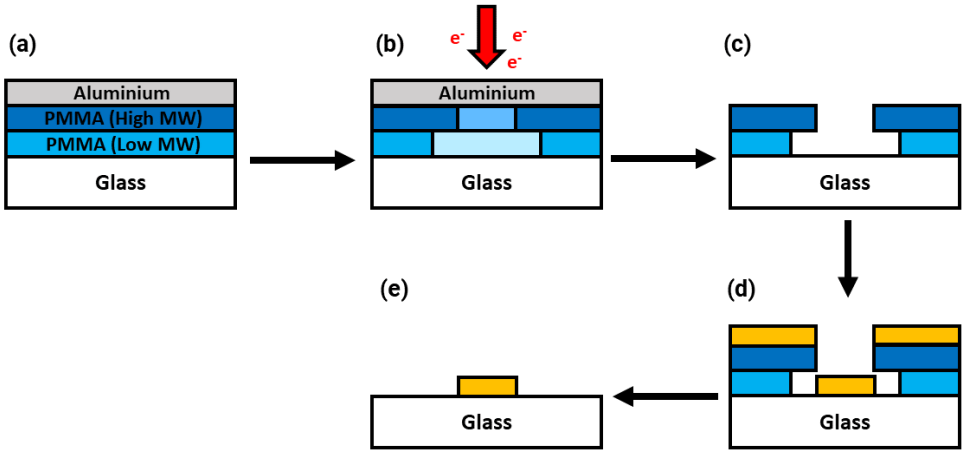

Figure 2.3 - Schematic of the fabrication of positive structures (a) Two layers of PMMA with different molecular weights (MW) are spun onto the borosilicate substrate and an aluminium layer is deposited to facilitate charge conduction. (b) EBL is used to selectively expose the PMMA resist creating weakened areas of resist. (c) The aluminium layer is removed with CD26 and MIBK is used to develop the weakened resist revealing an undercut profile. (d) A metallic bilayer of titanium and gold is deposited. (e) The excess gold and resist layers are removed by dissolving the remaining PMMA in acetone.

2.4.2.2. Annealing with a HSQ Encapsulation Layer

In an effort to mitigate the negative side effects of annealing some nanostructures were annealed with a protective HSQ (Dupont) layer (9). This was created by spinning a 1:1 HSQ:MIBK solution onto a sensor at 4000 rpm for 60 seconds and then baking it at 90 ˚C for 2 minutes. The sensor was then annealed at 500 ˚C for 10 minutes (Section 2.3.3) and

the HSQ layer then removed using 10:1 hydrofluoric (HF) acid. This process is summarised in Figure 2.4.

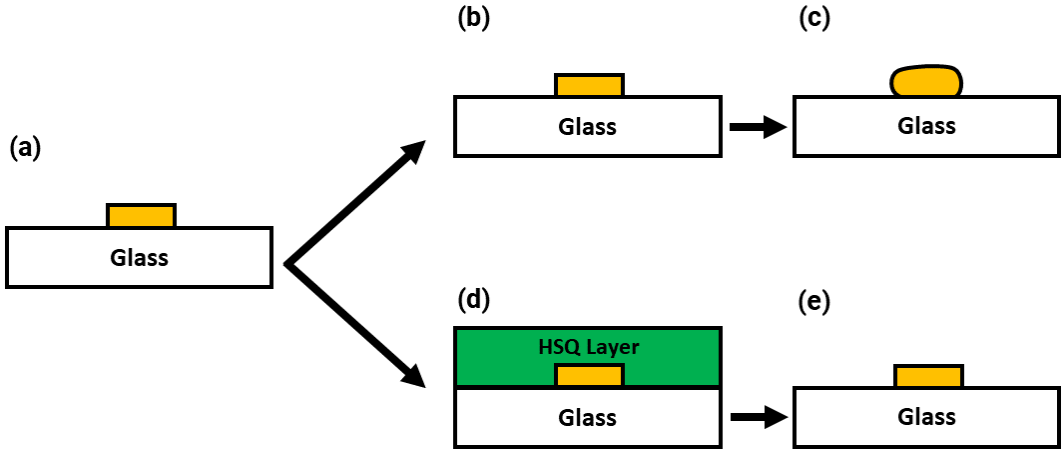

Figure 2.4 - The use of a HSQ encapsulation layer for preventing nanostructure deformation. (a) Nanostructures are fabricated as described in Section 2.3.2 (b,c) Non-encapsulated nanostructures are annealed at 500 ˚C for 10 minutes causing deformation. (d) The nanostructures are encapsulated with a HSQ layer and are annealed at 500 ˚C for 10 minutes. (e) The HSQ layer is removed using HF acid.

2.4.3. Fabricating Negative Arrays

2.4.3.1. Fabricating Nanoholes using a HSQ Mask

Initial work to fabricate nanoholes attempted to replicate a method shown in literature (10,11). First, the borosilicate glass (500 µm thickness, Pi-Kem) was cleaned by sonication in acetone and then in IPA for 5 minutes each before drying with nitrogen. A PMMA resist (AllResist – 600K molecular weight 4% in ethyl lactate) was then spun onto the substrate at 4000 rpm for 60 seconds and baked at 180 °C for 3 minutes. Following this, a 50:50 mixture of HSQ:MIBK was spun onto the sample and baked for 3 minutes at 90 °C. A 20 nm aluminium conduction layer was deposited (Plassys MEB 550S, Plassys MEB 400S) and the sample was exposed with EBL. To develop the HSQ, the sample was immersed in 25% TMAH for 30 seconds to initially removed the aluminium conduction layer and subsequently develop the HSQ layer. The sample was then exposed to oxygen plasma (RIE 80+, O_2 20 sscm, 100 W, 60 s, 50 mTorr) to remove the excess PMMA. Finally, a 2 nm titanium / 50 nm gold metallic bilayer was deposited and any excess PMMA removed by submersion in acetone at 50 ˚C resulting in an array of nanoholes (Fig. 2.5).

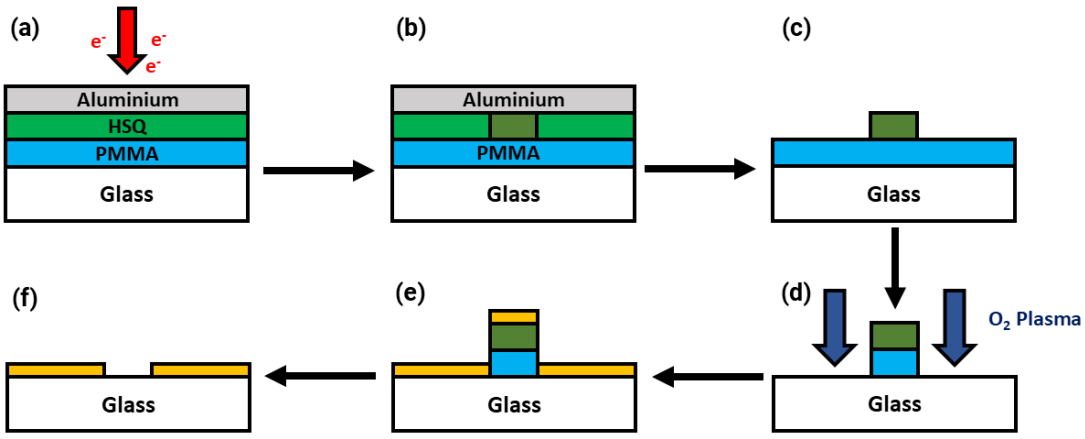

Figure 2.5 - Fabrication of nanoholes using HSQ as a mask and PMMA as a sacrificial layer. (a) Electron beam exposure on the resist stack. (b) A portion of the HSQ is cross-linked. (c) The HSQ is developed using 25% TMAH. (d) Excess PMMA is removed using directional oxygen plasma. (e) A metallic bilayer (2 nm titanium / 50 nm gold) is deposited using a metal evaporator. (f) The PMMA pillar is removed with acetone to give a nanohole.

Using the protocol previously described, nanoholes were fabricated with electron beam doses ranging from 600 to 2350 μC/cm^2 (Fig. 2.6).

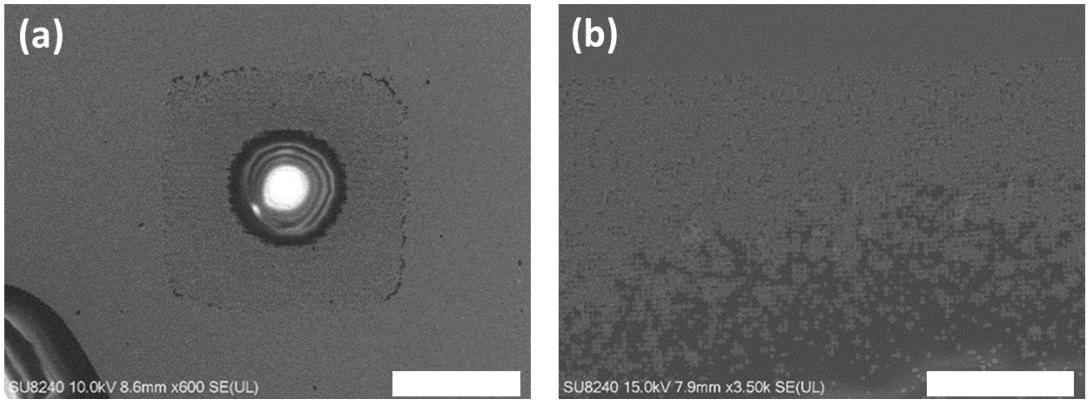

Figure 2.6 - The proximity effect causing mis-fabrication of nanohole arrays. (a) A 600x magnification SEM of a sensor region at 900 μC/cm^2 (Scale bar: 50 μm). (b) A magnified image (3.5K x) of the edge of the sensing region at 1200 μC/cm^2 (Scale bar: 10 μm)

Regardless of the applied dose, the initial trials showed a clear pattern of the proximity effect with the centre being overdosed and the edges being underdosed.

Monte Carlo simulations were performed (GenISys TRACER) to adjust the dose radially to account for the backscattering of electrons and create a dose profile to correct for the proximity effect. The following trials showed improvement with larger regions of successfully fabricated nanoholes, but the same proximity effect issues persisted (Fig. 2.7).

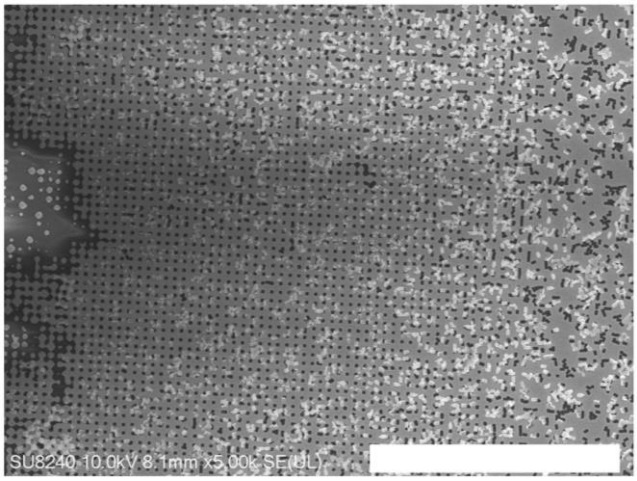

Figure 2.7 - Improvement in the HSQ fabrication process when PEC is applied. (Scale bar: 10 µm)

In addition to the persistent issues with the proximity effect, Figure 2.7 shows the difficulty with lifting off the HSQ. Often after the PMMA dissolved, the remaining gold and HSQ would remain adhered to the surface. The aforementioned problems with this fabrication technique resulted in it being discarded as, despite the quoted resolution being higher than that of a traditional negative resist, the persistent issues with the proximity effect make it unsuitable for writing negative arrays of discrete features.

2.4.3.2. Fabricating Nanoholes using Ma-N Series Resist

To fabricate nanoholes using Ma-N series resists (Microresist Technology), borosilicate glass (500 µm thickness, Pi-Kem) was first cleaned in an ultrasonic bath for 5 minutes in acetone followed by 5 minutes in IPA. The glass was then exposed to oxygen plasma at 150 W for 3 minutes. This served the double purpose of both ensuring the glass is clean and promoting adhesion by creating hydroxyl groups on the surface of the glass giving it hydrophilic properties. Without the exposure to oxygen plasma, the Ma-N 2401/2403 resist would not adhere to the substrate. After oxygen plasma, the resist was spun on at 3000 rpm for 30 seconds and baked at 90 °C for 3 minutes. The sample was then coated in 20 nm of aluminium to act as a charge conduction layer before being exposed using EBL. The EBL parameters used were identical to Table 2.1, except the dose which was increased from 800 µC/cm^2 to 1200 µC/cm^2. Following exposure, the sample which was immersed in 2.5% TMAH solution (Microposit MF-319, Shipley) for 4.5 minutes. The first 90 seconds of TMAH exposure removed the aluminium conduction layer with the remaining 3 minutes developing the resist. The sample was coated with a metal bilayer of 2 nm of titanium and 50 nm of gold with the excess resist being removed using an N-Methyl-2-pyrrolidone (NMP) based developer for 2 hours (Microposit Remover 1165, Shipley) in a 50 ˚C water bath. A summary of this process and a completed nanohole array can be seen in Figure 2.8.

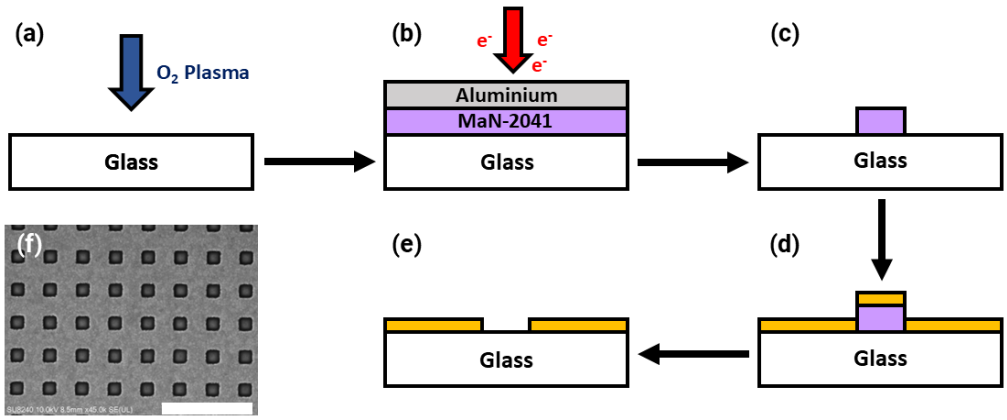

Figure 2.8 - Summary of the fabrication process using Ma-N Series resist to create nanohole arrays. (a) Glass is cleaned/activated with oxygen plasma. (b) The resist is exposed with EBL. (c) The resist cross-linked by the electron beam remains after development in Microposit MF-319. (d) A metallic bilayer (2 nm titanium / 50 nm gold) is deposited using a metal evaporator. (e) Removal of the remaining Ma-N resist with Microposit Remover 1165 to create a nanohole array. (f) An SEM image of a resulting nanohole array (Scale bar: 1 µm)

2.5. Sensor Modification

2.5.1. Thiol Modifications of Gold Sensors

Creating self-assembled monolayers on gold nanostructures relies on the coordination bond that forms between sulphur and gold atoms. This bond means that thiols will bind to and arrange themselves as a monolayer on gold surfaces (12–16). To create a monolayer, sensors are immersed in 10 mM thiol solutions with either an aqueous or ethanolic solvent. The gold nanostructures are then left for approximately 8 hours in the thiol solution to allow thiols to bind to the surface and rearrange to form a monolayer.

2.5.2. Silane Modification of Glass Substrates

Silane monolayers on glass substrates were created using gas-phase deposition (17,18). This was accomplished by placing the sensors inside a desiccator along with a small volume of the desired silane and then pumping the setup down to a low pressure causing the silane to become a vapour. This setup is then left for approximately 8 hours and the gas phase silane forms a monolayer on the glass substrate. Before use, the substrate is rinsed with methanol to remove any excess silane.

2.5.3. Modification with a Non-Contact Liquid Dispenser

For some experiments, many different modifications were required to be placed on the same substrate. One way to accomplish this is to use a non-contact liquid dispenser (Dispendix I.DOT). The printer was programmatically used to dispense 100 nL droplets onto precise locations on a microscope slide. In this case, 20 mM thiol solutions were printed onto each sensor with either an aqueous solvent or a solvent consisting of an 80/20 ratio of ethanol to ethylene glycol. To prevent these nanodroplets from mixing, a fluorous silane background

((heptadecafluoro-1,1,2,2-tetrahydrodecyl) trichlorisilane) is deposited around each sensing region using a photoresist mask. The mask consists of photoresist pillars created using S1818 resist which was exposed with a dose of 90 mJ/cm^2 and developed in a solution of 50:50 reverse osmosis water and Microposit developer for 2 minutes before silane deposition (Suss MA8 Mask Aligner). After silane monolayer formation, the remaining photoresist is stripped with 50 ˚C acetone. With the thiol droplets now pinned to the sensing regions, they were then incubated on the sensor overnight at 4 ˚C in a humid environment to minimise evaporation. After modification, the sensors were rinsed with ethanol to remove any excess thiol. Figure 2.9 depicts this process visually.

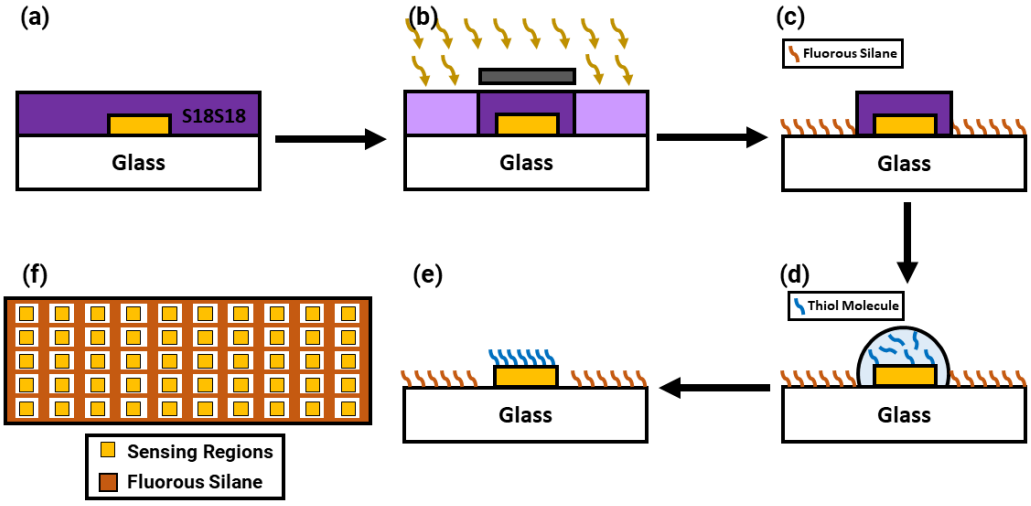

Figure 2.9 - Summary of the process used for pinning thiol droplets onto sensing regions. (a) The sensing regions are coated with S1818 photoresist. (b) The resist is exposed using a mask aligner. (c) The resist is developed using Microposit developer and a fluorous silane is deposited via gas-phase modification. (d) The thiol solutions are printed onto each sensing region and left for approximately 8 hours to create a monolayer. (e) The remaining thiol is rinsed off using ethanol leaving behind a thiol monolayer. (f) A schematic of the microscope slide with its 50 sensing regions.

2.6. Measuring Plasmonic Resonance

2.6.1. Spectrometers

Optical spectrometers separate light into its constituent wavelengths and quantify the intensity of each wavelength. They accomplish this by first directing light onto a diffraction grating. This grating will split light into different wavelengths with the groove density of the grating defining the dispersion of the light and hence limiting the resolution of the spectrometer. The split light is then directed to a detector made of many individual charge coupled devices which act as individual pixels whose response will vary depending on the intensity of light at a given wavelength. By combining the responses of all these sensors, the spectral profile of the light can be calculated (Fig. 2.10).

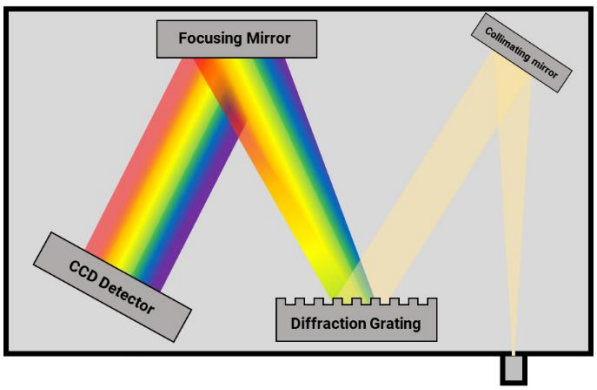

Figure 2.10 - Schematic of an optical spectrometer.

In this work, the majority of measurements were taken using a spectrometer with a 350 nm-1150 nm range and a resolution of 0.5 nm (StellarNet Blue Wave, VIS 25). Each reading obtained from this spectrometer was an automated average of 3 readings. A second spectrometer was used for a small number of readings (Optosky ATP3304) which had a smaller range (457-731 nm) but a finer resolution equal to 0.27 nm. For both spectrometers, the integration time was set to be the maximum duration without detector saturation. This was established before each experiment and remained consistent throughout each individual experiment.

2.6.2. Spectrometer Setup

A schematic of the microscope setup is given in Figure 2.11. The setup consists of a light source (Stellanet SL1) from which an optical fibre carries light to a condenser lens which focuses the light onto the sensor. The transmitted light is then focused by an objective lens onto a second optical fibre which guides the light to a spectrometer. The spectrometer then outputs this data for analysis.

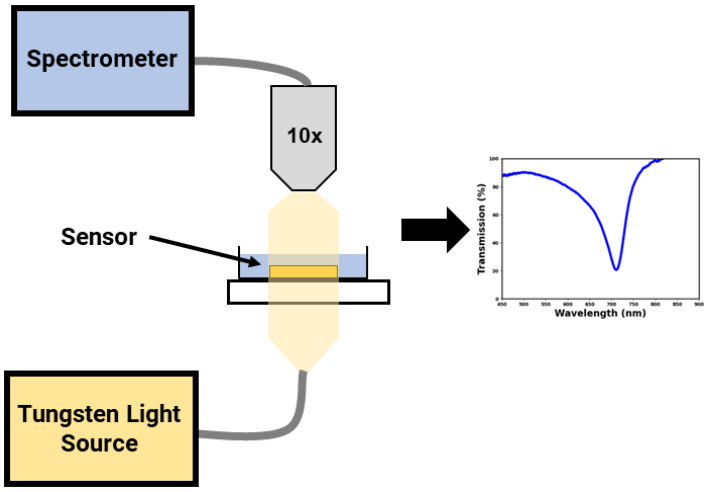

Figure 2.11 - Schematic of the setup used to record plasmonic spectra.

If relevant to the experiment at hand, the microscope could be augmented with a Peltier stage (Linkam Scientific, PE120) to precisely control the temperature of the stage. By applying a current to a semi-conductor, the Peltier stage could hold the sample at any temperature between -20 ˚C and 120 ˚C.

2.7. Data Analysis

2.7.1. Calculating the Resonance Wavelength of Plasmonic Spectra

Raw data from the spectrometer was analysed using a custom python script. Before finding the spectral minima, the raw data was subjected to a boxcar averaging function with a width of three to remove any high frequency noise. The data was then cropped around the absolute minima of the data by finding the inflection points of a high order polynomial fitted to the spectra. The cropped section of data was then smoothed with a 30-point wide boxcar averaging function and the minima of this smoothed section taken as the minima of the spectra. The data for each minima in the dataset was then output into a CSV file to be used for any further analysis or visualisation.

2.7.2. Calculating Full Width at Half Maximum of Spectra

To calculate the full width at half maximum (FWHM) of each spectra, the first 100 points of the spectra are averaged, and this point is taken as the baseline of the spectra. This baseline is then compared to the position of the minima of the spectra to find the half maximum position. The two points at which the spectra crosses the half maximum transmission value are then recorded and the difference between them is calculated as the FWHM. Missing data relates to a scenario under which the full spectra was not within the range of the spectrometer and hence, the FWHM could not be calculated. In this scenario, the data can be fitted with a Lorentzian to give an approximation of the FWHM. Erroneous data refers to a scenario where the automated code finds the FWHM of a secondary peak that is not of interest. In this scenario the data can be cropped in order to remove peaks that are not of interest. This is particularly relevant for negative structures where the bulk metal normally has a weak spectral peak of its own which is not related to the plasmonic properties of the surface.

2.7.3. Principle Component Analysis

Principle component analysis (PCA) is a method used to reduce the dimensionality of data while keeping as much of the original information as possible (19,20). PCA is an unsupervised classification technique meaning that unlike techniques such as linear discriminant analysis it does not require a set of data to be trained on.

PCA relies on maximising the variance in a given multidimensional dataset to find trends in the data that are not immediately obvious without dimensional reduction. PCA identifies the best fit line for all the data in the *n* dimensional space (*n* being the number of variables we are considering – in this case the number of sensing regions) (20,21). This is the first principle component (PC1). The second principal component will be perpendicular to PC1 and the third will be perpendicular to PC1 and PC2 with this trend continuing for all principle components (20,21). After identifying the principal components in this dimensionally reduced data is plotted along these new principle component axes. This will create clusters of datapoints with similar responses behaviour which can allow for the discrimination of different samples (Fig. 2.12 (a)) (20,21). The amount of variance each principal component is responsible for is displayed in a scree plot as shown in Figure 2.12 (b). Ideally, the maximum amount of variance is captured in the first two or three principal components to allow the clusters to be visually separated.

In the case of this thesis, PCA is applied to an array of plasmonic sensors, each with its own surface property. By monitoring the change in resonance wavelength each sensor has when interacting with a specific protein we can then create an array of values onto which PCA can be applied. This means that in the case of a successful experiment, the resulting clusters will represent the interaction of our plasmonic sensors with different proteins. If, however, there is not a sufficiently different response for each protein to the sensor array, the clusters will begin to overlap and may become indistinguishable.

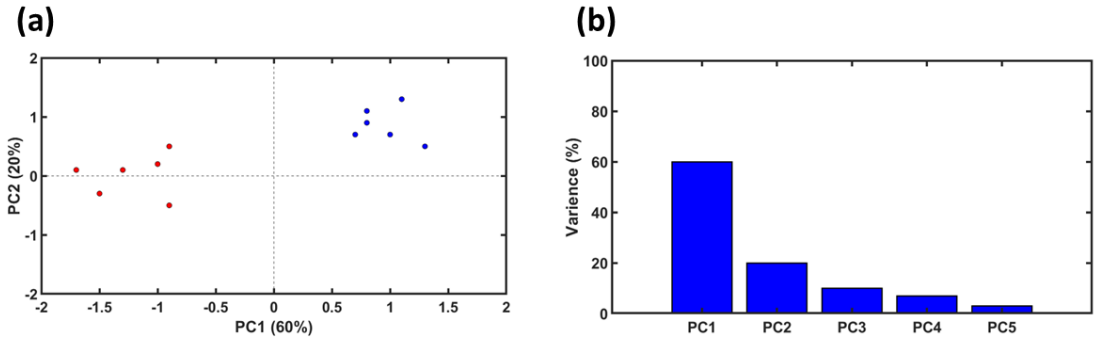

Figure 2.12 - An illustration of PCA discriminating example data (a) A PCA plot showing the groupings of two distinct samples (b) A Scree plot displaying the weighting of each principal component.

PCA is very commonly used in analyses involving cross-reactive sensors since it does not require training and minimises the data lost when combining the data received from many different sensing elements (22–37). In this thesis, PCA was carried out with JMP17 software.

2.7.4. Linear Discriminant Analysis

Linear discriminant analysis (LDA) works on similar principles to PCA whereby it works to maximise the variance in the presented data. The key difference between PCA and LDA is that LDA is a supervised technique meaning it requires the classes to be labelled before analysis can be carried out. Although this means data has to be pre-classified for the model to be created, the model is often more effective as it is now working to maximise inter-class variance as opposed to the variance between each individual datapoint (38,39). Often LDA is validated using a leave one out cross validation technique (LOOCV). LOOCV is a method of assessing the ability of a model to predict which the class of novel data (40). In the case of this thesis, this is determining if the model can accurately categorise protein solutions. To accomplish this, LOOCV splits the dataset into a defined number of subsets, in this case, each datapoint is individually tested. All but one of the datapoints is then used to create a model into which this remaining datapoint is inserted, by repeating this process for every datapoint we can then determine how often the data is accurately categorised. The LDA model can then be assigned a percentage value as to how many datapoints were correctly allocated.

2.8. Sensitivity Measurements

2.8.1. Bulk Sensitivity

The bulk sensitivity of plasmonic sensors quantifies their ability to detect refractive index changes to the macro environment around them. Experimentally, this is quantified by measuring the resonance wavelength of the sensors in solutions with varying refractive indices. These varying refractive indices are created using glycerol solutions of different concentrations. In this case, water, 10%, 20% and 30% (w/w) glycerol solutions were used to create a refractive index gradient. The refractive index of these solutions was measured with a refractometer (Kern ABBE Refractometer ORT 1RS) to ensure accuracy. This was particularly important when measuring glycerol solutions, as due to its viscosity, glycerol is challenging to precisely measure. The refractive indices of the glycerol solutions were always approximately as seen in Table 2.2 however between different batches of glycerol solution this refractive index would change slightly (in the 3rd and 4th decimal place) and hence this table only representative of the values.

Table 2.2 - The measured values of refractive index for glycerol solutions of different concentrations (n=3).

Solution	10% Glycerol (w/w)	20% Glycerol (w/w)	30% Glycerol (w/w)
Measured Refractive Index	1.3446 (+/- 0.0003)	1.3545 (+/- 0.0001)	1.3623 (+/- 0.0002)

After taking five readings in each of these solutions, a graph of refractive index and resonance wavelength is plotted, and a linear best fit line used to find the sensitivity of the sensor in nanometres per refractive index unit (nm/RIU). Figure 2.13 shows an example sensitivity plot using simulated data of how a plasmonic sensor responds to changing refractive index in an idealised environment.

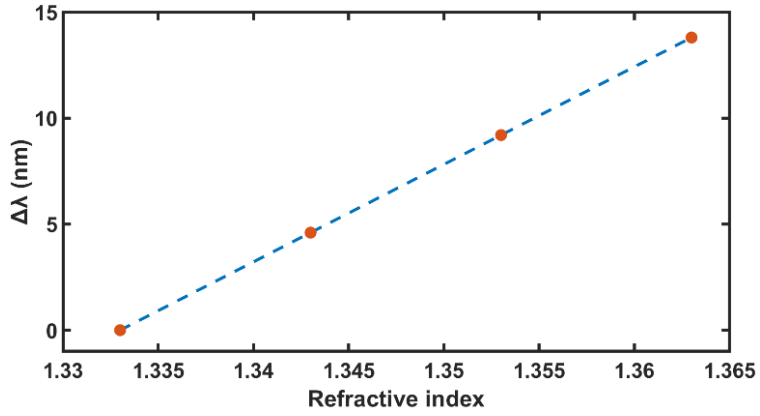

Figure 2.13 - Example of simulated sensitivity calculations.

It should be noted that the refractive index of aqueous solutions is dependent on wavelength. In this thesis, the sensors resonate between 600 and 850 nm. This means that for water at room temperature, there is a 0.08 shift in the refractive index for water at room temperature between the two extremes of this range (41). This same principle will also apply to glycerol solutions, although this would take its own independent study to verify, as the solutions are mostly water, it can be assumed that they this refractive index shift will be of approximately the same magnitude.

2.8.2. Localised Sensitivity

In contrast to bulk sensitivity, localised sensitivity is a measure of how sensitive a plasmonic sensor is to the environment very close to the surface of the sensor. Due to this, quantifying localised sensitivity requires changing the refractive index close to the surface of the sensor. This can be accomplished in a few different ways.

2.8.2.1. Thiolation

The first method used to measure localised sensitivity is by forming a thiol monolayer on the gold nanostructures. In this case, the thiol 11-mercaptodecanoic acid (Sigma-Aldrich) was used, which can be approximated as being 2 nm long. The sensors were left to modify in a 10 mM ethanolic solution of 11-mercaptodecanoic acid (Sigma-Aldrich) overnight. By taking five readings of the sensor before and after these modifications the shift in response to a thin local layer can be quantified. This method is beneficial as it creates a thin layer over the entire sensing surface making it analogous to an analyte binding to the sensors surface.

Although this method is useful for describing the local sensitivity of different plasmonic sensors, the density and conformity of the thin thiol films can be affected by many factors including thiol purity, solvent purity and temperature. For this reason, a second method can be used to confirm the differences in local sensitivity between sensors.

2.8.2.2. Aluminium Oxide Layer

As described in Section 2.3.2, very thin metal layers can be deposited using metal evaporators. Applying a 1 nm layer of aluminium on a sensor will give a coating which will quickly convert into aluminium oxide when exposed to atmospheric conditions (42–46). As with the thiol layer, readings before and after layer deposition allow quantification of the local sensitivity of sensors. Similar to the aforementioned, there are some drawbacks to this method. The aluminium oxide will only be present on top of the individual sensors and on the surrounding glass, but will not coat the sides of the sensor due to the directionality of the application method. In addition, there will always be slight variations in the thickness of the deposited layer depending on the exact deposition rate, although these differences should be negligible. In an extra measure to ensure these variations did not have a major effect on the results, in the majority of cases samples that were to be directly compared had aluminium deposited within the same run ensuring they had the same thickness of Al_2O_3 applied.

2.9. Biosensing Methods

2.9.1. Sensing Proteins in a Static System

Initial experiments used to detect proteins were conducted in a static setup. For data that did not require a time series, the sensors were simply immersed in the relevant solution and readings were taken using the setup described in Section 2.6.2. If time series data was required, a different methodology was used. This methodology consisted of initially recording a baseline reading in phosphate buffered saline (PBS, Sigma-Aldrich) before injecting proteins into the static solution and monitoring the progression of the sensor's resonance peak with time. To prevent increasing the volume of the solution when the proteins were injected, an identical volume of PBS was removed immediately before the protein solution was added. A summary of this setup is given in Figure 2.14.

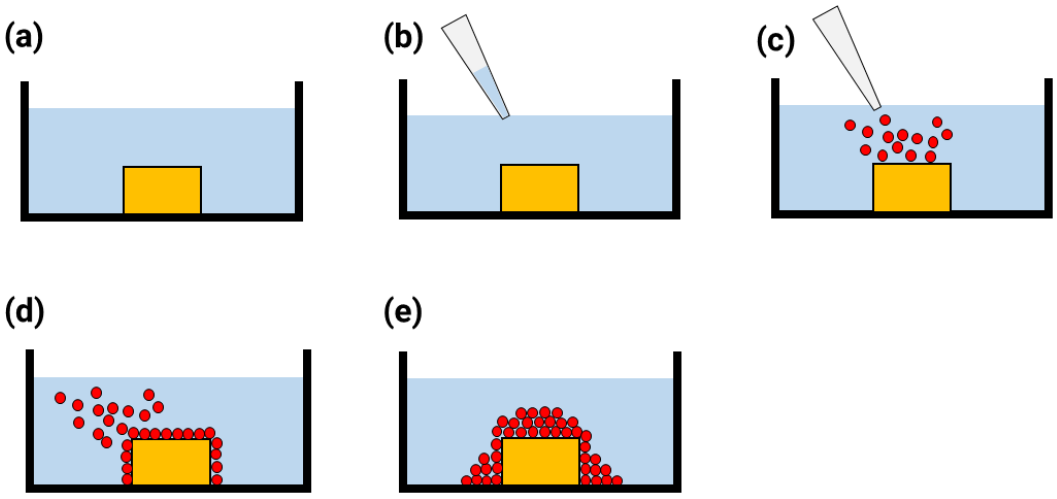

Figure 2.14 - The static system used to detect proteins (a) Readings begin while the sensor is immersed in PBS. (b) A calculated volume of PBS is removed so the volume of the protein solution remains constant. (c) The proteins are added to the solution increasing the volume back to its initial value. (d) Proteins diffuse towards the sensors and interact with its surface. (e) Proteins settle on the sensors surface.

Despite this setup allowing for limited, analysis of the interactions between proteins and sensors, it comes with several associated limitations. Firstly, the rate of the proteins associating with the sensor will be, almost entirely, dictated by diffusion. Additionally, the duration the proteins require before settling on the sensor will change depending on where exactly the sensors are injected into the solution as well as the velocity at which they are injected. Furthermore, when injecting the proteins, it is easily possible to slightly move the sensor. This can be due to the inflow of the protein solution or by knocking the containing dish itself. If this happens, it requires the sensor to be repositioned which may result in errors or changes in baseline. This setup also results in a prolonged interaction time between the sensor and the proteins, leading to more significant irreversible interactions and diminishes the ability of anti-fouling layers to prevent non-specific interactions.

2.9.2. Measuring Proteins Under Flow

A utilising flow creates a means of precisely controlling the mass transfer of proteins in solution as well as allowing multiple solutions to be introduced onto a sensing region in succession without interspersed drying steps. This creates a more robust and reliable system for characterising protein interactions while not allowing proteins to settle onto the surface of the sensor. The microfluidic devices used in this work consisted of 16 parallel channels (Microfluidic Chip Shop, Fluidic 152, 1 mm channel width, Topas polymer). The microfluidic system was adhered to a borosilicate glass microscope slide, placed across the short axis of the microscope slide, with plasmonic sensors fabricated to be contained within each channel (Schott Minifab, Nexterion borofloat 33 Microscope slides, 1 mm thickness). This system, utilising a syringe pump (New Era Pump Systems, NE4000) for solution

injection at a flow rate of 200 µL/min, provided a controlled environment for protein detection. Between each protein injection, sensors were rinsed by flowing PBS through the channel and over the sensor to remove any unbound proteins.

Microfluidics are useful for quantifying the specific 'lock and key' style bond that exists between antibodies and antigens. The most common model system for a specific interaction between two proteins is biotin-streptavidin. These proteins have a bond strength that is one of the strongest in nature ($k_d = 4x10^{-14}$ M) (47). To test the specificity of the sensor, the system was first modified with 1 mM thiolated PEG-biotin (TebuBio) in PBS solution overnight. Bovine serum albumin (Sigma-Aldrich) was used as a control protein and the interactions between biotin modified sensors and neutravidin (ThermoFisher Scientific) could then be examined. As before, the flow rate of proteins was maintained at 200 µL/min. For most readings in the microfluidic setup, the time between readings was set to 750 ms. However, due to the spectrometer averaging three readings per single output reading, each of which with an integration time, the total duration between readings was often longer than it was set to be – approximately 1.5 seconds.

2.9.3. Calculating the Limit of Detection

Limit of detection (LoD) is a measure used to assess the smallest concentration of a given analyte a sensor can detect. In the case of plasmonic sensors, this is accomplished by determining what the smallest possible change in resonance wavelength can be confidently detected (48). For plasmonic sensors, LoD ranges from the femtomolar to nanomolar range although whether or not a given LoD is sufficient is highly dependent on the application at hand (49,50). It should be noted however that a lower LoD is always preferable as it will allow for both very small concentrations and higher concentrations of relevant analytes to be detected.

To calculate the LoD of plasmonic sensors, the sensor response to analytes at different concentrations is measured. The response versus concentration is then plotted. A linear regression is then fitted to these points and is used to obtain the standard error of the fit (σ) and the slope of the fit (m). These parameters can then be inserted into Equation 2.1 to obtain the LoD.

$$\mathrm{LoD} = 3.3\frac{\sigma}{m} \tag{2.1}$$

Ideally, this LoD is calculated using as many datapoints as possible as well as having multiple repeats of the same experiment.

2.10. Conclusion

This chapter details the different fabrication protocols used to produce the sensors utilised throughout this thesis in addition to discussing the operating mechanisms of the tools used for sensor fabrication and characterisation. In addition to fabrication protocols, the methods used to gather and analyse different forms of data are detailed and the parameters used for both EBL and FDTD simulations are disclosed.

References

1. Kane Yee. Numerical solution of initial boundary value problems involving maxwell's equations in isotropic media. IEEE Trans Antennas Propag [Internet]. 1966 May;14(3):302–7. Available from: https://ieeexplore.ieee.org/document/1138693/
2. Lilley G, Messner M, Unterrainer K. Improving the quality factor of the localized surface plasmon resonance. Opt Mater Express. 2015 Oct 1;5(10):2112.
3. Siegfried T, Ekinci Y, Martin OJF, Sigg H. Engineering metal adhesion layers that do not deteriorate plasmon resonances. ACS Nano. 2013 Mar 26;7(3):2751–7.
4. Lamy de la Chapelle M, Shen H, Guillot N, Frémaux B, Guelorget B, Toury T. New Gold Nanoparticles Adhesion Process Opening the Way of Improved and Highly Sensitive Plasmonics Technologies. Plasmonics. 2013 Jun;8(2):411–5.
5. Haynes WM, Lide DR, Bruno TJ, editors. CRC Handbook of Chemistry and Physics [Internet]. CRC Press; 2016. Available from: https://www.taylorfrancis.com/books/9781498754293
6. Palik ED. Handbook of Optical Constants of Solids. Palik ED, editor. Vol. I. Elsevier; 1997.
7. Hatzakis M. Electron Resists for Microcircuit and Mask Production. J Electrochem Soc [Internet]. 1969;116(7):1033. Available from: https://iopscience.iop.org/article/10.1149/1.2412145
8. McPeak KM, Jayanti S V., Kress SJP, Meyer S, Iotti S, Rossinelli A, et al. Plasmonic films can easily be better: Rules and recipes. ACS Photonics. 2015 Mar 18;2(3):326–33.
9. Bosman M, Zhang L, Duan H, Tan SF, Nijhuis CA, Qiu CW, et al. Encapsulated annealing: Enhancing the plasmon quality factor in lithographically-defined nanostructures. Sci Rep. 2014 Jul 2;4.
10. Rommel M, Nilsson B, Jedrasik P, Bonanni V, Dmitriev A, Weis J. Sub-10 nm resolution after lift-off using HSQ/PMMA double layer resist. Microelectron Eng. 2013;110:123–5.
11. Yang H, Jin A, Luo Q, Li J, Gu C, Cui Z. Electron beam lithography of HSQ/PMMA bilayer resists for negative tone lift-off process. Microelectron Eng. 2008 May;85(5–6):814–7.
12. Voznyy O, Dubowski JJ, Yates JT, Maksymovych P. The Role of Gold Adatoms and Stereochemistry in Self-Assembly of Methylthiolate on Au(111). J Am Chem Soc [Internet]. 2009 Sep 16;131(36):12989–93. Available from: https://pubs.acs.org/doi/10.1021/ja902629y
13. Kankate L, Aguf A, Großmann H, Schnietz M, Tampé R, Turchanin A, et al. Vapor Phase Exchange of Self-Assembled Monolayers for Engineering of Biofunctional Surfaces. Langmuir. 2017 Apr 18;33(15):3847–54.
14. Woehrle GH, Brown LO, Hutchison JE. Thiol-functionalized, 1.5-nm gold nanoparticles through ligand exchange reactions: Scope and mechanism of ligand exchange. J Am Chem Soc. 2005 Feb 23;127(7):2172–83.
15. Schlenoff JB, Li M, Ly H. Stability and Self-Exchange in Alkanethiol Monolayers. J Am Chem Soc [Internet]. 1995 Dec 1;117(50):12528–36. Available from: https://pubs.acs.org/doi/abs/10.1021/ja00155a016
16. Bürgi T. Properties of the gold-sulphur interface: from self-assembled monolayers to clusters. Nanoscale. 2015 Oct 14;7(38):15553–67.

17. Bueno-Alejo CJ, Santana Vega M, Chaplin AK, Farrow C, Axer A, Burley GA, et al. Surface Passivation with a Perfluoroalkane Brush Improves the Precision of Single-Molecule Measurements. ACS Appl Mater Interfaces. 2022;

18. Munief WM, Heib F, Hempel F, Lu X, Schwartz M, Pachauri V, et al. Silane Deposition via Gas-Phase Evaporation and High-Resolution Surface Characterization of the Ultrathin Siloxane Coatings. Langmuir [Internet]. 2018 Sep 4;34(35):10217–29. Available from: https://pubs.acs.org/doi/10.1021/acs.langmuir.8b01044

19. Ringnér M. What is principal component analysis? Nat Biotechnol [Internet]. 2008 Mar;26(3):303–4. Available from: https://www.nature.com/articles/nbt0308-303

20. Jolliffe IT, Cadima J. Principal component analysis: a review and recent developments. Philosophical Transactions of the Royal Society A: Mathematical, Physical and Engineering Sciences [Internet]. 2016 Apr 13;374(2065):20150202. Available from: https://royalsocietypublishing.org/doi/10.1098/rsta.2015.0202

21. Lever J, Krzywinski M, Altman N. Principal component analysis. Nat Methods [Internet]. 2017 Jul 1;14(7):641–2. Available from: https://www.nature.com/articles/nmeth.4346

22. Shang L, Liu C, Watanabe M, Chen B, Hayashi K. LSPR sensor array based on molecularly imprinted sol-gels for pattern recognition of volatile organic acids. Sens Actuators B Chem. 2017;249:14–21.

23. Sun J, Lu Y, He L, Pang J, Yang F, Liu Y. A colorimetric sensor array for protein discrimination based on carbon nanodots-induced reversible aggregation of AuNP with GSH as a regulator. Sens Actuators B Chem. 2019 Oct 1;296.

24. Mohseni N, Bahram M, Baheri T. Chemical nose for discrimination of opioids based on unmodified gold nanoparticles. Sens Actuators B Chem. 2017;250:509–17.

25. Zhou Y, Huang W, He Y. pH-Induced silver nanoprism etching-based multichannel colorimetric sensor array for ultrasensitive discrimination of thiols. Sens Actuators B Chem. 2018 Oct 1;270:187–91.

26. Brenet S, John-Herpin A, Gallat FX, Buhot A, Livache T, Herrier C, et al. Development of a novel multiplexed optoelectronic nose for analysis of volatile organic compounds. ISOEN 2017 - ISOCS/IEEE International Symposium on Olfaction and Electronic Nose, Proceedings. 2017;1–3.

27. Maho P, Herrier C, Livache T, Rolland G, Comon P, Barthelmé S. Reliable chiral recognition with an optoelectronic nose. Biosens Bioelectron [Internet]. 2020;159(March):112183. Available from: https://doi.org/10.1016/j.bios.2020.112183

28. Tabassum S, Kumar R, Dong L. Plasmonic Crystal-Based Gas Sensor Toward an Optical Nose Design. IEEE Sens J. 2017;17(19):6210–23.

29. Sun C, Ohodnicki PR, Lu P, Feng R. Low-cost fiber optic sensor array for simultaneous detection of hydrogen and temperature. In: Du HH, Mendez A, Baldwin CS, editors. Fiber Optic Sensors and Applications XV [Internet]. SPIE; 2018. p. 4. Available from: https://www.spiedigitallibrary.org/conference-proceedings-of-spie/10654/2304633/Low-cost-fiber-optic-sensor-array-for-simultaneous-detection-of/10.1117/12.2304633.full

30. Li Z, Paul R, Ba Tis T, Saville AC, Hansel JC, Yu T, et al. Non-invasive plant disease diagnostics enabled by smartphone-based fingerprinting of leaf volatiles. Nat Plants [Internet]. 2019;5(8):856–66. Available from: http://dx.doi.org/10.1038/s41477-019-0476-y

31. Jafarinejad S, Ghazi-Khansari M, Ghasemi F, Sasanpour P, Hormozi-Nezhad MR. Colorimetric Fingerprints of Gold Nanorods for Discriminating Catecholamine Neurotransmitters in Urine Samples. Sci Rep [Internet]. 2017;7(1):1–8. Available from: http://dx.doi.org/10.1038/s41598-017-08704-5

32. Pu F, Ran X, Guan M, Huang Y, Ren J, Qu X. Biomolecule-templated photochemical synthesis of silver nanoparticles: Multiple readouts of localized surface plasmon resonance for pattern recognition. Nano Res. 2018;11(6):3213–21.

33. Fournel A, Mantel M, Pinger M, Manesse C, Dubreuil R, Herrier C, et al. An experimental investigation comparing a surface plasmon resonance imaging-based artificial nose with natural olfaction. Sens Actuators B Chem. 2020;320(January).

34. Jia J, Wu M, Wang S, Wang X, Hu Y, Chen H, et al. Colorimetric sensor array based on silver deposition of gold nanorods for discrimination of Chinese white spirits. Sens Actuators B Chem [Internet]. 2020;320(December 2019):128256. Available from: https://doi.org/10.1016/j.snb.2020.128256

35. Yu H, Long D, Huang W. Organic antifreeze discrimination by pattern recognition using nanoparticle array. Sens Actuators B Chem [Internet]. 2018;264:164–8. Available from: https://doi.org/10.1016/j.snb.2018.02.180

36. Chen B, Liu C, Shang L, Guo H, Qin J, Ge L, et al. Electric-field enhancement of molecularly imprinted sol-gel-coated Au nano-urchin sensors for vapor detection of plant biomarkers. J Mater Chem C Mater [Internet]. 2019;8(1):262–9. Available from: http://dx.doi.org/10.1039/C9TC05522C

37. Brenet S, John-Herpin A, Gallat FX, Musnier B, Buhot A, Herrier C, et al. Highly-Selective Optoelectronic Nose Based on Surface Plasmon Resonance Imaging for Sensing Volatile Organic Compounds. Anal Chem. 2018;90(16):9879–87.

38. Shang L, Liu C, Chen B, Hayashi K. Plant Biomarker Recognition by Molecular Imprinting Based Localized Surface Plasmon Resonance Sensor Array: Performance Improvement by Enhanced Hotspot of Au Nanostructure. ACS Sens. 2018;3(8):1531–8.

39. Shang L, Liu C, Watanabe M, Chen B, Hayashi K. LSPR sensor array based on molecularly imprinted sol-gels for pattern recognition of volatile organic acids. Sens Actuators B Chem [Internet]. 2017;249:14–21. Available from: http://dx.doi.org/10.1016/j.snb.2017.04.048

40. Backhaus K, Erichson B, Gensler S, Weiber R, Weiber T. Multivariate Analysis. Wiesbaden: Springer Fachmedien Wiesbaden; 2023.

41. Hale GM, Querry MR. Optical Constants of Water in the 200-nm to 200-μm Wavelength Region. Appl Opt. 1973 Mar 1;12(3):555.

42. Nguyen L, Hashimoto T, Zakharov DN, Stach EA, Rooney AP, Berkels B, et al. Atomic-Scale Insights into the Oxidation of Aluminum. ACS Appl Mater Interfaces. 2018 Jan 24;10(3):2230–5.

43. Aumann CE, Skofronick GL, Martin JA. Oxidation behavior of aluminum nanopowders. Journal of Vacuum Science and Technology B: Microelectronics and Nanometer Structures. 1995 May;13(3):1178–83.

44. Ayas S, Topal AE, Cupallari A, Güner H, Bakan G, Dana A. Exploiting Native Al2O3 for Multispectral Aluminum Plasmonics. ACS Photonics. 2014 Dec 17;1(12):1313–21.

45. Martin J, Plain J. Fabrication of aluminium nanostructures for plasmonics. J Phys D Appl Phys. 2015 May 13;48(18).

46. Gerard D, Gray SK. Aluminium plasmonics. J Phys D Appl Phys. 2015 May 13;48(18).

47. Holmberg A, Blomstergren A, Nord O, Lukacs M, Lundeberg J, Uhlén M. The biotin-streptavidin interaction can be reversibly broken using water at elevated temperatures. Electrophoresis. 2005 Feb;26(3):501–10.

48. Armbruster DA, Pry T. Limit of Blank, Limit of Detection and Limit of Quantitation. Vol. 29, Clin Biochem Rev. 2008.

49. Haes AJ, Chang L, Klein WL, Van Duyne RP. Detection of a biomarker for Alzheimer's disease from synthetic and clinical samples using a nanoscale optical biosensor. J Am Chem Soc. 2005 Feb 23;127(7):2264–71.

50. Zopf D, Pittner A, Dathe A, Grosse N, Csáki A, Arstila K, et al. Plasmonic Nanosensor Array for Multiplexed DNA-based Pathogen Detection. ACS Sens [Internet]. 2019 Feb 22;4(2):335–43. Available from: https://pubs.acs.org/doi/10.1021/acssensors.8b01073

Chapter 3 – Optimisation of Plasmonic Nanostructures for Biosensing Applications

3.1. Introduction

In this chapter, the properties of different nanoplasmonic sensors were investigated to better understand the effect geometric parameters have on resonance and sensitivity. By examining

different parameters such as periodicity, structure size and structure shape we can determine what parameters can be altered to improve sensor performance.

The structures described in this chapter are split into different categories, monomeric positive structures, monomeric negative structures, and trimeric positive structures. Monomeric structures consist of arrays of single gold structures which collectively resonate to produce a plasmonic response. Trimeric structures, instead of consisting of elements made up of a single nanostructure, consist of elements constructed of three resonating subunits. These resonating subunits, due to their proximity to each other, couple creating a much stronger localised electromagnetic (EM) field. Positive structures are created of free-standing lithographically shaped pillars of gold whereas negative structures are created by shaped holes within a gold film. Arrays of negative structures also create a plasmonic resonance with both propagating waves between holes and local resonances within holes combining to create a resonance mode. Due to this plasmonic resonance, negative structures can also be used to detect the refractive index of the environment.

To better understand the effect of these geometrical parameters, the sensitivity of different sensors is considered for both bulk and localised refractive index changes. Bulk refractive index sensitivity is the response of the sensor to a change in its bulk environment that envelopes the entire sensing volume of the sensor. Localised sensitivity on the other hand is defined as the sensitivity of a sensor to changes in refractive index very close to the sensors surface. The importance of field confinement for sensing applications varies depending on analyte size. Small analytes such as deoxyribonucleic acid (DNA) benefit from greater field confinement whereas larger analytes, such as proteins, may be better suited to larger sensing fields.

It should be noted that all structures discussed in this section are annealed. Chapter 4 will discuss the effects of annealing plasmonic nanostructures.

3.2. Experimental

3.2.1. Simulations

Finite-Difference Time-Domain (FDTD) simulations of different plasmonic geometries were carried out using Ansys Lumerical. The mesh resolution was set to 3 nm and light was projected from below the glass substrate to mimic the experimental setup. Metal dielectric data from the CRC library was used and the dielectric data for glass came from the Palik library (1,2).

3.2.2. Fabrication of Positive Structures

Borosilicate glass (Pi-Kem, 500 µm thick) was cleaned in an ultrasonic bath for 3 minutes in acetone followed by 3 minutes in isopropyl alcohol (IPA). A dual layer of resist was spun onto the sample with each layer being spun at 4000 rpm for 60 seconds and baked at 180 °C for 3 minutes per layer. A 20 nm aluminium layer was then deposited (Plassys MEB 550S, Plassys MEB 400S), and the sample exposed using electron beam lithography (EBL) (Raith EBPG 5200, 800 µC/cm^2, 2 nA beam). Following exposure, the aluminium layer was removed using 2.5% tetramethylammonium hydroxide (TMAH) solution (Microposit MF CD-26 developer) for approximately 90 seconds and the resist developed in 2.5:1 IPA: Methyl isobutyl ketone (MIBK) solution for 1 minute. A 2 nm titanium / 50 nm gold layer was deposited (Plassys MEB 550S, Plassys MEB 400S), and the excess metal was removed by dissolving the remaining polymethyl methacrylate (PMMA) in acetone leaving behind the array of positive nanostructures.

3.2.3. Fabrication of Negative Arrays

Following ultrasonic cleaning in acetone for 3 minutes and 3 minutes in IPA, borosilicate glass was then exposed to oxygen plasma for 3 minutes at 150 W. The resist (Microresist Technology Ma-N 2041/2403) was then spun on at 3000 rpm for 30 seconds and baked at 90 °C for 3 minutes. An aluminium layer (20 nm) was evaporated on top of the resist (Plassys MEB 550S, Plassys MEB 400S) which was exposed using EBL (Raith EBPG 5200, 1200 µC/cm^2, 2 nA beam). The sample was then developed in 2.5% TMAH solution (Microposit MF-319) for 4.5 minutes. A metallic bilayer (2 nm Ti / 50 nm Au) was evaporated onto the developed pattern resist (Plassys MEB 550S, Plassys MEB 400S) with the excess resist removed in N-Methyl-2-pyrrolidone (NMP) based developer for 2 hours (Microposit Remover 1165).

3.2.4. Imaging Nanostructures

Nanostructures were imaged using a scanning electron microscope (SEM, Hitachi SU8240, Hitachi SU8230). Either an approximately 10 nm layer of aluminium or gold/palladium was used as a charge conduction layer for these samples. The voltage for each SEM is listed in all provided figures however the amperage was always set at 10 µA.

3.2.5. Measuring Bulk Refractive Index Sensitivity

Specific quantities of glycerol (Table 3.1) were weighed and mixed in deionised (DI) water to yield 0%, 10%, 20% and 30% w/w solutions. The refractive index (RI) of these solutions was measured using a Kern ABBE Refractometer ORT 1RS. The sensors were immersed in

3 mL of each of these solutions in a 35 mm disposable petri dish and the transmission spectra was recorded five times. The resonance wavelength (transmission minima) was plotted against refractive index and the points linearly fitted using MATLAB. The gradient of this fit represents the sensitivity of the sensor in nanometres per refractive index unit (nm/RIU).

Table 3.1 - Glycerol solutions used for measuring bulk refractive index sensitivity.

	10% w/w	**20% w/w**	**30% w/w**
Deionised Water (ml)	100	100	100
Glycerol (g)	10	20	30

3.2.6. Measuring Localised Refractive Index Sensitivity

Local sensitivity was measured by the change in the transmission spectra minima position before and after the formation of a thiolated self-assembled monolayer (SAM) and deposition of 1 nm layer of aluminium (Plassys MEB 550S, Plassys MEB 400S). Five readings were taken in air before and after the application of each layer to calculate the resonance shift.

3.3. Results And Discussion

3.3.1. Monomeric Shapes

In this section, properties of nanoplasmonic arrays with square or disc elements are investigated. Due to the lack of multiple subunits in each resonating structure, these structures are designated as monomeric. Monomeric structures are faster to fabricate and have a higher tolerance to fabrication errors compared to trimeric shapes which will be discussed in Section 3.3.3

3.3.1.1. Discs

Discs are one of the most common shapes used in LSPR sensors as they lend themselves to quick and easy fabrication. The lower resolution required to write discs means they can be quickly fabricated with direct write methods and are also easily fabricated with more economical techniques such as nanoimprint lithography or nanosphere lithography (3–7).

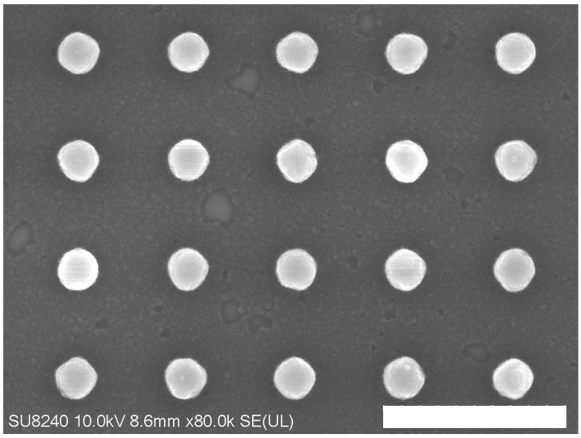

Figure 3.1 - An SEM of disc nanostructures (Scale bar: 500 nm).

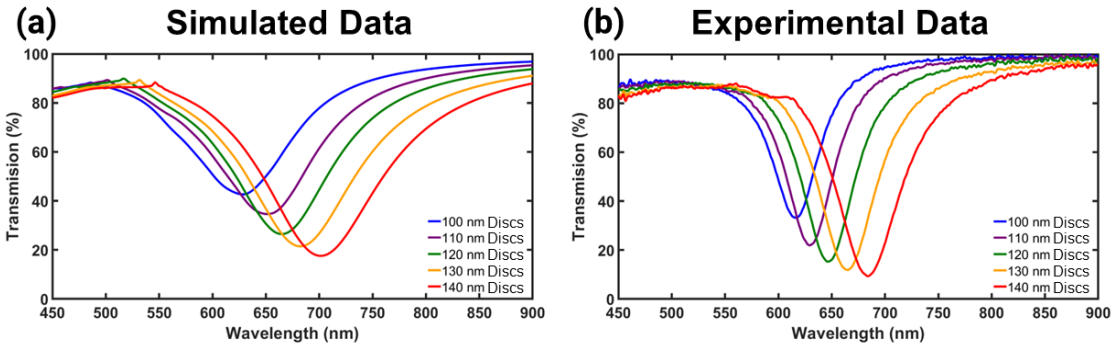

Figure 3.2 - Spectra of disc plasmonic structures in water. (a) FDTD simulations (b) Experimental data (period 235 nm edge-edge in both cases).

Figure 3.2. demonstrates the general trend of resonance wavelength changing with element size. Additionally, the magnitude of the transmission minima increases with size. This can be explained by the increased proportion of the sensing area filled with gold nanostructures given the constant edge-edge spacing of the structures.

When comparing the simulated structures (Fig. 3.2(a)) to the real structures (Fig. 3.2(b)) there are several differences. Firstly, the resonance wavelengths of the simulated structures are at higher wavelengths than those of the real structures. This is likely due to the inevitable variation in the dielectric equation used to calculate the response of the nanostructures in the simulation versus the dielectric equation of the annealed gold used for the real nanostructures. The sensitivity and figure of merit (FoM) of the disc nanostructures are displayed in Table 3.2.

Table 3.2 - Experimental sensitivity and FoM of disc nanostructures (period defined as centre-centre)**.** Resonance wavelength taken at transmission minima.

Structure Size (nm)	Period (nm)	Sensitivity (nm/RIU)	Resonance Wavelength in Water (nm)	FoM
100	335	129.80	616.3	2.72
110	345	144.25	629.80	2.94
120	355	166.80	646.7	3.14
130	365	190.45	664.45	3.30
140	375	209.67	683.65	3.30

Table 3.2 shows the clear trend of sensitivity scaling with resonance wavelength. This trend holds for all the geometries discussed in this thesis and will be examined in further detail in Section 3.3.4. Using the simulations for the disc nanostructures, the peak EM field observed for each structure was also examined.

Table 3.3 – Maximum simulated absolute value of the electric field intensity of disc nanostructures.

Structure Size (nm)	Period (nm)	Maximum Electric Field Intensity (V/m)
100	335	18.9
110	345	18.9
120	355	19.1
130	365	18.8
140	375	17.1

The maximum EM field seen for the discs stays approximately constant regardless of the structure size. Conversely, the other shapes examined in this chapter typically show a trend of the EM field either increasing or decreasing with size. This is one of the pieces of information that leads us to the conclusion that field extent is a key factor in determining bulk refractive index sensitivity as discussed in Section 3.3.4.

3.3.1.2. Squares

As with disc nanostructures, squares are relatively simple to fabricate and have a high tolerance to fabrication inconsistency. Figure 3.3 shows an SEM of a fabricated nanoplasmonic array of squares with Figure 3.4 comparing the simulated and experimental data of squares of different sizes and periodicities.

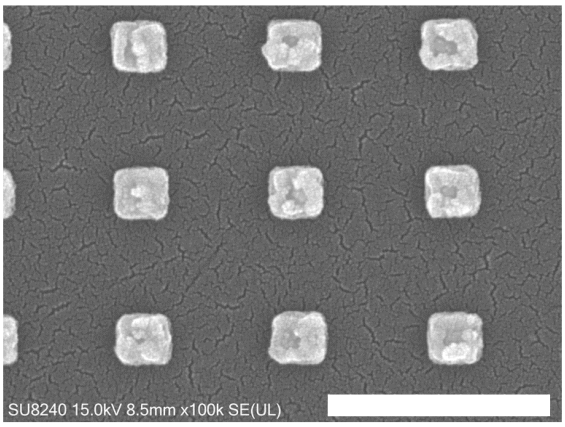

Figure 3.3 - SEM of square nanostructures (Scale bar: 500 nm).

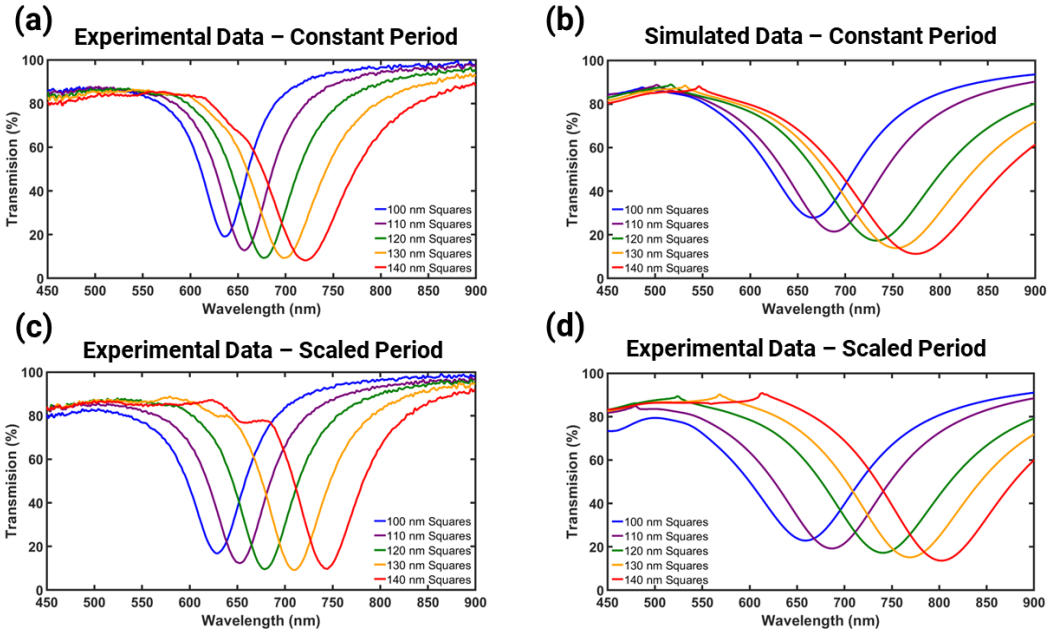

Figure 3.4 - Spectra of square plasmonic arrays. (a) Experimental and (b) simulated data of squares with a constant 235 nm edge-edge period. (c) Experimental and (d) simulated data of squares with a period 3x the element size.

Figure 3.4(b) shows an interesting progression as element size increases. When the squares increase from 110 nm to 120 nm, the 235 nm edge-edge period is no longer sufficient to prevent significant coupling between adjacent structures. When these structures begin to couple, an increase in the peak width and a red shift occurs. This effect is not as readily observed in the fabricated structures; however, the effects of coupling are clear when considering the full-width at half-maximum (FWHM) of the structures (Fig. 3.5).

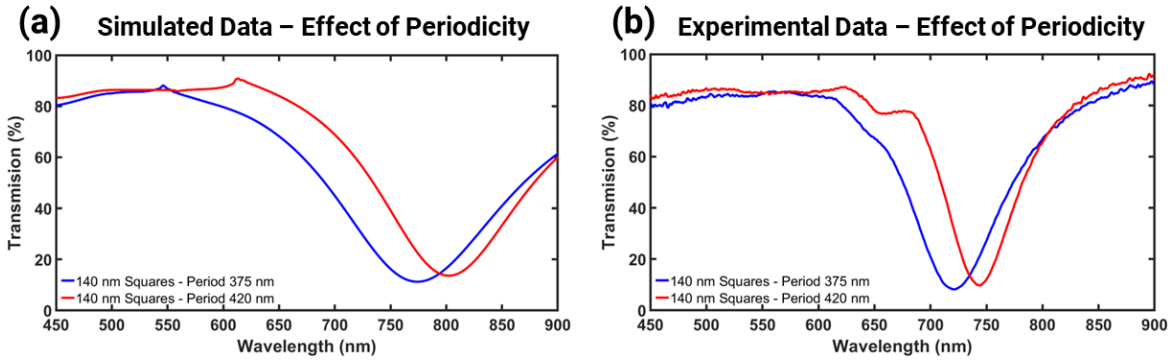

Figure 3.5 - The effect of periodicity of square nanostructures on plasmonic resonance (a) FDTD simulations and (b) experimental data.

This increase in FWHM results in a significant difference in spectral shape between the 140 nm squares with a 420 nm period as compared to the 375 nm period results (Fig. 3.4(d)). The increase in FWHM decreases the FoM from 3.50 for the squares with a 420 nm period to 2.41 for squares with a 375 nm period (Table 3.4). This shows that for monomeric structures, avoiding coupling between adjacent structures greatly enhances sensing performance.

Table 3.4 - The sensitivity and FoM of square nanostructures. Resonance wavelength taken at transmission minima.

Structure Size (nm)	Period (nm)	Sensitivity (nm/RIU)	Resonance Wavelength in Water (nm)	FoM
100	335	150.09	636.35	2.81
110	345	156.29	656.45	2.63
120	355	189.24	677.45	2.84
130	365	208.87	699.10	2.74
140	375	208.91	721.35	2.41
100	300	135.06	629.00	2.30
110	330	164.61	652.45	2.61
120	360	191.92	678.95	2.96
130	390	209.72	709.70	3.17
140	420	239.86	743.55	3.50

The maximum simulated electromagnetic field for each plasmonic sensors with square elements is shown in Table 3.5.

Table 3.5 - Maximum absolute value of the electric field from simulated square nanostructures.

Structure Size (nm)	Period (nm)	Maximum Electric Field Intensity (V/m)
100	335	54.5
110	345	48.6
120	355	27.6
130	365	31.1
140	375	22.6
100	300	47.2
110	330	18.3
120	360	18.0
130	390	32.1
140	420	25.6

Generally, square elements have a larger maximum EM field when compared to the simulated disc nanoplasmonic arrays (Table 3.3). The source of these heightened EM fields is the sharp corners of the squares which are known to focus EM fields (8–13). In addition, there is a trend that the smaller shapes have a significantly larger maximum EM field which is focused at the corners of the geometry. Literature suggests that the reason for this increased EM field at lower wavelengths is due to phase related effects in smaller nanostructures. Phase related effects may dampen the EM field intensity of larger nanostructures as their electrons no longer resonate as one continuous wave but will be slightly out of phase across the length of the nanostructure leading to some dampening (14–16). Katyal and Soni refer to this effect as 'phase retardation effect' and explain it as coming from the fact that at a certain size, the free electrons in the plasmonic structure are no longer displaced simultaneously (14). Instead, there is a slight mismatch between the phase of the electrons at opposing sides of the structure (14). This leads to multipolar resonances as well as a lesser concentration of EM field in the structures as is seen in multiple simulation papers (14–16) . It should be noted that the very high EM field for smaller shapes is incongruous with the experimental data discussed in Section 3.3.5, which suggests that there is a slight trend towards larger monomeric shapes having a higher sensitivity.

Although simulations indicate there is an extremely high EM field for the small squares, in reality, the peak EM field decreases rapidly with even the slightest rounding of the corners (Fig. 3.6).

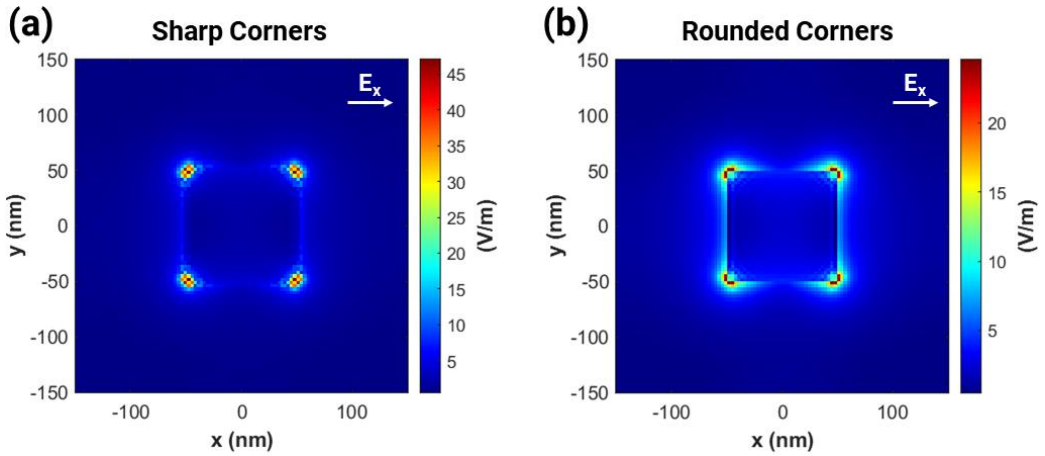

Figure 3.6 – Maximum simulated absolute value of the electric field for 100 nm squares with (a) idealised sharp corners and (b) corners with a 5 nm radius curve.

As Figure 3.6 shows, by rounding the corners of the squares with a 5 nm radius, there is a significant reduction in the maximum field intensity from 47.2 V/m to 24.6 V/m (47.9%) (17,18). This is particularly relevant when comparing the monomeric structures to trimer structures (Section 3.3.3) and when considering the effects of annealing on different plasmonic geometries (Chapter 4).

3.3.2. Negative Monomeric Shapes

As explained in Section 1.2.2.3, when excited by incident light, negative arrays exhibit a phenomenon known as extraordinary optical transmission (EOT). EOT originates from the combination of propagating waves between holes and localised resonances within holes (19–26). The combination of these two resonant modes results in a significant increase in light transmission through the array at the resonance wavelength. Due to the plasmonic origin of this enhanced transmission, the resonance peak is shifted by changes in localised refractive index meaning arrays of negative structures can act as sensors. In this section we characterise negative arrays and examine their differences in comparison to positive arrays.

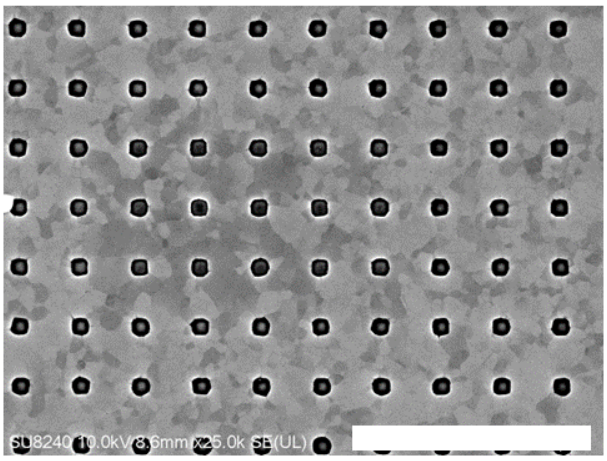

Figure 3.7 - Annealed square nanoholes (Scale bar: 2 µm).

3.3.2.1. Effect of Periodicity and Size

Negative arrays with varying element sizes and periodicity were fabricated and simulated with the resulting transmission spectra displayed in Figure 3.8.

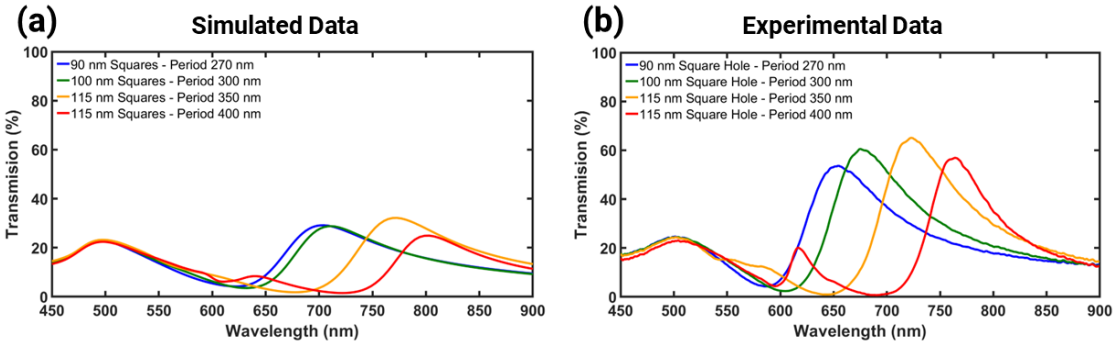

Figure 3.8 - Spectra of negative, square plasmonic structures in water. (a) FDTD simulations and (b) experimental data.

As with positive monomeric structures, it is clear that the resonance wavelength increases with structure size. The effect of periodicity is similar, with increasing periodicity resulting in a longer resonance wavelength with a lower FWHM (Table 3.6). Another effect of increasing periodicity is the reduction in transmission percentage due to reduced hole density. These trends are mirrored in the simulations although the spectra themselves have increased FWHMs and reduced transmission when compared to their experimental counterparts. This discrepancy can be explained by the effect of the titanium adhesion layer due to the increase in surface area occupied by the adhesion layer in the simulations being drastically increased (Appendix A.3.1). All the spectra for negative structures show a resonance peak at approximately 500 nm. This peak comes from the transmission of light through the thin gold film and therefore should be discounted (Appendix A.3.2) (27). There is a secondary peak for the 115 nm squares when the period is increased to 400 nm, which arises from coupling between the holes at 45˚ as opposed to the main spectral peak that comes from coupling between the nanoholes that are closest to each other (90˚) (Fig. 3.9(b)).

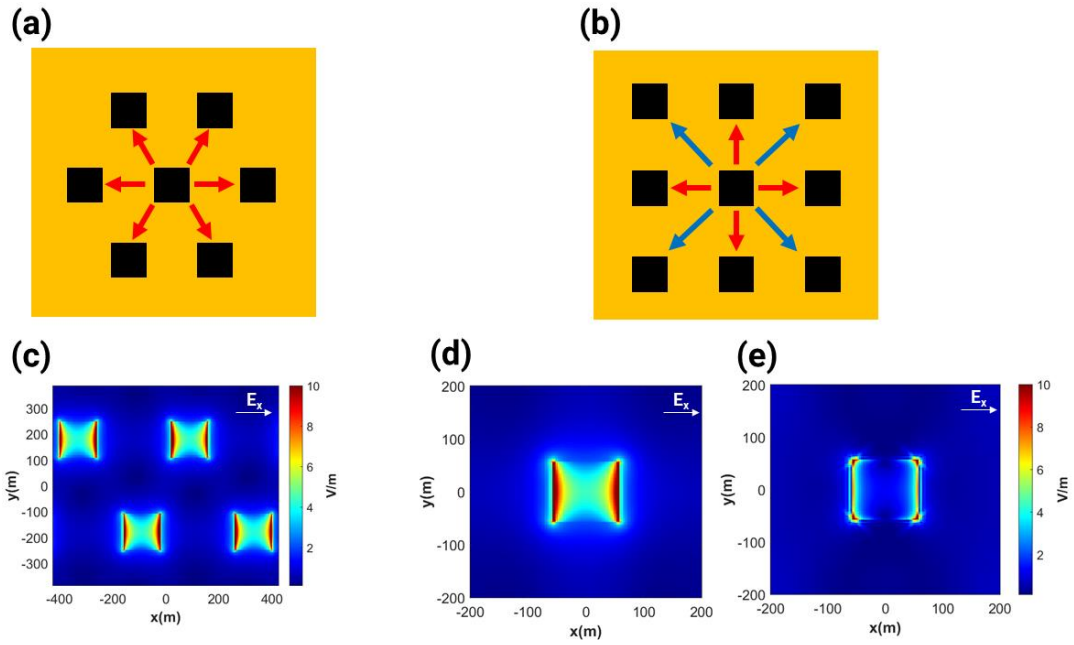

Figure 3.9 - The different modes present in nanohole arrays (a) Schematic of the hexagonal lattice pattern field distribution (b) Schematic of the square lattice pattern field distribution (c) The simulated field distribution in holes with a hexagonal lattice pattern (d) The simulated field distribution in holes with a square lattice pattern at the longer wavelength mode (e) The simulated field distribution in holes with a square lattice pattern at the shorter wavelength mode.

Table 3.6 shows the sensitivity and FoM of these holes.

Table 3.6 - Sensitivity and FoM of different negative square arrays. Resonance wavelength taken at transmission minima.

Sensor Size (nm)	Period (nm)	Resonance Peak in Water (nm)	Sensitivity (nm/RIU)	FoM
90	270	653.7	162.52	1.33
100	300	677.01	158.36	1.43
115	350	722.91	197.56	1.98
115	400	762.53	240.10	3.11

The FoM's of the negative arrays listed in Table 3.6 can be compared to the FoM's of the positive arrays listed in Tables 3.2 and 3.4. In general, the positive arrays all have a higher FoM than the negative arrays. The only exception to this is the 115 nm square holes with a period of 400 nm which have a comparable FoM to that of monomeric positive arrays. The maximum simulated EM fields of the negative structures are listed in Table 3.7.

Table 3.7 - Maximum simulated absolute value of the electric field of negative nanostructures.

Hole Size (nm)	Period (nm)	Maximum Electric Field Intensity (V/m)
90	270	12.6
100	300	11.6
115	350	13.1
115	400	14.1

Despite these structures being simulated with idealised conditions such as perfectly sharp corners and no annealing related deformation, the maximum EM fields are the lowest of any of the simulated shapes. This results in a low localised sensitivity as presented in Section 3.3.5.

Increasing periodicity between the negative structures results in a shift in the resonance wavelength of 39.6 nm whereas for the positive structures it only causes a shift of 22.2 nm. This is a result of the propagating resonances that occur between nanoholes which leads to a larger influence of periodicity when designing nanohole arrays.

3.3.2.2. Effect of Lattice Pattern on Nanohole Properties

As the effect of periodicity is important for nanohole arrays, we can examine the effect of different lattice patterns on the properties of EOT sensors (Fig. 3.10). Here we consider square and hexagonal lattices.

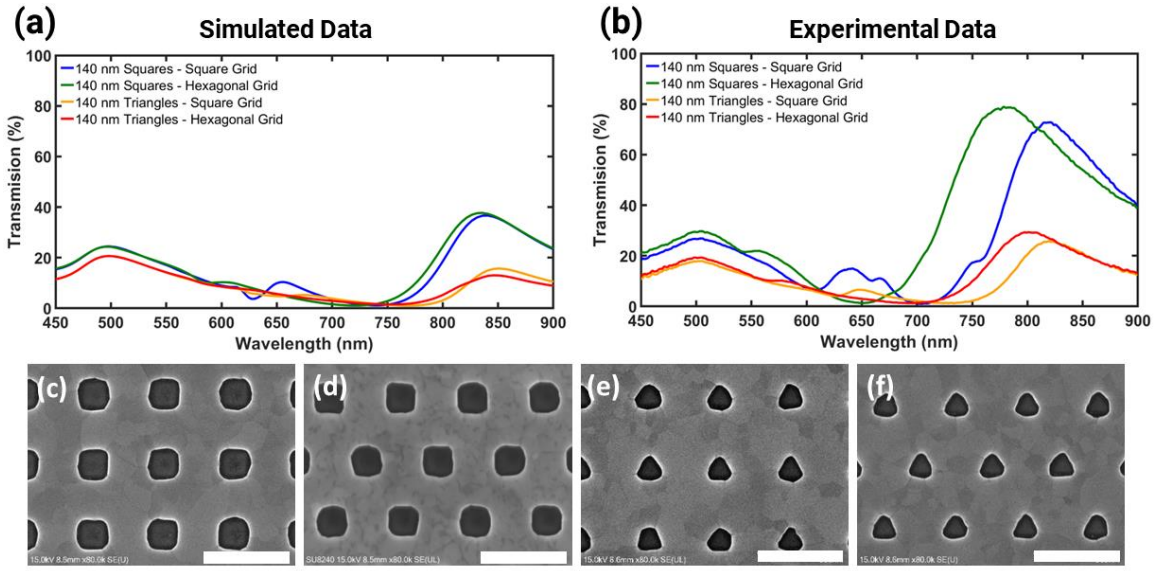

Figure 3.10 - Transmission spectra and SEMs of nanohole arrays with different shapes and lattice structures. (a) Simulated and (b) experimental transmission spectra, (c) 140 nm square holes on a square lattice (d) 140 nm square holes on a hexagonal lattice (e) 140 nm triangular holes on a square lattice (f) 140 nm triangular holes on a hexagonal lattice (Scale bars: 500 nm)

When testing the effect of lattice type, there is a significant mismatch between the simulations and the experimental data, particularly when it comes the intensity of transmitted light. As previously mentioned, this mismatch seems to be largely due to the simulation software overestimating the effect of the 2 nm titanium adhesion layer due to the large area of titanium under the holes (Appendix A.3.1).

Simulations in literature have shown a slim advantage for hexagonal lattices as opposed to square lattices of circular holes in terms of FoM which was driven by their smaller simulated FWHM (28). This is not replicated in either the experimental work or the simulations carried

out here. The trends in the simulations are similar in some respects to the experimental results with structures on a hexagonal lattice having higher FWHMs (Table 3.8).

Table 3.8 - FWHM of negative plasmonic structures with different lattice patterns.

Sensor	FWHM - Simulated Data (nm)	FWHM – Experimental Data (nm)
140 nm Squares – Square Lattice	60.49	165.7
140 nm Squares – Hexagonal Lattice	139.79	203.05
140 nm Triangles – Square Lattice	33.29	78.84
140 nm Triangles – Hexagonal Lattice	94.92	168.91

The disagreement of these results with literature could come from a few different sources, firstly, the structures simulated by Ekşioğlu *et al*. were circular holes which may couple differently in a manner as to not cause broadening (28). In addition to this, they used a finer mesh size than was used for the simulations in this thesis and hence potentially more accurately captured the plasmonic response. The counter to the mesh argument comes from the experimental results where the trend of the hexagonal lattice increasing FWHM still holds although it can be difficult to directly compare simulations with experimental data as simulations cannot take into account factors such as inhomogeneous broadening and rounded corners that are a factor for real structures.

When reflecting on the experimental data, the effect of the hexagonal lattice is consistent with the simulations with a shift to shorter wavelengths being recorded in both cases (26.5 nm for triangular holes, 40.6 nm for square holes). In addition, the secondary peak caused by coupling between holes at a 45˚ angle is almost entirely removed in the structures that are placed on the hexagonal lattice (Fig. 3.9). This confirms the previous point that this peak is due to the difference in spacing as in the hexagonal lattice all holes are the same distance apart. Table 3.9 shows how the sensitivity of the nanoholes vary with geometry and lattice structure.

Table 3.9 - Effect of lattice layout on the properties of negative arrays. Resonance wavelength taken at transmission minima.

Sensor	Resonance Peak in Water (nm)	Sensitivity (nm/RIU)	FoM
140 nm Squares – Square Lattice	831.95	211.4	1.28
140 nm Squares – Hexagonal Lattice	791.35	329.19	1.62
140 nm Triangles – Square Lattice	784.23	253.86	3.22
140 nm Triangles – Hexagonal Lattice	757.69	251.55	2.65

The data in Table 3.9 shows no clear trend as to if the hexagonal lattice is beneficial. For the square holes, the hexagonal lattice shows a significant increase in sensitivity accompanied by a slight increase in FoM. For the triangular holes, the sensitivity stays approximately

constant regardless of lattice, but the hexagonal lattice has a lower FoM due to its increased FWHM. However, the triangular holes do perform consistently better when compared to the square holes with FoM's approximately double that of the squares. With no data on the efficacy of triangular nanoholes for sensing applications in literature, this is an area that may benefit from further investigation.

3.3.3. Trimers

Trimeric structures such as split rings, disc trimers and triangle trimers take advantage of the plasmonic coupling that occurs between separate elements in a resonating structure. This coupling causes a significant increase in the intensity of the EM field close to the structure, resulting in an increased sensitivity to analytes that are close to the sensor surface.

3.3.3.1. Packing Density of Trimer Structures

When optimising trimers, a greater packing density was required when compared to monomeric shapes to create a plasmon with sufficient intensity. Figure 3.11 shows how the trimers spectra compares when having a 1 µm spacing compared to having a 235 nm edge-edge spacing.

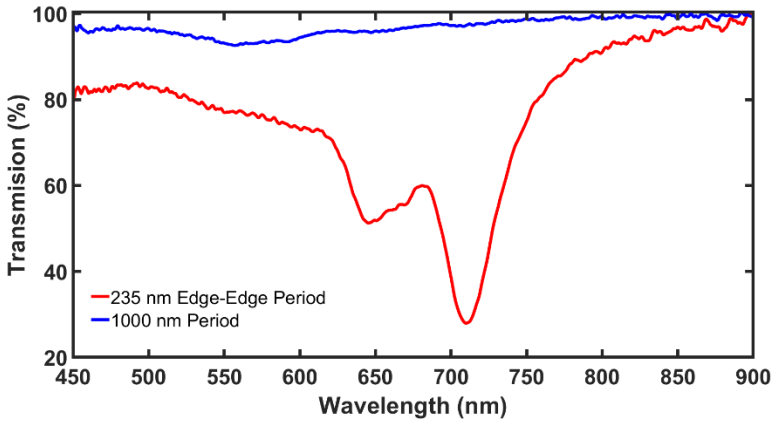

Figure 3.11 - The effect of periodicity on the resonance of triangle trimers (spectra in water).

These values are in agreement with the literature where it is shown that resonances for trimers with a period of 1 µm attenuate light by at least an order of magnitude less when compared to trimers packed more closely (29,30). For this reason, a constant inter-trimer spacing of 235 nm (edge-edge) was used when designing the trimers described in this thesis.

3.3.3.2. Disc Trimers

Disc trimers take advantage of the coupling that occurs between closely packed resonating structures while retaining the simplicity of fabricating discs.

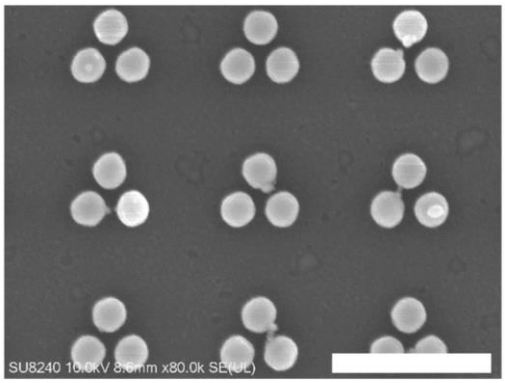

Figure 3.12 - SEM of disc trimer nanostructures (Scale bar: 500 nm).

Disc trimers of different sizes with a 25 nm gap between structures and a 235 nm edge-edge period were investigated both experimentally and with FDTD simulations (Fig. 3.13). It should be noted that each structure is labelled by the size of one of its sub-elements.

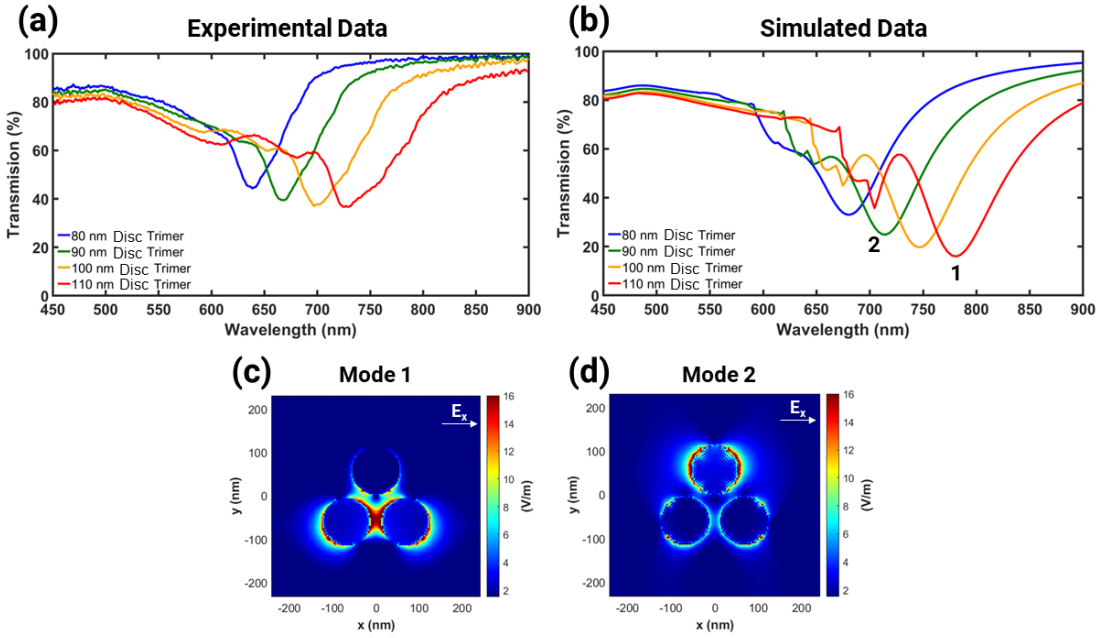

Figure 3.13 - The properties of disc trimer nanostructures. (a) Experimental and (b) simulated transmission spectra with (c) the resonance mode of a 110 nm circle trimer at 781 nm and (d) the resonance mode of a 110 nm disc trimer at 704 nm.

Both the simulated and fabricated structures show a clear trend of an increased resonance wavelength with increased size. In addition to this, they both show two peaks whose modes are displayed in Figure 3.13(c,d). The longer wavelength mode comes from the coupling between each element resulting in a much more localised field. The shorter wavelength mode on the other hand arises from the coupling between trimers and is less localised when compared to the longer resonance wavelength. Due to this, for sensing purposes we are more interested in the inter-element (higher wavelength) peak for these structures. The experimentally measured bulk refractive index and FoM of these structures is shown in Table 3.10.

Table 3.10 - The sensitivity and FoM of disc trimer sensors. Resonance wavelength taken at transmission minima.

Structure Size (nm)	Sensitivity (nm/RIU)	Resonance Wavelength in Water (nm)	FoM
80	153.46	638.40	2.86
90	222.61	667.30	3.97
100	281.37	699.35	4.21
110	200.77	727.60	2.66

As with all the structures presented in this thesis, there is a clear trend of sensitivity increasing with the size of the structures. In this dataset however, there is an outlier whereby the sensitivity and FWHM of the disc trimer sensors drops significantly for the 110 nm trimer. This anomaly does not align with theory, or the trend discussed in Section 3.3.4 and as a result is most likely the result of experimental error. When comparing the FoM for these trimeric structures to the monomeric structures, discounting the 110 nm trimer, the disc trimers have a higher FoM than the majority of the monomeric structures. The simulations also allow us to examine how the maximum EM field scale with structure size.

Table 3.11 - Maximum simulated absolute value of the electric field of disc trimer nanostructures.

Disc Trimer Size (nm)	Maximum Electric Field Intensity (V/m)
80	32.5
90	29.2
100	28.0
110	29.5

There is a slight trend towards larger structures having a lower maximum EM field although the change is minimal, with the maximum EM field increasing from 100 nm to 110 nm disc trimers. Compared to their monomeric disc counterparts, there is a significant increase in EM field with an average increase of 37.7%, indicating disc trimers will have a higher localised sensitivity as a result of intra-structure coupling (Table 3.3).

3.3.3.2. Split Rings

Split ring sensors consist of three separate segments of a ring separated by small gaps to cause a magnification of the local electromagnetic field. The split rings examined here have a split size of 25 nm, a wall thickness of 33 nm and an edge-edge periodicity of 235 nm. An SEM of these structures can be seen in Figure 3.14.

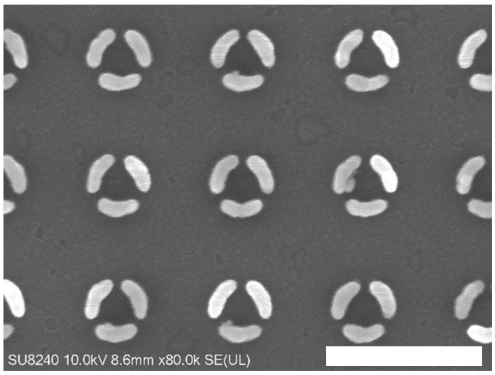

Figure 3.14 – An SEM of split ring structures (Scale bar: 500 nm).

The simulated and experimental spectra of these rings follows a similar pattern to the rest of the structures whereby a larger size results in a longer wavelength resonance (Fig. 3.15 a,b).

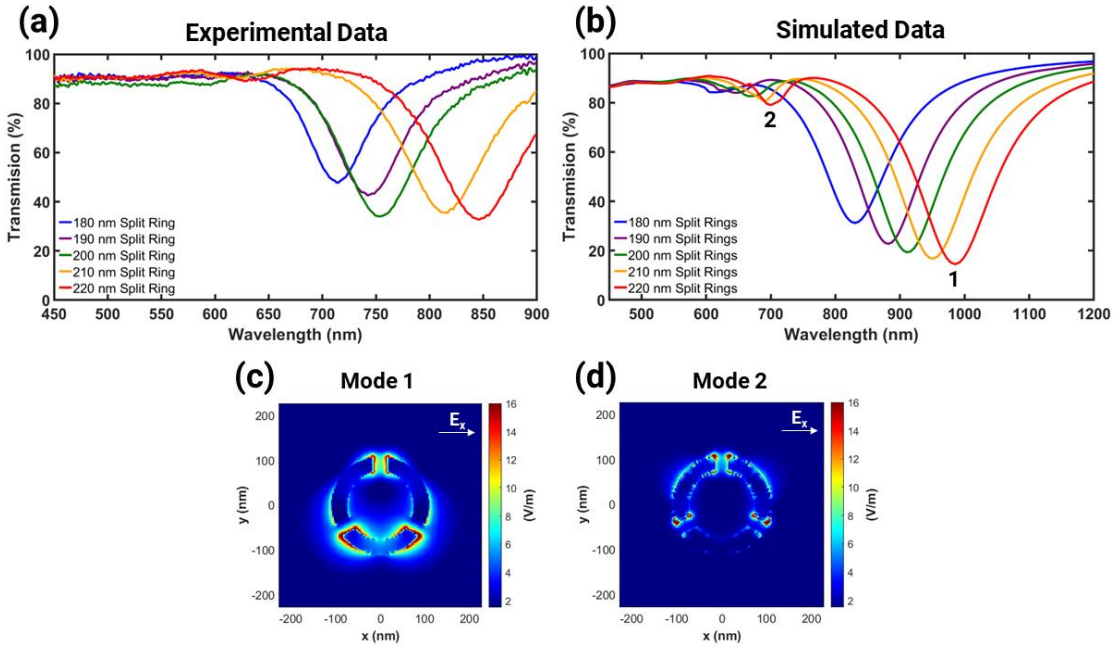

Figure 3.15 - The properties of split ring nanostructures. (a) Experimental and (b) simulated transmission spectra. (c) The resonance mode of a 220 nm split ring at 985 nm and (d) the resonance mode of a 220 nm split ring at 700 nm.

Although much weaker than for the disc trimers, the split rings also show a longer and shorter wavelength peak although this is only visible for the largest split rings in the experimental data. As before, the shorter wavelength peak corresponds to the inter-ring coupling whereas the longer wavelength mode comes from coupling between the resonating structures. The experimental data in Figure 3.15(a) does not show a trend as linear as the simulated data. This could be due to annealing causing deformation or a change in dielectric properties. The FoM and bulk refractive index sensitivity data for these sensors is collated in Table 3.12.

Table 3.12 - The sensitivity and FoM of split ring nanostructures. Resonance wavelength taken at transmission minima.

Structure Size (nm)	Sensitivity (nm/RIU)	Resonance Wavelength in Water (nm)	FoM
180	237.95	713.90	3.88
190	262.17	743.45	3.81
200	306.91	753.55	4.02
210	334.27	813.80	4.07
220	354.61	848.05	4.09

In this case, although the sensitivity increases with wavelength, the FoM does not change considerably throughout. This is due to the FWHM of the split ring structure increasing significantly as they get larger, negating any increases in sensitivity. Despite this, even the ring structure with the lowest FoM still outperforms all of the monomeric structures (Tables 3.2, 3.4).

Table 3.13 - The maximum simulated absolute value of the electric field of split ring sensors.

Split Ring Size (nm)	Maximum Electric Field Intensity (V/m)
180	26.0
190	39.6
200	38.3
210	50.8
220	55.5

The maximum EM field intensity calculated for each of the split rings shows a very clear trend of increasing with wavelength, unlike the disc trimers. This may result in larger rings having a greater localised refractive index sensing capability.

3.3.3.3. Triangle Trimers

Triangle trimers combine two mechanisms that concentrate EM fields, sharp points and coupling between tightly packed nanostructures. For these structures, the central points of each triangle are placed 20 nm from each other, and the edge-edge periodicity is maintained at 235 nm (Figure 3.16).

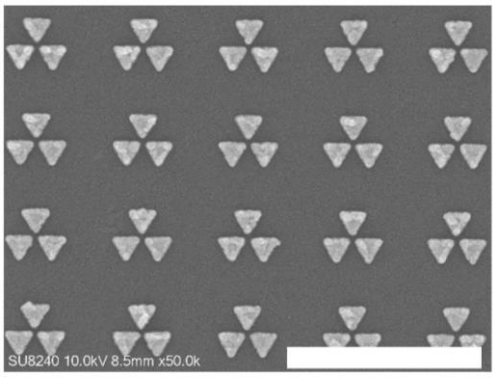

Figure 3.16 - SEM of triangle trimers (Scale bar: 1 μm).

The spectra and resonance modes of the triangle trimers are shown in Figure 3.17.

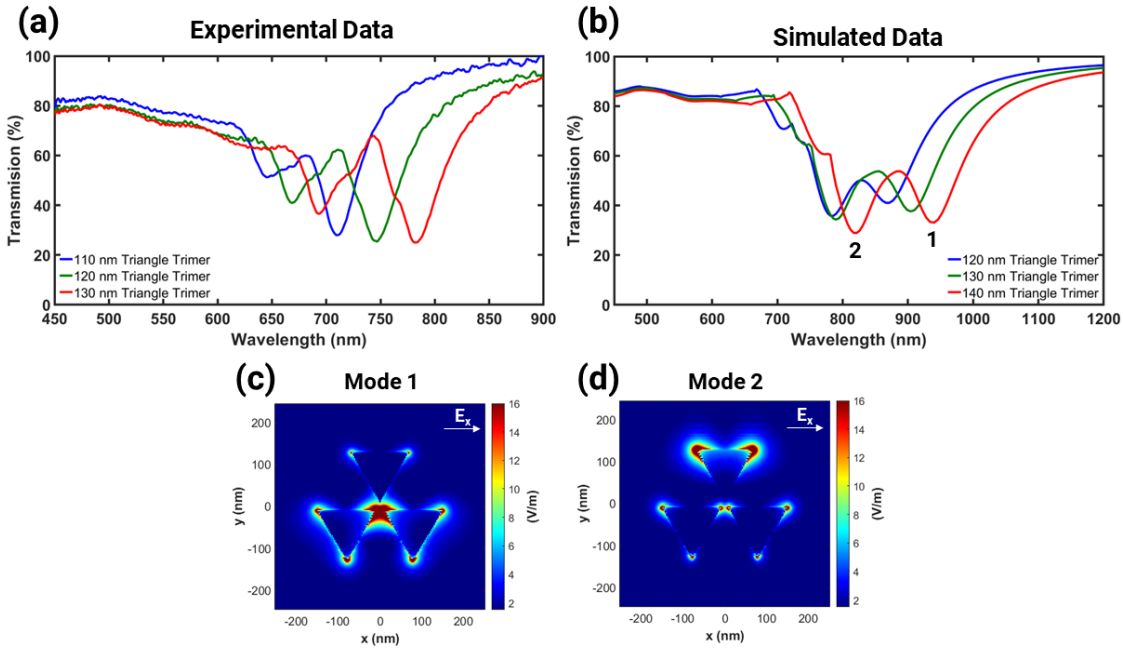

Figure 3.17 - The properties of triangle trimer nanostructures. (a) Experimental and (b) simulated transmission spectra. The resonance mode of (c) a 140 nm triangle trimer at 934 nm and (d) the resonance mode of a 140 nm triangle trimer at 812 nm.

As with all the trimers, two clear resonance peaks are created by the triangle trimers. In this case, the secondary shorter wavelength peak has higher intensity than for either the rings or the disc trimers which is a result of stronger inter-trimer coupling. As with previous shapes, the bulk refractive index sensitivity and FoM were calculated for the longer wavelength peak.

Table 3.14 – Experimental sensitivity and FoM of triangle trimer nanostructures. Resonance wavelength taken at transmission minima.

Structure Size (nm)	Sensitivity (nm/RIU)	Resonance Wavelength in Water (nm)	FoM
120	261.61	669.50	4.17
130	203.88	701.75	2.47
140	230.03	732.05	2.44

Unlike the rest of the shapes, triangle trimers do not show a trend of sensitivity with resonance wavelength. The FoM's of these shapes are also lower than those typically seen for the trimer structures with the 130 nm and 140 nm structures being more comparable to monomeric structures.

However, these structures were not designed to optimise bulk refractive index sensitivity, they were fabricated to create the strongest possible local EM field (Table 3.15).

Table 3.15 - Maximum simulated absolute value of the electric field of triangle trimer sensors.

Triangle Trimer Size (nm)	Maximum Electric Field Intensity (V/m)
120	64.1
130	67.8
140	71.8

As with the split rings, the triangle trimers show a clear trend of increasing EM field with longer resonance wavelength. In addition to this, they also display the largest EM fields of any structure simulated with a peak of 71.8 V/m. This should give them an excellent localised refractive index sensitivity despite their slightly diminished bulk refractive index sensitivity.

As previously mentioned, these simulations calculate the maximum EM field for an idealised scenario where shapes are perfectly formed (Section 3.3.1.2). To examine the limitations of simulation, a triangle trimer was given rounded corners with a radius of 5 nm. This is particularly relevant when considering the geometrical effects that techniques such as annealing can have (Chapter 4).

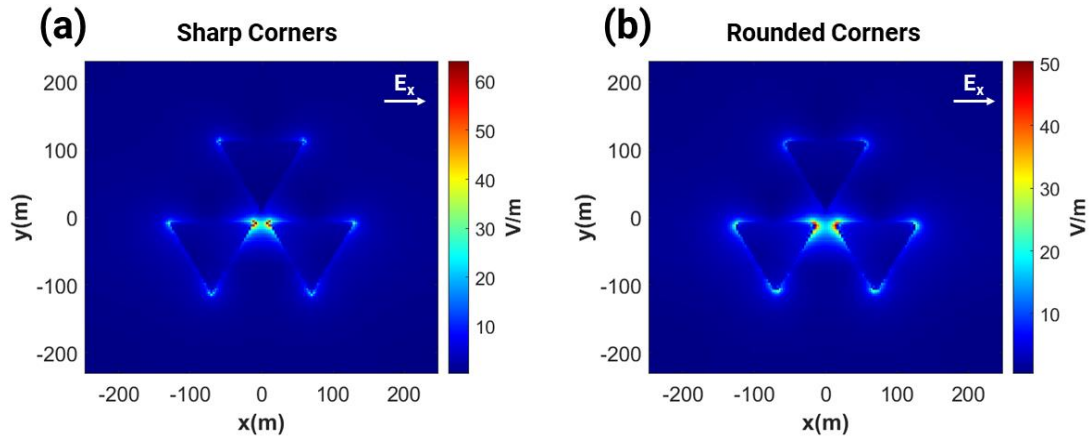

Figure 3.18 - The effect of rounded corners on the EM field of triangle trimers. (a) Sharp corners at 871 nm. (b) Rounded corners at 826 nm.

From Figure 3.18, the maximum electromagnetic field drops from 64.1 V/m to 50.3 V/m for 120 nm triangle trimers when the corners are rounded, a drop of 21.5% (17,18). When this drop is compared to monomeric structures (47.9% drop, Section 3.3.1.1) we can see that the effect is less dramatic. This is because the high intensity EM fields seen for trimeric structures are less reliant on sharp points and more reliant on coupling between adjacent structures which are not affected to the same extent by deformation. This makes trimers a better option for reliably achieving high intensity EM fields for detecting small molecule surface interactions.

3.3.4. The Relationship between Resonance Wavelength and Bulk Sensitivity

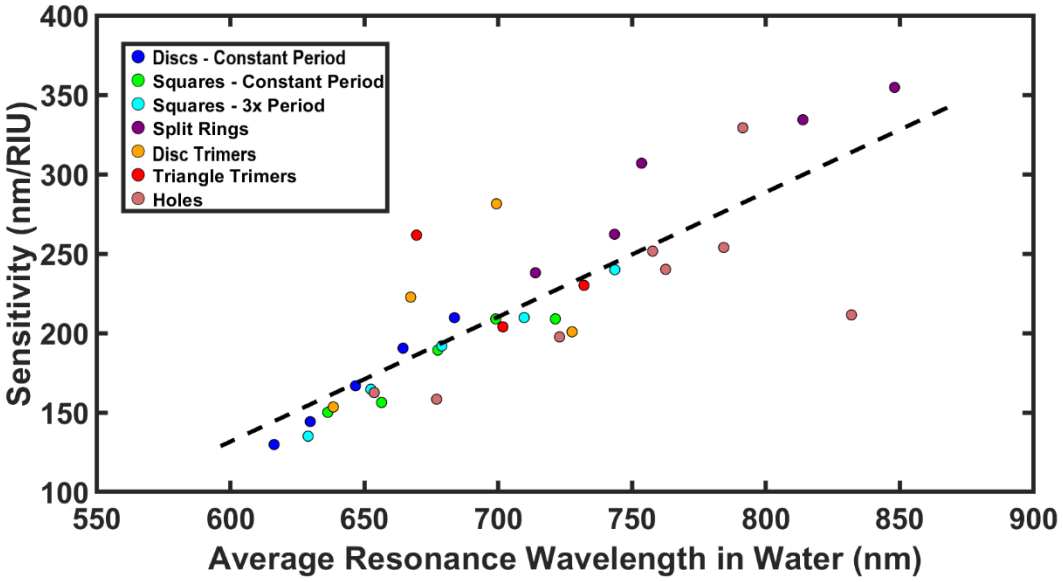

Figure 3.19 - The relationship between resonance wavelength and bulk refractive index sensitivity (R^2 = 67.3%).

The gradient of the best fit line shown in Figure 3.19 indicate that for every nanometre increase in resonance wavelength, on average the sensitivity of a sensor increases by 0.79 nm/RIU. One factor that can explain this relationship is the size of the electromagnetic field since it scales with resonance wavelength (31–35). Figure 3.20 shows the difference in field extent for a 100 nm square and a 140 nm square.

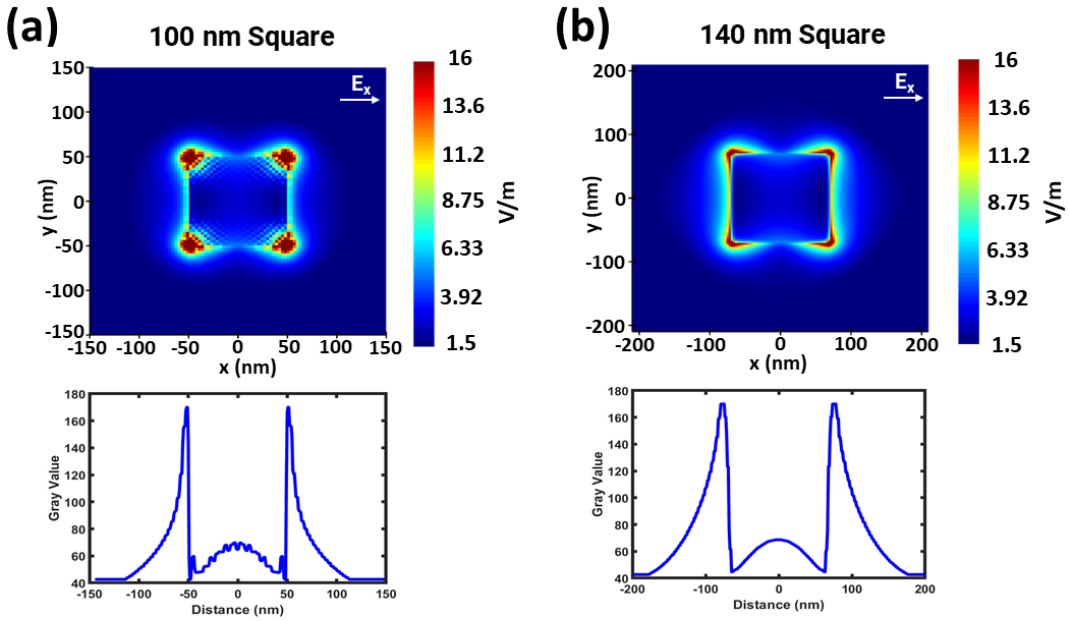

Figure 3.20 - The expansion in field size as the size of the plasmonic element increases. (a) The field extent of a 100 nm square (63 nm). (b) The field extent of a 140 nm square (107 nm).

The 100 nm square has a simulated field extent of 63 nm whereas the 140 nm square has a field extent of 107 nm. This results in a simulated sensitivity (experimental) of 351.5

nm/RIU (135.06 nm/RIU) for the 100 nm squares and 457.9 nm/RIU (239.86 nm/RIU) for the 140 nm squares. For the monomeric shapes, this field expansion explains the increase in sensitivity as despite the disc shapes having a simulated peak EM field that stays relatively constant with size (Table 3.3), the sensitivity of the discs increases in a linear manner with simulated field extent.

Although the disc and triangle trimers do not show a linear trend as opposed to the monomeric structures, it is clear that resonance wavelength explains almost all of the bulk sensitivity (R^2 = 67.3%). Much of the literature claims that particular nanostructure geometries increase bulk sensitivity while negating to correct for resonance wavelength (10,26,34–39). In this case, if the trimer's ability to concentrate an electromagnetic field truly increased their bulk sensitivity, we would see all split rings, disc trimers and triangle trimers lying above the trendline in Figure 3.19 but instead they are distributed approximately evenly around this line. This indicates that any deviation from this line is most likely down to experimental error.

This strong wavelength dependency indicates that if bulk refractive index sensing or sensing at a distance is required, simple monomeric structures will perform just as well if not better than trimeric structures with a less error prone and faster fabrication process. This is confirmed in simulations where an object was introduced 50 nm from the surface of the 100 nm and 140 nm squares depicted in Figure 3.20 causing a 0.74 nm and 1.93 nm shift respectively (Appendix A.3.3). An example of where this conclusion can be used to practical effect is discussed in Chapter 5 of this thesis whereby a polyethylene glycol linker spaces the biotin receptor from the plasmonic surface. In this case, a larger sensing volume is beneficial as it allows for more sensitive detection of these relatively distant binding events.

3.3.5. Local Refractive Index Sensitivity

For many sensing applications, analytes are bound very close to the plasmonic surface. In this case, a greater localisation of the plasmonic field will result in a greater shift in response to analytes that enter the area of concentrated EM field.

Techniques for measuring the bulk refractive index of plasmonic sensors are well established and relatively straight-forward to carry out. However, measuring the localised refractive index sensitivity is less straightforward. By drawing on techniques used in literature, the localised refractive index sensitivity of the sensors listed in this chapter can be compared (40,41).

3.3.5.1. Thiolation

The first technique to measure localised sensitivity utilised thiol modifications as a method of only changing the localised refractive index (Section 3.2.6). Sensors of different geometries were measured before and after the formation of a thiol SAM (Refractive index ~ 1.33) and the resonance shift was measured (42) (Table 3.16).

Table 3.16 - The shift of different sensors with the addition of 11-mercaptoundecanoic acid. Quoted shifts are the maximum shift for each geometry – 140 nm discs (period 375 nm), 120 nm squares (period 360 nm), disc trimers 110 nm (20 nm gap size), 180 nm split rings (25 nm splits), 140 nm triangle trimers (20 nm gap) and 100 nm square holes (period 300 nm). Full dataset available in Appendix A.3.4.

Geometry	Resonance Before Thiol (nm)	Resonance After Thiol (nm)	Shift
Discs	634.00 (+/- 0.16)	636.7 (+/- 0.19)	2.7
Squares	631.70 (+/- 0.19)	634.45 (+/- 0.10)	2.75
Disc Trimers	654.9 (+/- 0.41)	665.35 (+/- 0.41)	10.45
Split Rings	660.30 (+/- 0.91)	666.05 (+/- 0.29)	5.75
Triangular Trimers	674.10 (+/- 0.60)	678.6 (+/- 0.12)	4.5
Holes	640.85 (+/- 0.12)	643.15 (+/- 0.2)	2.3

Trimeric structures which focus the EM field close to the surface of the sensor mostly have larger shifts than the monomeric structures indicating they may have a higher localised sensitivity. This technique will give a realistic idea of how a sensor may perform in a real-world sensing scenario given that often the analyte will only be binding to the gold as the thiols did. However, thiolation can be inconsistent and dependent on many factors including the crystalline structure of gold, defects in the gold structure, the cleanliness of samples and modification solvent purity (43,44).

Figure 3.21 shows the resonance shift for all the shapes measured. The shifts approximately correlate with the maximum recorded EM fields discussed in this chapter with trimer structures generally having the largest shifts and negative structures having the smallest shifts.

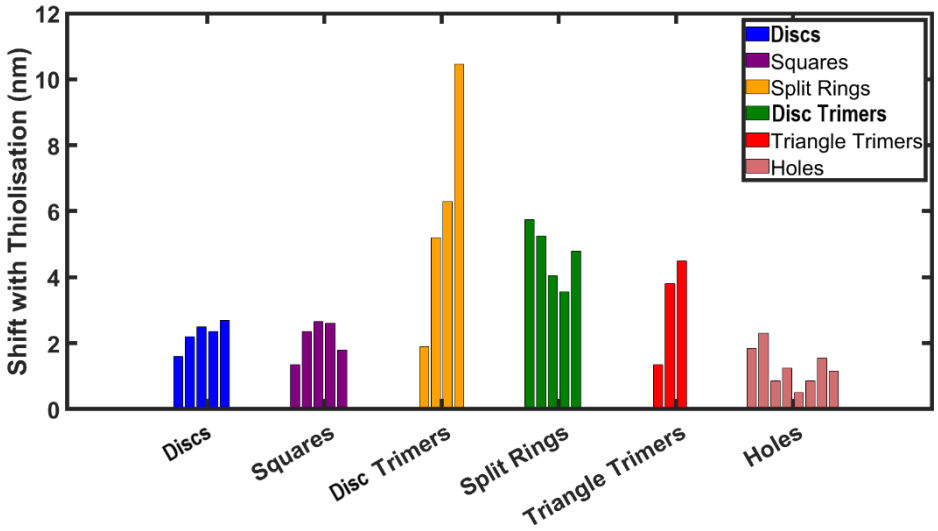

Figure 3.21 - The effect of element shape on shift with thiolation.

3.3.5.2. Aluminium Oxide Layer

This thiolation result can be confirmed with the second technique which relies on depositing 1 nm of aluminium and measuring the shift in spectra upon the addition of this aluminium layer. As these layers are so thin, they will oxidise fully meaning the layer will have the refractive index of aluminium oxide (1.76) (45,46). Table 3.17 lists the resonance shifts with the addition of an aluminium oxide layer for the best performing shape size of each geometry.

Table 3.17 - The shifts of different geometries with the addition of 1 nm of aluminium. Quoted shifts are the maximum for each geometry – 140 nm discs (period 375 nm), 140 nm squares (period 420 nm), disc trimers 110 nm (20 nm gap size), 220 nm split rings (25 nm splits) ,140 nm triangle trimers (20 nm gap) and 140 nm square holes (period 420 nm – hexagonal grid). Full dataset available in Appendix A.3.5.

Geometry	Resonance Before Aluminium Layer (1nm)	Resonance After Aluminium layer (1nm)	Shift
Discs	634.65 (+/- 0.25)	646.5 (+/- 0)	11.85
Squares	681.95 (+/- 0.29)	696.1 (+/- 0.1)	14.15
Disc Trimers	655.2 (+/- 0.37)	678.85 (+/- 0.25)	23.65
Rings	763.7 (+/- 2.8)	756.75 (+/- 2.3)	20.45
Triangular Trimers	684.65 (+/- 0.2)	704.6 (+/- 0.25)	19.95
Holes	717.55 (+/- 0.4)	726.3 (+/- 0.73)	8.75

Again, as with the thiolation method there is a general trend of trimeric structures showing a greater shift when coated (Fig. 3.21). The negative nanostructures again show that they have inferior sensing ability when compared to their positive counterparts due to their lower EM field concentration. However, it is interesting to note that for both the triangle holes and the square holes, the hexagonal grid had a significant advantage over the square grid. This is most likely due to the single resonance mode displayed by the hexagonal structures as a greater area of the surface is covered by this resonance when compared to the square grid.

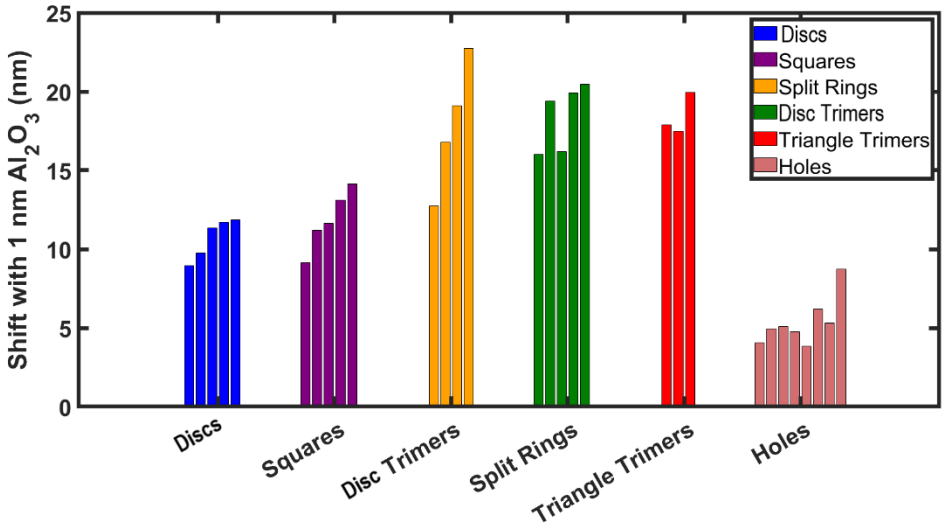

Figure 3.22 - Resonance wavelength shift with the addition of a 1 nm aluminium layer.

Due to the anisotropic nature of aluminium deposition, it does not cover the entirety of the sensing structure as the thiolation method did. Despite the addition of the Al_2O_3 layer not being as true to a real-world scenario as the addition of a thiol layer, if does give a very reproducible, consistent measurement by which to measure the localised sensitivities without the drawbacks of creating a thiol monolayer. By considering both results, we can see that trimeric structures have a higher localised sensitivity when compared to monomeric structures such as squares and discs with both techniques showing that in most cases, any trimer structure has a higher localised sensitivity than a monomeric shape.

3.4. Conclusion

In this chapter we investigated the effect of different parameters on the sensitivity of plasmonic structures. From this analysis, a few conclusions can be drawn. The most important of these conclusions is that resonance wavelength is the key factor that defines bulk sensitivity above everything else including the type of sensor and the geometry of the sensing elements. When considering field enhancement and localised sensitivity, there is a clear advantage for trimeric structures as the coupling between structures within each element creates a very strong EM field. This advantage in localised sensitivity is further enhanced due to the greater resilience trimers show to fabrication limitations such as slightly rounded corners which significantly diminish the localised sensing ability of square monomeric elements. Negative structures were shown to be generally inferior to positive structures in sensing ability. However, it was shown that further work exploring novel geometries for plasmonic nanoholes, such as the triangular holes shown in this chapter, may lead to enhancement of their sensitivity and FoM.

References

1. Haynes WM, Lide DR, Bruno TJ, editors. CRC Handbook of Chemistry and Physics [Internet]. CRC Press; 2016. Available from: https://www.taylorfrancis.com/books/9781498754293

2. Palik ED. Handbook of Optical Constants of Solids. Palik ED, editor. Vol. I. Elsevier; 1997.

3. Monkawa A, Nakagawa T, Sugimori H, Kazawa E, Sibamoto K, Takei T, et al. With high sensitivity and with wide-dynamic-range localized surface-plasmon resonance sensor for volatile organic compounds. Sens Actuators B Chem. 2014 Jun;196:1–9.

4. Cinel NA, Bütün S, Özbay E. Electron beam lithography designed silver nano-disks used as label free nano-biosensors based on localized surface plasmon resonance. Opt Express [Internet]. 2012 Jan 30;20(3):2587. Available from: https://opg.optica.org/oe/abstract.cfm?uri=oe-20-3-2587

5. Li H, Luo X, Du C, Chen X, Fu Y. Ag dots array fabricated using laser interference technique for biosensing. Sens Actuators B Chem. 2008 Sep 25;134(2):940–4.

6. Chang YC, Chung HC, Lu SC, Guo TF. A large-scale sub-100 nm Au nanodisk array fabricated using nanospherical-lens lithography: A low-cost localized surface plasmon resonance sensor. Nanotechnology. 2013 Mar 8;24(9).

7. Lee SW, Lee KS, Ahn J, Lee JJ, Kim MG, Shin YB. Highly sensitive biosensing using arrays of plasmonic Au nanodisks realized by nanoimprint lithography. ACS Nano. 2011 Feb 22;5(2):897–904.

8. Ma WY, Yang H, Hilton JP, Lin Q, Liu JY, Huang LX, et al. A numerical investigation of the effect of vertex geometry on localized surface plasmon resonance of nanostructures. Opt Express [Internet]. 2010 Jan 18;18(2):843. Available from: https://opg.optica.org/oe/abstract.cfm?uri=oe-18-2-843

9. Omrani MK, Mohammadi H, Fallah H. Ultrahigh sensitive refractive index nanosensors based on nanoshells, nanocages and nanoframes: effects of plasmon hybridization and restoring force. Sci Rep. 2021 Dec 1;11(1).

10. Nehl CL, Hafner JH. Shape-dependent plasmon resonances of gold nanoparticles. J Mater Chem [Internet]. 2008;18(21):2415. Available from: http://xlink.rsc.org/?DOI=b714950f

11. Dodson S, Haggui M, Bachelot R, Plain J, Li S, Xiong Q. Optimizing electromagnetic hotspots in plasmonic bowtie nanoantennae. Journal of Physical Chemistry Letters. 2013 Feb 7;4(3):496–501.

12. Jeon H Bin, Tsalu PV, Ha JW. Shape Effect on the Refractive Index Sensitivity at Localized Surface Plasmon Resonance Inflection Points of Single Gold Nanocubes with Vertices. Sci Rep. 2019 Dec 1;9(1).

13. Piliarik M, Kvasnička P, Galler N, Krenn JR, Homola J. Local refractive index sensitivity of plasmonic nanoparticles. Opt Express [Internet]. 2011 May 9;19(10):9213. Available from: https://opg.optica.org/oe/abstract.cfm?uri=oe-19-10-9213

14. Katyal J, Soni RK. Field Enhancement Around Al Nanostructures in the DUV–Visible Region. Plasmonics. 2015 Dec 1;10(6):1729–40.

15. Katyal J, Badoni V. Localized surface plasmon resonance and field enhancement of Au, Ag, Al and Cu nanoparticles having isotropic and anisotropic nanostructure. In: Materials Today: Proceedings. Elsevier Ltd; 2020. p. 5012–7.

16. Katyal J, Soni RK. Size- and shape-dependent plasmonic properties of aluminum nanoparticles for nanosensing applications. J Mod Opt. 2013 Nov 1;60(20):1717–28.

17. Ghosh PK, Debu DT, French DA, Herzog JB. Calculated thickness dependent plasmonic properties of gold nanobars in the visible to near-infrared light regime. PLoS One. 2017 May 1;12(5).

18. Chao BK, Lin SC, Nien LW, Li JH, Hsueh CH. Effects of corner radius on periodic nanoantenna for surface-enhanced Raman spectroscopy. Journal of Optics. 2015 Dec 1;17(12):125002.

19. Genet C, Ebbesen TW. Light in tiny holes. Nature [Internet]. 2007 Jan 4;445(7123):39–46. Available from: https://www.nature.com/articles/nature05350

20. Gordon R, Sinton D, Kavanagh KL, Brolo AG. A New Generation of Sensors Based on Extraordinary Optical Transmission. Acc Chem Res [Internet]. 2008 Aug 1;41(8):1049–57. Available from: https://pubs.acs.org/doi/10.1021/ar800074d

21. Monteiro JP, de Oliveira JH, Radovanovic E, Brolo AG, Girotto EM. Microfluidic Plasmonic Biosensor for Breast Cancer Antigen Detection. Plasmonics. 2016 Feb 1;11(1):45–51.

22. Escobedo C. On-chip nanohole array based sensing: a review. Lab Chip [Internet]. 2013 Jul 7;13(13):2445. Available from: http://xlink.rsc.org/?DOI=c3lc50107h

23. Sahin R. Control of EOT on sub-wavelength Au hole arrays via Fano resonances. Opt Commun [Internet]. 2020 Jan 1;454:124431. Available from: https://linkinghub.elsevier.com/retrieve/pii/S0030401819307424

24. Cetin AE, Etezadi D, Galarreta BC, Busson MP, Eksioglu Y, Altug H. Plasmonic Nanohole Arrays on a Robust Hybrid Substrate for Highly Sensitive Label-Free Biosensing. ACS Photonics. 2015 Aug 19;2(8):1167–74.

25. Van Beijnum F, Rétif C, Smiet CB, Liu H, Lalanne P, Van Exter MP. Quasi-cylindrical wave contribution in experiments on extraordinary optical transmission. Nature. 2012 Dec 20;492(7429):411–4.

26. Prasad A, Choi J, Jia Z, Park S, Gartia MR. Nanohole array plasmonic biosensors: Emerging point-of-care applications. Biosens Bioelectron [Internet]. 2019 Apr 1;130:185–203. Available from: https://linkinghub.elsevier.com/retrieve/pii/S0956566319300661

27. Loebich O. The optical properties of gold. Gold Bull. 1972 Mar;5(1):2–10.

28. Ekşioğlu Y, Cetin AE, Petráček J. Optical Response of Plasmonic Nanohole Arrays: Comparison of Square and Hexagonal Lattices. Plasmonics. 2016 Jun 1;11(3):851–6.

29. Teo SL, Lin VK, Marty R, Large N, Llado EA, Arbouet A, et al. Gold nanoring trimers: a versatile structure for infrared sensing. Opt Express [Internet]. 2010 Oct 11;18(21):22271. Available from: https://opg.optica.org/oe/abstract.cfm?uri=oe-18-21-22271

30. Lin VK, Teo SL, Marty R, Arbouet A, Girard C, Alarcon-Llado E, et al. Dual wavelength sensing based on interacting gold nanodisk trimers. Nanotechnology. 2010;21(30).

31. Miller MM, Lazarides AA. Sensitivity of Metal Nanoparticle Surface Plasmon Resonance to the Dielectric Environment. J Phys Chem B [Internet]. 2005 Nov 1;109(46):21556–65. Available from: https://pubs.acs.org/doi/10.1021/jp054227y

32. Mayer KM, Hafner JH. Localized Surface Plasmon Resonance Sensors. Chem Rev [Internet]. 2011 Jun 8;111(6):3828–57. Available from: https://pubs.acs.org/doi/10.1021/cr100313v

33. Akiyoshi K, Tanaka YY, Ishida T, Shimura T, Tatsuma T. Plasmonic-Diffractive Hybrid Sensors Based on a Gold Nanoprism Array. ACS Appl Nano Mater. 2018 Nov 26;1(11):5994–9.

34. Szunerits S, Boukherroub R. Sensing using localised surface plasmon resonance sensors. Chemical Communications [Internet]. 2012 Aug 13;48(72):8999. Available from: http://xlink.rsc.org/?DOI=c2cc33266c

35. Anker JN, Hall WP, Lyandres O, Shah NC, Zhao J, Van Duyne RP. Biosensing with plasmonic nanosensors. Nat Mater [Internet]. 2008 Jun;7(6):442–53. Available from: https://www.nature.com/articles/nmat2162

36. Wang S, Sun X, Ding M, Peng G, Qi Y, Wang Y, et al. The investigation of an LSPR refractive index sensor based on periodic gold nanorings array. J Phys D Appl Phys. 2018 Jan 4;51(4).

37. Liu F, Jia H, Chen Y, Luo X, Huang M, Wang M, et al. Dual-Function Meta-Grating Based on Tunable Fano Resonance for Reflective Filter and Sensor Applications. Sensors. 2023 Jul 1;23(14).

38. Gerislioglu B, Dong L, Ahmadivand A, Hu H, Nordlander P, Halas NJ. Monolithic Metal Dimer-on-Film Structure: New Plasmonic Properties Introduced by the Underlying Metal. Nano Lett. 2020 Mar 11;20(3):2087–93.

39. Liu J, Ma Y, Shao J, Zhang S, Chen Y. Ultra-tall sub-wavelength gold nano pillars for high sensitive LSPR sensors. Microelectron Eng. 2018 Sep 5;196:7–12.

40. Hao F, Sonnefraud Y, Van Dorpe P, Maier SA, Halas NJ, Nordlander P. Symmetry breaking in plasmonic nanocavities: Subradiant LSPR sensing and a tunable Fano resonance. Nano Lett. 2008 Nov;8(11):3983–8.

41. Das A, Kumar K, Dhawan A. Periodic arrays of plasmonic crossed-bowtie nanostructures interspaced with plasmonic nanocrosses for highly sensitive LSPR based chemical and biological sensing. RSC Adv. 2021 Feb 7;11(14):8096–106.

42. Ehler TT, Malmberg N, Noe LJ. Characterization of Self-Assembled Alkanethiol Monolayers on Silver and Gold Using Surface Plasmon Spectroscopy. J Phys Chem B [Internet]. 1997 Feb 1;101(8):1268–72. Available from: https://pubs.acs.org/doi/10.1021/jp961656a

43. Castner DG, Hinds K, Grainger DW. X-ray Photoelectron Spectroscopy Sulfur 2p Study of Organic Thiol and Disulfide Binding Interactions with Gold Surfaces. Langmuir [Internet]. 1996 Jan 1;12(21):5083–6. Available from: https://pubs.acs.org/doi/10.1021/la960465w

44. Vericat C, Vela ME, Benitez G, Carro P, Salvarezza RC. Self-assembled monolayers of thiols and dithiols on gold: new challenges for a well-known system. Chem Soc Rev. 2010 Apr 26;39(5):1805–34.

45. French RH, Müllejans H, Jones DJ. Optical Properties of Aluminum Oxide: Determined from Vacuum Ultraviolet and Electron Energy-Loss Spectroscopies. Journal of the American Ceramic Society [Internet]. 2005 Jan 21;81(10):2549–57. Available from: https://onlinelibrary.wiley.com/doi/10.1111/j.1151-2916.1998.tb02660.x

46. Saif MTA, Zhang S, Haque A, Hsia KJ. Effect of native Al2O3 on the elastic response of nanoscale Al films. Acta Mater [Internet]. 2002 Jun;50(11):2779–86. Available from: https://linkinghub.elsevier.com/retrieve/pii/S1359645402000897

Chapter 4 - Annealing as a Method of Enhancing Plasmonic Resonance

4.1. Introduction

Annealing is a method used to alter the properties of a material by raising its temperature until the recrystallization point is surpassed. On a macroscopic level, this can soften a material making it easier to reshape due to the changes to the crystal lattice of the material. In the context of plasmonic sensing, annealing is most often used to create nano-scale features on thin sheets of metal to achieve localised surface plasmon resonances (1–6). By heating thin sheets of metal to high temperatures, solid-state dewetting occurs whereby the high temperature allows face atoms of random defects in the sheet to become mobile, resulting in many randomly shaped, isolated islands of metal. This approach can be used to quickly fabricate large-scale plasmonic surfaces, however, due to the random nature of the process, the resonances are generally of low quality as defined by the parameters discussed in Section 1.3.1 (1,4–7). The effect of heat on the crystal lattice of nanostructures can be very useful for improving the performance of lithographically defined plasmonic sensors (8–13). By raising the temperature, gold grains in the nanostructures recrystalise, resulting in a lower number of grain boundaries which reduces scattering losses during resonance. This reduces the losses during resonance as dictated by the Drude-Lorentz model (Section 1.3.3, Eqn 1.9)

The narrower peak that results from this reduction in losses significantly increases the FoM and reduces error resulting in increased sensing performance.

Although annealing is a quick and simple method for improving the sensing performance of plasmonic sensors, it does come with drawbacks. As will be seen in this chapter, annealing nanostructures can result in deformation of the structures, rounding the corners of the structures and in turn, reducing their local sensitivities. To counter this limitation, there are multiple examples in the literature of protective layers being used to prevent structure deformation during annealing. Aluminium oxide has been used for this purpose both as a natural protective layer for aluminium structures and as a layer deposited onto silver structures (8,9). The drawback of using aluminium oxide for this purpose is that there is no practical way to remove it after annealing without damaging the nanostructures. This prevents it for being useful in applications where a SAM is required as well as reducing sensitivity. An alternative method is to use HSQ as a protective layer. HSQ has been seen in literature to prevent the deformation of gold nanostructures during thermal annealing and

can then be removed with exposure to hydrofluoric acid (HF) (10). As well as protective layers, this chapter also explores the use of a femtosecond laser for annealing gold nanostructures in collaboration with researchers from Complutense University of Madrid and Polytechnic University of Madrid with the aim of retaining nanostructure geometry and hence, retaining the benefits of annealing nanostructures without the drawback of deformation.

This chapter investigates the effect of annealing on lithographically fabricated plasmonic nanostructures using with the aim of improving their plasmonic response. To achieve such an aim, different methods of annealing nanostructures were tested and compared, paying special attention to the effect on the morphology of the structures.

4.2. Methods

4.2.1. Measuring Spectral Data

Spectral data was recorded using a Stellarnet spectrometer using a custom microscope setup unless specified otherwise. Further details of the setup for recording spectra are discussed in Section 2.6.

4.2.2. Measuring Bulk Refractive Index Sensitivity

Specific quantities of glycerol were weighed and mixed in deionised (DI) water to yield 0%, 10%, 20% and 30% w/w solutions. The refractive index of these solutions was measured using a Kern ABBE Refractometer ORT 1RS. The sensors were immersed in 3 mL of each of these solutions in a 35 mm disposable petri dish and the transmission spectra was recorded five times. The resonance wavelength was plotted against refractive index and the points linearly fitted using MATLAB. The gradient of this fit represents the sensitivity of the sensor.

4.2.3. Measuring Localised Refractive Index Sensitivity

Local sensitivity was measured by the change in the transmission spectra minima position before and after the formation of a thiolated self-assembled monolayer (SAM) and deposition of 1 nm layer of aluminium (Plassys MEB 550S, Plassys MEB 400S). Five readings were taken in air before and after the application of each layer to calculate the resonance shift.

4.2.4. Annealing using a Chamber Furnace

Sensors were placed inside a chamber furnace (Carbolite RWF 1100) within a ceramic crucible to prevent contamination. Sensors were annealed at a range of temperatures for 4

hours under atmospheric conditions with a heating rate of 1.6 ˚C/s. For temperatures above 500 ˚C, the normal substrate of borosilicate glass (Pi-Kem, borofloat BF33, 3” wafers) was replaced with fused silica (Microchemicals, JGS2, 3” wafers).

4.2.5. Annealing using a Rapid Thermal Annealer

Sensors were heated to 500 ˚C at 5 ˚C/s in a Rapid Thermal Annealer (Jipelec JetFirst RTA) and held there for 10 minutes under a nitrogen atmosphere before being cooled to room temperature.

4.2.6. Annealing with a Protective HSQ layer

A mixture of hydrogen silsesquioxane (HSQ) and methyl isobutyl ketone (MIBK) (50:50) was spun at 4000 rpm for 60 seconds to create a 180 nm thick layer of HSQ. After spinning, the sample was baked at 90 ˚C for 2 minutes on a hot plate. Following this, the sensors were annealed using the RTA (Section 4.2.5). After annealing, the layer was removed using hydrofluoric acid (HF) (10:1 Water:HF) for a range of times between 15 seconds and 60 seconds.

4.2.7. Annealing Using a Femtosecond Laser

Sensors were irradiated using a femtosecond Ti: Sapphire laser with 800 nm wavelength, a pulse length of 50 fs and a frequency of 1 kHz for 60 minutes. The sensors were irradiated with three different fluences: 8.9 J/m^2, 12.7 J/m^2 and 15.3 J/m^2 corresponding to 700 mW, 1000 mW and 1200 mW. Simultaneously to the irradiation, the absorption of the sensors was measured using a UV/vis spectrometer (QE6500, Ocean Optics Inc.). Irradiation experiments were conducted at the Centre for Ultra-Fast Lasers (CLUR, Centro de Láseres Ultrarrápidos) from the Complutense University of Madrid.

4.3. Results and Discussion

4.3.1. Annealing with a Chamber Furnace

Initial annealing experiments were carried out using a chamber furnace. Plasmonic nanostructures (115 nm squares, period 350 nm) were annealed at various temperatures for 4 hours to determine the effect on the plasmonic resonance (Fig. 4.1). UV-vis spectra were recorded before and after the annealing process, as summarised in Table 4.1.

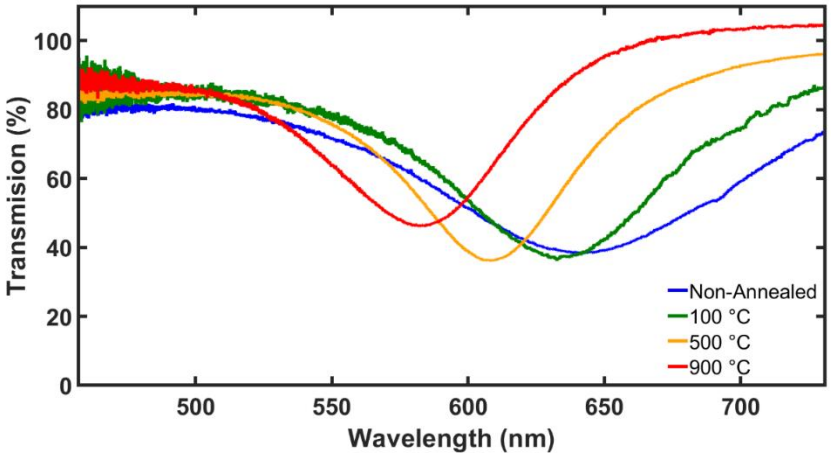

Figure 4.1 - The effect of annealing at different temperatures in a chamber furnace. Structures were 115 nm squares with a period of 350 nm (Spectra in air, **S**pectrometer used: Optosky).

Table 4.1 - The resonance wavelength and FWHM of 115 nm square sensors annealed at different temperature in a convection oven.

	Resonance Wavelength in Air (nm)	FWHM (nm)	Change in FWHM (%)
Non-Annealed	641.74	114.60	n/a
Annealed at 100 ˚C	632.73	83.19	27.41
Annealed at 500 ˚C	608.61	61.69	46.17
Annealed at 900 ˚C	582.29	66.78	41.73

As can be seen from Figure 4.1 and Table 4.1, the resonance wavelength of the LSPR peak shifts towards shorter wavelengths as the temperature increases. This is caused by the squares becoming rounded and smoother - as the temperature increases, which results in a blue shift of the LSPR wavelength.

Furthermore, we observe changes in the FWHM of the peaks, although this time the trend is not linear. Up to 500 ˚C, the FWHM decreases up to a 46.17%. This decrease in FWHM is a result of the changing grain size of the gold nanostructures. As the structure is heated, grains recrystalise resulting in a larger average grain size. This significantly reduces losses during the resonance of the nanostructures resulting in a narrower peak. However, the trend of decreasing FWHM is reversed when the temperature is raised to 900 ˚C. This is due to an interesting transformation that takes place when nanostructures are heated to this temperature as discussed in Section 4.3.8 however this transformation also increases inhomogeneity in the array accounting for the increase in FWHM.

4.3.2. Annealing with a Rapid Thermal Annealer

From the data presented in Section 4.3.1, it was concluded that 500 ˚C is the ideal temperature for annealing as it provides the best compromise between the positive effect of

increasing grain size and the negative effect caused by the loss of morphology. All the experiments presented in this section were performed at this annealing temperature.

The same 115 nm squares used in the chamber furnace were subjected to RTA for comparison. Additionally, some of the trimeric structures presented in Chapter 3 were also studied. The sensors were characterised spectroscopically, and SEM images were taken before and after the process, as shown in Figure 4.2.

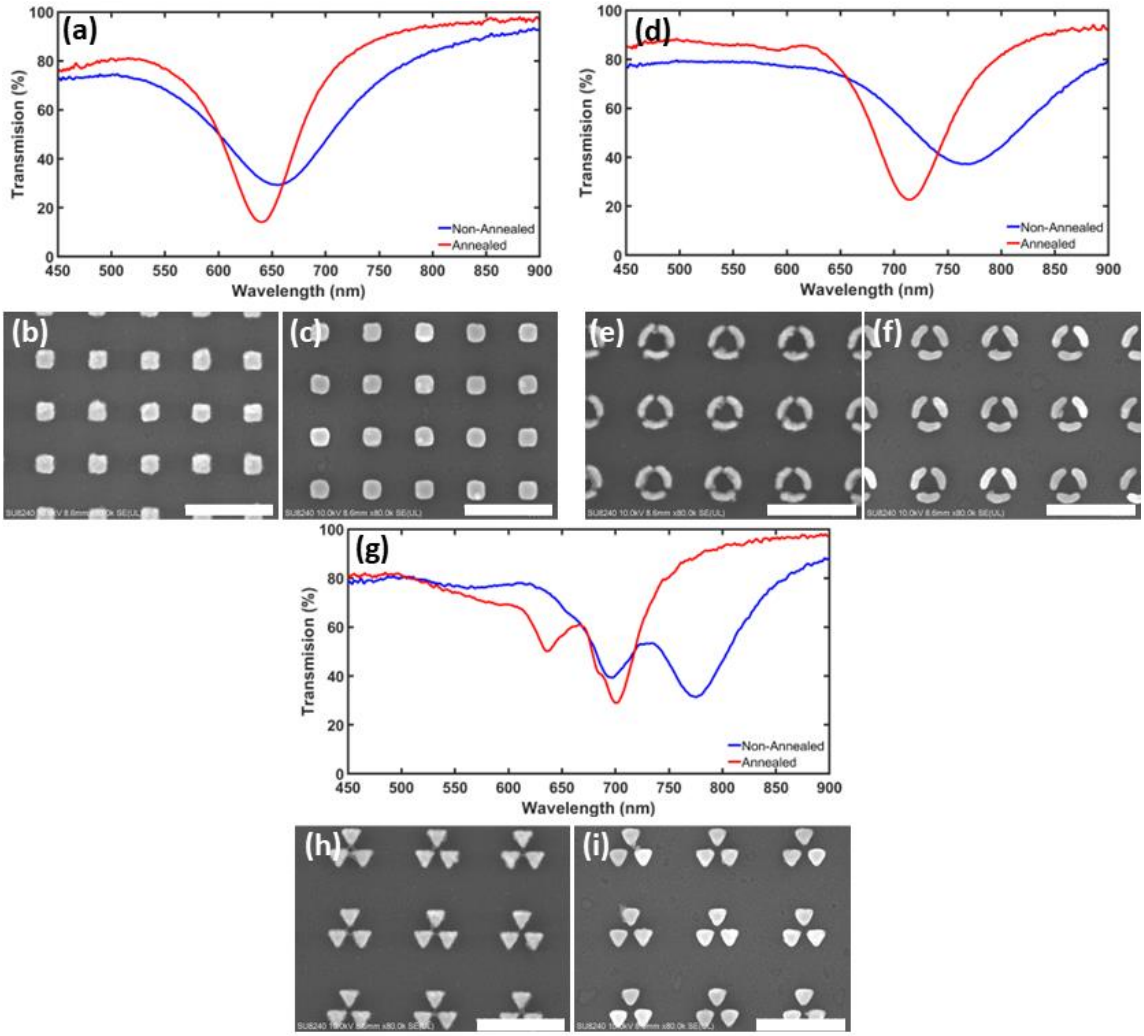

Figure 4.2 - Transmission spectra before (blue) and after (red) rapid thermal annealing of different geometries in water. (a) Square sensors (115 nm squares, period 350 nm) with SEMs (b) before and (c) after annealing. (d) Split rings (200 nm diameter, 25 nm gap, 335 nm period) with SEMs (e) before and (f) after annealing. (g) Triangular trimers (120 nm Triangles, 20 nm Gap, period 365 nm) with SEMs (h) before and (i) after annealing (Scale bars: 500 nm).

Table 4.2 - The change in resonance wavelength and FWHM caused by RTA at 500 ˚C for 10 minutes.

Sensor	Resonance Wavelength (nm)		FWHM (nm)	
	Before	After	Before	After
115 nm Squares	654.63	640.38	108.20	67.30
200 nm Split rings	766.75	714.43	127.33	75.78
120 nm Triangle trimers	774.25	700.75	80.63	41.23

As expected, even when the shape has multiple resonances in the vis/IR, all peaks blue-shift after annealing due to the rounding of all the geometries (Fig. 4.2). These images also show an additional benefit to annealing gold nanostructures. SEM images of non-annealed sensors revealed the presence of excess gold surrounding some of the nanostructures. This can occur during metal evaporations when pieces of gold attach beneath the PMMA undercut. Upon annealing, this excess gold is resorbed into the structure which prevents it from dampening the resonance (3).

When compared to the results obtained in a chamber furnace, annealing with the RTA produced smaller shifts, indicating a better preservation of the original geometry. This preservation can be attributed to the higher degree of environmental control provided by the RTA with the rates of heating and cooling being much more tightly controlled. As will be further discussed in Section 4.3.7, the heating and cooling time of the nanoparticles can affect how much they deform during annealing (11). This is confirmed by the comparison of square sensors annealed at 500 ˚C in the RTA to sensors annealed at 500 ˚C in the chamber furnace as the sensors annealed in the chamber furnace show a larger degree of deformation (Appendix A.4.1). In addition to the benefits the RTA provides in relation to control of heating and cooling, the cleanroom environment provides protection from contamination. When annealing using the chamber furnace, contamination was a persistent issue due to the high levels of particulates that are present in the oven. Annealing in a cleanroom environment removes the concern of contamination during annealing. Annealing using an RTA also massively increases potential throughput, with entire wafers being annealed in 10 minutes as opposed to the many hours it takes for the chamber furnace to rise to the required temperature and cool down again.

4.3.3. Negative Structures and Quantifying Grain Size Increase

So far, only positive structures have been discussed. However, negative arrays also undergo significant spectral improvements when annealed (Fig. 4.3).

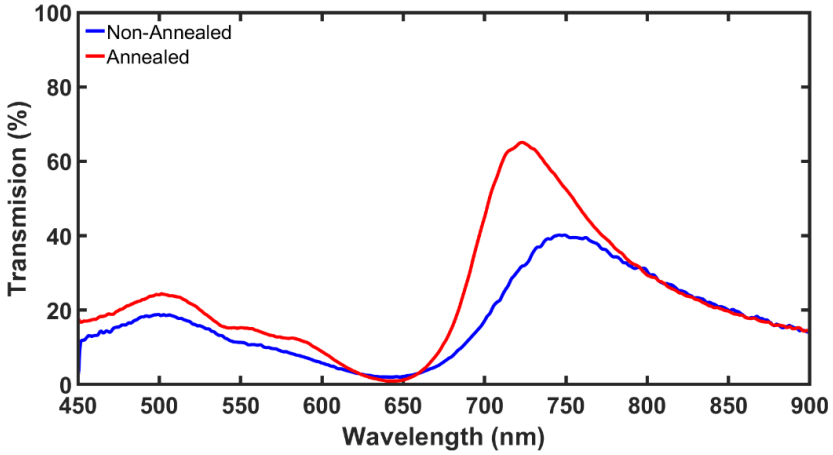

Figure 4.3 - Transmission spectra before (blue) and after (red) annealing 115 nm square nanoholes in an RTA.

In this example, as can be seen in Figure 4.3, the FWHM of the LSPR peak is dramatically reduced to from 154.3 nm to 100.75 nm after annealing.

When considering negative arrays, the physical causes of this decreased FWHM can be much more readily visualised due to the lack of a conduction layer required to image a gold coated substrate (Section 2.3.1, Fig. 2.1). Due to this lack of conduction layer, the SEM images in Figure 4.4 can show the effect of annealing on the grain size of gold surrounding a negative array.

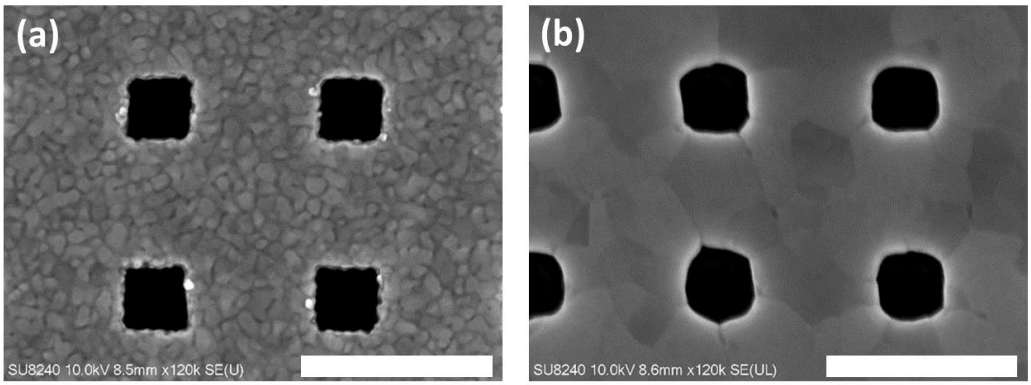

Figure 4.4 - The effect of annealing on negative arrays showing the expansion in average grain size. (a) Before annealing (Scale bar: 400 nm). (b) After annealing (Scale bar: 400 nm). Structures are 115 nm squares with a period of 400 nm.

In this case, the average grain area increases from approximately 1117 nm^2 to 13857 nm^2 - an increase of 1141%. Figure 4.4 does however further highlight one of the main drawbacks of annealing gold nanostructures. As previously discussed, during the annealing process, there is clear deformation of the structures as the grains expand. In the case of negative structures, this deformation is particularly prominent with inhomogeneity through the array increasing significantly with annealing (Fig. 4.5 (b)). Introducing inhomogeneity into the array means each structure will have a slightly different resonance compared to other

structures in the array. In isolation, this will result in a degree of broadening for the plasmonic resonance and is referred to as inhomogeneous broadening. However, despite this negative side effect, the inhomogeneous broadening experienced by the array is outweighed by the benefits of the expanding grain size resulting in a much narrower LSPR peak following annealing.

4.3.4. The Effect of Annealing on Thiolation

Annealing significantly effects the surface properties of gold. Annealing reduces the surface roughness of structures, as the gold atoms rearrange into a more energetically favourable state. In addition to this, adatoms, which are thought to have an important role in thiol bond formation, may be less available on an annealed metal surface when compared to a non-annealed surface (15–18). For this reason, the effectiveness of thiol bonding to annealed and non-annealed plasmonic structures was investigated. Sensors were left in a 1 mM 11-mercaptoundecanoic acid solution overnight, and the shifts in their resonant frequencies was compared (Table 4.3).

Table 4.3 - The shift upon thiol modification in annealed and non-annealed 150 nm squares with a period of 450 nm.

Sensor	LSPR minima before thiolation (nm)	LSPR minima after thiolation (nm)	LSPR shift (nm)
Non-Annealed	768.75 (+/- 0.22)	771.60 (+/-1.07)	3.50
Annealed	740.25 (+/- 0)	742.80 (+/- 0.1)	2.55

Annealed sensors undergo a smaller resonance shift after thiolation when compared to non-annealed sensors. This shift is indicative of less thiol binding to the sensor which in turn indicates a less conformal layer.

The packing of the thiolated molecules on the surface of the sensor can be of varying importance depending on the application, as will be discussed in more detail in Chapter 5. For example, in cross-reactive sensing platforms, the surface of the sensing elements is modified to provide a range of affinities for the analytes. In this case, the final output may not be adversely affected by the monolayer being less densely packed, as long as it is enough to alter the chemical properties of the surface enough to interact with the analytes differently from other sensing elements. On the contrary, if the surface chemistry is required to have an anti-fouling component, gaps in the monolayer may result in a significant drop in sensor performance as fouling molecules may be able to penetrate the less densely packed monolayer. This result creates a trade-off when it comes to annealing sensors. If a sensor is annealed, it will have a well-defined resonance peak and a FoM but this may be at the cost of densely formed SAMs. On the other hand, if sensors are non-annealed, their surface

properties may be more amenable to dense SAM formation, but the quality of the peaks will be reduced, resulting in larger errors and diminished sensing performance.

4.3.5. The Effect of Annealing on Bulk Refractive Index Sensitivity

As has been displayed in Figure 4.2, annealing influences both the spectra profiles of plasmonic sensors as well as the geometry of their constituent nanostructures. As a result of this it is important to assess how these changes affect the bulk refractive index sensitivity of the sensors. The effect of annealing on the bulk refractive index sensitivity of a 100 nm square sensor is displayed in Table 4.4.

Table 4.4 - The effect of annealing on the sensitivity and FWHM of annealed a non-annealed 100 nm squares (n=3).

Sensor	Resonance Wavelength in Water (nm)	Sensitivity (nm/RIU)	FoM
Non-Annealed	665.60 (+/- 1.57)	117.60 (+/- 23.14)	1.02 (+/- 0.22)
Annealed	638.25 (+/- 0.62)	130.74 (+/- 10.95)	2.04 (+/- 0.18)

As can be seen in Table 4.4, there is not a significant difference between the bulk sensitivity of the non-annealed structures and annealed structures. This is unexpected due to it breaking the trend discussed in Section 3.3.4 whereby resonance wavelength is a significant contributor to the bulk refractive index sensitivity of a sensor. This indicates that there may be some factors such as surface roughness or crystallinity that have an effect on sensitivity which would merit further investigation. Due to the sensitivities of the structures staying relatively stable before and after annealing, the significantly reduced FWHM of the annealed structures results in a FoM double that of the non-annealed structures, showing how annealing is beneficial for bulk refractive index sensing capabilities.

In addition to the clear benefits of annealing on a sensors FoM, it also has a significant effect on the ability to track the plasmonic resonance peak. By annealing, the error associated with each reading decreases, as shown in Figure 4.5.

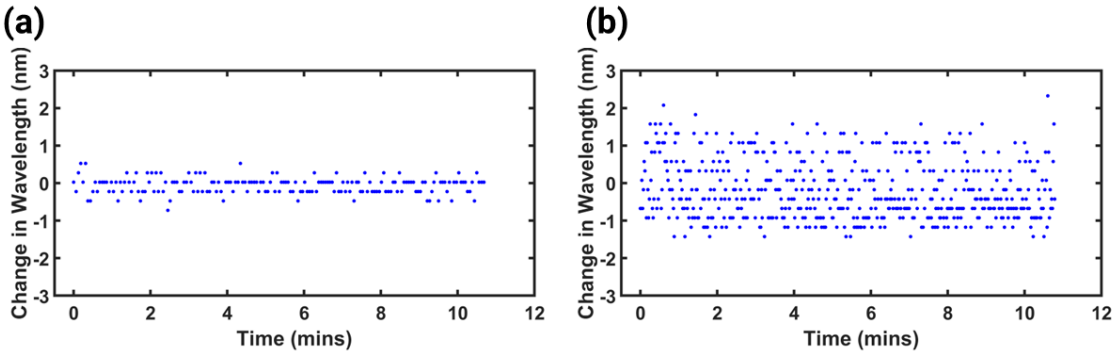

Figure 4.5 - The effect of annealing on the spread of readings. (a) Annealed and (b) non-annealed 200 nm split ring (gap size, 25 nm, period 335 nm) readings with time in a PBS solution.

By annealing the sensors, the spread of readings moves from 1.25 nm to 3.75 nm. This is particularly relevant when using sensors for biosensing applications in Chapter 5, where the trade-off between annealed sensors having narrower peaks and non-annealed sensors having surface characteristics more suited to self-assembled monolayer formation is an important factor.

4.3.6. Preventing Deformation of Nanostructures using a Protective Annealing Layer

As mentioned previously, one of the main drawbacks of annealing is the deformation of the nanostructures (Fig. 4.4). This is particularly important for retaining the localised sensing abilities of different nanostructures. As discussed in Sections 3.3.1.2 and 3.3.3.3 rounding the corners of nanostructures even slightly results in a significant reduction in EM field enhancement for both monomeric and trimeric structures. This section explores the use of protective layers during annealing as a method for preventing this deformation. The capability of these protective layers to improve the properties of annealed plasmonic nanostructures for sensing applications is assessed by examining to what extent this layer is capable of retaining geometry and what effect this has on sensor sensitivity.

As an initial experiment, a HSQ layer was applied to triangle trimer sensors before annealing in an RTA, as described in Section 4.2.5, and different exposures to HF were tested for HSQ removal. Figure 4.6 shows annealed and non-annealed trimers as well as the effect of four different HF exposure times on the triangle trimer sensors annealed under HSQ.

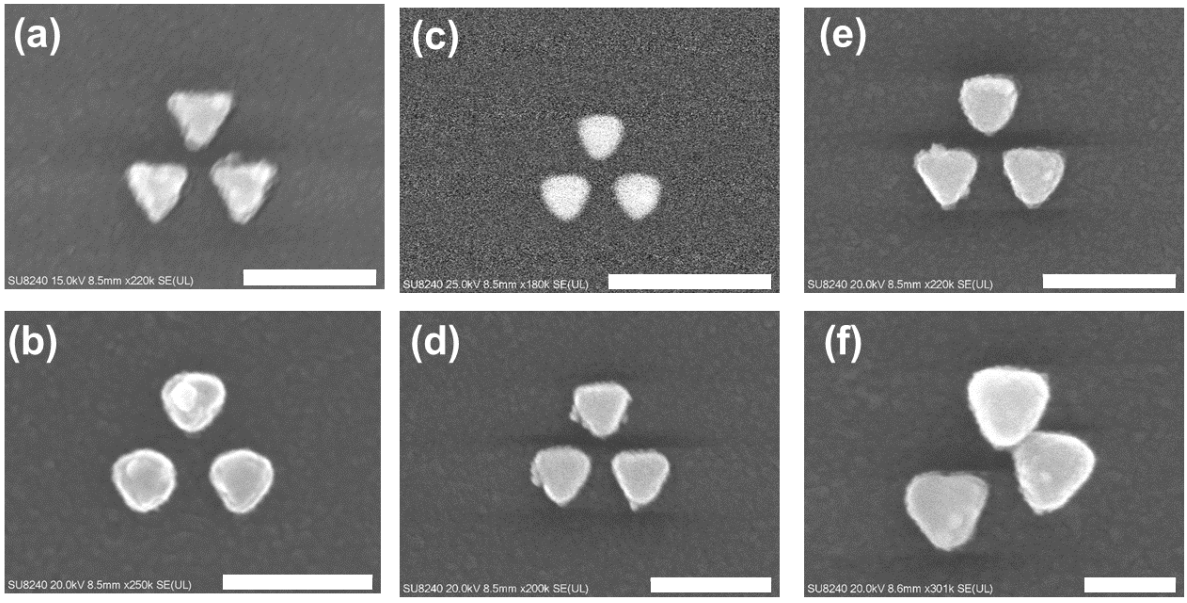

Figure 4.6 - The optimisation of HF exposure time to remove the protective layer. (a) Non-annealed triangle trimer (Scale bar: 200 nm) (b) Annealed trimer (Scale bar: 200 nm) compared to trimer annealed with HSQ layer and exposed to HF for (c) 15 seconds (Scale bar: 300 nm) (d) 30 seconds (Scale bar: 200 nm) (e) 45 seconds (Scale bar: 200 nm) and (f) 60 seconds (Scale bar: 100 nm). Structures are 110 nm Triangle trimers.

The SEM images in Figure 4.6 show the potential of HSQ as a protective layer during annealing to prevent structure deformation with the trimer in Figure 4.6(b) being more rounded when compared to the trimers in Figure 4.6(d,e). When considering the HF exposure time of the different trimers, with a 15 second exposure to HF, the image is noisy as the HSQ layer, which is a negative tone electron beam resist, is still encapsulating the shape. At 30 seconds and 45 seconds, the shapes can be seen clearly, indicating the protective layer has been fully removed. As both 30 seconds and 45 seconds fully remove the resist, the shorter time is preferred as to minimise the potential damage HF could do to the nanostructures. At 60 seconds, we start to see how the HF begins to damage the metasurface as the gold structures become dislodged. A comparison of the spectra of an unannealed triangular trimer, an annealed triangular trimer without a protective layer and a triangular trimer annealed with a protective layer is shown in Figure 4.7.

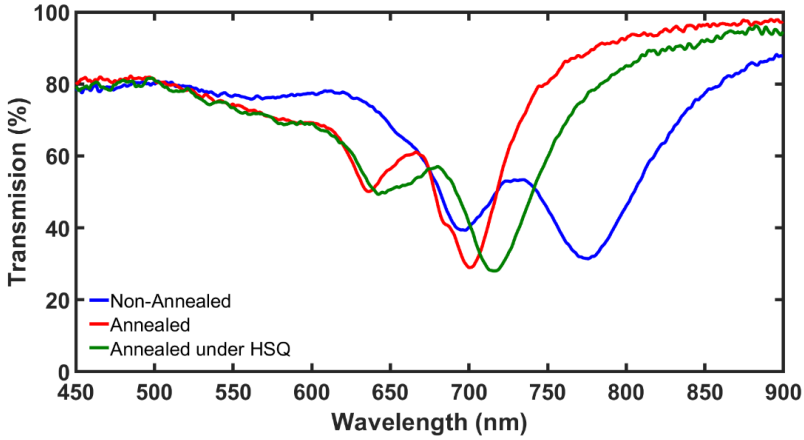

Figure 4.7 - UV/vis transmission spectra showing the effect of a protective HSQ layer when annealing triangle trimers in an RTA.

With the protective layer, the LSPR peaks are still blue shifted, however, it is to a lesser degree than with the shapes without the layer. In addition, when the sensor is annealed without the HSQ layer, there is a clear shoulder that appears in the primary peak at approximately 685 nm. This shoulder is most likely the result of deformation creating a new, weak resonance mode due to the deformation of the structures seen in Figure 4.6.

The spectral data and SEM images indicate, that the HSQ layer may be protecting the geometry of the structure, preventing the rounding of the corners to some extent. This is a desirable outcome for sensing applications since the retention of the sharper tips at the corners results in stronger localised sensitivity. Furthermore, as discussed in Sections 3.3.1.2 and 3.3.3.4, nanostructures resonating at longer wavelengths present higher bulk sensitivity.

To prove this hypothesis, the same protocol was used to assess whether this technique could increase either the bulk or local sensitivity. This time, the experiments were performed using split rings and square sensors because of their ease of fabrication and high reproducibility.

Figure 4.8 shows the geometry of the structures as fabricated, after annealing and after annealing with a HSQ layer.

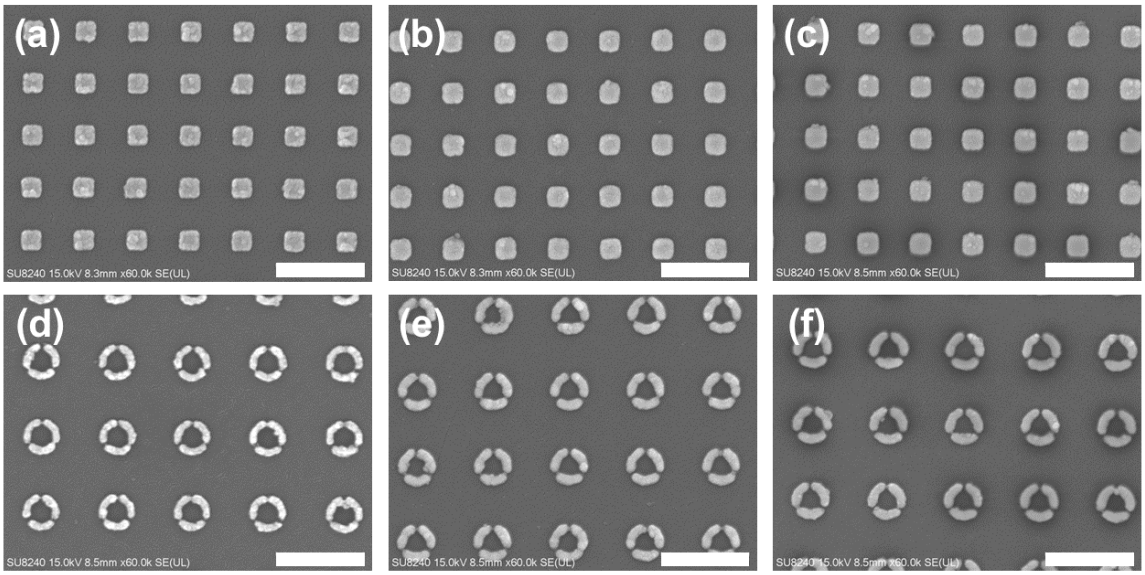

Figure 4.8 - The effect of different annealing conditions on plasmonic geometries (a) Non-annealed squares. (b) Squares annealed without HSQ (c) Squares annealed with HSQ. (d) Non-annealed split rings. (e) Split rings annealed without HSQ. (f) Split rings annealed with HSQ. Structures: 100 nm squares, period 300 nm; 200 nm split tings, 20 nm gap size, 335 nm period. (Scale bars: 500 nm)

As can be seen from Figure 4.8, there are not major differences in the geometry of the structures annealed with and without the HSQ layer. However, the spectra in Figure 4.9 indicate that the structures have a slightly different response to this technique. The squares annealed under HSQ resonate at a slightly shorter wavelength than their non-encapsulated counterparts, whereas the encapsulated rings resonate at a wavelength closer to non-annealed sensors, indicating they are slightly less deformed, although this difference is subtle and cannot be identified by looking at SEM characterisation exclusively.

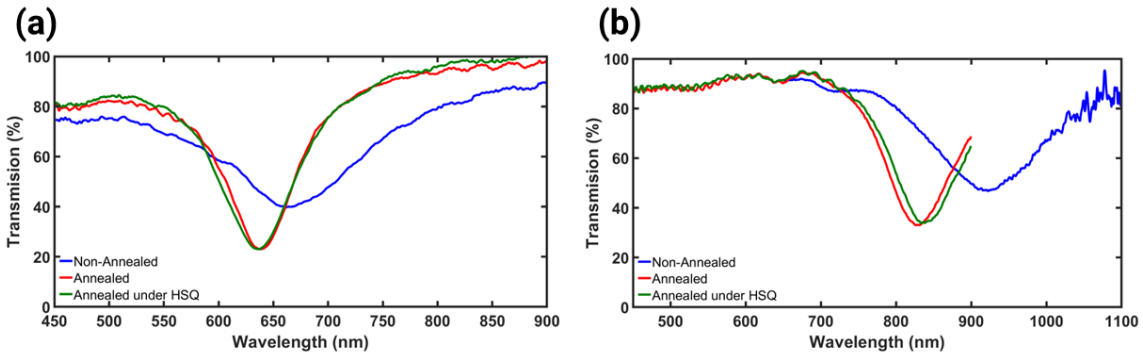

Figure 4.9 - The difference in spectra between non-annealed sensors, annealed sensors and sensors annealed with a HSQ encapsulation layer. (a) 100nm square sensors with a 300 nm period (b) 200 nm split rings with a 20 nm gap and a 335 nm period.

To determine the effect this annealing method had on sensor performance, the bulk refractive index sensitivity and FoM were measured by measuring their resonance wavelengths in solutions with different refractive indices as described in Section 4.2.2 (Table 4.5).

Table 4.5 - The sensitivity and FoM of squares and split rings annealed with and without HSQ (n=3). Structures: 100 nm squares, period 300 nm; 200 nm split tings, 20 nm gap size, 335 nm period.

Structures	Resonance Wavelength in Water (nm)	Sensitivity (nm/RIU)	FoM
Non-Annealed Squares	665.60 (+/- 1.39)	117.60 (+/- 23.14)	1.02 (+/- 0.22)
Squares without HSQ	638.25 (+/- 0.62)	130.74 (+/- 10.95)	2.04 (+/- 0.18)
Squares with HSQ	636.35 (+/- 0.57)	199.29 (+/- 7.45)	2.83 (+/- 0.07)
Non-Annealed Split Rings	919.77 (+/- 0.75)	251.08 (+/- 34.48)	2.54 (+/- 0.33)
Split Rings without HSQ	830.57 (+/- 2.04)	255.18 (+/- 6.92)	2.59 (+/- 0.09)
Split Rings with HSQ	840.78 (+/-2.31)	366.59 (+/- 28.07)	3.78 (+/- 0.09)

As can be seen from Table 4.5, there is a significant increase in FoM and sensitivity for the samples annealed with a HSQ layer versus the samples annealed without HSQ and the non-annealed samples. Since both annealing with and without a protective layer resulted in similar morphology and optical response, the presence of the HSQ layer cannot explain such a difference in sensitivity. A hypothesis for this observation is that the HF used to remove the HSQ layer could be etching the glass substrate supporting the gold nanostructures. If there is partial etching of the glass substrate, the fields created by the bottom edges of the shapes will also contribute to the refractive index sensitivity, whereas these fields are normally adsorbed by the substrate.

To assess this theory, the nano-squares were simulated with and without substrate etching (Fig. 4.10). In this simulation, the sensitivity of the structures increased from 221.2 nm/RIU to 232.9 nm/RIU when including a 5 nm etch on the substrate, confirming our hypothesis. Since the increase in sensitivity is much larger in the experimental data, we can assume that the etching of the glass substrate is more severe than the estimate used in the simulation.

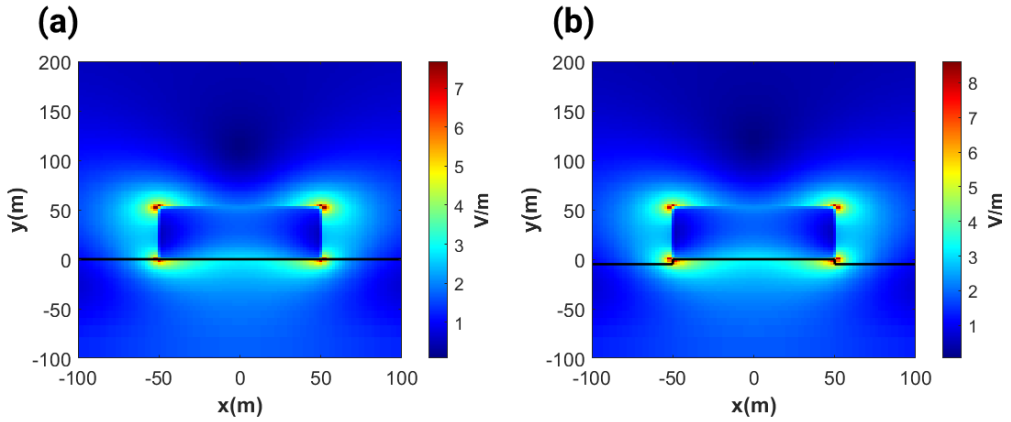

Figure 4.10 - The difference in field distribution of a 100 nm square sensor (period 300 nm) where the substrate has been either (a) not etched or (b) etched. Black line indicates the profile of the glass substrate.

The effect of this process on localised sensitivity was also tested. To do this, a 1 nm layer of aluminium oxide (Al_2O_3) was deposited on the sensor to record the magnitude of the spectral shift (Table 4.6).

Table 4.6 - The localised sensitivity of nanostructures annealed with and without a HSQ encapsulation layer. Experimental as described in Section 4.2.6. Structures: 100 nm squares, period 300 nm; 200 nm split rings, 20 nm gap size, 335 nm period.

Sensors	Shift with Thiolation	Shift With 1 nm Al_2O_3
Non-Annealed Squares	15.93 (+/- 9.22)	28.85 (+/- 0.2)
Squares without HSQ	0.33 (+/- 0.12)	8.93 (+/- 0.06)
Squares with HSQ	5.20 (+/- 0.12)	6.25 (+/- 0.12)
Non-Annealed Split Rings	16.58 (+/- 0.86)	24.67 (+/- 0.3)
Split Rings without HSQ	2.88 (+/- 0.47)	16.82 (+/- 0.51)
Split Rings with HSQ	9.70 (+/- 0.41)	12.40 (+/- 0.58)

The non-annealed samples show a greater localised sensitivity as measured by both thiolation and Al_2O_3 deposition. Both these phenomena are related to the surface roughness of the annealed structures when compared to the non-annealed ones. The rougher surface displayed by the annealed samples has the potential to create many small, localised points of EM field concentration resulting in a localised sensitivity (19–21). In addition, as previously discussed, the thiol SAM has the potential to form more densely packed monolayers on rougher surfaces due to more anchoring points being available for thiol molecules (15–18). This helps explain the increased shift experienced by non-annealed sensors after SAM formation.

Unexpectedly, samples annealed with a protective HSQ layer present a smaller shift upon the deposition of the aluminium layer than those annealed without the HSQ layer. This result may be explained by the same phenomenon depicted in Figure 4.10. As the glass is etched,

the thin aluminium oxide layer moves further from the corners on the back side of the gold structures, decreasing its influence on the resonance wavelength of the structure.

To confirm this hypothesis, the simulation shown in Figure 4.10 was then repeated with an added a 1 nm aluminium oxide layer. Before etching, the resonance shift is 9.73 nm, and after etching, it is 8.84 nm, in agreement with the observed experimental results.

However, the thiolation data shows a different trend (Table 4.6). As previously discussed, thiolation on annealed nanostructures may be less reliable due to a reduction in surface roughness and imperfections that may facilitate SAM formation. The lack of trend when depositing an aluminium layer versus SAM formation indicates that the exposure to hydrofluoric acid is creating these surface imperfections, allowing for a more conformal thiol layer to be created. In this way, despite the lack of effectiveness of the HSQ layer for protecting geometry, briefly exposing annealed nanostructures to hydrofluoric acid may serve as a way to maintain the benefits of annealed nanostructures while reproducing the desirable surface properties of a non-annealed nanostructure.

4.3.7. Annealing using a Femtosecond Laser

Ultrafast lasers emit extremely short pulses of light, typically femtoseconds to picoseconds in duration, enabling precise material processing. Their ultrashort pulses result in very fast heating and cooling rates, producing minimal thermal damage as discussed in Section 4.3.2. This makes laser irradiation a promising technique to anneal plasmonic sensors with minimal deformation. The results discussed in this section were obtained in collaboration with Prof. Andrés Guerrero-Martínez, from Complutense University of Madrid, and Prof. Ovidio Peña-Nieto, from Polytechnic University of Madrid. The laser irradiations were performed at the Centre for Ultra-fast Lasers from the Complutense University of Madrid (Section 4.2.7).

The laser was set to a wavelength of 800 nm. Since the LSPR wavelength of the nanostructures must match the excitation wavelength, square plasmonic nanostructures were chosen for the preliminary experiments due to their ease of tuneability. These sensors (165 nm squares, period 495 nm) were exposed to laser pulses at 700, 1000 and 1200 mW for an hour (Section 4.2.7), and spectra was collected before and after the irradiation (Fig. 4.11, Table 4.7).

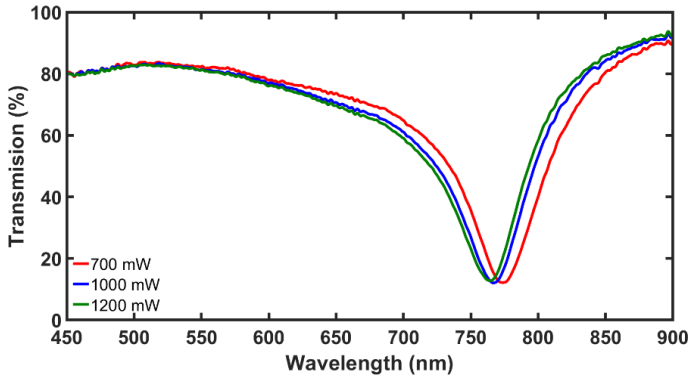

Figure 4.11 - UV/vis spectra collected before and after laser irradiation of sensors with LSPR at 800 nm. Graph with spectra before annealing available in Appendix A.4.2. Structure: 165 nm square; period 495 nm.

Table 4.7 - The peak position and FWHM of 165 nm squares with a period of 495 nm annealed with different laser powers.

Laser Power (mW)	LSPR wavelength before annealing (nm)	LSPR wavelength after annealing (nm)	Change in resonance wavelength (nm)	FWHM (nm)
700	790.00	774.00	16	66.0
1000	798.00	767.00	31	65.5
1200	790.00	764.00	26	65.5

From the data presented in Figure 4.11 and Table 4.7 it can be observed that, as the power increases, the LSPR peak shifts towards shorter wavelengths. As previously discussed, a shift towards a shorter wavelength is indicative of a disruption in morphology characterised by the rounding of the corners. However, at 700 mW the shift is much smaller while the FWHM is close to that of the structures annealed at higher power.

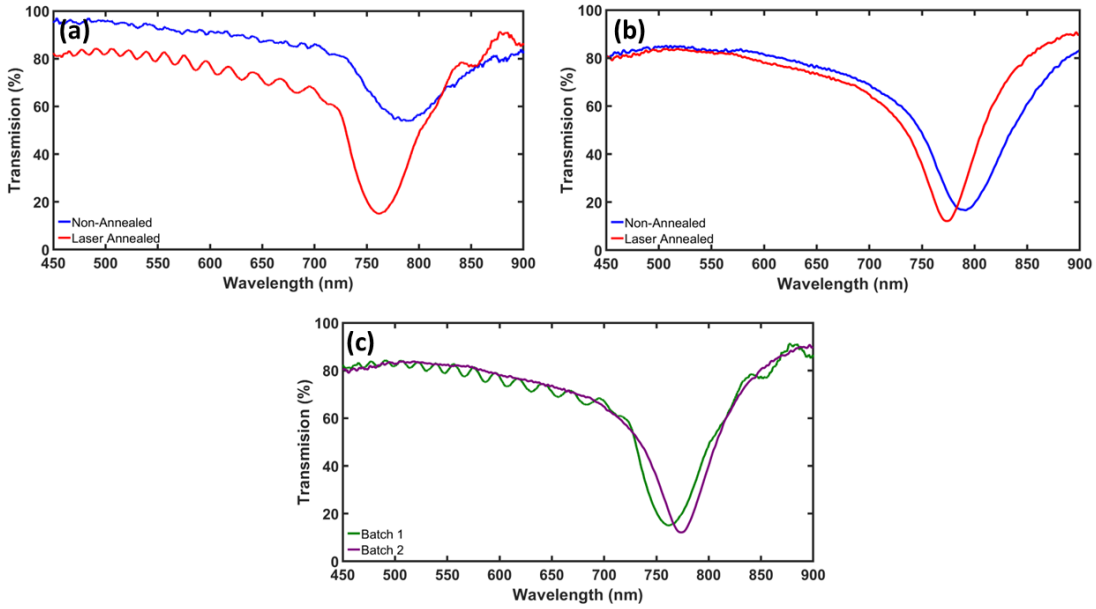

Figure 4.12 - Sensors from two separate batches being annealed using a 700 mW laser. (a) Batch 1 (b) Batch 2 (c) A comparison between sensors from both batches after laser annealing.

The same experiment was repeated with a new batch of sensors, fabricated several weeks after the first one. As can be seen from Figure 4.12, the LSPR peak of the sensors in the first batch is much broader and less intense than that of the second batch. This variation in as-fabricated sensor quality is affected by the supplier of the deposited metal as well as the parameters of metal deposition including the exact pressure under which deposition occurs and the rate and stability of deposition rate which will vary between depositions (22). However, despite these vastly different starting points, Figure 4.12 (c) shows how the LSPR peaks after laser irradiation are much more similar than the initial ones. It must be noted when considering this data that the variation between the position and width of the two peaks can be partially accounted for by the readings being taken on two different optical setups (Sections 4.21 and 4.27). Figure 4.13 shows a direct comparison of the effect of annealing in the RTA versus annealing with a laser.

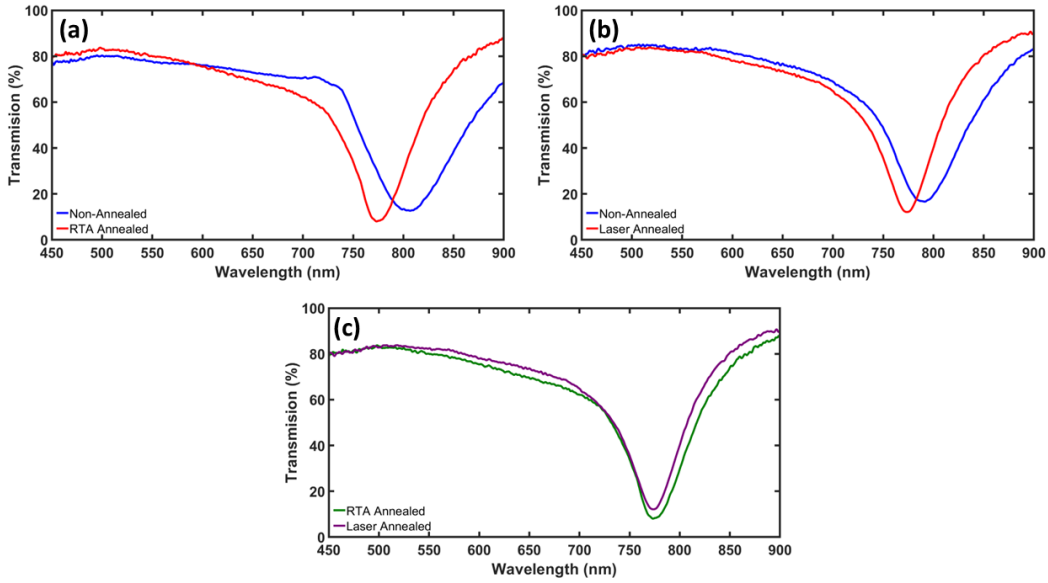

Figure 4.13 - The effect of annealing using different methods (a) Annealing with an RTA at 500 ˚C. (b) Annealing with a laser at 700 mW. (c) The difference between the resulting spectra from annealing with the different methods.

By comparing the laser-annealed sensor to the RTA-annealed sensor, we can quantify the difference between both methods. Table 4.8 shows the change in resonance wavelength in the spectra shown in Figure 4.13 (a,b).

Table 4.8 - The shift in resonance wavelength and FWHM of 165 nm squares with a period of 495 nm caused by annealing with the RTA and laser.

Sensor	LSPR Wavelength Before Annealing (nm)	LSPR Wavelength After Annealing (nm)	Change in LSPR Wavelength
RTA-Annealed	806.22	774.85	31.38
Laser-Annealed	790.00	774.00	16.00

The shift in resonance wavelength is smaller for the laser-annealed sample when compared to the sample annealed with the RTA. This is because the deformation of the structures is limited by the laser wavelength, since, once the grains recrystalise the resonance undergoes an optical shift away from the wavelength of the laser, stopping the excitation and thus the annealing process. Additionally, the FWHM of the annealed structures is significantly lower for the laser annealed structures compared to the RTA annealed structures (63.50 nm vs 73.43 nm). This indicates that the structures are more homogeneous, another added advantage of the laser-annealing method (11). A key benefit of the annealing using a laser is the reduced deformation during the annealing process which results in sharper corners for the nanostructures (Fig. 4.14).

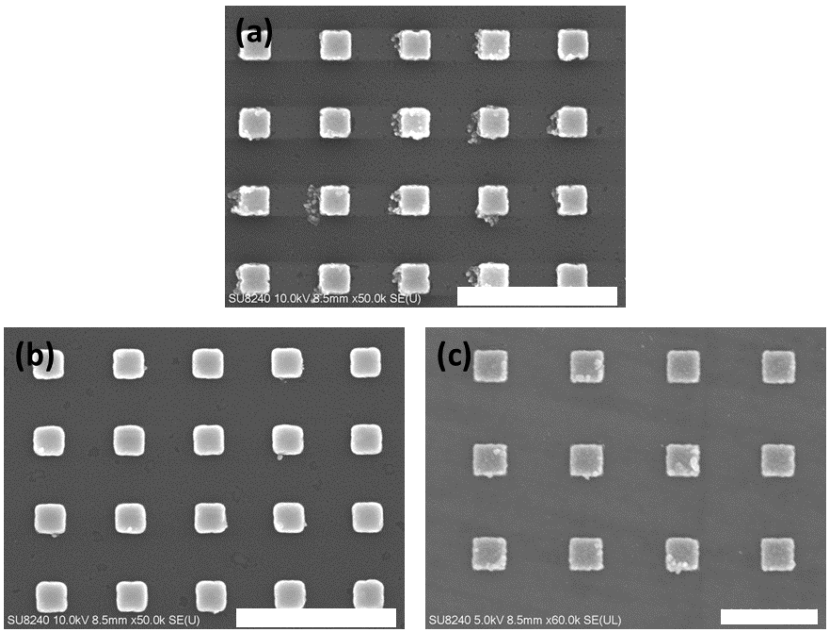

Figure 4.14 - SEM images of structures annealed with different methods. (a) Before annealing (Scale bar: 1 µm), (b) Annealed with the RTA (Scale bar: 500 nm) (c) Annealed using a laser (Scale bar: 500 nm). Structures: 165 nm squares with a 495 nm period.

Figure 4.14 shows the ability of the laser to maintain structure geometry to a much larger degree than the RTA with much sharper corners in addition to the improvement in the spectra shown in Figure 4.13. In this manner, and as discussed previously, the structures should host a stronger electromagnetic field and hence have a higher localised sensitivity.

A potential explanation for this phenomenon is the extremely fast heating and cooling rates experienced by the gold nanostructures while being irradiated by the laser. When compared to the hours or minutes the sensors take to go through the heating and cooling cycle with the chamber furnace or RTA, the heating and cooling from each pulse of the laser is nearly instantaneous. This may be giving the sensors enough energy to cause recrystallisation without giving the gold structure time to move towards a more stable, rounded form. To

confirm this hypothesis, more research is required to tease apart the effects that come from structure rounding and recrystallisation during the annealing process. Current research on the annealing of nanostructures does not comment on the effect of grain size on resonance wavelength, with the general consensus being that increasing grain size is responsible for the decreasing FWHM of a LSPR resonance whereas the rounding of the corners is responsible for the blue shift (3,8,10,12,13,23). This is most likely due to the fact that designing an experiment whereby internal grain size changes and geometry stays constant is very difficult. Even when considering traditional surface plasmon resonance on planar films of gold, the blue shift observed after annealing is attributed to a reduction in surface roughness, with no comment on the effect the grain size has on this shift (24). Further replicates of this study as well as designing experiments specifically to try and separate structure geometry from grain size could help confirm the potential of laser annealing as a way of optimising plasmonic nanostructures.

One of the key aspects of annealing with a laser such a is wavelength-specificity. This means that, by tuning the laser wavelength, specific nanostructures can be annealed while others remain entirely transparent to the laser. A use case for this is multi-metallic metasurfaces which may be fabricated using metals with different oxidation properties and melting points. For example, silver is prone to oxidation and cannot be annealed in an RTA. As a result, once fabricated, silver nanostructures cannot benefit from annealing. By using a laser, it would be possible to selectively anneal different elements of the array depending on their resonance wavelength. Another interesting application would be to excite different modes of a structure. For example, it may be possible to create interesting effects by annealing at one resonance mode while leaving the other pristine. For a nanorod shaped structure, we could potentially excite the mode corresponding to the shorter, less sensitive axis to cause recrystallisation without the risk of deforming the more sensitive ends of the structure.

4.3.8 Transformation of Nanostructures through High Temperature Annealing

When annealing at 900 ˚C in the chamber furnace, an interesting transformation to the nanostructures occurs (Fig. 4.15). The plasmonic spectra of these structures is displayed in Figure 4.1.

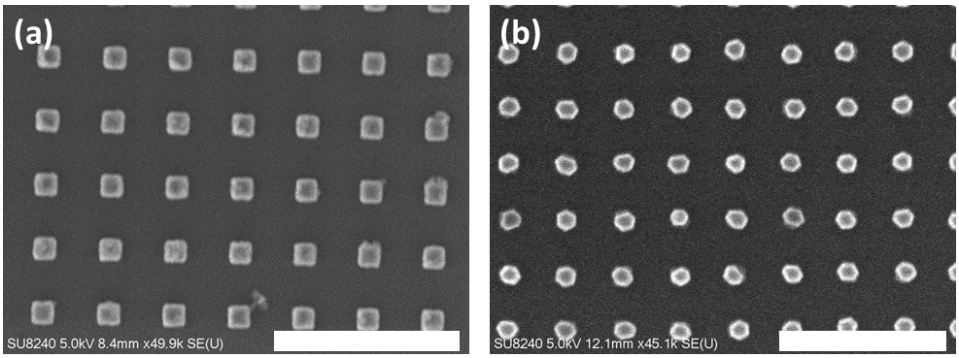

Figure 4.15 - The effect of high temperature annealing on 115 nm square gold nanostructures. (a) Before and (b) after annealing at 900 ˚C in a convection oven (Scale bars: 1000 µM).

Under extremely high temperatures, the square nanostructures are transformed into inhomogeneous hexagons. These hexagonal shapes are a result of grain boundary migrations causing each nanostructure to reach its lowest energy state. At temperatures as high as 900 ˚C, the grain boundaries move to the edges of the structure and rearrange themselves causing this transformation (2). This phenomenon of sharp hexagonal shapes being created by annealing gold at extremely high temperatures has been briefly discussed in literature when considering the formation of nanostructures from planar gold films, however, this transformation has not been discussed in lithographically defined structures or for plasmonic sensing (2,25).

The bulk sensitivity and FoM of the non-annealed squares (Fig. 4.15 (a)) and the hexagonal structures (Fig. 4.15 (b)) are compared in Table 4.9.

Table 4.9 - The bulk refractive index sensitivity of gold nanostructure before and after high temperature annealing (115 nm squares, period 350 nm).

Sensor	LSPR Wavelength in Water (nm)	Bulk Sensitivity (nm/RIU)	FoM
Non-Annealed Squares	675.60	220.50	2.33
Annealed Hexagons	619.95	218.72	3.26

Despite their shorter resonance wavelength, the hexagonal sensors have a similar bulk sensitivity to the non-annealed squares and a higher FoM. The trend seen in the bulk sensitivity of these shapes does not match the trend described in Section 3.3.4 with the shapes having approximately the same refractive index sensitivity despite the hexagonal shapes resonating at a wavelength 55.65 nm shorter than the non-annealed squares. This could be attributed to the unique crystallinity that forms upon such treatment, with the gold becoming one singular crystal with no grain boundaries. The data in Table 4.3 suggests that this crystallinity may have an impact on sensitivity as the annealed structure has approximately the same bulk sensitivity as the non-annealed sensor despite the shorter resonance

wavelength. It should be noted that this sensitivity and FoM are not as high as those seen in the trimers discussed in Sections 3.3.3.2., 3.3.3.3 and 3.3.3.4.

The localised sensitivity of these structures was measured using the same techniques as discussed in Section 3.3.5.

Table 4.10 - The local sensitivity of non-annealed 115 nm square sensors (period 350 nm) compared to the hexagonal shapes created by annealing these squares at 900 ˚C.

Sensor	Shift with Thiolation (nm)	Shift with Al_2O_3 Layer (nm)
Non-Annealed	7.6	10.95
900 ˚C Annealed	2.25	8.00

Unexpectedly, this data shows that, despite the sharper corners in the hexagonal shapes, the localised sensitivity is slightly lower. Section 4.3.4 discusses how annealing may affect the thiolation, but in this case the aluminium layer also shows a smaller shift than the annealed sample. As previously discussed, this is most likely due to the increased surface roughness exhibited by non-annealed shapes which can create small hotspots on the surface of the structure which will inevitably increase localised sensitivity (19–21). This effect will be further enhanced with the aluminium oxide technique as the only the top, continuous plane of the structure will be coated leading to a diminished response from the corners of the hexagonal shape.

4.4 Conclusion

In this chapter, we have explored different methods to anneal LSPR-based gold sensors and discussed the benefits and drawbacks of each technique. Overall, we can conclude that annealing is highly beneficial to the plasmonic response of the sensors and acts as a method to control the quality of the LSPR, even when there are inconsistencies in fabrication due to the quality of the gold precursor. The downsides of traditional thermal annealing methods are deformation and diminished SAM formation caused by the loss of surface roughness. The use of protective layers, such as HSQ, has a minimal effect on geometry preservation. However, further optimisation of this approach could provide better results by exploring different composition of the protective layer. Despise not providing the expected results in terms of preservation of morphology, during these experiments an improvement of sensitivity was achieved thanks to the etching of the substrate caused by exposure to HF. A secondary beneficial effect of HF exposure is its effect on the surface properties of the nanostructures which seemed to create conditions that allowed for a more densely packed monolayer to form. These two effects combined result in HF exposure being a quick way to retain the positive effects of annealing on grain structure while negating the negative effect

it has on SAM formation. The last section in this chapter shows how hexagonal structures can be achieved by exposing nano squares to very high temperatures. These sharp corners are beyond the ability of cutting-edge fabrication techniques such as electron beam lithography, and as a result, this approach could be a cost-effective way of getting highly sensitive nanostructures without the need for a high-resolution fabrication tool. The preliminary study carried out into the benefits of annealing with a laser as opposed to a rapid thermal annealer or chamber furnace also showed some interesting results. The results showed the ability of the laser to create more homogeneous arrays when compared to other forms of annealing due to its wavelength specific nature. This creates sensors with higher FoM's by reducing the broadening caused to the resonance peak due to inhomogeneity in the array. In addition, this chapter has shown the potential of laser annealing to significantly reduce the deformation experienced by structures, increasing the strength of their electromagnetic fields during resonance and hence, increasing localised sensitivity. This preliminary study leaves many avenues of research open including experimentally testing both the bulk and localised sensitivity of nanostructures annealed with a femtosecond laser, altering nanostructure geometry by annealing at different resonance modes and examining the effect of annealing on more complex nanostructures.

References

1. Lin HTH, Yang CK, Lin CC, Wu AMH, Wang LA, Huang NT. A large-area nanoplasmonic sensor fabricated by rapid thermal annealing treatment for label-free and multi-point immunoglobulin sensing. Nanomaterials. 2017 May 1;7(5).

2. Bai Y, Yan L, Wang J, Yang B, Chen N, Tan Z. Tuning driving forces for preparation of faceted single crystalline Au nanoparticles from Au films. Mater Charact [Internet]. 2017 Jun 1;128:1–6. Available from: https://linkinghub.elsevier.com/retrieve/pii/S1044580317300025

3. Holm VRA, Greve MM, Holst B. Temperature induced color change in gold nanoparticle arrays: Investigating the annealing effect on the localized surface plasmon resonance. Journal of Vacuum Science & Technology B, Nanotechnology and Microelectronics: Materials, Processing, Measurement, and Phenomena. 2016 Nov;34(6):06K501.

4. Lathika S, Raj A, Sen AK. LSPR based on-chip detection of dengue NS1 antigen in whole blood. RSC Adv. 2021 Oct 7;11(53):33770–80.

5. Jia K, Bijeon JL, Adam PM, Ionescu RE. Large Scale Fabrication of Gold Nano-Structured Substrates Via High Temperature Annealing and Their Direct Use for the LSPR Detection of Atrazine. Plasmonics. 2013 Mar 1;8(1):143–51.

6. Liu J, Chu L, Yao Z, Mao S, Zhu Z, Lee J, et al. Fabrication of Au network by low-degree solid state dewetting: Continuous plasmon resonance over visible to infrared region. Acta Mater. 2020 Apr 15;188:599–608.

7. Sui M, Kunwar S, Pandey P, Lee J. Strongly confined localized surface plasmon resonance (LSPR) bands of Pt, AgPt, AgAuPt nanoparticles. Sci Rep. 2019 Dec 1;9(1).

8. Zhang F, Proust J, Gérard D, Plain J, Martin J. Reduction of Plasmon Damping in Aluminum Nanoparticles with Rapid Thermal Annealing. The Journal of Physical Chemistry C [Internet]. 2017 Apr 6;121(13):7429–34. Available from: https://pubs.acs.org/doi/10.1021/acs.jpcc.7b00909

9. Higashino M, Murai S, Tanaka K. Improving the plasmonic response of silver nanoparticle arrays via atomic layer deposition coating and annealing above the melting point. Journal of Physical Chemistry C. 2020 Dec 17;124(50):27687–93.

10. Bosman M, Zhang L, Duan H, Tan SF, Nijhuis CA, Qiu CW, et al. Encapsulated annealing: Enhancing the plasmon quality factor in lithographically-defined nanostructures. Sci Rep. 2014 Jul 2;4.

11. González-Rubio G, Díaz-Núñez P, Rivera A, Prada A, Tardajos G, González-Izquierdo J, et al. Femtosecond laser reshaping yields gold nanorods with ultranarrow surface plasmon resonances. Science (1979) [Internet]. 2017 Nov 3;358(6363):640–4. Available from: https://www.science.org/doi/10.1126/science.aan8478

12. Chen KP, Drachev VP, Borneman JD, Kildishev A V., Shalaev VM. Drude relaxation rate in grained gold nanoantennas. Nano Lett. 2010 Mar 10;10(3):916–22.

13. Oikawa S, Minamimoto H, Murakoshi K. Low-Temperature Annealing of Plasmonic Metal Arrays for Improved Light Confinement. The Journal of Physical Chemistry C [Internet]. 2022 Jan 20;126(2):1188–95. Available from: https://pubs.acs.org/doi/10.1021/acs.jpcc.1c08931

14. Li Y. Optical Properties of Plasmonic Materials. In: Plasmonic Optics Theory and Applications [Internet]. SPIE PRESS; Available from: http://ebooks.spiedigitallibrary.org/content.aspx?bookid=2051&sectionid=153917732

15. Maksymovych P, Voznyy O, Dougherty DB, Sorescu DC, Yates JT. Gold adatom as a key structural component in self-assembled monolayers of organosulfur molecules on Au(111). Prog Surf Sci [Internet]. 2010 May;85(5–8):206–40. Available from: https://linkinghub.elsevier.com/retrieve/pii/S0079681610000122

16. Torres E, Biedermann PU, Blumenau AT. The role of gold adatoms in self-assembled monolayers of thiol on Au(111). Int J Quantum Chem [Internet]. 2009 Nov 15;109(14):3466–72. Available from: https://onlinelibrary.wiley.com/doi/10.1002/qua.22055

17. Voznyy O, Dubowski JJ, Yates JT, Maksymovych P. The Role of Gold Adatoms and Stereochemistry in Self-Assembly of Methylthiolate on Au(111). J Am Chem Soc [Internet]. 2009 Sep 16;131(36):12989–93. Available from: https://pubs.acs.org/doi/10.1021/ja902629y

18. Maza FL, Carro P, Vericat C, Kern K, Salvarezza RC, Grumelli D. Role of Gold Adatoms in the Adsorption of Sulfide Species on the Gold(001)-hex Surface. The Journal of Physical Chemistry C [Internet]. 2018 Feb 1;122(4):2207–14. Available from: https://pubs.acs.org/doi/10.1021/acs.jpcc.7b11059

19. Macias G, Alba M, Marsal LF, Mihi A. Surface roughness boosts the SERS performance of imprinted plasmonic architectures. J Mater Chem C Mater [Internet]. 2016;4(18):3970–5. Available from: http://xlink.rsc.org/?DOI=C5TC02779A

20. Rodríguez-Fernández J, Funston AM, Pérez-Juste J, Álvarez-Puebla RA, Liz-Marzán LM, Mulvaney P. The effect of surface roughness on the plasmonic response of individual sub-micron gold spheres. Physical Chemistry Chemical Physics [Internet]. 2009;11(28):5909. Available from: http://xlink.rsc.org/?DOI=b905200n

21. Tinguely JC, Sow I, Leiner C, Grand J, Hohenau A, Felidj N, et al. Gold Nanoparticles for Plasmonic Biosensing: The Role of Metal Crystallinity and Nanoscale Roughness. Bionanoscience. 2011 Dec;1(4):128–35.

22. McPeak KM, Jayanti S V., Kress SJP, Meyer S, Iotti S, Rossinelli A, et al. Plasmonic films can easily be better: Rules and recipes. ACS Photonics. 2015 Mar 18;2(3):326–33.

23. Zheng YB, Juluri BK, Mao X, Walker TR, Huang TJ. Systematic investigation of localized surface plasmon resonance of long-range ordered Au nanodisk arrays. J Appl Phys. 2008;103(1).

24. Chang P, Liu K, Jiang J, Zhang Z, Ma J, Zhang J, et al. Performance Enhancement of the Surface Plasmon Resonance Sensor through the Annealing Process. IEEE Access. 2020;8:33990–7.

25. Bechelany M, Maeder X, Riesterer J, Hankache J, Lerose D, Christiansen S, et al. Synthesis Mechanisms of Organized Gold Nanoparticles: Influence of Annealing Temperature and Atmosphere. Cryst Growth Des [Internet]. 2010 Feb 3;10(2):587–96. Available from: https://pubs.acs.org/doi/10.1021/cg900981q

Chapter 5 – Plasmonic Metasurfaces for Protein Detection

5.1 Introduction

Plasmonic sensors are well established as a method for the label-free detection of analytes (1–4). This detection comes from receptors that can be attached to the sensors surface to capture a specific analyte enabling low limits of detection (LoD). As described in Chapter 3, these LoDs can be further improved by engineering LSPR resonances through advancements in nanostructure design. However, one of the main limitations of this method is that it only allows for the detection of one analyte at a time (5–10). Although specific, single-analyte LSPR sensors have proven to be very effective for various single analyte biosensing applications, the diagnosis of many diseases requires the detection of two or more biomarkers simultaneously (11–14). Cross-reactive sensing offers a promising solution to this limitation, since it takes advantage of the great sensitivity of LSPR without the need to use costly – and often single use – specific receptors, allowing for the development of sensing platforms with multiplexing capability. Cross-reactive sensing relies on each element within a sensing array being partially selective for different markers in a solution (15–18). For example, positive biomarkers will be attracted to negative surfaces and hydrophobic biomarkers will be attracted to hydrophobic surfaces. Then, by taking the responses of all the sensing elements, multi-variant analysis is used to analyse trends in the data. The multi-variant analysis can be "trained" to detect anomalies in these trends, indicating signs of disease.

In this chapter, we examine different approaches for protein detection using some of the LSPR platforms previously discussed in this thesis, including lock-in-key style and cross-reactive approaches. Furthermore, we explore and compare methodologies to address protein fouling, one of the main challenges in protein biosensing. Fouling, also referred to as non-specific binding, occurs when biomolecules stick to a surface via a combination of electrostatic and dispersion forces (19–23). To combat this limitation, we examine methods for either cleaning proteins from surfaces or preventing their irreversible immobilization onto sensors. Finally, following signs that we can create differential interactions between proteins and an array of surface chemistries, the ability of a cross-reactive sensor to discriminate between protein solutions is assessed.

5.2. Experimental

5.2.1. Measuring Protein Interactions in a Static Setup

To measure the interaction of sensors with proteins in a static setup, sensors were immersed in 3 mL of protein solution in a 35 mm disposable petri dish and measured using a UV/Vis spectrometer (StellarNet Blue Wave, VIS 25).

5.2.2. Measuring Protein Interactions Under Flow

To measure the interactions of proteins with the sensor under flow, a disposable microfluidic device with 16 channels was employed (Microfluidic Chip Shop, Fluidic 152, channel width: 1 mm, channel height, 200 µm). A flow rate of 200 µL/min was used (New Era Pump Systems, NE-4000) and spectra were acquired every 750 ms.

5.2.3. Removing Proteins from Fouled Sensors

The majority of experiments utilised Tween-20 (Sigma-Aldrich)/ Phosphate Buffer Serum (PBS, Sigma-Aldrich) solutions. Sensors were agitated to different degrees using either a shaker (Polymix, Vibrax) or an ultrasonic bath (Ultrasonic Cleaner, RS PRO) as described below.

5.2.3.1. Cleaning Protocol using Solvents

Three readings were taken of each sensor in PBS before proteins attached to the surface. After incubation in 1 mg/mL bovine serum albumin (BSA) for 15 minutes, three readings were taken of each sensor. Sensors were then rinsed with the solvent before being incubated in the solvent for a further 20 minutes. The sensors were then rinsed with water before 3 more readings were taken in PBS.

5.2.3.2. Detergent Cleaning Protocol 1

Before exposure to proteins, 5 readings were taken in PBS. In this case, the detergent solution was either 1% Tween-20 or 1% Triton-X. Sensors were then incubated in 1 mg/mL BSA solution for 15 minutes before being rinsed with the detergent solution, sonicated for 1 minute in the detergent solution, incubated in the detergent solution for 5 minutes, rinsed with water and dried with N_2. Measurements were taken in PBS after the washing protocol to assess cleaning ability.

5.2.3.3. Detergent Cleaning Protocol 2

The next washing protocol was as follows. Three readings were taken in PBS before protein exposure. The sensor was then cleaned with water and ethanol before being incubated in a BSA solution for 15 minutes and three readings were taken. Then the sensor was rinsed with Tween-20 solution before being dip-rinsed with Tween-20 solution 50 times (24). The sensor was then sonicated in Tween-20 solution for 60 seconds to aid in removing proteins before being sonicated in PBS for a further 2 minutes. The sensor was then cleaned with water and ethanol before three more readings were taken in PBS.

5.2.3.4. Detergent Cleaning Protocol 3

After protein exposure, the sensor was first agitated by continuously moving 5% Tween-20 solution over its surface using a pipette. The sensor was then dip-rinsed 50 times (24). The sensor was then sonicated in Tween-20 solution for 60 seconds before being agitated using the shaker for a further 5 minutes. Readings were taken in PBS before protein exposure, after exposure to 1 mg/mL BSA solution and after cleaning.

5.2.3.5. Detergent Cleaning Protocol 4

After taking readings in PBS, the sensor had 5% Tween-20 solution continuously flowed over each side of the sensor for 30 seconds. It was then agitated in Tween-20 solution for either a further 5 minutes or approximately 8 hours on the shaker before being rinsed with deionised (DI) water. For sections 5.3.3.2 and 5.3.3.3 when testing anti-fouling surface chemistries, this protocol was used but the agitation step was missed.

5.2.4. Formation of Self-Assembled Monolayers on Individual Gold Sensors

Glass chips supporting the sensing platforms were immersed in 10 mM of various thiol solution with either an ethanolic or aqueous solvent and left undisturbed overnight, before being rinsed thoroughly with the immobilization solvent and dried with a N_2 flow. To attach thiolated PEG-Biotin to sensors, a 1 mM solution of the thiol in PBS was flowed over the sensor using microfluidics and held there for approximately 8 hours before rinsing with PBS. A list of the different chemistries in this chapter are listed in Table 5.1. It should be noted that for the samples with the solvent ethylene glycol/ethanol (EG/EtOH) the ethylene glycol is only used in the printing system (Section 5.2.7) and if the sensors are modified outside of that system only pure ethanol is used.

Table 5.1 - A list of thiol chemistries used in this chapter. EG/EtOH: Ethylene Glycol/Ethanol.

Chemistry	Abbreviation	Printing Solvent
Phenylethyl mercaptan	PEM	EG/EtOH
12-Mercaptododecylphosphonic acid	MDP	EG/EtOH
1-dodecanethiol (DDE)	DDE	EG/EtOH
Thiolated PEG-Biotin	n/a	PBS Solution
Cysteine	Cys	Water
Glutathione	Glu	Water
Cysteamine	CA	EG/EtOH
Sodium 2-mercaptoethanesulfonate	MES	Water
11-mercaptoundecanoic acid	MUA	EG/EtOH
4-Nitrothiophenol	NTP	EG/EtOH
4-aminothiophenol	ATP	EG/EtOH
1-octanethiol	OT	EG/EtOH
1H,1H,2H,2H-Perfluorodecanethiol	PFDT	EG/EtOH

5.2.5 Formation of Silane Monolayers on Glass Substrates

After fabrication, sensors were placed in a glass vacuum desiccator along with 200 µL of (heptadecafluoro-1,1,2,2-tetrahydrodecyl) trichlorisilane in a small watch glass. Following this, the chamber was pumped and left under vacuum overnight for the SAM to form. SAM formation was quickly tested by observing the hydrophobicity of the glass chip when exposed to water, then the sensors were rinsed with methanol and dried with a flow of N_2.

5.2.6. Functionalisation of Multiple Sensors on a Glass Slide using Droplet Pinning

A droplet pinning layer was first created by using photolithography (Suss Mask Aligner, MA6) to block the desired functionalisation regions and then using a vacuum chamber to coat the remaining glass with a fluorous silane ((heptadecafluoro-1,1,2,2-tetrahydrodecyl) trichlorisilane). Following this, 10 mM solutions of each thiol in either an 80:20, ethanol: ethylene glycol (Sigma-Aldrich) solution or an aqueous solution were printed onto each sensor as 100 nL drops. These drops were left on the sensor surface in a humid environment overnight to prevent evaporation. The sensor was then rinsed with ethanol and dried under a N_2 flow. More detail of this process can be found in Section 2.5.3.

5.2.7. Cross-Reactive Sensors Sensing

After fabrication of the cross-reactive sensors as described in Section 2.5.3, a microfluidic chip was attached to the sensors creating 10 usable channels. As displayed in Figure 5.1, two of these channels were connected to create a total of 10 sensing elements for each sensor.

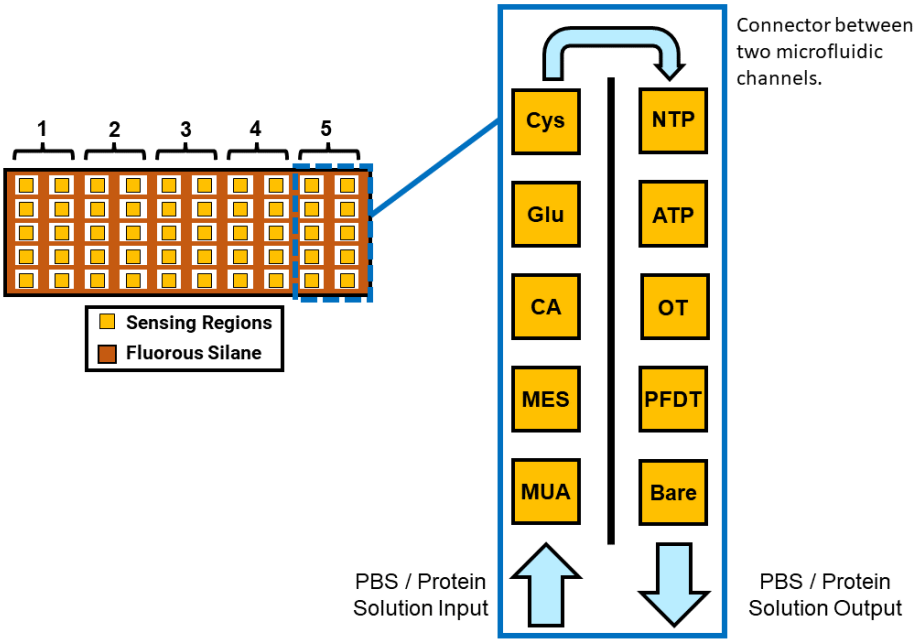

Figure 5.1 - The experimental setup for cross-reactive sensing of proteins. Slide is as fabricated in Section 2.5.3. Chemistries are as described in Table 5.1.

The resonance wavelengths of these sensors were first recorded in PBS (5 readings each) before having proteins flowed over their surfaces at 200 µl/min. The response of the sensing regions to each protein were then recorded by taking 5 readings in each protein solution. Once the sensors were exposed to proteins, they were not reusable and the same procedure was repeated on the next sensor with a new protein. The resulting data was analysed using principle component analysis and linear discriminant analysis on JMP17 software. See Section 2.7.3 and 2.7.4 for further details on multi-variant analysis.

5.3. Results and Discussion

5.3.1. Protein Interactions on Thiol-modified Sensors

Using the static setup described in Section 2.9.1, the UV/vis absorption profile of sensors featuring different surface modifications was recorded in a 0.3 mg/mL solution of BSA, pepsin and lipase as well as a PBS solution without proteins. Different surface properties were introduced using thiol monolayers of phenylethyl mercaptan (PEM), 12-mercaptododecylphosphonic acid (MDP), 1-dodecanethiol (DDE) and 1-octanethiol (OE). These compounds were chosen to provide a range of interactions with the selected proteins; for example, PEM is neutral and aromatic, MDP is acidic and aliphatic, and DDE and OE are neutral and aliphatic.

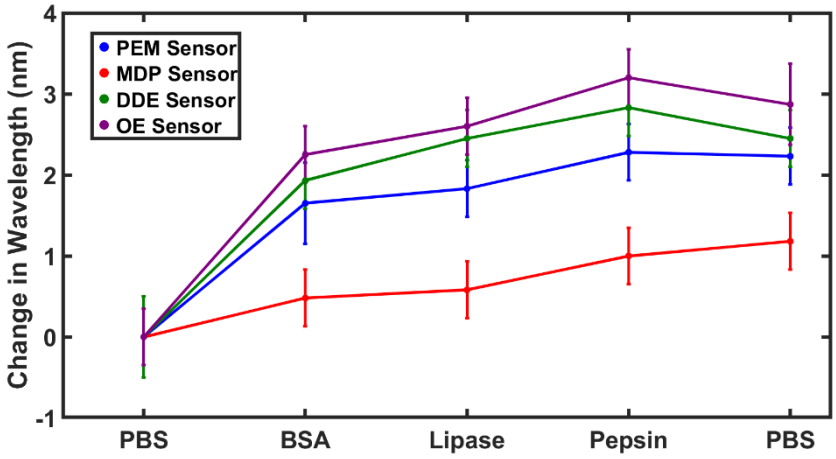

Figure 5.2 - The progression of resonance wavelength for four different sensors when exposed to three different proteins in succession (n=5)**.**

Table 5.2 - The shift of the resonance wavelength with exposure to each protein.

Surface Chemistry	Shift with BSA (nm)	Shift with Lipase (nm)	Shift With Pepsin (nm)
PEM	1.65	0.18	0.45
MDP	0.48	0.1	0.42
DDE	1.93	0.52	0.38
OE	2.25	0.35	0.6

We can see there is a very clear red shift when the sensors are exposed to proteins showing a clear ability for these sensors to detect proteins on the surface of the sensor. In addition to this, the data in Table 5.2 shows that each surface chemistry responds differently to each protein, indicating there is potential for a cross-reactive protein sensing system. A limitation of the sensors is highlighted by this dataset, despite rinsing the sensors between readings, the red shift created by each protein when they are exposed to the surface is never reversed. This is due to unspecific and undesirable immobilisation, or fouling: when proteins bind to the sensors surface, they increase the local refractive index causing a red shift. To create a reusable cross-reactive sensor, proteins must be able to be removed from the sensor and as such, we attempted to optimise a cleaning protocol for the sensors.

5.3.2. Methods of Removing Proteins from Sensors Following Detection

5.3.2.1 Organic Solvents

Initial attempts to remove proteins from the surface of the sensor used common laboratory solvents. This included DI water, ethanol, methanol, acetone, isopropyl alcohol (IPA) and PBS. The sensors were cleaned using the method detailed in Section 5.2.3.1. Table 5.3 shows the spectral shifts recorded after rinsing the sensors with each solvent.

Table 5.3 - The effect of different common lab solvents as methods of removing proteins from plasmonic biosensors. Sensors incubated in 1 mg/mL BSA for 15 minutes before washing (n=3).

Solvent	PBS Reading before proteins (nm)	Reading after incubation in BSA (nm)	PBS Reading after proteins (nm)	Shift from Initial Baseline (nm)
Water	670.81 (+/- 0.31)	675.01 (+/- 0.32)	673.84 (+/- 0.10)	3.03
PBS	661.98 (+/- 0.01)	665.44 (+/- 0.91)	665.38 (+/- 0.32)	3.40
Ethanol	672.88 (+/- 0.36)	676.83 (+/- 0.15)	677.99 (+/- 0.29)	5.11
Acetone	671.22 (+/-0.1)	673.94 (+/- 0.14)	673.64 (+/- 0.17)	2.42
Methanol	673.71 (+/- 0.19)	678.27 (+/- 0.05)	680.44 (+/- 0.15)	6.73
IPA	673.20 (+/- 0.15)	677.18 (+/- 0.64)	677.80 (+/- 0.33)	4.60

As can be seen from these results, the selected solvents were not successful at restoring the sensor to its initial resonance wavelength before its incubation in protein solution. For the water and PBS, the proteins are most likely remaining stuck to the surface as they are too strongly bound for enough of them to be displaced upon just rinsing. Organic solvents are not more successful than aqueous ones, even showing a larger red-shift than the initial reading. The most likely explanation for this behaviour is the denaturalisation of proteins. This denaturing is a result of the polar nature of the solvents, which will strip water molecules from the surface of the protein, breaking the hydrogen bonds that hold their secondary and tertiary structure (25). This, in turn, may result in proteins spreading out on the surface causing stronger bonds and greater levels of surface coverage or fouling.

5.3.2.2. Detergents

Detergents are designed to help break up biofilms by disrupting the hydrophobic interactions between proteins and the substrate (24,26). Due to these cleaning properties and evidence in literature, Triton-X and Tween-20 were investigated (24,26). Sensors were cleaned using the protocol in Section 5.2.3.2. Measurements were taken in PBS before and after the exposure to proteins to assess if the detergents were any more effective than organic solvents.

Table 5.4 - The ability of Triton-X and Tween-20 solutions to remove proteins from fouled sensors (n=3).

Solvent	PBS reading before proteins (nm)	Reading after incubation in BSA (nm)	PBS reading after proteins (nm)	Shift from initial baseline (nm)
1% Triton-X	661.87 (+/- 0.17)	663.82 (+/- 0.19)	663.15 (+/- 0.15)	1.28
1% Tween-20	673.03 (+/- 0.18)	674.99 (+/- 0.17)	674.19 (+/- 0.09)	1.16

As can be seen in Table 5.4, detergents were more successful at protein removal than the aqueous and organic solvents discussed above. However, the small shift recorded after cleaning the sensors indicates that a small amount of protein remains bound to the surface, which prevents full sensor reusability.

Following the partial success of this method, different protocols were developed inspired by the protocol reported by Kratz *et al.* This involved dipping the sensor in and out of a Tween-20 solution 50 times, as this was shown to have the best results in their experiments for removing proteins from a gold surface indicating that physical force is useful for removing proteins (24). In addition to the dip steps, the sensor was also sonicated and agitated in Tween-20 solution for varying lengths of time in an attempt to remove the proteins as described in Section 5.2.3 (Table 5.5).

Table 5.5 - The cleaning properties of Tween-20 solution. Cleaning protocols can be found in the experimental section. Protocol 2: Section 5.2.3.3, Protocol 3: Section 5.2.3.4 and Protocol 4: Section 5.2.3.5. DDE: 1-dodecanethiol, OE: 1-octanethiol, PEM: Phenylethyl mercaptan and MDP: 12-Mercaptododecylphosphonic acid**.** See Appendix A.5.1 for full datasets.

Cleaning Protocol	Protein	Surface Chemistry	Shift from initial PBS reading (nm)
2 (1% Tween-20)	BSA	Bare Gold	2.15
2 (5% Tween-20)	BSA	Bare Gold	0.77
3	BSA	Bare Gold	4.34
3	BSA	DDE	4.00
3	BSA	OE	4.51
3	BSA	PEM	5.05
3	BSA	MDP	1.72
4 (Agitated 5 minutes)	BSA	Bare Gold	3.78
4 (Agitated 5 minutes)	Pepsin	Bare Gold	1.94
4 (Agitated 5 minutes)	Lipase	Bare Gold	1.12
4 (Agitated 8 hours)	BSA	Bare Gold	2.66
4 (Agitated 8 hours)	Pepsin	Bare Gold	0.52
4 (Agitated 8 hours)	Lipase	Bare Gold	0.98

The first results using this methodology were very encouraging, with a small shift of 0.77 nm recorded after dipping and sonicating the sensor in 5% Tween. However, subsequent experiments following the similar methodology resulted in larger shifts, even when using longer sonication times. Although promising, the capricious nature of the cleaning methods reported in this chapter limits reusability and reliability. A different approach was adopted to achieve this by using anti-fouling coatings on the sensor and substrate surface, as described in the next section.

5.3.3. Anti-Fouling Surface Modifications on Gold Nanostructures

As stated above, the approach to achieve reusability moved from attempting to remove irreversibly bound proteins to preventing them from permanently associating with the surface. To do this while maintaining a cross-reactive element to the sensing setup, multiple anti-fouling surfaces with different properties were investigated as a method of obtaining a reversible interaction. Traditional methods of protecting surfaces from bio-fouling usually

employ steric hinderance. Steric hindrance relies on physically blocking the surface to prevent non-specific attachment. Although effective, LSPR sensing requires the analyte to be in close proximity to the sensor surface, with sensitivity decreasing exponentially as the analytes are forced further away. To avoid this degradation of sensitivity, thin anti-fouling SAMs were selected and studied. To best take advantage of the thin layers, all the measurements in this section are on split ring sensors due to their highly concentrated electromagnetic field.

5.3.3.1. Bare Gold

The graph below shows the spectral shift observed when exposing a bare split-ring sensors to BSA, pepsin and lipase with the cleaning protocol in Section 5.2.3.4 used to clean the sensors between readings.

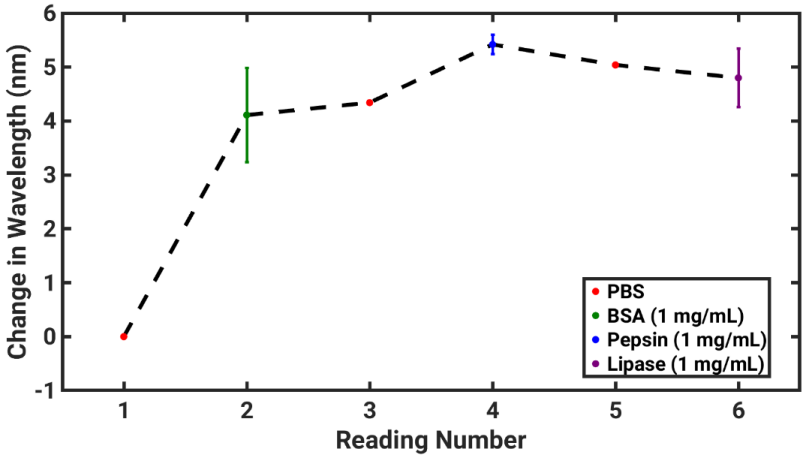

Figure 5.3 - The ability of a bare gold split ring to reversibly detect protein interactions at 1 mg/mL (PBS readings, n=1; Protein readings n=5).

Figure 5.3 shows that for a non-modified sensor, despite the rigorous cleaning methodology utilised for this experiment there is no shift back towards the baseline after exposure to the proteins (Section 5.2.3.4.). As there is no layer preventing permanent interactions from occurring, the proteins become very hard to remove from the surface as has been previously described in Section 5.3.2. This gives us a baseline to compare the subsequent anti-fouling chemistries to.

5.3.3.2. Cysteine

Cysteine is a zwitterionic amino acid that has proven to have anti-fouling properties when attached to a bulk gold substrate (27,28). These anti-fouling properties arise from the hydration layer formed upon the interaction of the carboxyl group with the water molecules in the solvent, which prevents proteins from sticking to the sensor surface. It is well known that proteins adhere to glass, so, in addition to the thiol SAM, a perfluoroalkane silane was

used to passivate the glass substrate for these sensors using the method described in Section 5.2.5 (29). Section 5.3.3.3 offers more details about the use of perfluorinated compounds as anti-fouling coatings.

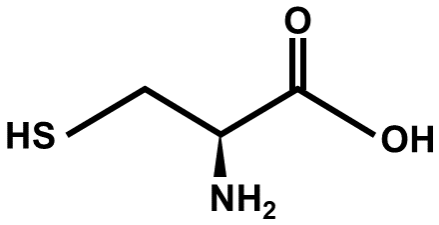

Figure 5.4 – The chemical structure of cysteine.

The first experiments utilising a cysteine layer as a potential anti-fouling layer were carried out using the static setup as described in Section 2.9.1. For all readings in this section, the cleaning protocol described in Section 5.2.3.5. was followed. The result of this initial experiment is shown in Figure 5.5.

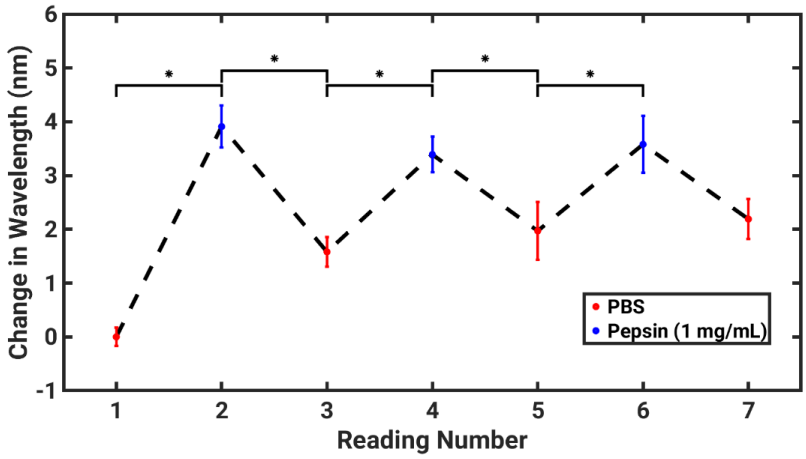

Figure 5.5 - Annealed sensor split ring with cysteine SAM detecting 1 mg/mL pepsin (n=3, Paired T-Test, $p < 0.05$)

As can be seen from the graph, cysteine shows great potential to achieve reversible interactions. It allows for proteins to get close to the surface and be detected, but it facilitates the removal upon cleaning unlike the surface chemistries presented in 5.3.2. In this case, there is an initial large red-shift upon pepsin being introduced to the sensor and despite not returning to baseline, there is still a significant temporary red-shift when pepsin is measured in subsequent readings. However, it is important to note that, although the resonance wavelength of the sensor in the pepsin solution does not shift much between readings, the PBS readings are slowly red-shifting towards the pepsin readings. This indicates there is a limit to this reusability. Despite this trend, we still get three uses of the sensor whereby the pepsin readings are statistically significant from the PBS readings showing enhanced reusability compared to bare gold.

Section 4.3.4 discusses the differences between annealed and non-annealed sensors, with data indicating that there may be a greater level of thiol binding when using non-annealed sensors due to the higher roughness of the surface. This should result in denser SAMs and in turn, enhance anti-fouling capabilities.

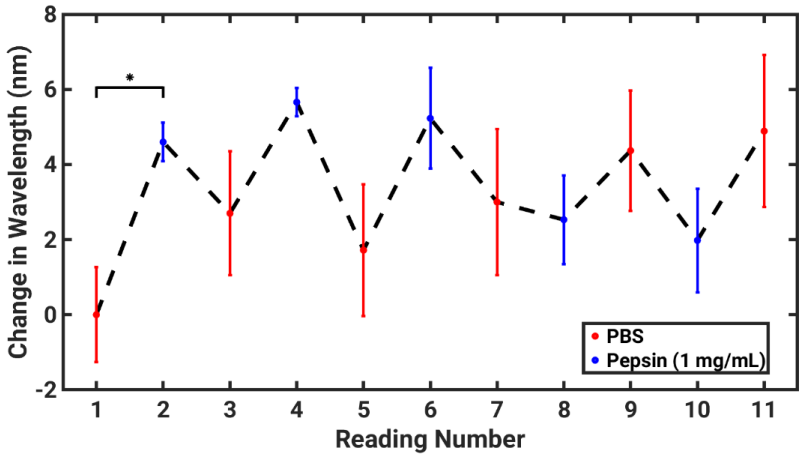

Figure 5.6 - Non-annealed split ring with cysteine SAM detecting pepsin (n=5, Paired T-Test, $p < 0.05$)

The non-annealed structure showed good reusability, as seen in Figure 5.6, however, as expected, the error in the readings is significantly higher due to the higher FWHM of LSPR peaks resulting from non-annealed structures. Despite a visible trend that three protein readings may be distinguishable from PBS, the large errors mean that only the first protein reading is statistically significant. This reinforces the importance of optimising sensor design to have a low FWHM, as discussed in Chapter 4; even though non-annealed sensors do more readily create conformal thiol monolayers, the larger error in the measurement negates this advantage.

Having established that cysteine allows for some reversible interactions, the concentration of proteins was reduced from 1 mg/mL to 0.1 mg/mL to move towards physiologically relevant concentrations (Figure 5.7). This resulted in a smaller initial shift as fewer proteins reached the sensor surface and, as with the previous experiments on annealed sensors, the sensor was able to be used three times before detecting pepsin failed to be separated from PBS.

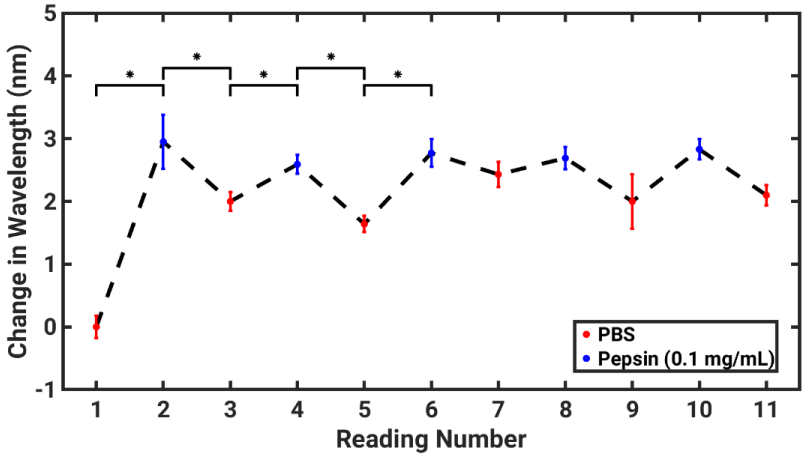

Figure 5.7 - Annealed split ring with cysteine SAM detecting 0.1 mg/mL pepsin concentration (n=5, Paired T-Test, $p < 0.05$)

This section proves the potential of cysteine layers as a means to detect proteins whilst preventing non-specific binding. Although these layers are not as robust as reported in literature, it should be noted that there are very few studies of thiolation onto lithographically defined gold nanostructures, with most studies being carried out on planar gold films or on spherical nanoparticles. This may explain some of the incongruity between the results reported here and those found in literature (27,28). Further characterisation would be needed to determine the conditions required for the maximum level of coverage of thiol SAMs on gold nanostructures.

5.3.3.3. Fluorinated Thiols

Perfluorinated compounds have unique properties which can be useful for anti-fouling applications (29,30). These properties arise from the low polarizability of fluorine atoms, that prevents significant dipole-dipole interactions, resulting in very low Van der Walls forces. This causes perfluorinated phases to favour interactions with other perfluorinated phases before aqueous or organic ones, a property known as the “fluorous effect”. The amphiphobicity of these phases makes them ideal candidates for anti-fouling applications. In addition to these anti-fouling properties, fluorous molecules are also very small compared to traditional anti-fouling methods such as poly(ethylene glycol) (PEG) layers. This should allow proteins to get close enough to the surface of the sensor to be detected while still preventing irreversible binding.

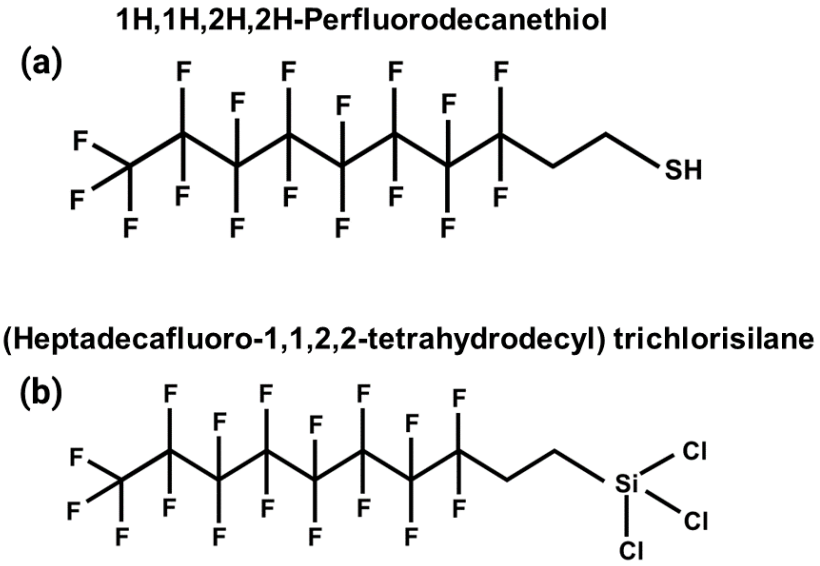

Figure 5.8 – The chemical structures of the fluorous compounds. (a) PFDT and (b) the structure of the fluorous silane used for surface passivation ((heptadecafluoro-1,1,2,2-tetrahydrodecyl) trichlorisilane).

In this section we use a thiolated fluorous compound, 1H,1H,2H,2H-Perfluorodecanethiol (PFDT), to create a monolayer of fluorous molecules on the gold sensors and assess its anti-fouling abilities. As before, this fluorous thiol layer is accompanied by a fluorous silane layer to prevent proteins non-specifically binding to the glass substrate supporting the gold nanostructures (Section 5.2.5) (29).

Repeating the experiments carried out with cysteine, a sensor modified with PFDT was immersed in PBS, measured and then immersed in 1 mg/mL pepsin before being rinsed with 5% Tween-20/PBS for 30 s on each side of the sensor chip (Fig. 5.9, Section 5.2.3.5).

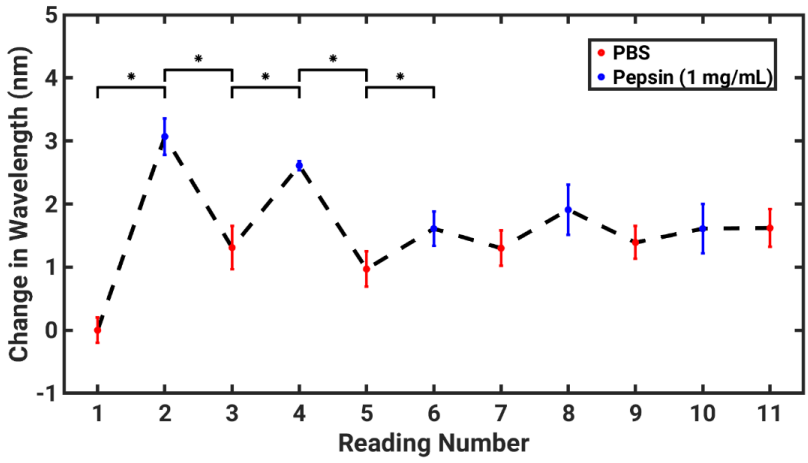

Figure 5.9 - Detecting pepsin repeatedly using a gold split rings with a PFDT (n=5, Paired T-Test, $p < 0.05$)

The PFDT modified sensor shows a degree of reusability with the protein being distinguishable from the PBS solution three times before it becomes difficult to distinguish between the solutions. As this is a relatively high concentration of proteins, PFDT coated

sensors were also assessed for reusability at a lower concentration of proteins which is more relevant in a physiological environment (Fig. 5.10).

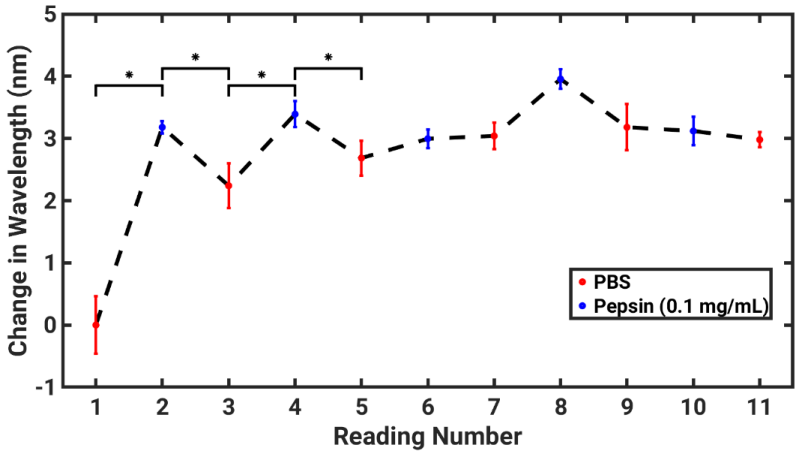

Figure 5.10 - Detecting pepsin repeatedly using a PFDT monolayer on gold split rings at a 0.1 mg/mL protein concentration (n=5, Paired T-Test, $p < 0.05$)

The protein could be detected on the first two cycles of the experiment, a result comparable to that observed when using cysteine. Overall, both PFDT and cysteine show great promise as anti-fouling coatings for reusable, cross-reactive sensing platforms as they allow for the detection of the analytes whilst partially preventing irreversible binding. However, as previously mentioned, the understanding of thiolation on lithographically defined nanostructures is still poor and not well reported in the literature. Formation of thiolated SAMs on planar gold films and spherical nanoparticles, however, has been extensively studied. Planar gold systems give the thiols an infinite plane on which to bind and organise themselves. According to the literature, the formation of SAMs in this case happens upon the binding of one single molecule that acts as an anchor point for a larger, organised area of self-assembled molecules (31–37). Lithographically defined structures offer a much more constrained space onto which thiols can bind in addition to the various geometrical factors the nanostructures impose.

On the other hand, colloidal nanoparticles are synthesised in solution following a bottom-up approach. The bottom-up methods used in their production result in gold crystals with very different surface properties compared to thermally evaporated metal. As a result, they will interact differently with thiolated molecules than lithographically defined structures (31,37–41). All of this could explain the reason why the SAMs created onto the sensing structures presented here do not present the same anti-fouling capabilities are those reported in the literature.

Despite the uncertainty in SAM quality, there is a clear increase in sensor reusability with the addition both PFDT and cysteine layers making multiple uses of the sensor possible where the bare gold sensor becomes unusable after a single exposure to proteins.

5.3.3.4. Potential of Anti-Fouling Surface Chemistries for Cross-Reactive Sensing

In order to create a cross-reactive system which is reusable, the selected chemistries must have different affinities for the proteins of interest while still maintaining the ability to host reversible surface-protein interactions. To examine the response of the sensors to the proteins, proteins were injected into the solution as described in Section 2.9 and the response of the sensors was monitored.

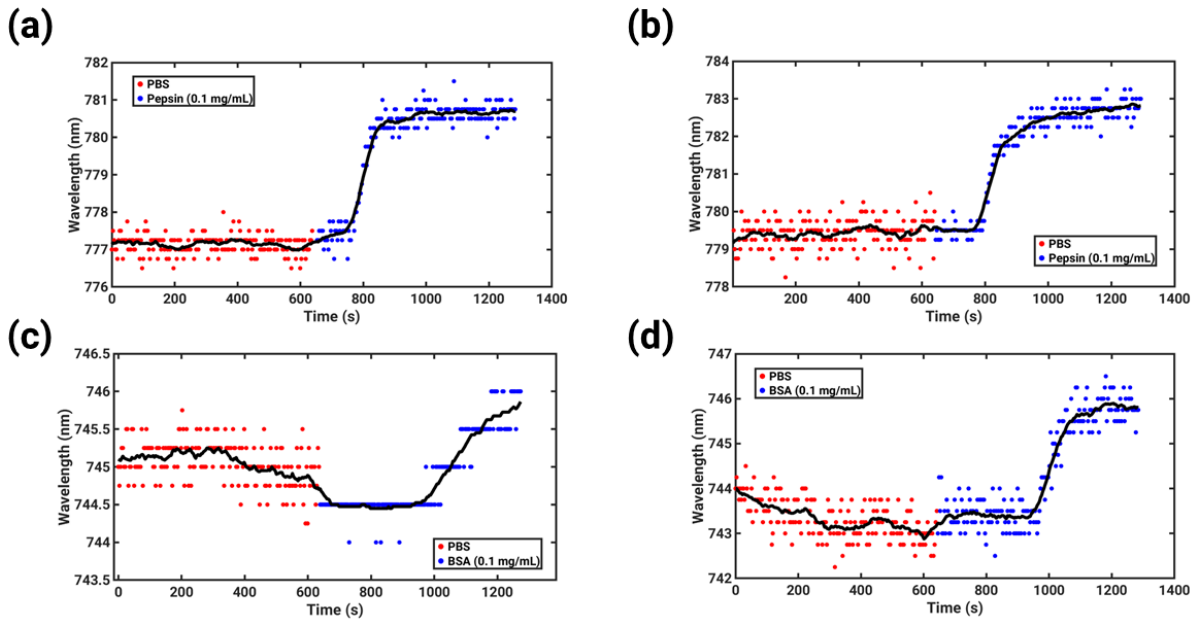

Figure 5.11 - The response of annealed split ring sensors to different proteins with different anti-fouling chemistries (a) Pepsin interacting with a cysteine coated sensor. (b) BSA interacting with a cysteine coated sensor. (c) Pepsin interacting with a PFDT coated sensor. (d) BSA interacting with a PFDT coated sensor. Data recorded every 750 ms.

As seen in Figure 5.11, the response of the surface to the proteins being injected varies depending on the surface chemistry and protein. The magnitude of these shifts as taken from Figure 5.11 is summarised in Table 5.6.

Table 5.6 - The shift in resonance peak caused by pepsin and BSA on cysteine and PFDT coated sensors.

Surface Modification	Shift in Response to Pepsin (nm)	Shift in Response to BSA (nm)
Cysteine	3.25	1.25
PFDT	5	2.5

We can see that, in general, the proteins have a stronger interaction with PFDT-coated sensors when compared to cysteine-coated ones. In addition, pepsin seems to always have a stronger interaction with the sensor when compared to BSA. The stronger interaction seen

by pepsin is most likely due to its higher binding coefficient to gold nanoparticles. Although no directly comparable studies exist, the binding constant of pepsin on citrate coated nanoparticles is seen to be significantly higher than that of BSA (42,43). The PFDT-coated sensors showing a stronger interaction with the proteins when compared to the cysteine-coated sensors may be due to the PFDT forming a less conformal monolayer on the nanostructures. However, the anti-fouling mechanism in each of the SAMs is very different and hard to compare while cysteine relies on the formation of a hydration layer, PFDT's anti-fouling properties are due to the lack of dipole-dipole interactions caused by the presence of fluorine atoms (29,44).

The results discussed in this section suggest that the anti-fouling SAMs under study are good candidates for reusable, cross-reactive sensing applications. Unfortunately, there is a limit in the number of times these sensors are capable of detecting proteins before the surface fouls. As discussed, a potential reason for this limitation could be the lack of homogeneity in the coating. In fact, as described in Section 2.9.1, defects in the SAM can lead to the observation of a 'snowfall effect'. In this setup, proteins slowly diffuse towards the sensor and spend extensive amount of time on the surface of the sensor. This allows any gaps in the monolayer to be infiltrated, accelerating protein fouling. Further investigation into SAM formation on gold nanostructures would be needed to confirm this theory.

5.3.5. Microfluidics to Aid in Protein Detection

Microfluidics allow for the controlled delivery of analytes to a sensor without the need to remove it from solution. In addition, they allow for a much easier integration into existing systems making academic research more easily translatable to real world applications. Before attempting cross-reactive sensing, this microfluidic system was tested using a more traditional 'lock and key' style protein detection system. As described in Section 2.9.2, this was accomplished by utilising one of the strongest biological bonds found in nature between biotin and streptavidin. Biotin was anchored to the substrate using a short PEG linker (~20 nm) to prevent the analytes from being too far away from the substrate to be detected, but long enough to take advantage of its anti-fouling properties. To ensure the sensor has a sensing volume large enough to detect binding events in this setup with high sensitivity, non-annealed 150 nm square sensors were used (resonance wavelength ~ 840 nm).

5.3.5.1. Specificity

The first parameter that must be established is the specificity of the system. Figure 5.12 shows that the system has no reaction to a high concentration of BSA and an almost

immediate, large shift in response to neutravidin due to the high specificity of the interaction between the analyte and the receptor.

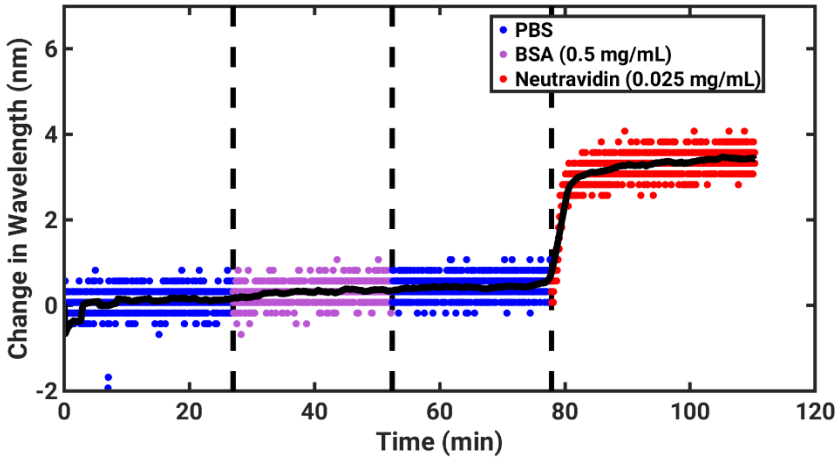

Figure 5.12 - Time series data showing the specificity of a PEG-biotin coated square sensor for neutravidin. Data recorded every 750 ms.

This is aided by the PEG linker attached to the biotin, which prevents non-specific binding thanks to the well-known antifouling properties of PEG coatings (21,23,45,46). As opposed to the methods previously discussed that relied on the chemical properties of the molecules to prevent non-specific interactions, PEG prevents non-specific binding via steric hindrance. PEG causes steric hinderance by physically blocking the surface due to its large size (2000 MW). When compared to cysteine and PFDT, it is clear that PEG is a much more effective anti-fouling method with only a negligible 0.15 nm increase in resonance wavelength during the time BSA is exposed to the sensor. This excellent anti-fouling ability comes at the cost of sensor sensitivity as the interactions will now occur further from the surface, where the sensors sensitivity is at its greatest. In this case, because of the high specificity of the lock-key mechanism reported in Figure 5.12, the larger size of the PEG layer does not prevent detection. However, its applications in cross-reactive sensing, where the interactions with the proteins are more transient and nonspecific, might be limited due to its size.

5.3.6.2. Amplification

In Section 1.4.1, sandwich style amplifiers were discussed as a method for increasing the signal obtained from the binding of a protein. By using biotinylated BSA, we demonstrated how a sandwich amplifier could be used to increase the signal from neutravidin binding (Fig. 5.13).

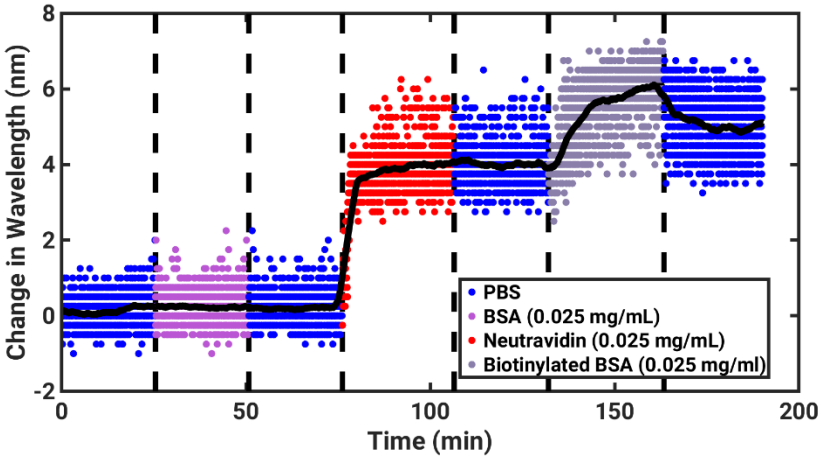

Figure 5.13 - Time series data showing the amplification effect that can be created using a sandwich assay. Data recorded every 750 ms.

This result shows the potential of this system to be used as a sandwich style biosensor. The drawback of this system is the smaller shift created by the biotinylated BSA when compared to the neutravidin. This smaller shift comes from the limited sensing volume of LSPR sensors. The system now has a string of 2000 MW biotin-PEG, neutravidin and biotinylated BSA. The 150 nm squares used for this sensor were chosen due to their high resonance wavelength which as discussed in Section 3.3.4, should give them a larger sensing volume. Despite these sensors being at the higher edge of the spectrometer's wavelength limits, they still have a relatively small, exponentially diminishing sensing volume. This means that the further the analyte gets from the surface of the sensor, the smaller the shift it will create when binding. Despite this diminished shift, the addition of this amplification step does increase the shift caused by the analyte by 51.5% (3.96 nm to 6.00 nm).

5.3.6.3 Measuring the Limit of Detection of LSPR Sensors

Using this specific system, we can get an estimate of the limit of detection of these sensors, which are made up of 150 nm gold squares. By taking the resonance shift of the sensor at various concentrations of neutravidin and plotting a linear regression, we can get an estimate of the LoD using Eqn 5.1 (47,48).

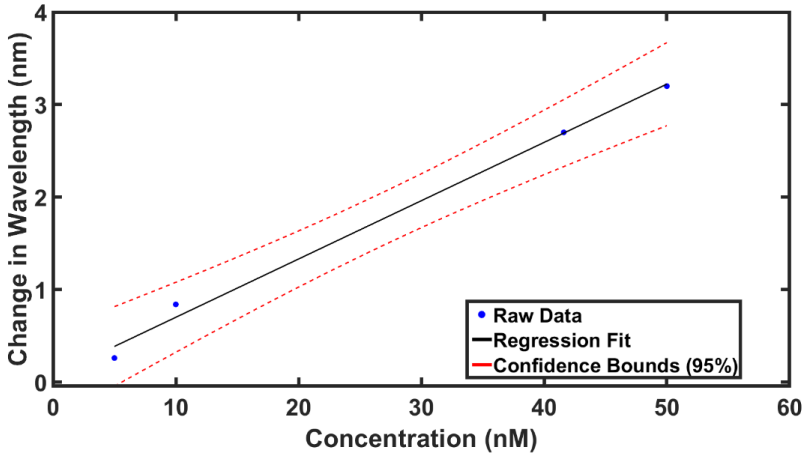

Figure 5.14 - Linear regression for calculating the LoD of square sensors. Using 5 nM, 10 nM, 41.6 nM and 50 nM neutravidin concentrations.

$$\mathrm{LoD} = 3.3\frac{\sigma}{m} \tag{5.1}$$

where is σ is the standard error of the regression fit and m is the slope of the fit line. Using this fit, the limit of detection for these squares is calculated as 6.28 nM. In comparison to other plasmonic biosensors, this is at the high end of limit of the limit of detection reported for LSPR based sensors in literature, with LoD's ranging from 7 nM to 0.5 pM (49–58). It should be noted that this LoD figure is very much an estimate, with more concentrations and extra independent experiments being carried out before a LoD can be confidently stated.

In the future it would be interesting to compare the square sensors used here with the geometries explored in Chapter 3 and the sensitivity enhancing effects of exposure to hydrofluoric acid explored in Section 4.3.5 to investigate how much the LoD of this system could be reduced.

5.3.4. Cross-Reactivity of Proteins using Disposable Sensors

The results reported in Sections 5.3.1 and 5.3.3 suggest that proteins interact differently with a sensor depending on its surface chemistry. Unfortunately, the anti-fouling molecules in this thesis to not provide a range of interactions wide enough for a cross-reactive sensor system. For this reason, and despite the promising results obtained with cysteine and PFDT layers, it was decided to move to single-use experiments. This allowed for the introduction of more surface chemistries with more varied functionalities needed to achieve effective cross-reactive sensing. In this section, this cross-reactive concept is integrated with the microfluidics that were previously characterised with the traditional receptor/analyte system.

5.3.4.1. Selection of Surface Chemistries

Table 5.7 summarises some of the chemical properties of the compounds selected to modify each sensing element in the cross-reactive platform. These chemistries were selected to provide a range of functionalities that would cause proteins to interact with each of them with different affinities. Each of these chemistries were printed onto the surface using an iDOT printer as described in Section 2.5.3.

Table 5.7 - The properties of the different chemistries used to make the disposable cross-reactive tongue system.

Chemistry	Abbreviation	Printing Solvent	Properties
Cysteine	Cys	Water	Zwitterionic
Glutathione	Glu	Water	Zwitterionic
Cysteamine	CA	EG/EtOH	Basic
Sodium 2-mercaptoethanesulfonate	MES	Water	Very Acidic
11-mercaptoundecanoic acid	MUA	EG/EtOH	Aliphatic Acid
4-Nitrothiophenol	NTP	EG/EtOH	Neutral, aromatic
4-aminothiophenol	ATP	EG/EtOH	Basic, aromatic
1-octanethiol	OT	EG/EtOH	Aliphatic Alkane
1H,1H,2H,2H-Perfluorodecanethiol	PFDT	EG/EtOH	Amphiphobic

The chemical structure of each of these thiols is shown in Figure 5.15.

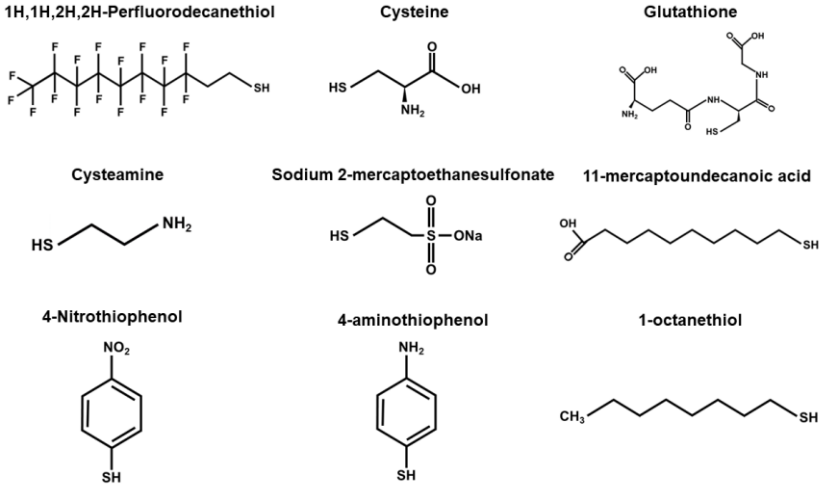

Figure 5.15 - The chemical structure of each of the thiol structures in Table 5.7.

5.3.4.2. Protein Discrimination at a High Concentrations

The first cross-reactive protein sensing experiment was carried out at a high concentration of 5 µM. This allowed us to determine if the concept was feasible without the concerns of negligible interactions at very low concentrations. Using a microfluidic chamber, 5 readings were recorded for each sensor in PBS and in a protein solution. These shifts caused by

protein exposure were used to create a data matrix for PCA and LDA (Section 2.7.3 and 2.7.4) to be performed on (Fig. 5.16).

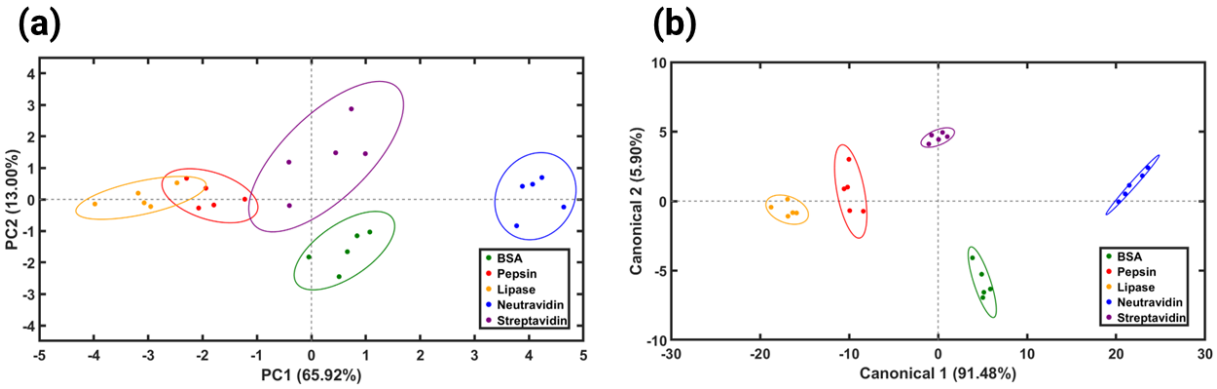

Figure 5.16 - Segregation of protein solutions using a disposable LSPR sensing chip at 5 µM (a) Principal component and (b) linear discriminant analysis. Confidence ellipses p=0.95. Eigenvectors in Appendix A.5.3.

Figure 5.16 shows the potential of disposable sensors for cross reactively detecting proteins. In this case, each protein is well distinguished from each other with very little overlap in the PCA and 100% classification success for the LDA.

5.3.4.3. Discrimination at a Lower Concentrations

After showing discrimination at 5 µM, a series of experiments were conducted to determine the lowest concentration that could be detected with a shift large enough to be reliable. This concentration was found to be 100 nM, which was the concentration used in the next experiment (Appendix A.5.2). The PCA and LDA analysis of proteins at 100 nM is presented in Figure 5.17.

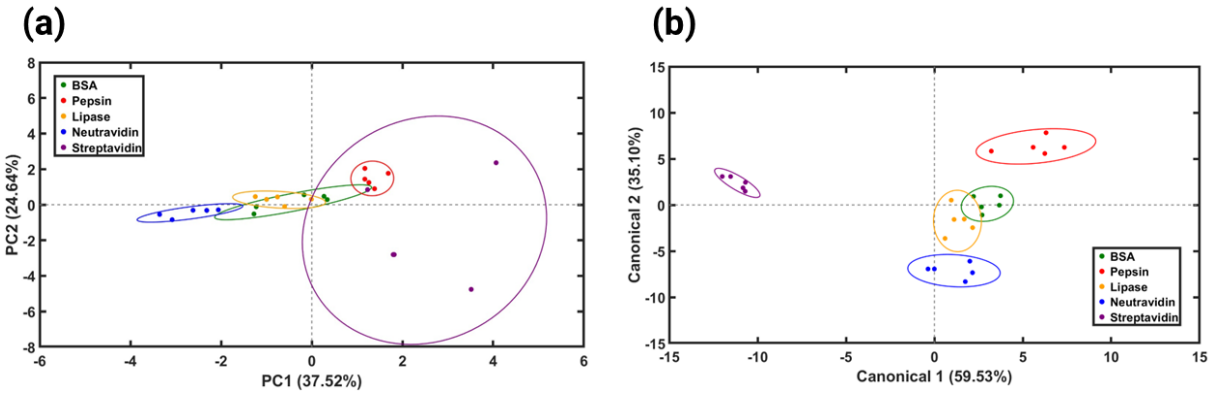

Figure 5.17 - Segregation of protein solutions using a disposable LSPR sensing chip at 100 nM (a) Principal component and (b) linear discriminant analysis. Confidence ellipses p=0.95. Eigenvectors in Appendix A.5.3.

As expected, at this lower concentration the segregation in the analysis becomes more difficult as shifts become smaller in magnitude. Despite this, even at this lower concentration we can see that proteins are discriminated with 100% accuracy. There is a larger spread in the streptavidin data that causes it to be very well categorised in the LDA. This large spread

is almost certainly the cause of error in readings. Appendix A.5.3 shows this PCA and LDA without the streptavidin which shows the remaining proteins being less tightly packed without the influence of the streptavidin readings.

5.3.4.4. Categorising Proteins from Separate Experiments

To assess the repeatability of this method, a second experiment was carried out on a newly fabricated chip to add to the dataset presented in Section 5.3.4.2. By repeating this experiment under the same conditions, multivariant analysis such as PCA and LDA should be able to group the proteins together, recognising a protein from the first experiment to be the same as the one from the second. Figure 5.18 shows the combined PCA and LDA utilising readings from the first experiment (circles) from the second experiment (crosses).

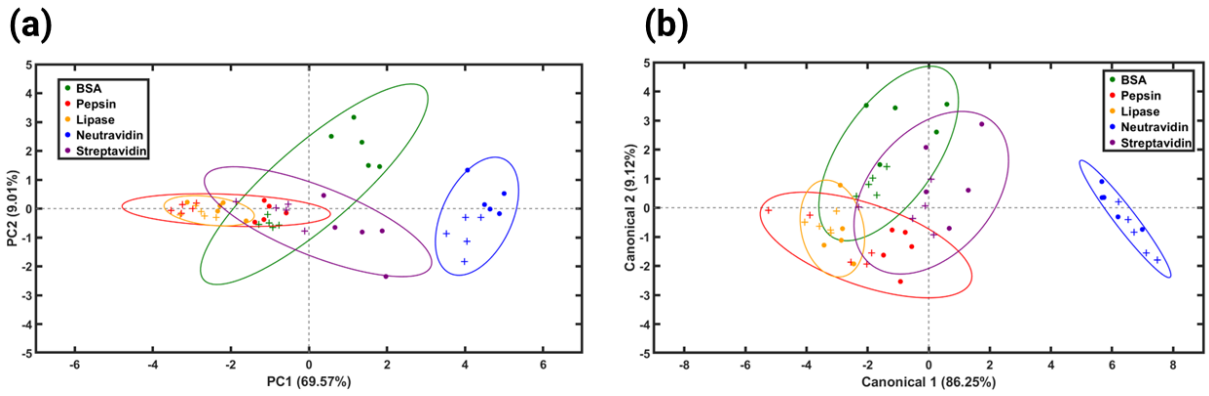

Figure 5.18 - Segregation of protein solutions using data from two separate disposable LSPR sensing chip at 5 µM (a) Principal component and (b) linear discriminant analysis. Confidence Ellipses p=0.95. Eigenvectors in Appendix A.5.3.

The PCA shows a trend of the same protein not always clustering together when the data from the two sensors is combined. There is a degree of clustering when considering neutravidin (blue), streptavidin (purple) and lipase (orange), however, other proteins, particularly BSA, show clear separations between the two experiments. The LDA still shows a reasonable level of classification, with 88% of proteins correctly classified (See Appendix A.5.3 for full classification matrix), however this can be partially explained by overclassification. Due to the limited number of readings in this dataset, statistical methods such as LDA can be prone to exaggerating differences in data that may not correspond to an actual difference between samples when a larger dataset is used.

The reason for these inconsistent results can be explained with a multitude of factors, often stemming from the fact that sensors cannot be easily reused. First, as has been extensively discussed in this thesis, the process of forming a thiol SAM can be inconsistent, particularly on annealed sensors. If the thiol layers are inconsistent in terms of packing density, this could

lead to changes in how each protein interacts with each surface chemistry. Additionally, due to inevitable fabrication inconsistency, not every sensor will resonate at the same wavelength, with the average resonance wavelength of every sensor used in Sections 5.3.4.2, 5.3.4.3 and 5.3.4.4 in PBS being 810.23 nm (+/- 5.83) with a 46.25 nm spread between the maximum and minimum reading recorded. This inconsistency in sensor behaviour between sensors will contribute to the different interactions between sensors leading to protein misclassification.

Although not perfected here, the concept of a cross-reactive sensor for classifying protein mixtures shows potential. In particular the ability of the sensor to clearly distinguish between neutravidin and streptavidin even when runs are combined in Figure 5.18 is a feat that a traditional lock-in key style receptor would struggle with due to the functional groups on these proteins being identical. Furthermore, when performing experiments in the same chip, a good degree of protein segregation is possible. Further optimisation of sensor fabrication consistency, cleaning methods, surface chemistry choice and thiolation protocols, there is the potential for this concept to provide a very useful new way of sensing proteins.

5.4. Conclusion

In this chapter we have investigated the use of LSPR sensors for detecting proteins in different ways. The use of thin anti-fouling layers such as cysteine and PFDT allowed for the detection of proteins in solution at least three times before the sensor surface fouled. Furthermore, differential interactions between proteins and the anti-fouling surface chemistries suggests a reusable cross-reactive system may be achievable. Additionally, we investigated the use of a single-use, microfluidic-based, cross-reactive system for segregation of proteins in complex mixtures. This system was able to segregate proteins upon LDA and PCA analysis with great success when using sensors fabricated at the same time and on the same chip. Furthermore, it was capable of distinguishing neutravidin from streptavidin, two proteins which are very similar in structure and that bind the same receptors, indicating the success of the concept. However, more work is required in creating consistent SAM layers and sensors to achieve the repeatability required to translate this technology to real life applications. Additional future work may also include quantifying the difference in LoD that different plasmonic geometries could provide as well as the benefits of additional post-fabrication optimisation techniques such as substrate etching.

References

1. Malmqvist M. Surface plasmon resonance for detection and measurement of antibody-antigen affinity and kinetics. Curr Opin Immunol [Internet]. 1993 Jan;5(2):282–6. Available from: https://linkinghub.elsevier.com/retrieve/pii/095279159390019O

2. Liedberg B, Nylander C, Lundström I. Biosensing with surface plasmon resonance — how it all started. Biosens Bioelectron [Internet]. 1995 Jan;10(8):i–ix. Available from: https://linkinghub.elsevier.com/retrieve/pii/0956566395969652

3. Jönsson U, Fägerstam L, Ivarsson B, Johnsson B, Karlsson R, Lundh K, et al. Real-time biospecific interaction analysis using surface plasmon resonance and a sensor chip technology. Biotechniques [Internet]. 1991 Nov;11(5):620–7. Available from: http://www.ncbi.nlm.nih.gov/pubmed/1804254

4. Fägerstam LG, Frostell-Karlsson Å, Karlsson R, Persson B, Rönnberg I. Biospecific interaction analysis using surface plasmon resonance detection applied to kinetic, binding site and concentration analysis. J Chromatogr A [Internet]. 1992 Apr;597(1–2):397–410. Available from: https://linkinghub.elsevier.com/retrieve/pii/002196739280137J

5. Hu J, Fu K, Bohn PW. Whole-Cell Pseudomonas aeruginosa Localized Surface Plasmon Resonance Aptasensor. Anal Chem. 2018 Feb 6;90(3):2326–32.

6. Li X, Soler M, Özdemir CI, Belushkin A, Yesilköy F, Altug H. Plasmonic nanohole array biosensor for label-free and real-time analysis of live cell secretion. Lab Chip. 2017 Jul 7;17(13):2208–17.

7. Su JL, Youn BS, Ji WP, Niazi JH, Yeon SK, Man BG. ssDNA aptamer-based surface plasmon resonance biosensor for the detection of retinol binding protein 4 for the early diagnosis of type 2 diabetes. Anal Chem. 2008 Apr 15;80(8):2867–73.

8. Calvo-Lozano O, Sierra M, Soler M, Estévez MC, Chiscano-Camón L, Ruiz-Sanmartin A, et al. Label-Free Plasmonic Biosensor for Rapid, Quantitative, and Highly Sensitive COVID-19 Serology: Implementation and Clinical Validation. Anal Chem. 2022 Jan 18;94(2):975–84.

9. Campu A, Lerouge F, Chateau D, Chaput F, Baldeck P, Parola S, et al. Gold NanoBipyramids Performing as Highly Sensitive Dual-Modal Optical Immunosensors. Anal Chem. 2018 Jul 17;90(14):8567–75.

10. Tang L, Casas J, Venkataramasubramani M. Magnetic Nanoparticle Mediated Enhancement of Localized Surface Plasmon Resonance for Ultrasensitive Bioanalytical Assay in Human Blood Plasma. Anal Chem [Internet]. 2013 Feb 5;85(3):1431–9. Available from: https://pubs.acs.org/doi/10.1021/ac302422k

11. Piñero F, Dirchwolf M, Pessôa MG. Biomarkers in Hepatocellular Carcinoma: Diagnosis, Prognosis and Treatment Response Assessment. Vol. 9, Cells. NLM (Medline); 2020.

12. Dhingra R, Vasan RS. Biomarkers in cardiovascular disease: Statistical assessment and section on key novel heart failure biomarkers. Trends Cardiovasc Med [Internet]. 2017 Feb 1;27(2):123–33. Available from: https://linkinghub.elsevier.com/retrieve/pii/S1050173816301050

13. Dorcely B, Katz K, Jagannathan R, Chiang SS, Oluwadare B, Goldberg IJ, et al. Novel biomarkers for prediabetes, diabetes, and associated complications. Diabetes Metab Syndr Obes [Internet]. 2017 Aug 14;Volume 10:345–61. Available from: https://www.dovepress.com/novel-biomarkers-for-prediabetes-diabetes-and-associated-complications-peer-reviewed-article-DMSO

14. Sharma A, Demissei BG, Tromp J, Hillege HL, Cleland JG, O'Connor CM, et al. A network analysis to compare biomarker profiles in patients with and without diabetes mellitus in acute heart failure. Eur J Heart Fail [Internet]. 2017 Oct 21;19(10):1310–20. Available from: https://onlinelibrary.wiley.com/doi/10.1002/ejhf.912

15. Macias G, Sperling JR, Peveler WJ, Burley GA, Neale SL, Clark AW. Whisky tasting using a bimetallic nanoplasmonic tongue. Nanoscale. 2019 Aug 28;11(32):15216–23.

16. Jafarinejad S, Ghazi-Khansari M, Ghasemi F, Sasanpour P, Hormozi-Nezhad MR. Colorimetric Fingerprints of Gold Nanorods for Discriminating Catecholamine Neurotransmitters in Urine Samples. Sci Rep. 2017 Dec 1;7(1).

17. Jia J, Wu M, Wang S, Wang X, Hu Y, Chen H, et al. Colorimetric sensor array based on silver deposition of gold nanorods for discrimination of Chinese white spirits. Sens Actuators B Chem [Internet]. 2020;320(December 2019):128256. Available from: https://doi.org/10.1016/j.snb.2020.128256

18. Sperling JR, Poursat B, Savage L, Christie I, Cuthill C, Aekbote BL, et al. A cross-reactive plasmonic sensing array for drinking water assessment. Environ Sci Nano. 2023;10(12):3500–8.

19. Mauriz E. Low-Fouling Substrates for Plasmonic Sensing of Circulating Biomarkers in Biological Fluids. Biosensors (Basel) [Internet]. 2020 Jun 10;10(6):63. Available from: https://www.mdpi.com/2079-6374/10/6/63

20. D'Agata R, Bellassai N, Giuffrida MC, Aura AM, Petri C, Kögler P, et al. A new ultralow fouling surface for the analysis of human plasma samples with surface plasmon resonance. Talanta. 2021 Jan 1;221.

21. Wang F, Zhang H, Yu B, Wang S, Shen Y, Cong H. Review of the research on anti-protein fouling coatings materials. Prog Org Coat [Internet]. 2020 Oct 1;147:105860. Available from: https://linkinghub.elsevier.com/retrieve/pii/S0300944020303350

22. Rodriguez-Emmenegger C, Brynda E, Riedel T, Houska M, Šubr V, Alles AB, et al. Polymer brushes showing non-fouling in blood plasma challenge the currently accepted design of protein resistant surfaces. Macromol Rapid Commun. 2011 Jul 1;32(13):952–7.

23. Liu B, Liu X, Shi S, Huang R, Su R, Qi W, et al. Design and mechanisms of antifouling materials for surface plasmon resonance sensors. Acta Biomater [Internet]. 2016 Aug 1;40:100–18. Available from: https://linkinghub.elsevier.com/retrieve/pii/S1742706116300782

24. Kratz F, Grass S, Umanskaya N, Scheibe C, Müller-Renno C, Davoudi N, et al. Cleaning of biomaterial surfaces: Protein removal by different solvents. Colloids Surf B Biointerfaces. 2015 Apr 1;128:28–35.

25. Mattos C. Proteins in organic solvents. Curr Opin Struct Biol [Internet]. 2001 Dec 1;11(6):761–4. Available from: https://linkinghub.elsevier.com/retrieve/pii/S0959440X01002780

26. Minhua Feng, Berdugo Morales A, Poot A, Beugeling T, Bantjes A. Effects of Tween 20 on the desorption of proteins from polymer surfaces. J Biomater Sci Polym Ed [Internet]. 1996 Jan 2;7(5):415–24. Available from: https://www.tandfonline.com/doi/full/10.1163/156856295X00427

27. Lin P, Chuang TL, Chen PZ, Lin CW, Gu FX. Low-Fouling Characteristics of Ultrathin Zwitterionic Cysteine SAMs. Langmuir [Internet]. 2019 Feb 5;35(5):1756–67. Available from: https://pubs.acs.org/doi/10.1021/acs.langmuir.8b01525

28. Lin P, Ding L, Lin CW, Gu F. Nonfouling property of zwitterionic cysteine surface. Langmuir. 2014 Jun 10;30(22):6497–507.

29. Bueno-Alejo CJ, Santana Vega M, Chaplin AK, Farrow C, Axer A, Burley GA, et al. Surface Passivation with a Perfluoroalkane Brush Improves the Precision of Single-Molecule Measurements. ACS Appl Mater Interfaces. 2022;

30. Wang Z, Zuilhof H. Antifouling Properties of Fluoropolymer Brushes toward Organic Polymers: The Influence of Composition, Thickness, Brush Architecture, and Annealing. Langmuir [Internet]. 2016 Jul 5;32(26):6571–81. Available from: https://pubs.acs.org/doi/10.1021/acs.langmuir.6b00695

31. Bürgi T. Properties of the gold-sulphur interface: from self-assembled monolayers to clusters. Nanoscale. 2015 Oct 14;7(38):15553–67.

32. Torres E, Biedermann PU, Blumenau AT. The role of gold adatoms in self-assembled monolayers of thiol on Au(111). Int J Quantum Chem [Internet]. 2009 Nov 15;109(14):3466–72. Available from: https://onlinelibrary.wiley.com/doi/10.1002/qua.22055

33. Green JBD, Clarke E, Porter MD, McDermott CA, McDermott MT, Zhong CJ, et al. On the Counter-intuitive Heterogeneous Electron Transfer Barrier Properties of Alkanethiolate Monolayers on Gold: Smooth versus Rough Surfaces. Electroanalysis. 2022 Dec 1;34(12):1936–52.

34. Guo LH, Facci JS, McLendon G, Mosher R. Effect of Gold Topography and Surface Pretreatment on the Self-Assembly of Alkanethiol Monolayers. Langmuir [Internet]. 1994 Dec 1;10(12):4588–93. Available from: https://pubs.acs.org/doi/abs/10.1021/la00024a033

35. Creager SE, Hockett LA, Rowe GK. Consequences of microscopic surface roughness for molecular self-assembly. Langmuir [Internet]. 1992 Mar 1;8(3):854–61. Available from: https://pubs.acs.org/doi/abs/10.1021/la00039a020

36. Losic D, Shapter JG, Gooding JJ. Influence of surface topography on alkanethiol SAMs assembled from solution and by microcontact printing. Langmuir. 2001 May 29;17(11):3307–16.

37. Vericat C, Vela ME, Benitez G, Carro P, Salvarezza RC. Self-assembled monolayers of thiols and dithiols on gold: new challenges for a well-known system. Chem Soc Rev. 2010 Apr 26;39(5):1805–34.

38. Hill HD, Millstone JE, Banholzer MJ, Mirkin CA. The role radius of curvature plays in thiolated oligonucleotide loading on gold nanoparticles. ACS Nano. 2009 Feb 24;3(2):418–24.

39. Kassam A, Bremner G, Clark B, Ulibarri G, Lennox RB. Place exchange reactions of alkyl thiols on gold nanoparticles. J Am Chem Soc. 2006 Mar 22;128(11):3476–7.

40. Colangelo E, Comenge J, Paramelle D, Volk M, Chen Q, Lévy R. Characterizing Self-Assembled Monolayers on Gold Nanoparticles. Bioconjug Chem [Internet]. 2017 Jan 18;28(1):11–22. Available from: https://pubs.acs.org/doi/10.1021/acs.bioconjchem.6b00587

41. Woehrle GH, Brown LO, Hutchison JE. Thiol-functionalized, 1.5-nm gold nanoparticles through ligand exchange reactions: Scope and mechanism of ligand exchange. J Am Chem Soc. 2005 Feb 23;127(7):2172–83.

42. Li X, Ma X, Zhang C, Xu R. A comparative study on the interaction of gold nanoparticles with trypsin and pepsin: thermodynamic perspectives. New Journal of Chemistry. 2022 Oct 17;46(44):21386–400.

43. Brewer SH, Glomm WR, Johnson MC, Knag MK, Franzen S. Probing BSA binding to citrate-coated gold nanoparticles and surfaces. Langmuir. 2005 Sep 27;21(20):9303–7.

44. Cametti M, Crousse B, Metrangolo P, Milani R, Resnati G. The fluorous effect in biomolecular applications. Chem Soc Rev. 2012 Dec 5;41(1):31–42.

45. Yu Q, Zhang Y, Wang H, Brash J, Chen H. Anti-fouling bioactive surfaces. Acta Biomater. 2011;7(4):1550–7.

46. Hedayati M, Marruecos DF, Krapf D, Kaar JL, Kipper MJ. Protein adsorption measurements on low fouling and ultralow fouling surfaces: A critical comparison of surface characterization techniques. Acta Biomater. 2020 Jan 15;102:169–80.

47. Zhang S, Wong CL, Zeng S, Bi R, Tai K, Dholakia K, et al. Metasurfaces for biomedical applications: Imaging and sensing from a nanophotonics perspective. Nanophotonics. 2021 Jan 1;10(1):259–93.

48. Spackova B, Wrobel P, Bockova M, Homola J. Optical Biosensors Based on Plasmonic Nanostructures: A Review. Proceedings of the IEEE [Internet]. 2016 Dec 1;104(12):2380–408. Available from: https://ieeexplore.ieee.org/document/7745836/

49. Horrer A, Krieg K, Freudenberger K, Rau S, Leidner L, Gauglitz G, et al. Plasmonic vertical dimer arrays as elements for biosensing. Anal Bioanal Chem. 2015 Sep 7;407(27).

50. Lin Y, Zou Y, Mo Y, Guo J, Lindquist RG. E-Beam Patterned Gold Nanodot Arrays on Optical Fiber Tips for Localized Surface Plasmon Resonance Biochemical Sensing. Sensors [Internet]. 2010 Oct 20;10(10):9397–406. Available from: http://www.mdpi.com/1424-8220/10/10/9397

51. Yavas O, Aćimović SS, Garcia-Guirado J, Berthelot J, Dobosz P, Sanz V, et al. Self-Calibrating On-Chip Localized Surface Plasmon Resonance Sensing for Quantitative and Multiplexed Detection of Cancer Markers in Human Serum. ACS Sens. 2018 Jul 27;3(7):1376–84.

52. Hall WP, Ngatia SN, Van Duyne RP. LSPR biosensor signal enhancement using nanoparticle-antibody conjugates. Journal of Physical Chemistry C. 2011 Feb 10;115(5):1410–4.

53. Austin Suthanthiraraj PP, Sen AK. Localized surface plasmon resonance (LSPR) biosensor based on thermally annealed silver nanostructures with on-chip blood-plasma separation for the detection of dengue non-structural protein NS1 antigen. Biosens Bioelectron. 2019 May 1;132:38–46.

54. Mayer KM, Lee S, Liao H, Rostro BC, Fuentes A, Scully PT, et al. A label-free immunoassay based upon localized surface plasmon resonance of gold nanorods. ACS Nano. 2008 Apr;2(4):687–92.

55. Funari R, Chu KY, Shen AQ. Detection of antibodies against SARS-CoV-2 spike protein by gold nanospikes in an opto-microfluidic chip. Biosens Bioelectron. 2020 Dec 1;169.

56. Nusz GJ, Marinakos SM, Curry AC, Dahlin A, Höök F, Wax A, et al. Label-Free Plasmonic Detection of Biomolecular Binding by a Single Gold Nanorod. Anal Chem [Internet]. 2008 Feb 1;80(4):984–9. Available from: https://pubs.acs.org/doi/10.1021/ac7017348

57. Marinakos SM, Chen S, Chilkoti A. Plasmonic Detection of a Model Analyte in Serum by a Gold Nanorod Sensor. Anal Chem [Internet]. 2007 Jul 1;79(14):5278–83. Available from: https://pubs.acs.org/doi/10.1021/ac0706527

58. Nath N, Chilkoti A. Label-Free Biosensing by Surface Plasmon Resonance of Nanoparticles on Glass: Optimization of Nanoparticle Size. Anal Chem [Internet]. 2004 Sep 1;76(18):5370–8. Available from: https://pubs.acs.org/doi/10.1021/ac049741z

Chapter 6 - Conclusions and Future Work

In this thesis, we have presented different ways to optimise plasmonic nanostructures. This has included examining the effect of nanostructure geometry on sensing capability as well as the effect of post-fabrication optimisation techniques such as annealing.

First, we assessed the sensing performance of arrays of different positive monomeric and trimeric structures as well as nanoholes with different shapes and lattice patterns. One of the main conclusions from this investigation is that resonance wavelength is the most important metric in determining the bulk refractive index sensitivity of a sensor with a highly linear relationship between sensitivity and resonance wavelength. In addition to assessing bulk refractive index sensitivity, we also examined local refractive index sensitivity. By using both thiol SAMs and aluminium oxide layers, we could assess how different structures responded to changes in their local environment. Due to the coupling experienced within trimeric structures during resonance, they exhibit a larger local refractive index sensitivity when compared to both monomeric and negative structures.

Despite showing lower bulk and local sensitivity when compared to positive structures, the investigation of nanohole arrays in this chapter also lead to some interesting conclusions. We show that triangular nanoholes have an advantage over square nanoholes in bulk refractive index sensing ability with their lower FWHM leading to higher FoM's. As there is very little literature examining the effect nanohole geometry has on plasmonic resonance, further study into the effect of nanohole geometry on its sensing ability would be an interesting avenue of research.

As all the structures discussed in Chapter 3 were annealed, the effects of annealing were extensively discussed in Chapter 4 of this thesis. Annealing nanostructures results in an increase in gold grain size, reducing losses during resonance due to electron scattering and as a result, decreasing the width of plasmonic resonances (1–6). This results in significantly higher FoM's for annealed structures when compared to non-annealed ones. However, there are drawbacks to annealing. One of these drawbacks is the effect annealing has on the surface properties of metallic nanostructures. For many biosensing applications, the formation of a thiolated SAM is crucial whether this be for applying a specific receptor to the surface of the sensor or simply changing the surface of the sensor to have a particular property such as a certain charge or level of hydrophobicity. After annealing, the surface of the nanostructures becomes much smoother which may make a conformal monolayer hard to form. Although there is disagreement about this point in the literature, the data presented in this thesis points

to a degradation in the quality and consistency of SAMs on annealed nanostructures when compared to non-annealed ones (7–12). In addition to the change in surface properties, thermal annealing also creates a rounding of the corners of plasmonic nanostructures. This causes their resonance to blue-shift and will degrade local sensing abilities due to less intense EM fields that occurs at rounded corners. To prevent this degradation, a protective layer was deposited onto the nanostructure arrays before annealing to prevent nanostructure deformation (1). Although this protective monolayer did not have an obvious effect on the resulting geometry of the nanostructures it did improve the sensing performance of the nanostructures in a few ways. It appears that the hydrofluoric acid used to remove the protective layer after annealing etches the substrate the nanostructures are fabricated on as well as creating surface roughness on the gold nanostructures. This has two beneficial effects. First, the etching of the glass results in a ~50% increase in bulk sensitivity as a result of more of the electromagnetic field of the structure being able to penetrate into the surrounding media. Second, the roughening effect the hydrofluoric acid has on the surface of the gold nanostructures, results in a more conformal SAM on the nanostructure while retaining the narrower peak created by annealing. This work could be expanded by assessing the effect of this HF treatment on a variety of different nanostructure geometries and further optimising the ideal amount of time to etch the glass before the structures become dislodged. Additionally, the use of this technique as a method for improving the biosensing potential of plasmonic nanostructures is an area that deserves more research.

Finally in this chapter, we examine the benefits of annealing using a femtosecond laser. By annealing using a femtosecond laser, the heating and cooling of the nanostructures becomes nearly instantaneous resulting which allows the grain boundaries to reorganise within the structure without allowing the structure to reach a lower energy state which would come with rounded corners. Future work to better understand this transformation has the potential to prevent nanostructure deformation when annealing almost entirely. The wavelength-specific nature of the sensor also results in a greater homogeneity of sensing elements as if the resonance wavelength of an element shifts outside the wavelength of the laser, it will stop being annealed unlike with traditional annealing methods. In addition to preventing deformation, using a laser to anneal nanostructures would allow for specific structures on a substrate to be annealed while others remain pristine. For example, if we have a multi-metallic sensor, heat sensitive structures/components or a substrate that is sensitive to temperature, annealing a sensor using traditional techniques may result in damage to the sensor. By using a wavelength-specific laser, we can avoid these potential problems by only annealing structures that are designed to fall within a specific resonance wavelength.

This thesis also investigates the application of LSPR metasurfaces as protein biosensors. In this chapter, we see the potential of anti-fouling surface SAMs to allow for reversible protein interactions and hence, repeated sensing. We also show the potential of cross-reactive sensing for discriminating different protein solutions, with preliminary results showing an array of ten sensors with different surface chemistries can discriminate between very similar proteins such as neutravidin and streptavidin.

A clear avenue for future work regarding protein sensing is assessing the benefits different plasmonic geometries could have on the limit of detection (LoD) for more traditional, specific sensing applications. By using geometries with unique properties as described in Chapter 3 combined with the optimisation techniques discussed in Chapter 4, we may be able to significantly reduce the LoD of label-free LSPR biosensors.

The overarching aim of Chapter 5 is to create a cross-reactive protein sensor utilising different surface chemistries to create differential interactions with proteins. Despite the successes shown when using disposable sensors for cross-reactive sensing, further research is needed to fully optimise this technique. Firstly, a more effective cleaning protocol would allow these sensors to be fully reusable and hence would reduce the negative effects that come from sensor-to-sensor variation such as fabrication inconsistency and inconsistency in SAM formation. This inconsistency in SAM formation on gold nanostructures is the factor that would be the most interesting to investigate further. In this thesis, we see indications that the surface properties of gold nanostructures effect the conformity of SAM formation, but more information is needed to ensure optimal conditions are being used to create these SAMs including the optimum time, solvent and concentration for each thiol. This study would require a comparison of the SAM formation on both annealed and non-annealed gold nanostructures using molecules of different lengths and with different functional groups. In addition, it would be interesting to observe if there are any geometrical effects on SAM formation such as if a curved or small nanostructure is less prone to dense SAM formation when compared to larger nanostructures which may provide a larger plane onto which thiols can initiate binding sites. These experiments could utilise tools such as atomic force microscopy, cyclic voltammetry or x-ray diffraction in order to get a better understanding as to how all these factors can be optimised. This optimisation would allow us to create dense, repeatable SAMs with more confidence ensuring that sensors have exactly the same properties each time they are fabricated.

References

1. Bosman M, Zhang L, Duan H, Tan SF, Nijhuis CA, Qiu CW, et al. Encapsulated annealing: Enhancing the plasmon quality factor in lithographically-defined nanostructures. Sci Rep. 2014 Jul 2;4.

2. Chen KP, Drachev VP, Borneman JD, Kildishev A V., Shalaev VM. Drude relaxation rate in grained gold nanoantennas. Nano Lett. 2010 Mar 10;10(3):916–22.

3. Oikawa S, Minamimoto H, Murakoshi K. Low-Temperature Annealing of Plasmonic Metal Arrays for Improved Light Confinement. The Journal of Physical Chemistry C [Internet]. 2022 Jan 20;126(2):1188–95. Available from: https://pubs.acs.org/doi/10.1021/acs.jpcc.1c08931

4. Zhang F, Proust J, Gérard D, Plain J, Martin J. Reduction of Plasmon Damping in Aluminum Nanoparticles with Rapid Thermal Annealing. The Journal of Physical Chemistry C [Internet]. 2017 Apr 6;121(13):7429–34. Available from: https://pubs.acs.org/doi/10.1021/acs.jpcc.7b00909

5. Higashino M, Murai S, Tanaka K. Improving the plasmonic response of silver nanoparticle arrays via atomic layer deposition coating and annealing above the melting point. Journal of Physical Chemistry C. 2020 Dec 17;124(50):27687–93.

6. Zheng YB, Juluri BK, Mao X, Walker TR, Huang TJ. Systematic investigation of localized surface plasmon resonance of long-range ordered Au nanodisk arrays. J Appl Phys. 2008;103(1).

7. Creager SE, Hockett LA, Rowe GK. Consequences of microscopic surface roughness for molecular self-assembly. Langmuir [Internet]. 1992 Mar 1;8(3):854–61. Available from: https://pubs.acs.org/doi/abs/10.1021/la00039a020

8. Green JBD, Clarke E, Porter MD, McDermott CA, McDermott MT, Zhong CJ, et al. On the Counter-intuitive Heterogeneous Electron Transfer Barrier Properties of Alkanethiolate Monolayers on Gold: Smooth versus Rough Surfaces. Electroanalysis. 2022 Dec 1;34(12):1936–52.

9. Li Z, Zhang L, Zeng S, Zhang M, Du E, Li B. Effect of surface pretreatment on self-assembly of thiol-modified DNA monolayers on gold electrode. Journal of Electroanalytical Chemistry. 2014 May 1;722–723:131–40.

10. Losic D, Shapter JG, Gooding JJ. Atomically Flat Gold for Biomolecule Immobilization and Imaging. Aust J Chem [Internet]. 2001;54(10):643. Available from: http://www.publish.csiro.au/?paper=CH01122

11. Losic D, Shapter JG, Gooding JJ. Influence of surface topography on alkanethiol SAMs assembled from solution and by microcontact printing. Langmuir. 2001 May 29;17(11):3307–16.

12. Guo LH, Facci JS, McLendon G, Mosher R. Effect of Gold Topography and Surface Pretreatment on the Self-Assembly of Alkanethiol Monolayers. Langmuir [Internet]. 1994 Dec 1;10(12):4588–93. Available from: https://pubs.acs.org/doi/abs/10.1021/la00024a033

Appendix

A.3. Appendices for Chapter 3

A.3.1 The Effect of Adhesion Layers on Simulations

Figure A.1 shows the effect of the titanium adhesion layer on both a positive and negative shape compared to an experimentally tested sensor. For the positive shape, the shift between with and without an adhesion layer is minimal and would reflect the magnitude of change expected in experimental data. However, for the negative shape, the influence of the adhesion layer is overestimated with the transmitted light intensity being reduced significantly compared to both the simulation without the adhesion layer and the experimental data.

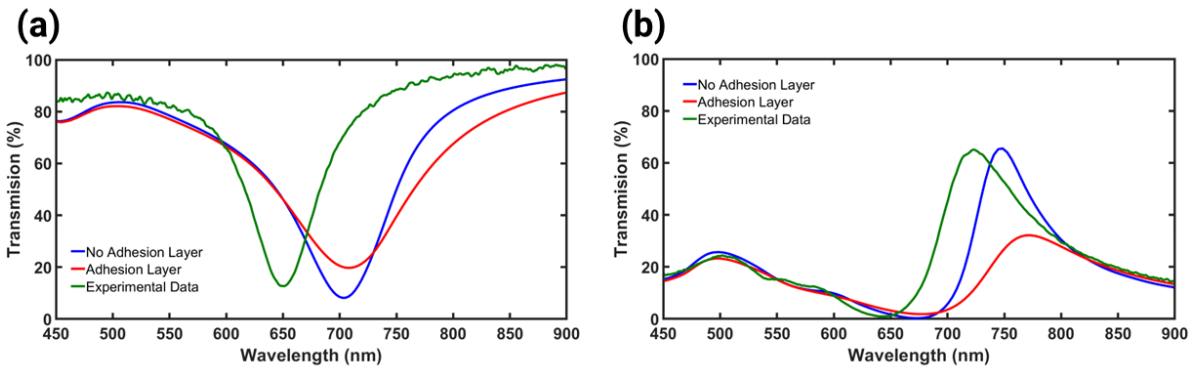

Figure A.1 - The effect of adhesion layers (a) on positive nanostructures (100 nm squares, Period 300 nm) and (b) negative nanostructures (115 nm, Period 350 nm).

A.3.2. The Origin of the 500 nm Peak for Negative Nanostructures

Figure A.2 shows simulated data of light passing through a gold film with changing thickness. As the film thickness decreases, the peak at 500 nm slightly increase in wavelength and significantly more light is transmitted. This shows that this peak is not a plasmonic resonance and is merely dictated by the thickness of the gold sheet.

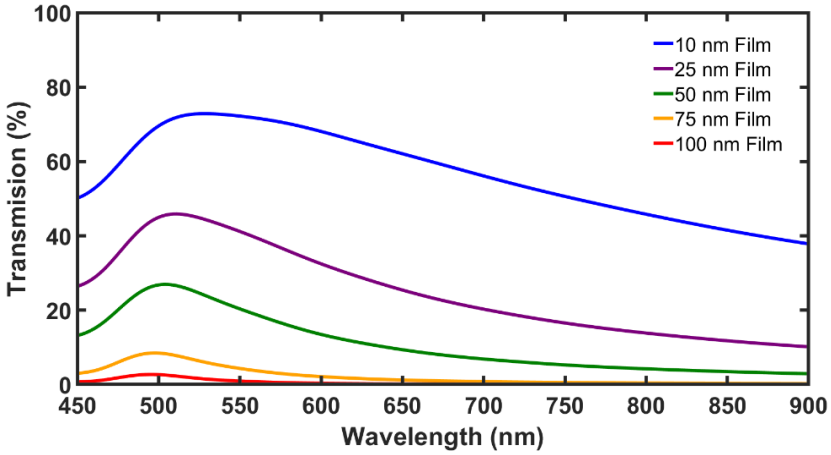

Figure A.2 - The origin of the 500 nm peak present in negative nanostructures

A.3.3. The Effect of Resonance Wavelength on Sensing at a Distance

Figure A.3 shows the difference in plasmonic spectra for both a 100 nm square and a 140 nm square when a 200 x 200 x 20 nm cuboid of refractive index 1.6 is placed 50 nm from the surface of the sensors. This results in a 0.74 nm resonance shift for the 100 nm square and a 1.93 nm shift for the

140 nm square. This is as a result of the larger field extent of the 140 nm square despite the fact is has a lower simulated maximum EM field when compared to the 100 nm square.

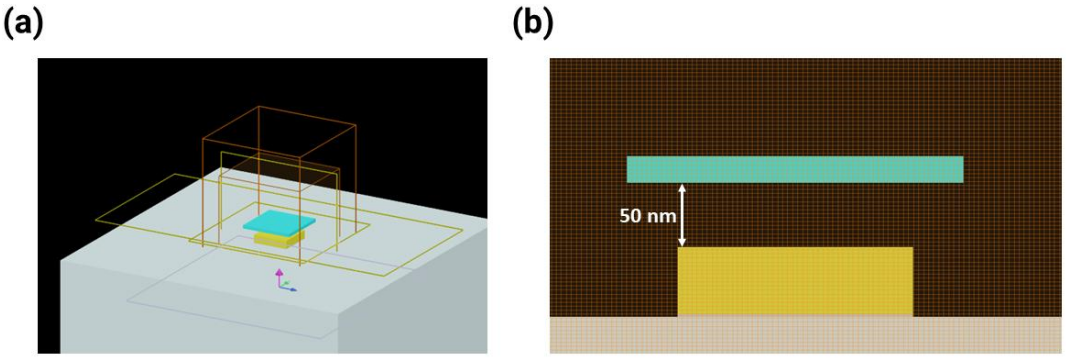

Figure A.3.1 – The simulation setup as described above. (a) The setup from an isometric perspective. (b) The view of the setup in the CC plane showing the distant object in comparison to the plasmonic structure.

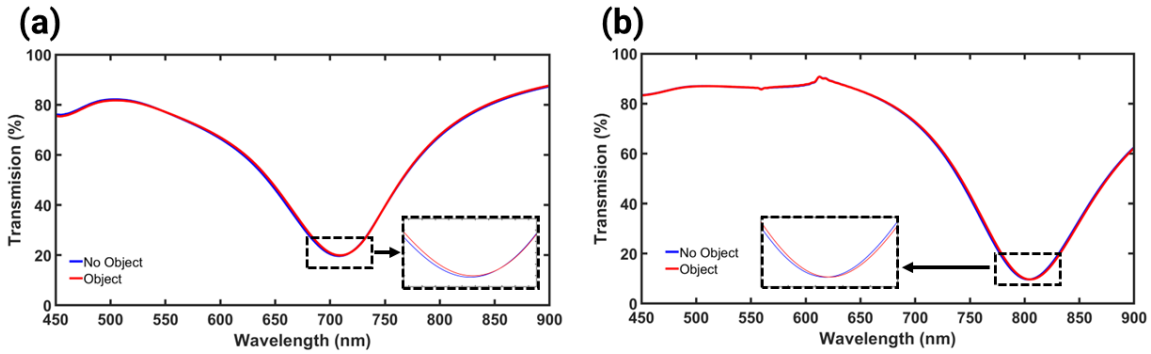

Figure A.3.2 - The ability of sensors with larger field extents to detect objects at a distance. (a) A 100 nm square sensor (period 300 nm) with a resonance wavelength shift of 0.74 nm. (b) A 140 nm square sensor (period 420 nm) with a shift of 1.93 nm.

A.3.4. The localised sensitivity of all described nanostructures as measured by thiolation

Structure	Period (nm)	Resonance Before Thiol (nm)	Resonance After Thiol (nm)	Shift (nm)
100 nm Disc	335	584.60 (+/- 0.30)	586.20 (+/- 0.19)	1.6
110 nm Disc	345	593.35 (+/- 0.20)	595.55 (+/- 0.10)	2.2
120nm Disc	355	605.40 (+/- 0.20)	607.90 (+/- 0.37)	2.5
130 nm Disc	365	618.85 (+/- 0.20)	621.20 (+/- 0.10)	2.35
140 nm Disc	375	634.00 (+/- 0.16)	636.70 (+/- 0.19)	2.7
100 nm Square	300	595.60 (+/-0.20)	596.95 (+/- 0.10)	1.35
110 nm Square	330	611.45 (+/- 0.24)	613.80 (+/- 0.19)	2.35
120 nm Square	360	631.70 (+/- 0.19)	634.45 (+/- 0.10)	2.75
130 nm Square	390	655.60 (+/- 0.20)	658.20 (+/- 0.10)	2.6
140 nm Square	420	681.55 (+/- 0.19)	683.35 (+/- 0.12)	1.8
180 nm Split Ring	235 edge-edge	660.30 (+/- 0.91)	666.05 (+/- 0.29)	5.75
190 nm Split Ring	235 edge-edge	682.85 (+/- 0.20)	688.10 (+/- 0.37)	5.25
200 nm Split Ring	235 edge-edge	691.95 (+/- 0.33)	696.00 (+/- 0.16)	4.05
210 nm Split Ring	235 edge-edge	736.55 (+/- 0.48)	740.10 (+/- 0.44)	3.55
220 nm Split Ring	235 edge-edge	766.15 (+/- 0.60)	770.95 (+/- 1.84)	4.8
80 nm Disc Trimer	235 edge-edge	590.00 (+/- 0.27)	591.90 (+/- 0.12)	1.9
90 nm Disc Trimer	235 edge-edge	605.75 (+/- 0.27)	610.95 (+/- 0.19)	5.2

100 nm Disc Trimer	235 edge-edge	633.95 (+/- 0.10)	640.25 (+/- 0.16)	6.3
110 nm Disc Trimer	235 edge-edge	654.90 (+/- 0.41)	665.35 (+/- 0.41)	10.45
120 nm Triangle Trimer	235 edge-edge	629.2 (+/- 0.19)	630.55 (+/- 0.1)	1.35
130 nm Triangle Trimer	235 edge-edge	648.65 (+/- 0.2)	652.45 (+/- 0.84)	3.8
140 nm Triangle Trimer	235 edge-edge	674.1 (+/- 0.60)	678.6 (+/- 0.12)	4.5
90 nm Square Holes	270	619.9 (+/- 0.2)	621.75 (+/- 0.22)	1.85
100 nm Square Holes	300	640.85 (+/- 0.12)	643.15 (+/- 0.2)	2.3
115 nm Square Holes	350	683.75 (+/- 0.16)	684.6 (+/- 0.12)	0.85
115 nm Square Hole	400	726.35 (+/- 0.12)	727.6 (+/- 0.12)	1.25
140 nm Square Hole	420 - Square Grid	771.8 (+/- 0.73)	773.35 (+/- 0.34)	1.55
140 nm Square Hole	420 – Hexagonal Grid	718.4 (+/- 0.3)	719.55 (+/- 0.1)	1.15
140 nm Triangular Hole	420 - Square Grid	747.4 (+/- 0.2)	747.9 (+/- 0.12)	0.5
140 nm Triangular Hole	420 – Hexagonal Grid	710.05 (+/- 0.1)	710.9 (+/- 0.25)	0.85

A.3.5. The localised sensitivity of all nanostructures as measured by the deposition of a 1 nm Al_2O_3 layer

Structure	Period (nm)	Resonance Before Aluminium Layer (1nm)	Resonance After Aluminium layer (1nm)	Shift (nm)
100 nm Disc	335	585.35 (+/- 0.25)	594.30 (+/- 0.29)	8.95
110 nm Disc	345	593.75 (+/- 0.22)	603.50 (+/- 0.00)	9.75
120nm Disc	355	605.65 (+/- 0.25)	617.00 (+/- 0.16)	11.35
130 nm Disc	365	619.70 (+/- 0.29)	631.40 (+/- 0.12)	11.70
140 nm Disc	375	634.65 (+/- 0.25)	646.50 (+/- 0.00)	11.85
100 nm Square	300	595.85 (+/- 0.12)	605.00 (+/- 0.00)	9.15
110 nm Square	330	611.80 (+/- 0.19)	623.00 (+/- 0.16)	11.20
120 nm Square	360	632.10 (+/- 0.20)	643.75 (+/- 0.00)	11.65
130 nm Square	390	655.60 (+/- 0.25)	668.70 (+/- 0.10)	13.10
140 nm Square	420	681.95 (+/- 0.19)	696.10 (+/- 0.12)	14.15
180 nm Split Ring	235 edge-edge	662.95 (+/- 0.51)	678.95 (+/- 0.24)	16.00
190 nm Split Ring	235 edge-edge	683.90 (+/- 0.25)	703.30 (+/- 0.19)	19.40
200 nm Split Ring	235 edge-edge	692.00 (+/- 0.42)	708.20 (+/- 0.46)	16.20
210 nm Split Ring	235 edge-edge	736.85 (+/- 0.34)	756.75 (+/- 0.50)	19.90
220 nm Split Ring	235 edge-edge	763.70 (+/- 2.81)	784.15 (+/- 2.31)	20.45
80 nm Disc Trimer	235 edge-edge	590.05 (+/- 0.40)	601.60 (+/- 0.25)	11.55
90 nm Disc Trimer	235 edge-edge	605.50 (+/- 0.16)	626.40 (+/- 0.49)	20.90
100 nm Disc Trimer	235 edge-edge	633.70 (+/- 0.40)	650.25 (+/- 0.16)	16.55
110 nm Disc Trimer	235 edge-edge	655.20 (+/- 0.37)	678.85 (+/- 0.25)	23.65
120 nm Triangle Trimer	235 edge-edge	636.95 (+/- 0.33)	654.85 (+/- 0.34)	17.90
130 nm Triangle Trimer	235 edge-edge	658.85 (+/- 0.89)	676.35 (+/- 0.34)	17.50
140 nm Triangle Trimer	235 edge-edge	684.65 (+/- 0.20)	704.60 (+/- 0.25)	19.95
90 nm Square Holes	270	620.05 (+/- 0.19)	624.10 (+/- 0.20)	4.05
100 nm Square Holes	300	640.85 (+/- 0.12)	645.80 (+/- 0.10)	4.95
115 nm Square Holes	350	682.60 (+/- 0.20)	687.70 (+/- 0.19)	5.10
115 nm Square Hole	400	725.75 (+/- 0.00)	730.50 (+/- 0.16)	4.75
140 nm Square Hole	420 - Square Grid	770.65 (+/- 0.30)	775.95 (+/- 0.46)	5.30
140 nm Square Hole	420 – Hexagonal Grid	717.55 (+/- 0.40)	726.30 (+/- 0.73)	8.75
140 nm Triangular Hole	420 - Square Grid	746.55 (+/- 0.10)	750.40 (+/- 0.25)	3.85
140 nm Triangular Hole	420 – Hexagonal Grid	707.65 (+/- 0.12)	713.85 (+/- 0.20)	6.20

A.4. Appendices for Chapter 4

A.4.1. Deformation in the RTA versus the chamber furnace

Figure A.4.1 shows the effect of annealing on square nanostructures in the RTA versus a chamber furnace. Annealing using the RTA causes less deformation of the structures due to the faster heating and cooling rates.

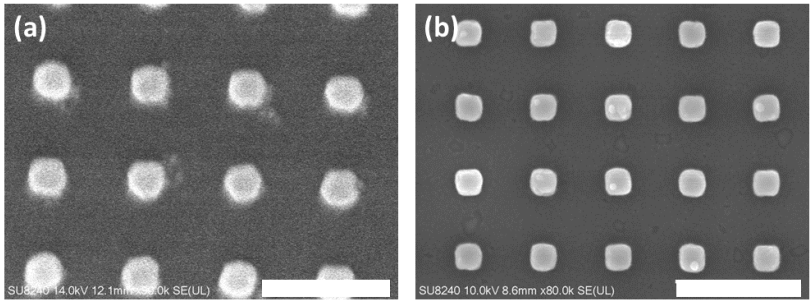

Figure A.4.1 - The effect of heating and cooling rates on nanostructure deformation. (a) Annealing 100 nm square sensors in a chamber furnace (b) Annealing 100 nm square sensors in an RTA. (Scale bars: 500 nm)

A.4.2. Sensor before and after laser annealing

Figure A.4.2 shows the spectra of sensors before and after being irradiated with lasers of different powers. The dashed lines represent the sensor before annealing and the solid lines represent their spectra after an hour of irradiation.

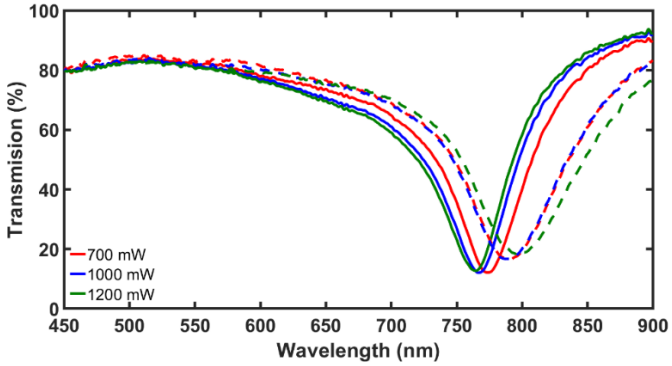

Figure A.4.2 – The effect of annealing with a laser at different powers. Dashed lines represent the spectra before annealing and solid lines represent data after annealing.

A.5. Appendices for Chapter 5

A.5.1. Removing Proteins using Tween-20 Solutions

Experiment 1

All sensors bare gold

Cleaning Protocol:

Step	Protocol
1	Wash sensor with water and EtOH, dry with N_2.
2	Incubate in PBS for 15 minutes
3	Take 3 readings in PBS
4	Wash sensor with water and EtOH, dry with N_2.
5	Incubate in 1mg/mL of BSA for 15 minutes
6	Take 3 readings in 1mg/mL BSA
7	Rinse in 5% Tween-20 solution
8	Dip-rinse sensor in Tween-20 50 times.
9	Sonicate in Tween-20 solution for 60s.
10	Agitate in Tween-20 solution for 5 minutes
11	Rinse with Tween, Water and EtOH. Dry with N_2.
12	Incubate in PBS for 15 minutes
13	Take 3 readings in PBS
14	Wash sensor with water and EtOH, dry with N_2.

Readings:

Detergent Solution	PBS Before (nm)	BSA (1 mg/mL) (nm)	PBS After(nm)
1% Tween	660.04 (+/-0.09)	664.31 (+/-0.12)	662.19 (+/- 0.21)
5% Tween	661.14 (+/- 0.14)	663.97 (+/- 0.12)	661.91 (+/- 0.25)

Experiment 2

Cleaning Protocol:

Step	Protocol
1	Rinse sensor in Tween-20 (5%) using 5 mL pipette
2	Dip rinse sensor in 3 mL Tween-20 (5%) solution 50 times (26)
3	Place sensor in 15/20 mL of Tween-20 solution
4	Repeat for each sensor.
5	Sonicate sensors for 60 s in Tween-20
6	Agitate in Tween for 5 minutes
7	Rinse sensors with tween, water then EtOH – dry with N_2

Readings:

Sensor Modification	PBS Before (n=1)	BSA (1 mg/mL) (n=5)	PBS After (n=2)
Bare	782.50 nm (+/- 0)	786.1 nm (+/- 0.87)	786.84 nm (+/- 0.44)
1-dodecanethiol (DDE)	763.45 nm (+/- 0)	767.77 nm (+/- 0.29)	767.45 nm (+/- 0.1)
1-octanethiol (OE)	777.93 nm (+/- 0)	782.53 nm (+/- 0.75)	782.44 nm (+/- 0.34)
Phenylethyl mercaptan (PEM)	784.28 nm (+/- 0)	788.90 nm (+/- 0.32)	789.33 nm (+/- 0.98)
12-Mercaptododecylphosphonic acid (MDP)	786.06 nm (+/- 0)	788.13 nm (+/- 1.15)	787.78 nm (+/- 1.3)

Experiment 3

All sensors used were bare gold.

Cleaning Protocol:

Step	Protocol
1	Rinse senor with flowing 5% Tween-20 / PBS for 30 s on each side.
2	Leave sensor in 5% Tween-20 / PBS bath for 5 minutes.
3	Rinse with DI Water.
4	Dry with N_2 gas.

Protein Readings:

Protein Used (1 mg/mL)	PBS Before (n=3)	Protein Reading (n=3)	PBS After (n=3)
BSA	750.93 nm (+/- 0.33)	754.52 nm (+/- 0.66)	754.71 nm (+/- 0.17)
Pepsin	750.58 nm (+/- 0.49)	754.96 nm (+/- 0.32)	752.52 nm (+/- 0.34)
Lipase	747.56 nm (+/- 0.27)	749.87 nm (+/- 0.29)	748.68 nm (+/- 0.20)

Experiment 4

All sensors used were bare gold.

Cleaning Protocol:

Step	Protocol
1	Rinse senor with flowing 5% Tween-20 / PBS for 30 s on each side.
2	Leave sensor in 5% Tween-20 / PBS bath overnight.
3	Rinse with DI Water.
4	Dry with N_2 gas.

Protein Readings:

Protein Used (1 mg/mL)	PBS Before (n=3)	Protein Reading (n=3)	PBS After (n=3)
BSA	747.13 nm (+/- 0.50)	749.46 nm (+/- 0.55)	749.79 nm (+/- 0.08)
Pepsin	744.98 nm (+/- 0.25)	746.32 nm (+/- 0.21)	745.50 nm (+/- 0.20)
Lipase	747.33 nm (+/- 0.05)	748.33 nm (+/- 0.45)	748.31 nm (+/- 0.37)

A.5.2. Determining the minimum concentration suitable for Cross-Reactive Sensing

Using the protein that showed the smallest shift in Section 5.3.4.3, experiments were run to determine at what concentration the protein caused an appreciable shift on a bare sensor.

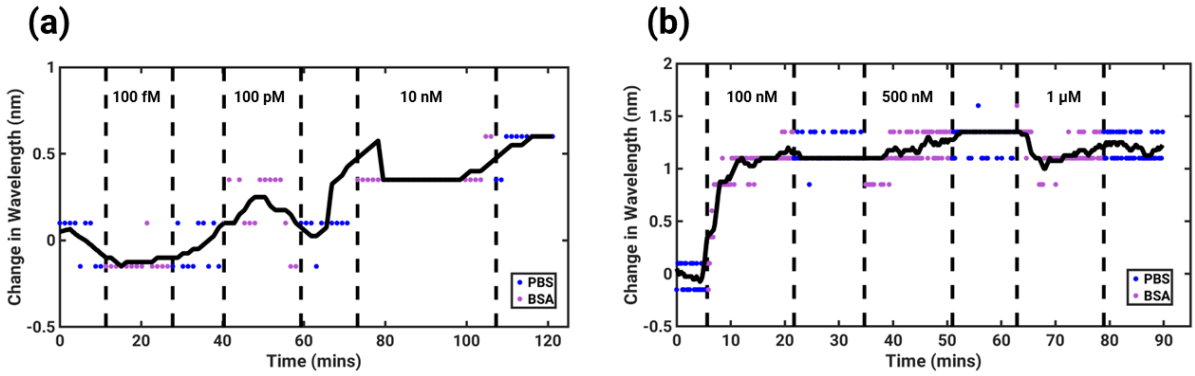

Figure A.5.1 – The response of bare, square sensors to BSA at different concentrations (a) Run 1: Very low concentrations (b) Run 2: Increased concentrations.

Despite a small shift being present at 10 nM, it was decided that 100 nM was an appropriate concentration as it still gave an easily detectable shift while being 50x lower than the concentration previously used.

A.5.3. Additional Data describing PCA and LDA for cross-reactive protein sensing

Eigenvalues for PCA graphs

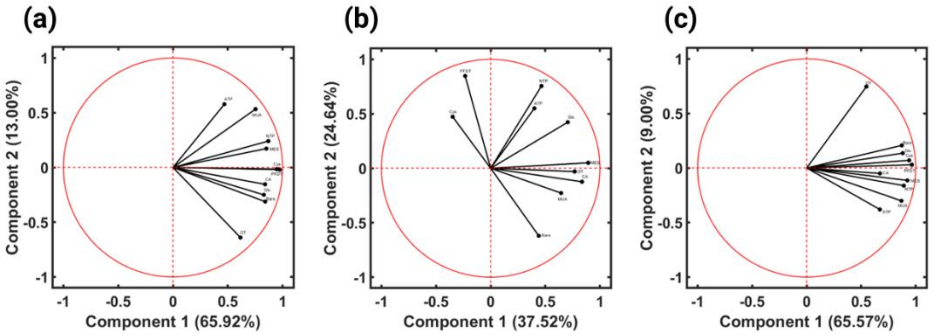

Figure A.5.2 – The Eigenvectors describing the PCA plots in Section 5.3.4. (a) Discrimination at 5 µM (b) discrimination at 100 nM (c) Discrimination when two 5 µM experiments are combined

PCA and LDA at 100 nM excluding Streptavidin

Below is the PCA and LDA for the data collected at a 100 nM protein concentration. The PCA shows the proteins to be better separated than is initially apparent on Figure A.5.3(a) although the LDA still shows that in this case lipase and BSA were challenging to separate.

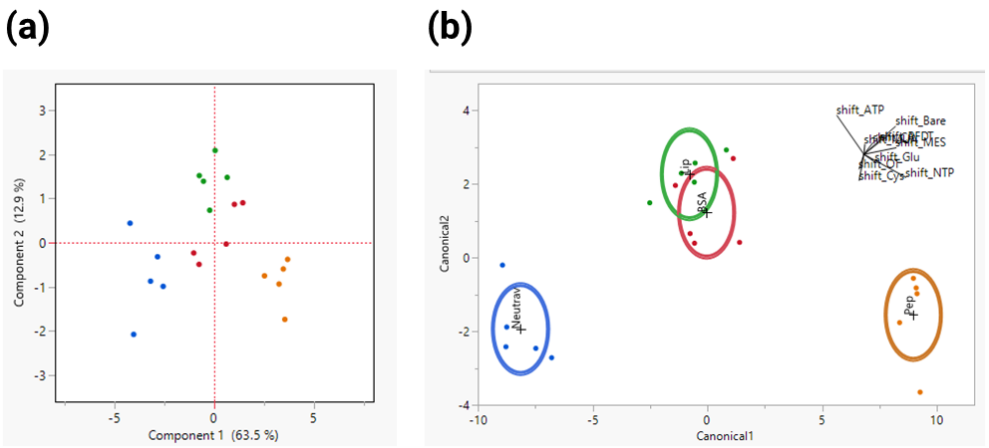

Figure A.5.3 - The multi-variant analysis of protein discrimination at 100 nM without streptavidin. (a) PCA (b) LDA

Classification Matrix of 5 µM Experiments Combined

The classification matrix of 5 proteins at 5 µM measured with two separate disposable chips is displayed in Table A.1. It shows an 88% classification success although this result may be artificially inflated due to issues related to oversampling.

Table A.5.1 - Classification Matrix combining two cross-reactive protein sensing experiments carried out on two separate plasmonic sensors.

Actual Protein	Predicated Protein				
	BSA	Lipase	Neutravidin	Pepsin	Streptavidin
BSA	9	1	0	0	0
Lipase	0	10	0	0	0
Neutravidin	0	0	10	0	0
Pepsin	0	2	0	8	0
Streptavidin	0	1	0	2	7

Publications and Conference Proceedings

Sperling JR, Poursat B, Savage L, Christie I, Cuthill C, Aekbote BL, et al. A cross-reactive plasmonic sensing array for drinking water assessment. Environ Sci Nano. 2023;10(12):3500–8.

Christie I, Peveler WJ, Clark AW. Optimising cross-reactive plasmonic arrays for biosensing applications. In SPIE-Intl Soc Optical Eng; 2023. p. 18.

Zou J, Stammers AC, Taladriz-Sender A, Withers JM, Christie I, Santana Vega M, et al. Fluorous-Directed Assembly of DNA Origami Nanostructures. ACS Nano. 2023 Jan 10;17(1):752–9.